Stratification and Internal Waves in lakes and reservoirs:

Theory, Experiments, Modeling, and Applications

Rafael de Carvalho Bueno
Tobias Bleninger
Andreas Lorke

February 22, 2024

Contents

How to use the book

This book presents a complete understanding of the fundamental concepts of lake mixing and internal wave generation in thermally stratified lakes and reservoirs. Readers will learn how internal waves in thermally stratified lakes and reservoirs are identified and analyzed, understanding all concepts related to spectral analysis and internal wave models, including a general overview of the historical developments responsible for revealing the beauty of the internal wave mechanisms. Readers will also have access to practical applications, similar to the problems faced by scientists. This book also introduces the idea of fluid mechanics applied to stratified systems and can be used to introduce some advanced concepts of fluid mechanics, which can be easily followed by undergraduate and graduate students, field engineers, researchers, or lake and reservoir managers and regulators.

Pre-requisites: Knowledge of the undergraduate level of Environmental Fluid Mechanics is essential. This includes topics such as those from conventional Fluid Mechanics courses, but also those from Environmental Engineering applications and/or Transport Phenomena, including substance and heat transport and mixing.

Additionally, we strongly recommend knowledge from course(s) on Turbulent Diffusion and Mixing, usually offered at graduate level. Topics should include mixing and transport processes in unstratified systems (without density effects), such as turbulent shear flows and dispersion, with a focus on the derivation and solutions of the advection-diffusion equation, including turbulence and dispersion effects.

Recommended books for acquiring graduate-level pre-requisite knowledge are:

- Heide Nepf MIT
- Scotts book combined with Gerhards lecture notes from EFM courses
- Fischer, chapter,
- Environmental Transport and Fate, 2012, Benoit Cushman-Roisin (free pdf download http://www.dartmouth.edu/~cushman/courses/engs43.html)

Not covered: Even though, highly related to stratified flows, this book does not cover topics on Jets and Plumes or outfall related applications. On one hand, because completely new concepts would need to be covered, and on the other hand, because already good books are available here for. Recommended reading in this respect is the following:

- Chapter from EFM
- My Thesis
- Book from Desal?
- Book by Phil Roberts

For specific (and advanced) topics on environmental fluid mechanics applications, we recommend Joe Fernando for all types of mixing and transport in environmental fluid systems.

Objective: Our main goal was to have a textbook for teaching and learning. We did not want another compendium of research articles or like (Web of Science, ResearchGate, GoogleScholar, and others do a good job with their search engines), but really something to study for students and provide help for teachers to set up simple experiments and learning stratified flows.

Publishing format: Open access format would be great. However, most students here (how it is nowadays in Europe or China?) still study with printed books or study materials, and I myself like to have a printed version too, but I might be old fashioned already. Of course, it could be the printed pdf, this would be fine for me too. Are your students using pdfs only or do they work with printed books? And what about university libraries? In Brazil, they still acquire lots of printed books, making them available to students. Thus, the only advantage of professional publishers is having a printed version, which is easily buyable in stores, and having an ISBN. We have seen that Springer (https://www.springeropen.com/books) also offers open access, but probably for considerable costs (minimum 1500 euros). An option could be publishing through university editors (university press). UFPR has one (https://www.editora.ufpr.br/), but very bad English information, and burocratic and intense peer review. Or using Amazon Publishing (https://www.amazon.com/gp/education-publishing), looks very simple, includes perfect marketing and ISBN, and print-on-demand, but needs to be commercial (at least 1 USD per book). Or just put the pdf with all additional files on a webpage, which can be updated whenever needed. UFPR has free hosting for that. Or through the water associations (e.g. IAHR or IWA, https://www.iwapublishing.com/).

Additional material This book provides a key link to additional materials, including up-to-date content, data sets, videos, and algorithms that are available to download on the website *www.website/stratifica.com*. The additional material provides useful support for the readers. Where appropriate, supplementary materials have been added to help readers better understand what is being discussed in this book. Many supplemental content is available for exercises and also to explain theories through laboratory experiments.

The icon shown in the margin will appear throughout the text where additional material is available.

The icon shown in the margin will appear throughout the text where additional video material is available.

Book structure: The book has a modular format, allowing it to be covered in different semesters and courses. Examples of combinations are as follows:

Acknowledgements: Scott, Jirka, Heidi Nepf, etc.

Chapter 1

Introduction

Internal gravity waves are propagating disturbances within a stable, density stratified fluid. In natural systems, such as oceans, lakes, and reservoirs, these density differences are often caused by variations in water temperature or salt concentrations. In laboratory settings, internal waves have been replicated using various fluids with differing densities (e.g., water and oil). To generate internal waves, similar to surface waves, the interface must be disrupted. *However, what sets surface waves apart from internal waves?*

Waves occur at fluid interfaces. These could be an interface between water and air or an interface between two phases (liquid and gas). These are commonly called surface waves. However, fluid interfaces can also occur within a fluid, and within the same phase, whenever there are density differences.

Internal waves occur in every perturbed stratified system. As the energy needed to increase a water volume in the air is greater than the energy needed to increase a water volume in the lower water density due to buoyancy force, internal waves often are much larger than surface waves generated by the same energy input. Internal waves have been reported in different scientific areas, from cosmology to limnology. The scientific community has observed internal waves in the ocean, atmosphere, lakes, reservoirs, ponds, and stellar interiors (Figure 1.1). In a simple view, the formation of internal waves depends on the stratification condition and the strength of the perturbation that creates the waves.

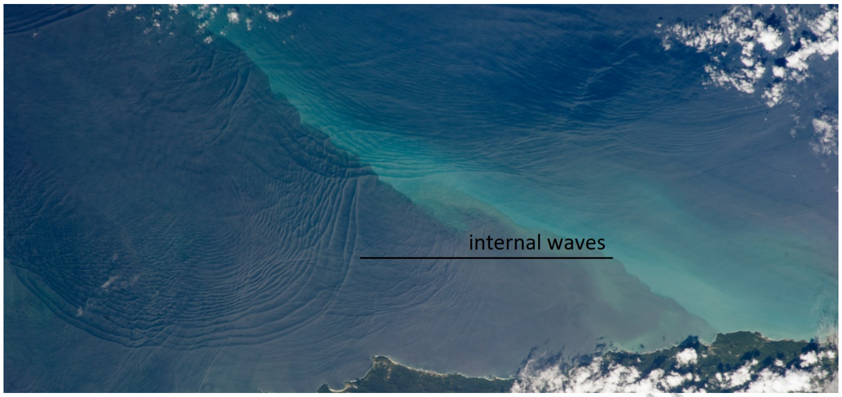

Figure 1.1 Train of internal waves off Northern Trinidad. Taken on January 18, 2013, from the International Space Station (NASA/JSC).

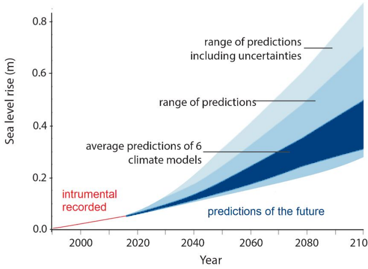

Figure 1.2 Every climate model predicts an increase in sea level in the next hundred years. The difference between the models is essentially due to the number of uncertainties. One of these uncertainties that needs to be better understood is the comprehension of the formation, evolution, and breaking of internal waves.

Recently, investigations have pointed out that internal waves of 170 meters in amplitude produced in the Luzon Strait, between Taiwan and the Philippines, are a key to understanding climate change and are an important missing piece of the puzzle in climate modeling (Alford et al., 2015). Internal waves in the ocean influence the ocean turbulence and consequently affect the ocean currents that carry heat and salinity around the globe. This phenomenon increases the mixing of the sea, which transfers heat from the upper ocean to deeper layers and leads to even more ice loss.

One of the first scientific observations[1] of internal waves in natural environment were made by Nansen (1897) during an expedition to the North Pole in 1893. The Norwegian explorer Fridtjof Nansen felt an extra drag on his Fram boat due to internal waves as the ship passed the Nordenskiold Archipelago, north of Siberia. He called the phenomenon *dead water*, reporting that it slowed his boat to a quarter of its normal speed:

> *"Fram appeared to be held back, as if by some mysterious force,*
> *and she did not always answer the helm. In calm weather,*
> *with a light cargo, Fram was capable of* 6 *to* 7 *knots.*
> *When in dead water she was unable*
> *to make* 1.5 *knots*[2]*."*
> F. Nansen (1897)

Ekman (1904), as a Ph.D. student motivated by the observations made by Nansen (1897), was the first researcher to study in detail the dead water effect:

---

[1] There are some evidences raised recently from ancient sources that indicate that internal waves could be one of the reasons behind the defeat of Antony and Cleopatra against Octavian at the naval battle of Actium. For years, historians have believed that the bad weather condition could be the probable reason for the surprised strategy adopted by Antony, which remained at a standstill for at least three hours, until midday, instead of, as was customary in ancient times, attacking at dawn.

[2] The knot is a unit of speed equal to one nautical mile per hour, 1 knot ≡ 1.852 km/h

> *"The present investigation of "Dead-Water" was occasioned by a letter in November 1898 from Prof. NANSEN asking my opinion on the subject. In my reply to Prof. NANSEN I remarked that in the case of a layer of fresh water resting on the top of salt water, a ship will not only produce the ordinary visible waves at the boundary between the water and the air, but will also generate invisible waves at the salt-water fresh-water boundary below; I suggested that the great resistance experienced by the ship was due to the work done in generating these invisible waves."*
>
> Vagn Walfrid Ekman (1904)

He explained that energy from the ship is transmitted to internal waves, which occur between layers of different densities. The boat experiences an important loss of steering power and, consequently, the speed of the vessel decreases dramatically (Figure 1.3). The interest of investigations involving internal waves grew up after 1965, when the most tragic incident involving a USA submarine with a crew of 129 on board fell down to deep water due to a passage of a large internal wave. The US Thresher submarine was going along the thermocline when an internal wave took it down quickly to really deep waters. The submarine lost orientation and had problems due to high pressure, killing the 129 people on board (Govorushko, 2011).

The Dead Water phenomenon described by Nansen (1897) was essentially caused by the friction caused by the boat. In contrast, internal waves observed in the South China Sea are mainly generated by tidal flow that passes through the topography of the seafloor and wind blowing through the ocean surface (Alford et al., 2015). As the internal waves propagate west from the Luzon Strait, they steepen, producing a package of internal waves propagating with 150 meters of amplitude. Similarly, the formation of internal waves in lakes and reservoirs is caused by many sources, but the action of the wind on the surface of the lake is one of the most important sources of energy for the internal wave fields (Mortimer, 1952). Since the system is closed, the long wave formed by the wind creates a stationary internal seiche.

The first observation of internal seiches in thermal stratified lakes was provided by Thoulet (1894), Watson (1903) was nevertheless the first limnologist to provide the right interpretation of internal seiches in thermally stratified lakes. Watson (1903) concluded that the temperature oscillation observed during a campaign in Lake Loch Ness was due to an uninodal baroclinic internal wave caused by the action of the wind on the lake surface.

Fridtjof Nansen (1861–1930, Norwegian) was born at Store Froen, near Oslo, the capital of Norway. He was an explorer, scientist, diplomat, humanitarian and Nobel Peace Prize laureate. Nansen received his Ph.D. from the University of Oslo in 1888. He made several discoveries with polar expeditions with his ship, *The Fram*, which served as an oceanographic, meteorological, and biological laboratory. In 1922 he was awarded the Nobel Peace Prize for his work on behalf of the victims of the First World War and related conflicts.

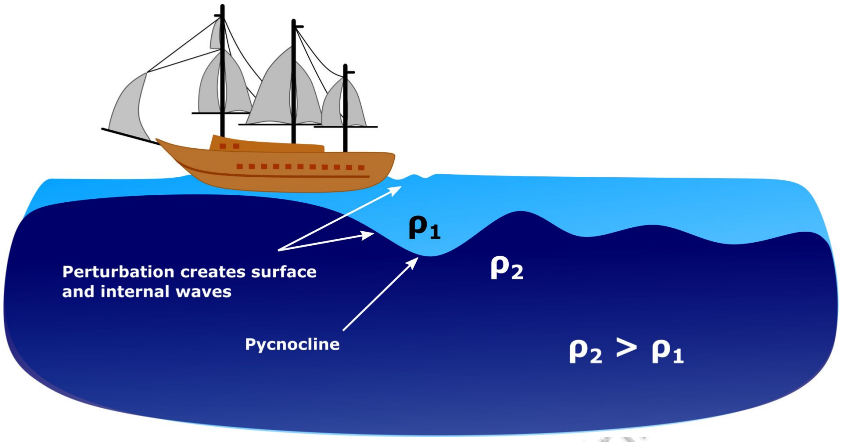

Figure 1.3 Interfacial wave generated by a boat moving on a two-layer stratified fluid.

Since the beginning of the 20th century, internal waves in thermally stratified lakes have been extensively studied. Many researchers have defended the importance of internal waves in lakes and reservoirs, spreading the knowledge of their existence and importance (Wedderburn, Williams, 1911; Mortimer, 1952). New technologies have provided a better understanding of internal wave patterns in lakes, revealing its strong influence on the system dynamics. Spectral analysis and improved water temperature measurement have proven to be useful for improving the detection of internal waves in lakes. A phenomenon that initially appeared to be excited just in some rare cases actually occurs frequently in lakes and reservoirs of different sizes and shapes, playing a crucial role in the turbulence level, biogeochemical cycles, and water quality of these ambients.

Recent research has addressed the importance of internal waves in reservoirs and lakes. Although only a small fraction of total wind energy crosses the surface boundary layer and energizes internal seiche fields (Wetzel, 2001; Wüest, Lorke, 2003; Wüest et al., 2000), studies have shown that the wind-induced internal wave is responsible for large-scale motions in the benthic boundary layer, favoring episodes of sediment resuspension (Bruce et al., 2008). Another study in Lake Geneva has observed that up to 40% of hypolimnetic volume was exchanged after internal seiche events (Umlauf, Lemmin, 2005). Internal seiches play an important role in the transfer of energy to smaller-scale motions and vertical mixing in the interior of the basin (Boehrer et al., 2000; Etemad-Shahidi, Imberger, 2006; Lorke, 2007; Preusse et al., 2010), and in the bottom boundary layer (BBL), where the friction of the wave-induced current bed can induce levels of turbulence 30 times higher than the magnitude found in the interior of the basin (Wüest, Lorke, 2009). Vertical displacement of water masses associated with internal seiches also affects the vertical position and distribution of phytoplankton and zooplankton and, consequently, also their productivity and ecological interactions (Mortimer, Horn, 1982; Rinke et al., 2007; Hingsamer et al., 2014), or can lead to anoxic water upwelling from deeper layers to the surface (Flood et al., 2021).

Importance of internal waves in stratified lakes

- Influence the population dynamics of many organisms, such as the metalimnetic phytoplankton and planktonic larvae populations;
- Influence the dispersion of pollutant discharges;
- influence sediment resuspension, which can lead to an increase in greenhouse gas emissions;
- Influence the thermal stratification, increasing vertical mixing, and instabilities in different regions of the system;
- In large lakes, influence the microclimate of the region;
- The break of the internal wave may affect the shoreline;

The knowledge of stratification and internal waves is essential for lake and reservoir management, as well as analysis of system changes due to climate change.

Table 1.1 Internal wave importance

Furthermore, seiche-induced bottom currents enhance oxygen penetration into sediment, favoring microbial organic matter degradation (Frindte et al., 2013).

The energy deposited into such long internal wave is eventually transformed through a down-scale energy cascade across the spectrum of internal wave due to the strong turbulence production in the benthic boundary layer. Observations have shown that it allows a fundamental internal seiche to degenerate into a train of propagating waves, increasing the mixing of the system (Boegman et al., 2005b). Recent observation also indicates that internal seiches are susceptible to break on the lakeshore, being a mechanism that creates a mixing hotspot in a specific location ().

According to Mortimer (1952), internal waves have been considered one of the most important processes of vertical water movement and mixing in lakes and reservoirs. Therefore, mechanical understanding and prediction of internal seiche activity is of great importance for understanding the energy flux paths, as well as ecological and biogeochemical processes in stratified lentic ecosystems.

This book starts with a detailed description of stratified flows in Chapter 2. Theories, experiments, and exercises on density-induced flows are presented. Chapter 3 applies and deepens the theory on stratified flows on lakes and reservoirs, covering all aspects of physical limnology.

Readers interested in field studies and laboratory experiments will find guidance and examples in Chapter 4. For those interested in further processing field or laboratory data, we present data processing techniques and spectral analysis in Chapter 5.

The theory on interfacial waves and internal waves is presented in Chapters 6 and 7, respectively, including numerical model applications.

Chapter 2

Stratified Flows

This chapter serves as an introductory section, outlining the fundamental knowledge necessary to comprehend the content of this book. Before delving into the topic of internal waves, it is essential to have a solid foundation in stratified fluids, fluid mechanics, and wave theory. Therefore, this chapter offers a concise review of these subjects to provide a comprehensive understanding of the motion of internal waves.

The chapter begins by providing an overview of stratified fluids, including an introduction to hydrostatics and the derivation of equations of motion. These concepts are presented to establish the necessary groundwork for subsequent discussions on internal waves.

For readers who are already familiar with the principles of fluid mechanics, wave theory, and stratified fluids, it is recommended to participate at least in the exercises provided at the end of this chapter. These exercises offer an opportunity to reinforce and apply the knowledge covered in the introductory material.

Figure 2.1 Pycnometer and densimeter, devices to measure the density of water.

2.1 Stratified Fluids

A stratified fluid is characterized by spatial variations in its properties. One of the primary and significant forms of stratification in lakes and reservoirs is the variation in density along the vertical axis, resulting in a layered system. Fluid stratification is a common occurrence in various natural environments, such as lakes, reservoirs, oceans, and the atmosphere, and in many aspects of our daily lives. Density stratification has a profound impact on mass fluxes, which may not always adhere to Fick's law (Imboden, 2003). Typically, the density gradient plays a crucial role in determining the pattern of fluid movement.

Therefore, we define a stratified fluid when its density ρ is a function of space and/or time,

$$\rho = f(x, y, z, t) = [\mathrm{M/L^3}].$$

In laboratory tanks, it is possible to create systems using different fluids, such as water-oil or water-gasoline. Due to variations in density, these fluids segregate into distinct layers. For instance, in the case of a water-oil mixture, the lighter oil will naturally rise to the top, while the denser water will settle at the bottom.

Now, let us address the question: "Can a fluid, such as water, have different densities?" The answer is a resounding "yes!". A compelling example can be observed when diving into a deep pool. As you descend further, you may see that the water is becoming progressively colder. This phenomenon occurs because as the water cools, its density increases, causing it to become heavier. In situations where density variations are primarily induced by temperature differences, we can refer to this as thermal stratification.

Liquid density
Densimeters and pycnometers (Figure 2.1) are devices that are used to measure the density of most liquids (e.g. water, oil, and gasoline). These devices make direct measurements based on the weight of a measured volume of fluid. In chapter 4 some exercises to measure the density of fluids are presented.

Chapter 4 is dedicated to experimentally demonstrating many ways to measure the density of different liquids.

Table 2.1 Liquid density measurements

Another way to vary the density of water is by varying its salt concentration (salinity), which is called salinity stratification. A classical example of this difference may be observed when you try to float in a swimming pool or in seawater. Technically, you can float more easily in seawater than in a swimming pool because seawater is heavier than freshwater. The buoyancy force over your body, a net upward force that acts over any object in any fluid, is higher in seawater, pushing you upward to the water surface.

Another way of altering the density of water is by adjusting its salt concentration. An illustrative example highlighting this disparity can be experienced when attempting to float in both a swimming pool and seawater. Technically speaking, it is generally easier to float in seawater compared to a swimming pool due to the higher density of seawater in relation to freshwater. This disparity in density results in a greater buoyancy force acting on your body. The buoyancy force, which represents the net upward force exerted on any object submerged in a fluid, becomes more pronounced in seawater, propelling you toward the water's surface.

The physical characteristics of water, such as temperature and salt concentrations, play a pivotal role in the generation of density stratification within the water. It should be noted that these influences extend beyond water alone. For example, Table 2.2 presents an illustration of how changes in temperature can lead to variations in air density. While numerous examples highlight fluid density as a function of various properties, our primary focus in this context revolves around waves within natural systems, placing our attention squarely on water.

Air density
Why is a room heater placed near the floor and an air conditioner near the ceiling?
The answer is related to the influence of temperature on air density, since colder air is denser than warm air, it sinks to the bottom of the room. Since we do not want a stratified system, we create the ideal conditions to mix the air to obtain a more uniform temperature throughout the room.

Table 2.2 Stratified air

Due to our focus on computing the water density of lakes and reservoirs, direct measurements utilizing densimeters and pycnometers are not practical. This could help measure the water density near the water surface, however, estimating water density in deeper regions is not as trivial. Extracting water samples at various depths from a stratified lake can be time-consuming and has the potential to alter water properties, thereby affecting water temperature and, subsequently, water density. To achieve high temporal and spatial resolution, we rely on indirect measurements for the analysis of water density. Understanding how physical properties, particularly temperature and salinity, influence the density of water becomes crucial as we recognize their significant impact.

2.1.1 Properties that control water density

Pressure

Under natural environmental conditions, pressure only significantly affects the density of water in the abyssal zone, which is a layer within the pelagic zone of the ocean, typically found between 1 km and 5 km deep. The presence of an immense water column above this region compresses the seawater, resulting in increased pressure in the deepest portions. As a consequence, high pressure causes a slight reduction in water volume, leading to a density change of approximately 4.5%.

☞ Water density in natural environments is influenced not only by variations in water temperature and salinity, but also by pressure, chemical compositions, and suspended matter.

In the abyssal zone, seawater exhibits slight compressibility, similar to the behavior observed in most gases under moderate pressures. However, it is important to note that for most lakes, which have depths less than 300 m, pressure does not exert a substantial influence on the density of the water. Instead, temperature and salinity emerge as the main driving factors shaping water density in such cases.

Temperature

The density of pure water at 4 °C and atmospheric pressure is approximately 1000 kg/m^3. When water is heated from 4 °C to 25 °C, for example, its density undergoes a slight decrease. This reduction in density can be attributed to the increased kinetic energy of the water molecules as heat is added. Consequently, water atoms vibrate at a faster rate, causing the water to occupy a larger volume. However, this expansion in volume is not readily noticeable. Even at its boiling point, when the system is saturated with thermal energy, the water begins to evaporate.

In contrast, when the water temperature drops below 4 °C, the formation of ice crystals begins within the lattice structure, leading to the formation of numerous stable hydrogen bonds among water molecules (see Figure 2.2). As water molecules occupy a larger volume due to the crystal formation, the density of water gradually decreases until it reaches the freezing point.

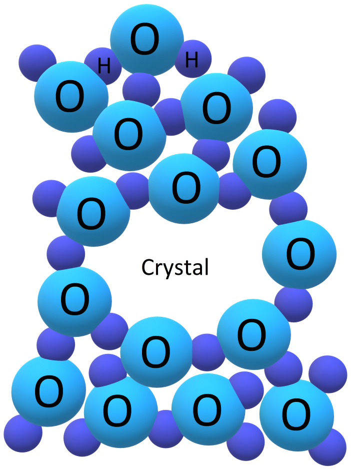

Figure 2.2 Liquid water structure with crystal lattice formation.

Salinity

Salinity can be defined as the ratio of conductivity. The conductivity of water is influenced by the number of dissolved ions per unit volume and their ability to move freely. However, the mobility of ions is also influenced by temperature. Moreover, temperature can affect the dissociation of molecules, leading to an increase in the number of ions in the solution. When examining natural water bodies such as seas, rivers, reservoirs, and lakes, the relationship between temperature and conductivity exhibits highly nonlinear behavior.

In these natural-water systems, higher temperatures, combined with an increased number of ions, result in elevated water conductivity. This relationship is the underlying reason why seawater demonstrates higher conductivity and, consequently, higher density compared to freshwater. The conductivity and density of water are thus influenced by factors such as temperature, ion concentration, and their complex interactions in natural water environments.

Equation of state

Since the late nineteenth century, researchers have dedicated their efforts to establishing an empirical equation capable of determining the density of water using measurements of pressure, temperature, and salinity. This endeavor to create an equation that encompasses the entire range of these three variables has been the result of numerous laboratory experiments that have been frequently reviewed over the years. The resulting equation, known as the **Equation of State for Water**, represents a nonlinear function used to estimate the density of water, or its specific volume, based on measurements of salinity, temperature, and pressure.

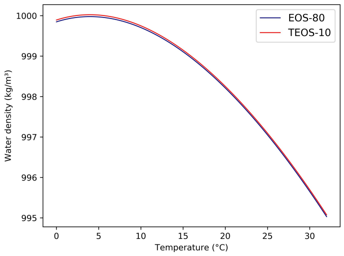

Figure 2.3 Comparison between water density calculated by EOS-80 and TEOS-10 as a function of temperature only.

One of the first formulations for pure water was proposed by Tait (1888), which allowed the estimation of the water density using only temperature values. Building on the predictive capabilities of Tait (1888), Kell (1975) presented a polynomial equation of state specifically designed for pure water. This equation remains valid for temperatures ranging from 0 °C to 30 °C and pressures below 10^8 Pa:

$$\rho_{\text{pure}} = \frac{\rho_o + a_1\,\tau - a_2\,\tau^2 - a_3\,\tau^3 + a_4\,\tau^4 - a_5\,\tau^5}{1 + a_6\,\tau}, \tag{2.1}$$

in which $\rho_o = 999.83952$ kg/m^3 is the reference density, τ is the water temperature, $a_1 = 16.945176$ kg/(m^3 °C), $a_2 = 7.9870401\ 10^{-3}$ kg/(m^3 °C^2), $a_3 = 46.170461\ 10^{-6}$ kg/(m^3 °C^3), $a_4 = 105.56302\ 10^{-9}$ kg/(m^3 °C^4), $a_5 = 280.54253\ 10^{-12}$ kg/(m^3 °C^5), $a_6 = 16.879850\ 10^{-3}$ 1/°C.

Throughout the years, numerous studies have made significant contributions by proposing new equations of state for water. These advances have been aimed at improving accuracy and expanding the range of applicability. Tanaka et al. (2001)have proposed a new equation of state for pure water valid from 0 °C to 40 °C, under a pressure of approximately 101 325 Pa:

$$\rho_{\text{pure}} = \rho_o - \frac{\rho_o(\tau + b_1)^2\ (\tau + b_2)}{b_3\ (\tau + b_4)}, \tag{2.2}$$

in which $\rho_o = 999.974950 \pm 0.00084$ kg/m^3, $b_1 = -3.983035 \pm 0.00067$ 1/°C, $b_2 = 301.797$ 1/°C, $b_3 = 522528.9$ 1/°C^2, and $b_4 = 69.34881$ 1/°C.

One of the most famous algorithms for estimating water density was introduced by Fofonoff, Millard (1983) in the UNESCO technical report (EOS-80). This algorithm, which gained significant recognition, utilizes a polynomial function consisting of 25 terms. It effectively characterizes the density of water as a function of temperature (τ), salinity (s), and pressure (p):

$$\rho(\tau, s, p) = \rho_o(1 - \beta_\tau(\tau - \tau_o) - \beta_s(s - s_o) - \beta_p(p - p_o)), \tag{2.3}$$

in which β_τ is the thermal expansion coefficient, β_s is the saline contraction coefficient, and β_p is the compressibility coefficient. The parameters β exhibit variations dependent on temperature, salinity, and pressure, resulting in interdependence between these variables. However, it is important to note that this interdependence extends beyond just pressure, salinity, and temperature. In reality, there exists a complex interplay among multiple quantities, including dissolved substances and the chemical and physical characteristics of water (see Figure 2.4).

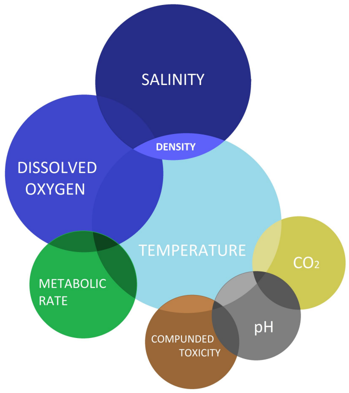

Figure 2.4 Water density and its direct and indirect interdependence.

The equation of state formulated by Fofonoff, Millard (1983) is valid for seawater, with a salinity range that typically varies from 2 to 42; however, observations have demonstrated good applicability even for salinities lower than 2.

Recently, important developments toward a new International Thermodynamic Equation of Seawater (TEOS-10) have been made. The new formulation updates the thermodynamic descriptions and also incorporates the solute compositions. Although the new approach is totally consistent with Maxwell's thermodynamic cross-differentiation relations and incorporates the new thermodynamic description of pure water, considering a thermally stratified lake without salinity contribution, the solutions of the EOS-80 and TEOS-10 equations of state fit very well with water density measurements, which presents a small difference between both expressions (Figure 2.3).

Taking into account the contribution of salinity s (g/kg) and temperature τ (°C) to the estimation of water density, equation 2.3 can be reduced to

$$\rho = \rho_{\text{pure}} + c_1 s + c_2 s^{1.5} + c_3 s^2, \tag{2.4}$$

in which ρ is the density of water, ρ_{pure} is the density of pure water (which can be obtained from equation 2.1), and the coefficients c_1, c_2, and c_3 are

$$\begin{aligned} c_1 &= 0.824493 - 0.0040899\tau \\ c_2 &= -0.005724 + 1.0227 \times 10^{-4}\tau \\ c_3 &= 0.00048314. \end{aligned}$$

☞ We neglected the c's coefficients terms with order higher than τ!

The influence of chemical composition and suspended matter

The presence of dissolved substances in water can introduce notable changes in density, particularly in geochemical lakes characterized by high concentrations of dissolved substances. While most natural systems do not exhibit elevated concentrations of dissolved substances that exert a dominant influence on water density, it is essential to recognize that in certain environments, such as areas with volcanic activity, this factor can become significantly important. For example, lakes or ocean regions experiencing volcanic activities might encounter elevated concentrations of specific substances, such as methane, which can have a substantial impact on water density. In such scenarios, the concentration of dissolved substances plays a significant role in the density variation, affecting the hydrodynamics of these systems.

Studies have identified that iron accumulation in deep waters and carbon dioxide and calcite production can generate density stratification (Hongve, 2002; Rodrigo et al., 2001), which could play an important role in vertical circulation and wave propagation (Boehrer et al., 2009, 2010).

To model chemical stratification, Boehrer et al. (2010) have proposed an implementation to incorporate the chemical composition of lakes to estimate water density. The algorithm RHOMV calculates the partial molal concentration of dissolved substances. The RHOMV algorithm is coupled with equation 2.1 for pure water, as proposed by Kell (1975), to determine the combined effect of temperature and chemical components on water density. Further information and an online calculator can be found at https://www.ufz.de/index.php?en=39156). This combined approach allows for a more comprehensive modeling of water density, taking into account both the temperature and the chemical composition of the water to capture the complexities of chemical stratification in lakes.

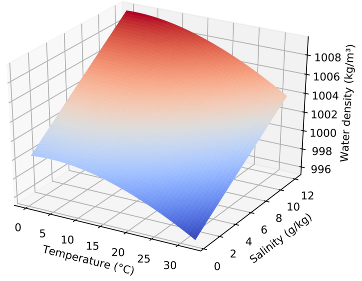

Figure 2.5 A temperature-salinity-density diagram obtained from equation 2.4.

To incorporate the density of dissolved substances, a straightforward approach is to consider the mass and volume of each substance based on its molar concentration. By summing the mass and volume contributions of each dissolved substance, the overall density of the solution can be found:

$$\rho = \frac{1 + \sum_i b_i M_i}{1/\rho_{\text{pure}} + \sum_i b_i \forall_i}, \tag{2.5}$$

in which ρ_{pure} is the density of pure water (kg/m^3), b_i is the molal[1] concentration (kg/mol), M_i is molar mass of the substance i (kg/mol) and $\forall_i$ is the partial volume of molal, which is slightly dependent on the ionic strength and temperature (which can vary depending on the substances considered). The index i indicates each dissolved substance present in the water.

Although electrical conductivity can be influenced by dissolved substances in lakes, the influence of the composition and concentration of solutes plays a crucial role in determining the water density of electrical conductivity, and cannot be accurately obtained by assuming constant coefficients as defined in equation 2.4. Based on this concept, Moreira et al. (2016) proposed a new approach to account for the composition of different solutes presented in geochemical lakes from temperature and conductivity measurements, but assuming two different coefficients (λ_o and λ_1) that vary depending on the composition and concentration of solutes in lakes:

$$\rho = \rho_{\text{pure}} + \lambda_o\, \kappa_{25} + \lambda_1\, \kappa_{25}(\tau - \tau_{25}), \tag{2.6}$$

in which ρ_{pure} is the density of pure water (kg/m)^3, κ_{25} is the electrical conductivity in 25 °C (mS/cm), τ is the temperature of water (°C), and $\tau_{25} = 25$ °C is the reference temperature.

Field measurements from different lakes have identified a dominance of double-charged ions (e.g. $CaSO_4$) and a higher concentration of solutes, leading to higher values of λ_o, which can vary between 0.48 kg cm/(m^{3}mS) and

---

[1] 1-molal means 1 mol dissolved in 1 kg of water

0.83 kg cm/(m^{3}mS) (Figure 2.6). However, unlike λ_o, which varies strongly, the coefficient λ_1 is around -0.0015 kg cm/(K mS m^3), not showing significant variations from lake to lake (Moreira et al., 2016).

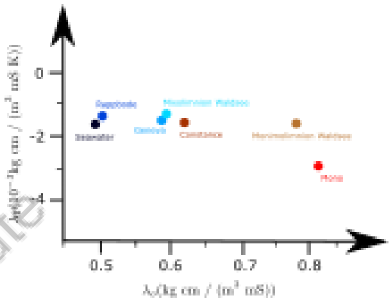

Figure 2.6 Distribution of values of λ_o and λ_1 obtained for different lakes (data assembled from Moreira et al. (2016)).

Fluid systems can also be stratified by the variation in suspended matter concentrations (e.g. turbidity currents). The contribution of suspended matter to the density of water can be obtained by the sum of the density of water for pure water (equation 2.4) and the fraction of the mass of suspended matter. Mathematically, it can be expressed as

$$\rho = \rho_{\text{pure}} + \sum_{i=0}^{i_{\text{sed}}} C^i \left(1 - \frac{\rho_{\text{pure}}}{\rho^i_{\text{sed}}}\right), \tag{2.7}$$

in which ρ_{pure} is the density of pure water, ρ^i_{sed} is the density of the suspended matter fraction i, i_{sed} is the number of suspended matter fractions, and C^i is the mass concentration of the suspended matter fraction i.

2.1.2 Stratification in natural water bodies

Now that we have identified the key factors that influence changes in water density, the question remains: *What mechanisms drive these variations in natural environments, such as lakes and oceans?*

The temperature in natural environments is largely governed by solar radiation, which comprises short-wave radiation emitted by the Sun. However, the overall heat flux at the water surface is a composite of various factors, including long-wave radiation (infrared and water surface radiation), evaporation, precipitation, heat convection, and inflow and outflow fluxes. This comprehensive balance provides information on the mechanisms through which heat energy is transferred to the water body.

Figure 2.7 shows the individual contributions of each component to the heat balance of Lake Zurich in different seasons. When the heat balance is positive, the lake serves as a heat reservoir and retains excess energy, commonly observed during the summer season. On the contrary, in the winter season, the lake experiences heat loss, with a substantial portion of the heat energy being transferred to the atmosphere.

In general, heat radiation strikes the water's surface, and some of this radiation is reflected back into the atmosphere. The remaining energy penetrates the surface of the water and is subsequently transported through the water column. However, because of the low conductivity of water, the amount of solar radiation absorbed decreases with increasing depth, resulting in the formation of a vertical thermal gradient. Consequently, surface water tends to be warmer than the deeper layers of the lake. During the summer season, most lakes exhibit a stratified structure characterized by three distinct vertical zones: the **epilimnion**, **metalimnion**, and **hypolimnion**.

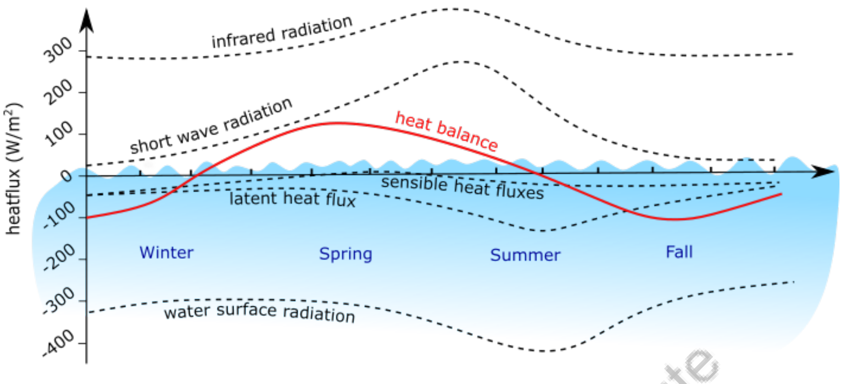

Figure 2.7 Illustration of the monthly heat flux based on Lake Zurich measurements (Imboden, Wüest, 1995). x-axis indicates the temporal (seasonal) variation. y-axis shows the amount of monthly mean heat flux between water and the atmosphere, in which negative values indicate that the lake is losing heat to the atmosphere.

The epilimnion is the top layer of a lake formed as a result of the accumulation of heat energy from the atmosphere. It is characterized by warmer temperatures and higher oxygen levels, creating favorable conditions for microorganisms at the base of the aquatic food web. This region plays a crucial role in supporting the biodiversity of lakes. Unlike terrestrial ecosystems, lighter organisms in aquatic ecosystems often have an advantage in capturing light because of the buoyancy effect, which keeps them near the water surface where light is abundant.

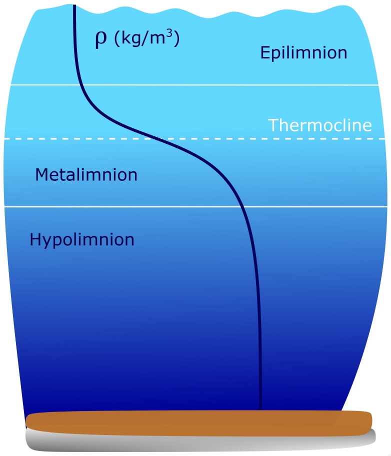

Figure 2.8 Thermal stratification in a typical stratified freshwater basin during summer.

The mixing of the epilimnion can vary depending on factors such as wind exposure and intensity. In larger water bodies with stronger winds, the depth of mixing can be greater. The temperature of the epilimnion can vary across different regions of the water body and is influenced by several factors, including wind intensity, lake size, suspended matter, accumulation of microorganisms, and geographical location.

In freshwater lakes, hypolimnion is the bottom layer and is characterized by being the coldest and densest layer. This zone is typically anoxic and supports only a limited number of species. When a lake is thermally stratified, the hypolimnion becomes isolated from atmospheric conditions, and as a result, solar radiation does not reach this zone.

The lower heat energy in the deeper regions of the hypolimnion is accompanied by the dissipation of turbulent kinetic energy from large-scale currents (Lemckert, Imberger, 1998; Wüest et al., 2000; Fricker, Nepf, 2000), internal seiches that propagate through the lake (Lorke et al., 2005; Cossu, Wells, 2013) and break near the lake shore (Carvalho Bueno de et al., 2023), the breaking and reflection of high-frequency internal waves (Thorpe, 1997; Michallet, Ivey, 1999; Lorke, 2007), and the interaction of large-scale currents with the lake's topography (Rudnick et al., 2003). These turbulent mechanisms within the hypolimnion often result in small temperature gradients, often lower than 0.03 °C (Lorke et al., 2005).

The metalimnion is a zone in freshwater lakes where the water temperature drops very fast, in which the point of greatest water temperature change is called the thermocline. It is important to note that, while some sources use the term "thermocline" interchangeably with "metalimnion," we will use "thermocline" specifically to refer to the point of the fastest temperature drop, avoiding any confusion. Thus, the thermocline represents a single interface within the larger metalimnion (Figure 2.8).

The metalimnion is situated between the epilimnion (upper layer) and the hypolimnion (lower layer) of the lake. Its thickness can vary from one body of water to another. In smaller lakes, the thermocline is typically located around 3 meters below the water surface. In larger lakes, the thermocline can extend up to 10 meters, and the metalimnion may occupy several meters (Hunkins, Fliegel, 1973).

Pycnocline

In a similar manner to the thermocline's relationship to temperature, the pycnocline represents a distinct point where the density gradient within the water column is most pronounced. Consequently, in freshwater lakes, the thermocline aligns with the pycnocline, as temperature variations serve as the main driving force behind the stratification observed throughout the water column (see Section 2.1.1).

In scenarios where the stratification of the water column is mainly driven by salinity, pycnocline corresponds to halocline, indicating the region with the fastest decline in salinity. However, in larger water bodies, such as oceans and extensive lakes and reservoirs, where both temperature and salinity contribute to density variations, the pycnocline does not necessarily align with any specific cline.

In these cases, the pycnocline characterizes the area within the water column where the density changes most abruptly due to combined effects of temperature and salinity fluctuations. It is important to note that the precise location and characteristics of pycnocline can vary depending on the specific water body and the interplay between temperature, salinity, and other substances.

Figure 2.9 provides a visual representation of the seasonal changes in the vertical temperature and density profiles of a hypothetical dimictic lake. This type of lake undergoes two complete mixing events per year, resulting in periods of unstratified conditions. Additionally, the lake is covered by ice during the winter season.

The figure helps illustrate the variations in temperature and density throughout the year, demonstrating the presence of pycnocline during stratified periods. Pycnocline is observed as a distinct layer where the density gradient is most pronounced, separating the stratified layers of the lake. By examining this figure, we can better understand how the temperature and density profiles fluctuate seasonally, with the presence of pycnocline being a notable characteristic during periods of stratification.

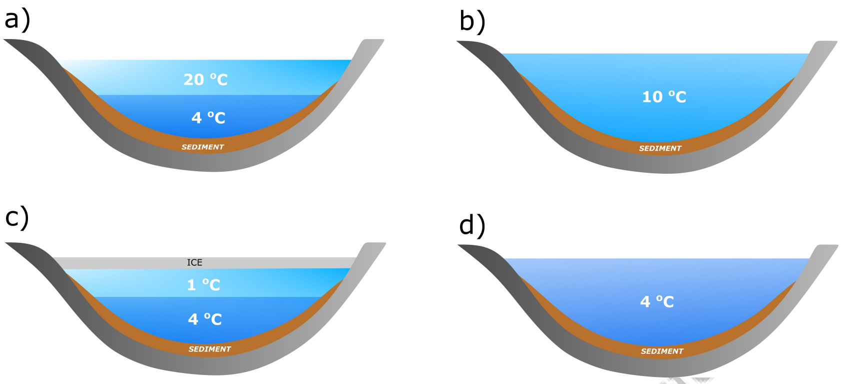

Figure 2.9 Seasonal variation of the thermal structure of a dimictic lake. a) Summer, b) Fall, c) Winter, and d) Spring.

2.2 Theory of Stratified Flows

Fluid mechanics is a fundamental field that encompasses the study of gases and liquids and their behavior under various conditions. It can be divided into two primary branches: fluid dynamics and statics. Fluid dynamics focuses on the movement of fluids, with subdisciplines such as aerodynamics and hydrodynamics. These branches share fundamental concepts, as the motion of both liquids and gases is governed by similar equations. However, their assumptions differ significantly.

Fluid dynamics employs mathematical techniques to solve problems, similar to those in other scientific disciplines. However, due to the complexity of real-world situations and limitations in current mathematical tools, substantial simplifications are often necessary. Consequently, the motion of fluids can be simplified in various ways. For instance, in aerodynamics, the influence of gravity is typically disregarded, while the compressibility of gases remains essential and cannot be overlooked, even in low-pressure conditions.

As our objective is to investigate stratified flows in natural systems, this section focuses solely on the flow of liquids, particularly water. While we disregard the compressibility of the liquid, we do take into consideration the influence of gravity. It is important to note that this chapter provides a comprehensive review of hydrostatics and hydrodynamics, which are crucial for successfully navigating this book. A solid grasp of mathematical techniques and fundamental principles of fluid mechanics will undoubtedly facilitate comprehension in this section. To initiate our analysis, we begin by examining the hydrostatic properties of stratified flow, assuming that readers are already well acquainted with the fundamental concepts of fluid mechanics.

2.2.1 Hydrostatic

The presence of a gravitational field significantly affects buoyant forces and has a profound influence on the dynamics of stratified flows (Socolofsky, Jirka, 2005). Density variations between layers give rise to buoyancy-restoring forces that alter density and pressure, thus suppressing vertical movements. This stratification enables us to characterize the behavior of the system in terms of stability, which can manifest itself in three states: unstable, neutral, and stable (Figure 2.10).

The neutral fluid state is characterized by an unstratified fluid, where the particles encounter similar resistance to motion in all directions (Socolofsky, Jirka, 2005). On the contrary, unstable stratification occurs when a heavier fluid resides above a lighter fluid. When a fluid parcel is displaced, it tends to move away from its original position, leading to elevated levels of mixing and turbulence. Table 2.2 provides examples of mechanisms that exemplify the conditions of unstable stratification.

In lakes and reservoirs, these events occur primarily near the surface of the water, where the wind generates a thin, uniform layer. This process, known as *surface cooling*, induces a decrease in the water temperature close to the water surface. Consequently, there is an increase in vertical mixing of surface waters.

▶ V2.1

However, stable stratified fluids exhibit a configuration in which a heavier layer resides above lighter layers. When a fluid parcel is displaced in such a system, it tends to retrace its path back to its original position. Freshwater lakes frequently show stable stratification as a result of the mechanism described in Section 2.1.2. In this context, the warmer layer, formed by atmospheric heat energy, is primarily concentrated near the water surface. It is important to note that stable stratification is the only state capable of supporting internal waves within the fluid.

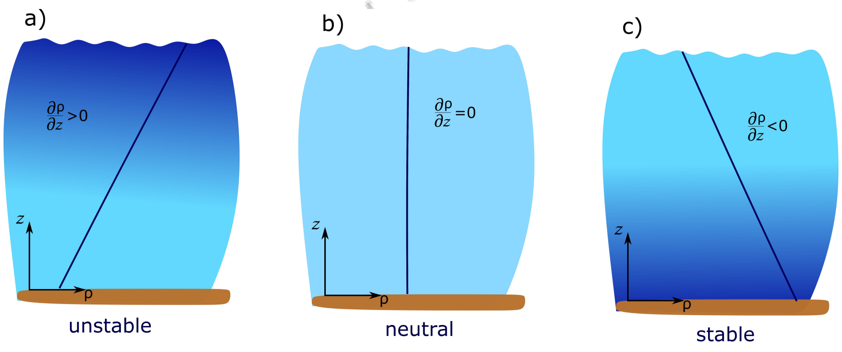

Figure 2.10 Stability definition according to the density profile.

Since internal gravity waves are exclusively supported in stable stratified systems, our analysis primarily centers on stable stratification conditions. However, we also touch upon an unstable condition arising from internal wave motion and the mixing regimes within lakes.

Buoyancy-Frequency

An essential characteristic of a stratified environment with density distribution is the **buoyancy frequency**, also known as the **Brunt-Väisälä frequency**. This frequency serves as a measure of static stability within the system. To comprehend the static stability, we begin by assuming the presence of a perturbation, which, in the case of static stability, can be described as a vertical displacement of a fluid parcel $\forall$.

Initially, we consider the vertical movement of a water parcel ρ_{par} with a volume $\forall$, which is balanced by buoyancy force F_b and gravitational force F_m, thus maintaining equilibrium between the fluid parcel and the surrounding ambient fluid ρ_{amb} (Figure 2.11):

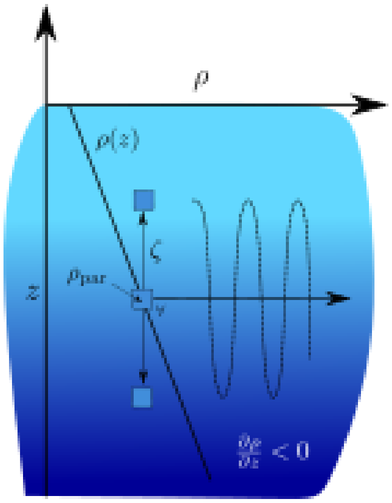

Figure 2.11 The movement of a fluid parcel $\forall$ by a small amount ζ from the equilibrium position.

$$m_{\text{par}} \frac{\partial^2 \zeta}{\partial t^2} = -g\left(\rho_{\text{par}} - \rho_{\text{amb}}\right)\forall = g\left(\rho_{\text{amb}} - \rho_{\text{par}}\right)\forall, \tag{2.8}$$

in which ζ is the vertical displacement and m_{par} is the mass of the fluid parcel. Note that the parcel volume is $\forall = m_{\text{par}}/\rho_{\text{par}}$.

Considering that the volume parcel $\forall$ undergoes density variations as a result of vertical displacement, we can modify equation 2.8 to determine the necessary acceleration needed to induce this change:

$$\frac{\partial^2 \zeta}{\partial t^2} = \frac{g}{\rho_{\text{par}}}\left(\frac{\partial \rho_{\text{amb}}}{\partial z} - \frac{\partial \rho_{\text{par}}}{\partial z}\right)\zeta, \tag{2.9}$$

in which equation 2.9 is an ordinal differential equation in ζ with a general solution $\zeta = \cos(\omega\, t)$

Applying the general solution to 2.9, we find

$$-\omega^2 - \frac{g}{\rho_{\text{par}}}\left(\frac{\partial \rho_{\text{amb}}}{\partial z} - \frac{\partial \rho_{\text{par}}}{\partial z}\right) = 0. \tag{2.10}$$

Rearranging equation 2.10, we can find

$$\omega = \sqrt{-\frac{g}{\rho_{\text{par}}}\left(\frac{\partial \rho_{\text{amb}}}{\partial z} - \frac{\partial \rho_{\text{par}}}{\partial z}\right)}. \tag{2.11}$$

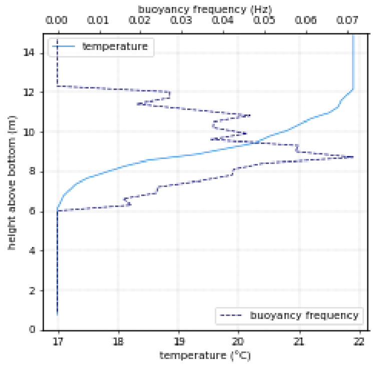

Figure 2.12 The distribution of buoyancy frequency (Hz), derived from typical temperature profiles.

Assuming that the variation of pressure p causes a density change in the parcel volume that leads to a density similar to the surrounding ($\rho_{\text{par}} = \rho_{\text{amb}}$), we can write equation 2.11 as

$$\omega = \sqrt{-\frac{g}{\rho_{\text{amb}}}\left(\frac{\partial \rho_{\text{amb}}}{\partial z} - \frac{\partial \rho_{\text{amb}}}{\partial p}\frac{\partial p}{\partial z}\right)} \tag{2.12}$$

The potential density ρ_{amb} can be calculated taking the contribution of temperature τ, salinity S, and pressure p, leading to

$$\frac{\partial \rho_{\text{amb}}}{\partial z} = \frac{\partial \rho_{\text{amb}}}{\partial \tau}\frac{\partial \tau}{\partial z} + \frac{\partial \rho_{\text{amb}}}{\partial S}\frac{\partial S}{\partial z} + \frac{\partial \rho_{\text{amb}}}{\partial p}\frac{\partial p}{\partial z}. \tag{2.13}$$

By combining equation 2.12 with equation 2.13, we obtain the following expression:

$$\omega = \sqrt{-\frac{g}{\rho_{\text{amb}}}\left(\frac{\partial \rho_{\text{amb}}}{\partial \tau}\frac{\partial \tau}{\partial z} + \frac{\partial \rho_{\text{amb}}}{\partial S}\frac{\partial S}{\partial z}\right)}, \tag{2.14}$$

The expression 2.14 indicates that, while pressure may contribute to changes in water density, it does not play a role in stability considerations. Often, for simplicity, equation 2.14 is commonly presented as

$$\omega \equiv N = \sqrt{-\frac{g}{\rho}\frac{\partial \bar{\rho}}{\partial z}}, \tag{2.15}$$

in which g is the gravitational acceleration, $\bar{\rho}$ is the potential density, ρ is the characteristic density of the fluid.

Physically, the buoyancy frequency represents the frequency at which a displaced fluid volume would oscillate when vertically displaced. In this mechanism, the fluid parcel gains vertical velocity and, upon reaching its initial level, its inertia drives it further downward. Consequently, the parcel is lifted upward by a buoyant force, resulting in persistent oscillations around the equilibrium level (Cushman-Roisin, Beckers, 2011).

The buoyancy frequency characterizes the maximum frequency of internal waves (oscillatory disturbances) that the stratification can sustain before being overwhelmed by turbulence and mixing. A larger density difference between the epilimnion and hypolimnion corresponds to a higher buoyancy frequency, resulting in an increased stability of the system. As a consequence, the metalimnion layer acts as a barrier to the transfer of heat, aquatic microorganisms, chemical compounds, and nutrients. Furthermore, the metalimnion layer contributes to reducing current velocities and affecting light reflection (Imberger, 1998).

Buoyancy frequency distribution
The buoyancy frequency can be obtained for thermally stratified lakes and has a typical distribution as illustrated in Figure 2.12. Generally, the buoyancy frequency is estimated as

$$N(z) = \sqrt{-\frac{g}{\rho(i+1)}\frac{\Delta\rho}{\Delta z}}, \tag{2.16}$$

in which Δz is the distance between two measurements, ρ is the mean water density, and $\Delta\rho = \rho(i+1) - \rho(i)$. The index i indicates the discretized position of each measurement, where $i = 0$ is the measurement closest to the water surface. The water density is obtained from the equation of states described in Section 2.1.1 and is based on discretized measurements.

Table 2.3 Buoyancy frequency in stratified lakes

Lake stability

Lake stability, also known as Schmidt stability, refers to the energy required per unit of surface area to overcome the resistance to mechanical mixing within a lake. It serves as an indicator of both the strength of stratification and the density stability of the water column. The concept of lake stability was initially derived by Schmidt (1928) and later modified by Mortimer (1959).

Schmidt stability, typically expressed in units of $\mathrm{J/m^2}$, quantifies the amount of energy needed to homogenize the entire system to the same temperature without any additional heat flux.

Figure 2.13 shows a lake that exhibits a typical stratification pattern. It is important to note that the density difference that must be overcome during mixing by each volume element is directly proportional to $\Delta\rho = (\rho_z - \overline{\rho})$. Here, ρ_z represents the density at a specific depth z, while $\overline{\rho}$ represents the mean density of the system, which is obtained when the lake is thoroughly mixed. The mean density is defined as:

$$\overline{\rho} = \frac{1}{\forall}\int_0^H \rho_z A_z \,\mathrm{d}z, \tag{2.17}$$

where $\forall$ is the volume of the lake, H is the total water depth, and A_z is the interfacial area at depth z. It is important to note that the mean density $\overline{\rho}$ is not simply an average calculated from a single profile. This is only applicable to rectangular tanks. In other cases, the mean density must be calculated considering the center of mass of the stratified lake, taking into account the total volume of the lake $\forall$.

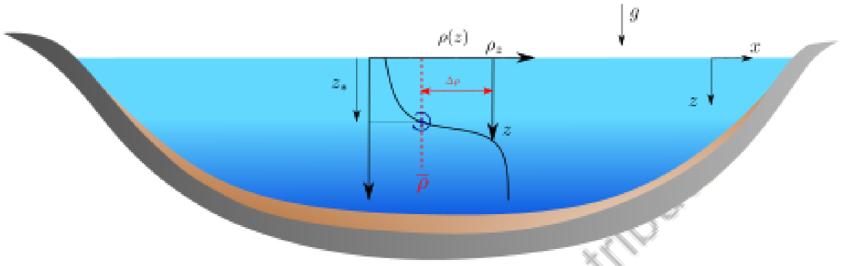

Figure 2.13 Typical lake and the work required to break the stratification.

The force associated with this density gradient can be expressed as

$$F = \int (\rho_z - \overline{\rho})\ g\ A_z\ \mathrm{d}z, \tag{2.18}$$

in which g is the acceleration of gravity.

If we consider the forces acting at a distance $d = z - z_*$, where z_* represents the center mass of the lake (the depth at which the mean density is located), we can express the work required per unit area for this transformation as follows

Another approach
There is another approach to evaluate lake stability (equation 2.22) as described by Schmidt (1928). However, although the expression gives the same result, the value is negative, indicating that the water below the centroid supply works for the system (Idso, 1973). Obviously, this concept is not correct when we want to find the total work, which indicates that equation 2.22 is "*more meaningful*" (Idso, 1973).

Table 2.4 Schmidt stability.

$$W_s = \frac{F\ d}{A_o} = \frac{g}{A_o}\int_0^H (\rho_z - \overline{\rho})\ (z - z_*)\ A_z\ \mathrm{d}z. \tag{2.19}$$

Expanding 2.19 gives us:

$$\begin{aligned}
W_s &= \frac{g}{A_o}\int_0^H (\rho_z - \overline{\rho})\ (z - z_*)\ A_z\ \mathrm{d}z,\\
&= \frac{g}{A_o}\left(\int_0^H \rho_z z\ A_z\ \mathrm{d}z - \int_0^H \rho_z\ z_*\ A_z\ \mathrm{d}z - \int_0^H \overline{\rho}\ z\ A_z\ \mathrm{d}z + \int_0^H \overline{\rho}\ z_*\ A_z\ \mathrm{d}z\right)\\
&= \frac{g}{A_o}\left(\int_0^H \rho_z z\ A_z\ \mathrm{d}z - z_* \underbrace{\int_0^H \rho_z\ A_z\ \mathrm{d}z}_{\overline{\rho}\ \forall} - \overline{\rho} \underbrace{\int_0^H z\ A_z\ \mathrm{d}z}_{z_v\ \forall} + \overline{\rho}\ z_* \underbrace{\int_0^H A_z\ \mathrm{d}z}_{\forall}\right),
\end{aligned}$$

in which the second term of the right-hand side can be simplified by applying the mean density, exactly as defined in 2.17. The integration specified in the last term is a clear description of the lake volume $\forall$, and the integration of the third term on the right-hand side is the definition of the depth of the centroid (geometric center):

$$z_v = \frac{1}{\forall}\int_0^H z\ A_z\ \mathrm{d}z. \tag{2.20}$$

Thus, finally, we have

$$W_s = \frac{g}{A_o}\left(\int_0^H \rho_z z\ A_z\ \mathrm{d}z \cancel{- z_* \overline{\rho}\ \forall} - \overline{\rho} z_v\ \forall \cancel{+ \overline{\rho}\ z_*\ \forall}\right),$$

$$W_s = \frac{g}{A_o}\left(\int_0^H \rho_z z\ A_z\ \mathrm{d}z - \overline{\rho} z_v\ \forall\right), \tag{2.21}$$

By substituting Equation 2.17 into Equation 2.22, we can determine the well-known form of **Schmidt Stability**

$$W_s = \frac{g}{A_o}\left(\int_0^H \rho_z z\ A_z\ \mathrm{d}z - z_v \int_0^H \rho_z A_z\ \mathrm{d}z\right),$$

$$W_s = \frac{g}{A_o}\int_0^H \rho_z\ A_z\ (z - z_v)\ \mathrm{d}z. \tag{2.22}$$

The value of W_s increases as the stratification condition becomes stronger. A deeper lake will also require more energy to mix, resulting in higher values of W_s compared to shallower lakes. The Schmidt stability typically ranges from 11 J/m^2 to 43000 J/m^2 (Read et al., 2011; Mortimer, 1959), although there is no defined limit for this index. It is important to note that W_s is not influenced by the intensity of the wind, indicating that this index does not provide information on the actual state of mixing within the body of water. Instead, it reflects the lake's capacity to resist mixing because of density gradients and the volume of water present.

For a discrete data set, we can rewrite equation 2.22 as

$$W_s = \frac{g}{A_o}\left(\sum_{z=0}^{H} \rho_z\ A_z\ (z_v)\ \Delta z\right), \tag{2.23}$$

in which z_v is the depth of the geometric center of the lake.

Hydrostatic Pressure

Hydrostatic pressure is the pressure that fluids exert at a given point without the presence of motion. mathematically, hydrostatic pressure is defined as follows:

$$\frac{\partial \overline{p}}{\partial z} = -\overline{\rho} g, \tag{2.24}$$

in which $\overline{p}(z)$ is the hydrostatic pressure, g is the acceleration of gravity, and $\overline{\rho}(z)$ is the density of water.

The hydrostatic pressure within a multilayer system ($\overline{p_{\text{total}}}$) can be determined by summing the hydrostatic pressures within each individual layer, as follows:

$$\overline{p_{\text{total}}} = \sum_{i=0}^{N} \overline{\rho}_i\ g\ \Delta z_i, \tag{2.25}$$

in which N represents the total number of layers, g denotes the acceleration due to gravity, $\overline{\rho}_i$ signifies the fluid density in layer i, and Δz_i represents the thickness of that specific layer.

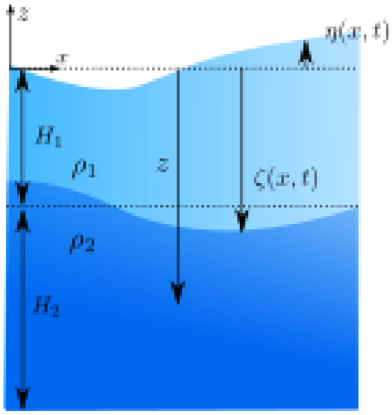

Figure 2.14 Two-layer stratification with perturbed motion on the surface of water (η) and the pycnocline region (ζ).

Consider the scenario depicted in Figure 2.14 as an illustrative example. In this two-layer system, we aim to derive an expression that describes the hydrostatic pressure within the lower layer. It is important to note that both interfaces, the water surface and the thermocline, deviate from their equilibrium positions, denoted by the functions η and ζ, respectively. It is worth mentioning that both functions (η and ζ) are defined with respect to the lake surface.

Assuming that the hydrostatic pressure in the lower layer is described by the contribution of the hydrostatic pressure in each layer above z, we can divide $P_2(z)$ into one component from the upper layer and another from the lower layer:

$$P_2(z) = P_{\text{layer 1}}(\eta,\zeta) + P_{\text{layer 2}}(\zeta,z). \tag{2.26}$$

The contribution of the upper layer to hydrostatic pressure $P_2(z)$ is defined as

$$P_{\text{layer 1}}(\eta,\zeta) = \overline{\rho_1}gH_1 + \overline{\rho_1}g\eta - \overline{\rho_1}g(H_1+\zeta)$$

$$P_{\text{layer 1}}(\eta,\zeta) = \overline{\rho_1}g(\eta-\zeta). \tag{2.27}$$

The contribution of the lower layer is given by

$$P_{\text{layer 2}}(\zeta,z) = -\overline{\rho_2}g(H_1+z) + \overline{\rho_2}g(H_1+\zeta)$$

$$P_{\text{layer 2}}(\zeta,z) = \overline{\rho_2}g(\zeta-z) \tag{2.28}$$

By substituting equations 2.27 and 2.28 into equation 2.26, we obtain the following expression:

$$P(z) = \overline{\rho_1}g\eta + \Delta\rho g\zeta - \overline{\rho_2}gz. \tag{2.29}$$

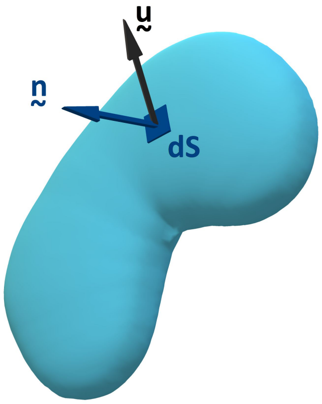

Figure 2.15 System and control volume configuration.

Mass Conservation

The concept of mass conservation dates back to 1789 when Antoine Lavoisier established, through chemical reactions, that mass remains constant in an isolated system; it is neither created nor destroyed. In fluid mechanics, this principle holds, where the change in mass within a fixed control volume ($C\forall$) must be equivalent to the net mass inflow through its boundary conditions, known as the control surface ($S\forall$). Mathematically, this relationship can be expressed in the integral form as follows:

$$\frac{\mathrm{d}}{\mathrm{d}t}\int_{C\forall}\varrho\,\mathrm{d}\forall + \oint_{S\forall}\varrho(\mathbf{n}\cdot\mathbf{u})\,\mathrm{d}S = 0, \tag{2.30}$$

in which ϱ is the density of the fluid, $\mathbf{u} \equiv u_i$ is the velocity vector, and $\mathbf{n}$ is the normal outward point for the surface segment $\mathrm{d}S$.

The first term in equation 2.30 accounts for the rate of change of mass within the control volume $C\forall$, while the second term denotes the net inflow of mass. As the mass conservation equation is formulated in the Eulerian reference frame, the total-time derivative can be moved inside the integral as a partial derivative. Therefore, by applying this transformation and utilizing the divergence theorem, equation 2.30 can be expressed as follows:

$$\int_{C\forall}\left(\frac{\partial \varrho}{\partial t}+\frac{\partial \varrho u_i}{\partial x_i}\right)\mathrm{d}\forall = 0. \tag{2.31}$$

Equation 2.31 remains valid for any arbitrarily large volume, which is only possible if the integrand vanishes completely. Hence, we can deduce the following:

$$\frac{\partial \varrho}{\partial t}+\frac{\partial \varrho u_i}{\partial x_i} = 0. \tag{2.32}$$

Incompressibility

By employing the product rule, we can express equation 2.32 as follows:

$$\frac{\mathrm{D}\varrho}{\mathrm{D}t} = -\frac{\partial u_i}{\partial x_i}, \tag{2.33}$$

in which the derivative $\mathrm{D}\varrho/\mathrm{Dt}$ represents the rate of density change experienced by a fluid particle. It is important to note that this term is typically neglected when the density remains constant under pressure variations. In such cases, the flow is referred to as **incompressible** or **solenoidal**. Consequently, equation 2.33 simplifies to an incompressible form:

$$\frac{\partial u_i}{\partial x_i} = 0. \tag{2.34}$$

The density field does not need to be uniform in an incompressible flow. However, the crucial characteristic of an incompressible flow is that a fluid element retains its density throughout its motion in the flow. This means that the density of a fluid element remains constant over time. For instance, the flow in stratified lakes can be regarded as incompressible despite the non-uniform density caused by stratification.

Imagine a fluid particle following a typical trajectory in a two-dimensional space, influenced by a steady velocity field as depicted in Figure 2.16. In the fluid, there exists an imaginary line tangent to the velocity vector at each point, which is referred to as a **streamline**. Consequently, we can define a stream function $\overline{\psi}$ that relates to the velocity components of the flow as follows:

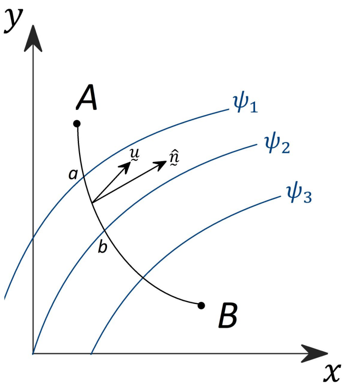

Figure 2.16 Streamlines.

$$\varrho u = \frac{\partial \overline{\psi}}{\partial y} \quad \text{and} \quad \varrho v = \frac{\partial \overline{\psi}}{\partial x}. \tag{2.35}$$

In the case of incompressible flow, the stream function can be characterized by the density of the fluid, denoted ϱ. The relationship between the stream function and density can be established through the derivative of $\psi(x,y)$, where ψ is defined as the product of ϱ and $\overline{\psi}$:

$$\mathrm{d}\psi = \frac{\partial \psi}{\partial x}\mathrm{d}x + \frac{\partial \psi}{\partial y}\mathrm{d}y. \tag{2.36}$$

Streamlines and stream function
The flow velocity can be expressed through the vector potential $\boldsymbol{\psi}$ such that

$$\mathbf{u} = \nabla \times \boldsymbol{\psi} \tag{2.37}$$

However, defining the stream function $\boldsymbol{\psi}$ becomes more complex when it involves multiple components. As a result, the stream function $\boldsymbol{\psi}$ is primarily defined in axisymmetric three-dimensional (3D) flows and in all two-dimensional (2D) flows where $\boldsymbol{\psi}$ has only one component,

$$\boldsymbol{\psi} = (0, 0, \psi).$$

If the velocity vector is a known function, the stream function is determined analytically by integrating the equation 2.38.

Table 2.5 Stream function.

There are two approaches to obtain the stream function $\psi(x,y)$. The first method involves replacing $\mathrm{d}x_i$ with the corresponding velocity field and considering $\mathrm{d}\psi = 0$ along a streamline. This approach leads to a linear, first-order partial differential equation:

$$u\frac{\partial \psi}{\partial x}\mathrm{d}x + v\frac{\partial \psi}{\partial y}\mathrm{d}y = 0,$$

in which shows that streamlines are parallel to the velocity vector field, $\mathbf{u}\cdot\nabla\psi$.

Another approach is to utilize the incompressible flow condition (Equation 2.34). When this condition is fulfilled, it implies the existence of a function ψ, as described by equation 2.35. As a result, the stream function can always be defined in the context of two-dimensional (2D) incompressible flows as follows:

$$\mathrm{d}\psi = -v\mathrm{d}x + u\mathrm{d}y. \tag{2.38}$$

Since along a streamline $\mathrm{d}\psi = 0$ so

$$\frac{\mathrm{d}y}{\mathrm{d}x} = \frac{v}{u}. \tag{2.39}$$

Irrotationality

A fluid particle moving in a three-dimensional (3D) space, influenced by a velocity field, can experience rotation due to viscous forces and variations in mass density. To quantify this rotation, we use the concept of **circulation** (Γ), which is a scalar integral quantity. Circulation is defined as the line integral of tangential velocity components evaluated along a closed curve. The magnitude of circulation represents the total **vorticity**, meaning that the circulation around a closed contour corresponds to the enclosed vorticity. Mathematically, the rate of change of circulation, obtained through the Stokes' theorem, can be expressed as follows:

☞ In Section 2.2.3, we provide the vorticity equation derived from the momentum equation. This equation facilitates the identification of the forces responsible for the generation or enhancement of vorticity.

$$\frac{\mathrm{D}\Gamma}{\mathrm{D}t} = \frac{\mathrm{D}}{\mathrm{D}t}\iint_S (\nabla \times \mathbf{u})\cdot\hat{\mathbf{n}}\,\mathrm{d}S, \tag{2.40}$$

in which $\nabla \times \mathbf{u}$ is the vorticity.

Assuming a constant mass density and neglecting viscous forces, we can deduce that

$$\nabla \times \mathbf{u} = 0, \tag{2.41}$$

which implies that the flow is **irrotational** ($\xi = 0$), meaning there is no vorticity present. Assuming an incompressible, inviscid, and irrotational flow, it suggests the existence of a function that satisfies the conservation of mass and momentum. This function is known as the **potential velocity function** ϕ, which is valuable as it reduces the velocity vector field to a single scalar function, introducing an additional relationship to the problem:

$$u_i = -\frac{\partial \phi}{\partial x_i}. \tag{2.42}$$

Lines of constant ϕ are called **potential lines** and represent points of equal pressure. In a two-dimensional (2D) space, the expression for the potential velocity function $\phi(x, y)$ can be obtained by taking its derivative, similar to the equation 2.36 for $\psi(x, y)$. Consequently, as $\mathrm{d}\phi = 0$ along a potential line, the expression simplifies to:

$$\frac{\mathrm{d}y}{\mathrm{d}x} = -\frac{u}{v}. \tag{2.43}$$

Incompressibility and Boussinesq approximation
While numerous books define an incompressible flow as

$$\nabla \cdot \mathbf{u} = 0,$$

by employing the Boussinesq approximation for mass conservation, it is possible to demonstrate that the mean flow velocity, denoted as U, is

$$\frac{\partial \langle U_i \rangle}{\partial x_i} \approx 0,$$

for many fluid flows.
In other words, even in a compressible flow, $\nabla \cdot \langle \mathbf{U} \rangle \approx 0$.

Table 2.6 Incompressibility considerations.

Two-Dimensional Irrotational Flow

If the flow is irrotational and incompressible, equations 2.39 and 2.43 can be combined, leading to

$$\frac{\partial \phi}{\partial x} = \frac{\partial \psi}{\partial y}, \tag{2.44a}$$

$$\frac{\partial \phi}{\partial y} = -\frac{\partial \psi}{\partial x}. \tag{2.44b}$$

The system of differential equations represented by equation 2.44 is widely recognized as the Cauchy-Riemann equations in the field of complex analysis in mathematics. In the context of fluid mechanics, this expression takes the form of $\nabla\phi \cdot \nabla\psi = 0$, which means that the potential lines are perpendicular (normal) to the streamlines. It is worth noting that stream functions are not exclusively associated with irrotational flows; they can also be used in the analysis of other flow conditions.

To illustrate the physical meaning of these lines, consider steady-state water flowing beneath a dam in permeable soil (Figure 2.17). The flow in porous media is governed essentially by Darcy's law (Equation 2.45). The smaller the flow length, the higher the flow rate. Thus, the shortest streamline in Figure 2.17 has a higher velocity than the second and third.

The cutoff structure reduces the pressure of the uplift on the heel of the dam and erosion on the toe. Without the cutoff point, the flow rate would be higher, leading to stronger erosion on the toe. If the pressure stays the same but the path gets shorter, the gradient increases, speeding up the fluid. This loop can cause the erosion to reach the reservoir, leading to a dam failure.

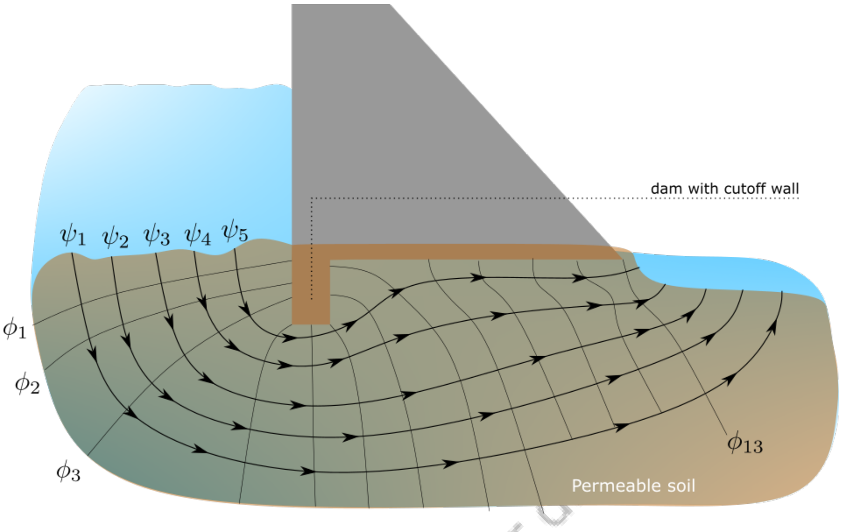

Figure 2.17 Hydrodynamic flow net beneath a dam with an impermeable cutoff.

2.2.2 Momentum equation

The principle of conservation of momentum asserts that the combined forces acting on a fluid element result in a temporal change in its momentum. This principle essentially applies Newton's laws to fluid dynamics. The momentum equations, also known as the Cauchy equations, describe the motion of any fluid and can be expressed in a comprehensive form as follows:

$$\frac{\partial \varrho u_i}{\partial t} + \frac{\partial \varrho u_i u_j}{\partial x_j} = \varrho(g_i - 2\varepsilon_{ijk}\overline{\omega_j}u_k) + \frac{\partial T_{ij}}{\partial x_j}, \tag{2.46}$$

in which, g is the acceleration due to gravity, T_{ij} is the stress tensor, and $\overline{\omega_j} = 2\epsilon\sin\left(\overline{\phi}\right)$ is the inertial frequency, where ϵ is the angular frequency of the earth and $\bar{\phi}$ is the mean latitude of the phenomenon. The stress tensor is defined as

$$T_{ij} = \left(-\frac{\partial P}{\partial x_i} + \Lambda\frac{\partial u_k}{\partial x_k}\right)\delta_{ij} + 2\varrho\mu\frac{\partial S_{ij}}{\partial x_j}, \tag{2.47}$$

where P is the total thermodynamic pressure and, Λ and μ are the dynamic viscosity coefficients.

When the stress tensor S_{ij} is written as a linear strain tensor rate (Newtonian fluid),

$$S_{ij} = \frac{1}{2}\left(\frac{\partial u_j}{\partial x_i} + \frac{\partial u_i}{\partial x_j}\right), \tag{2.48}$$

equation 2.46 reduces to the well-kown **Navier-Stokes equation**.

The left-hand side of the equation 2.46 represents the rate of change of momentum for a fluid particle, which must be equal to the sum of all forces acting

Darcy's Law
Darcy's law was formulated by Henri Darcy in 1856 through a series of laboratory experiments to describe flow through granular media. Darcy's law states that the flow rate is proportional to the length of the flow, Δx, and the total pressure drop, Δp:

$$Q = -\frac{\tilde{k}A}{\mu}\frac{\Delta p}{\Delta x} \tag{2.45}$$

in which A is the cross-sectional area of the flow, k is the hydraulic conductivity and μ is the viscosity of the fluid.
Although the equation of fluid mechanics had already been formulated, Henri Darcy did not derived it directly from the Navier-Stokes equation. Actually, upscaling the Navier-Stokes equations for flow through a porous medium turns out to be an extra viscous term, a drag force term, due to the viscous friction of the fluid with the walls of the porous medium. This theoretical homogenization gives **Darcy-Brinkman equation**.

Table 2.7 Darcy's Law and the flow through porous media.

on the fluid parcel (right-hand side of the equation 2.46). The rate of change in momentum can be expressed using the incompressibility assumption (equation 2.34), leading to a simplified material derivative. Additionally, certain terms on the right-hand side of equation 2.46 can be neglected as they have little impact on the propagation of internal waves. In particular, based on the assumption of incompressibility, the term involving viscosity Λ can be ignored.

Another term in the momentum equation that is frequently omitted is the Coriolis force term. The angular speed of the Earth in equation 2.46 is directly related to the Coriolis force, which deflects internal waves and affects their phase. However, for small-scale processes, this term is often considered negligible. It is worth noting that the Earth's rotation can have significant effects on internal waves, leading to the generation of internal Kelvin and Poincaré waves during large-period motions. For now, we neglect the contribution of the Coriolis force, but in Sections 6.1.5 and 6.2.6, we delve into the details of the Earth's rotation and its impact on wave acceleration.

Given all these simplifications, equation 2.46 reduces to the Navier-Stokes equation,

$$\varrho\left(\frac{\partial u_i}{\partial t}+u_j\frac{\partial u_i}{\partial x_j}\right)=-\frac{\partial P}{\partial x_i}+\varrho g_i+\mu\frac{\partial^2 u_i}{\partial x_j^2}, \tag{2.49}$$

in which $\mu=\varrho\nu_u$, where ν_u is the kinematic viscosity.

Equation 2.49 can be reduced even further by assuming an inviscid flow. In this case, we find another well-known equation, the **Euler equation**:

$$\varrho\left(\frac{\partial u_i}{\partial t}+u_j\frac{\partial u_i}{\partial x_j}\right)=-\frac{\partial P}{\partial x_i}+\varrho g_i. \tag{2.50}$$

Hydrostatic balance

In Section 2.2.1, we introduced the concept of hydrostatic pressure, which deviates from the momentum equation in z-direction for a stationary system. However, in the presence of fluid motion, the dynamics of the flow can generate additional pressure within the system. Therefore, the total pressure in the flow is a combination of two pressures: the hydrostatic pressure $\overline{p}(z)$ and the dynamic pressure $p(\mathbf{x},t)$.

$$P=\overline{p}+p. \tag{2.51}$$

Following a similar approach as in equation 2.51, we can define the density of the fluid by considering contributions from both hydrostatic and dynamic effects as follows:

$$\varrho=\overline{\rho}+\rho, \tag{2.52}$$

in which $\overline{\rho}$ is the hydrostatic fluid density and ρ is the dynamic fluid density.

To simplify the analysis, it is often valuable to separate the hydrostatic and non-hydrostatic contributions when deriving the governing equations of motion, such as equations 2.32 and 2.50. For instance, substituting equation 2.51 into the Euler equation 2.50 in the z-direction yields the following expression:

$$\varrho\left(\frac{\partial w}{\partial t}+u_j\frac{\partial w}{\partial x_j}\right)=-\frac{\partial}{\partial z}\left(\overline{p}+p\right)-\rho g. \tag{2.53}$$

Applying the hydrostatic solution, equation 2.24, we find

$$\varrho\left(\frac{\partial w}{\partial t}+u_j\frac{\partial w}{\partial x_j}\right)=-\frac{\partial p}{\partial z}-(\varrho-\overline{\rho})g, \tag{2.54}$$

in which $p(\mathbf{x},t)$ is the non-hydrostatic contribution for the total pressure.

Substitution of equation 2.52 into the Euler equation 2.54, gives

$$\frac{\partial w}{\partial t}+u_j\frac{\partial w}{\partial x_j}=-\frac{\partial p}{\partial z}-\frac{\rho}{\varrho}g. \tag{2.55}$$

2.2.3 The vorticity on internal wave analysis

Although the density gradient in nature is typically continuous, numerous studies adopt the use of homogeneous layers to represent stratified systems, as illustrated in Figures 2.14 and 2.9. The real advantage of the layered model is that we can make the irrotational flow assumption. Consequently, a velocity potential can be defined, resulting in a reduction of variables in the problem.

Although the layered model often provides accurate predictions in many scenarios, it is important to note that in a continuously stratified environment, the flow is inherently rotational. This distinction is one of the key differences between surface waves and internal waves. Surface waves exhibit an irrotational flow, whereas internal waves involve rotational motion. This contrast becomes more apparent when we examine the vorticity equation. By taking the curl of each term in the momentum equations, the vorticity can be expressed as:

$$\frac{\partial\Omega_k}{\partial t}+u_j\frac{\partial\Omega_k}{\partial x_j}=(\Omega_n+2\overline{\omega_{on}})\frac{\partial u_k}{\partial x_n}+\frac{1}{\varrho^2}\varepsilon_{pmk}\frac{\partial\varrho}{\partial x_p}\frac{\partial P}{\partial x_m}+\nu\frac{\partial^2\Omega_k}{\partial x_j\partial x_j}, \tag{2.56}$$

in which the vorticity is generated by the second term on the right-hand side. This term becomes non-zero when baroclinic effects significantly influence the dynamics of the system, leading to the formation of internal waves. It serves as a source of vorticity, indicating that a flow under the influence of baroclinic effects is always rotational.

The first term on the right-hand side of equation 2.56 is called vortex stretching and tilting and is responsible for amplifying the vorticity, being more important for turbulent analysis. The last term accounts for diffusion of vorticity as a result of viscous effects. As we can note, for an inviscid flow, this term can be neglected.

Indeed, it is important to note that, in an inviscid flow with baroclinic activity, the second term on the right-hand side of the equation does generate vorticity.

This implies that the irrotational flow assumption is not entirely valid for the baroclinic mode. However, despite this limitation, the assumption of irrotational flow still yields satisfactory solutions in numerous cases when studying internal waves in lakes and reservoirs.

2.3 Introduction to turbulent flow

Turbulent flow is characterized by an unstable, irregular, chaotic, and seemingly unpredictable motion that causes fluctuations in velocity, pressure, and other parameters (Figure 2.18). The classification of flow as laminar or turbulent is based on the balance between viscous and inertial forces. When inertial forces outweigh viscous forces, perturbations within the flow become intense and cannot be dissipated by viscosity alone, resulting in flow destabilization. The Reynolds number (Re) serves as a dimensionless quantity that is used to examine the flow pattern and determine whether it is laminar or turbulent. It is defined as follows:

$$Re = \frac{uL}{\nu_u}, \tag{2.57}$$

in which u is the velocity of the fluid, L is a characteristic linear dimension, and ν_u is the kinematic viscosity of the flow. When $Re > 1000$, the flow is classified as turbulent.

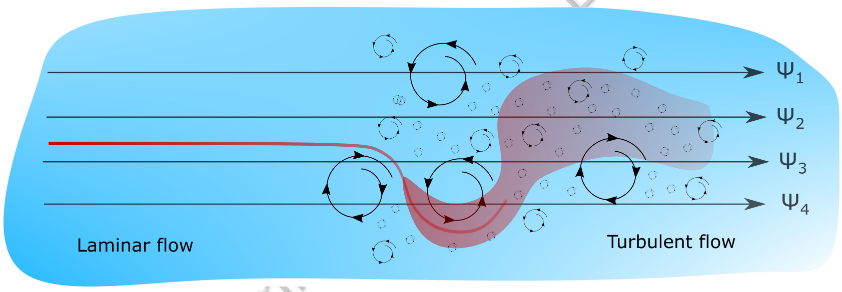

Figure 2.18 Tracer transport in laminar and turbulent flows. The streamline ψ is parallel to the mean flow that has superposed a wide range of vortexes with different scales.

Turbulent mixing plays a crucial role in the dynamics of stratified fluids. In thermally stratified lakes, mixing processes arise from various sources. Small-scale mixing originates from the breaking of internal waves. At the same time, substantial turbulent mixing occurs in the presence of shear instabilities near the bottom boundary layer, turbulent plumes, and gravity currents. Furthermore, the interaction between deflected isopycnals caused by internal wave motion and bathymetry can also contribute to turbulent mixing (Figure 2.19). These mechanisms collectively shape the intricate patterns of turbulent mixing in thermally stratified lakes.

A key feature of turbulent flows is the presence of a broad spectrum of spatial and temporal scales. As depicted in Figure 2.18, turbulent flow consists of eddies ranging in various sizes. Some eddies are comparable in magnitude to the overall flow width, while others are so minuscule that they cannot be visually discerned. It is worth noting that as the Reynolds number increases, the turbulence length scales of the flow become smaller. This relationship highlights the intricate multiscale nature of turbulence.

The size of the eddies plays a crucial role in characterizing the turbulence field. Initially, the turbulence kinetic energy (TKE) is predominantly concentrated in large-scale eddies, influenced by the flow geometry and boundary conditions. During this stage, the inertial forces outweigh the viscous forces, rendering the influence of viscosity negligible. These large-scale eddies govern the mixing and transport processes within the flow.

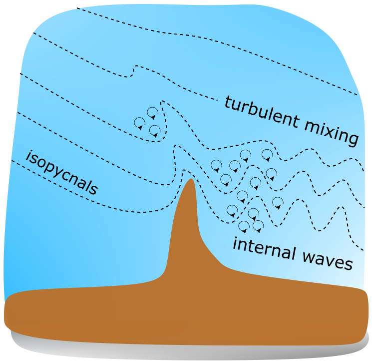

Figure 2.19 Turbulent mixing in a submerged ridge.

Large eddies, formed through non-viscous processes, exhibit length scales that are comparable to the overall flow scale, ranging from ℓ_o to ℓ_e. This range is called the production range, since it is where turbulent kinetic energy is primarily generated (Figure 2.20). The Reynolds number associated with these largest eddies (Re_o) is typically large and similar in magnitude to the Reynolds number of the overall flow ($\approx Re$). Due to the negligible effects of viscosity, the transfer rate of kinetic energy from large eddies to smaller eddies is independent of viscosity and is solely determined by flow parameters, specifically expressed as u_o^3/ℓ_o, where u_o denotes the characteristic velocity ($\equiv u(\ell_o) \approx U$).

The interaction of large eddies leads to a cascade process in which energy is transferred from larger scales to smaller scales. This phenomenon, known as the nonlinear vortex stretching process, can be observed in the vorticity equation (Equation 2.56). As large eddies break down, they generate smaller eddies through this nonlinear process. These smaller eddies subsequently undergo a similar breakdown, transferring their energy to even smaller eddies. This energy cascade continues until it reaches the smallest scales of turbulence, where dissipation occurs due to the influence of viscosity.

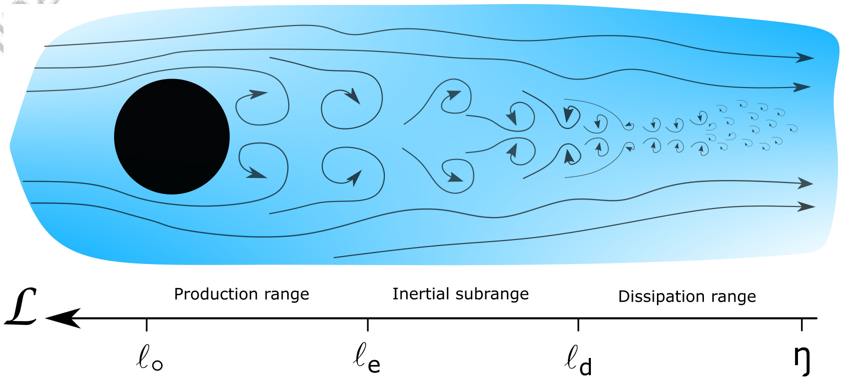

Figure 2.20 Length scales in turbulent energy cascade. The example shows the size of the separated eddies along the flow field, but the region occupied by the large eddies can also contain smaller eddies.

A significant portion of the kinetic energy generated by large eddies, approximately 90%, is transferred to smaller scales within the turbulence. In the range of eddies with turbulence length scales between ℓ_e and ℓ_d, the energy exchange between large and small eddies reaches equilibrium. This specific range is referred to as the inertial sub-range. In this sub-range, the energy input from large eddies is balanced by the energy transfer via inertial forces to smaller turbulence length scales.

As the eddies become smaller in size, the viscous shear stress intensifies because the viscous forces become relatively larger compared to the eddy size. Consequently, this increased friction causes the dissipation of turbulent kinetic energy, converting it into heat energy. The range of the smallest scales where this dissipation occurs is called the dissipation range. This range has a characteristic turbulence length scale ℓ_η, which is determined by the viscosity of the fluid:

$$Re_\ell \equiv \frac{u(\ell)\ell}{\nu_u},$$

in which $Re_\ell \ll Re_o$, and consequently, viscosity plays a major role in energy dissipation at this scale. The turbulent kinetic energy dissipation can be defined as

$$\varepsilon = \nu_u \left(\frac{u_\eta}{\eta} \right)^2, \tag{2.58}$$

in which $u_\eta = (\nu_u\ \varepsilon)^{1/4}$ is the Kolmogorov velocity scale and η is the Kolmogorov length scale, the microscale of turbulence. Often η varies from 1 to 10 mm. The Kolmogorov cutoff frequency is on the order of 10 to 100 Hz. The transfer of turbulence energy across various scales, as shown in Figure 2.20, can be effectively described by the turbulence spectrum. The turbulence spectrum provides insight into the distribution of turbulent energy with respect to different length scales. Typically, the length scale is characterized by the wavelength k, while the energy associated with each scale is represented by the spectral density of the turbulence (Figure 2.21). The turbulence spectrum enables us to analyze and understand the distribution and behavior of turbulent energy across different scales within the flow.

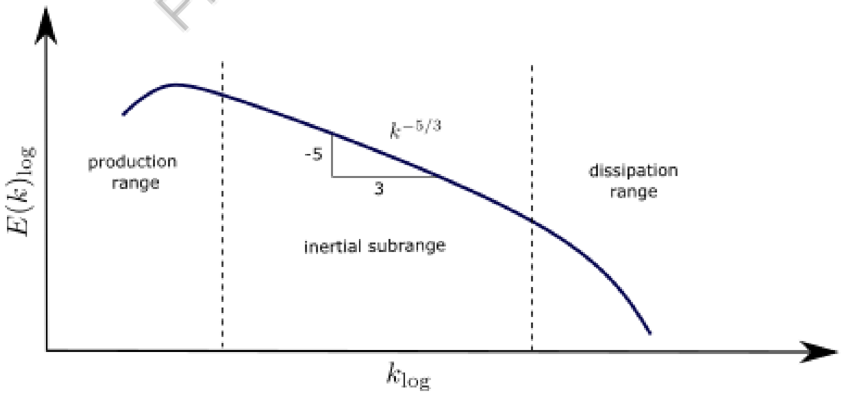

Figure 2.21 The turbulence spectrum (energy cascade).

As discussed earlier, equations of motion are often simplified to a level where analytical solutions can be obtained. For example, when the Cauchy equation (Equation 2.46) is simplified to the Euler equation (Equation 2.50) under steady and irrotational assumptions, we can easily derive an analytical solution known as **Bernoulli's equation**. In Chapter 6, we present the analytical solution for a free surface and an interfacial internal wave using the unsteady Bernoulli equation and the conservation of mass for an irrotational flow. In this scenario, a potential velocity can be defined, facilitating the analysis and solution of the problem.

In fact, analytical solutions are feasible only for simple flow conditions. However, in many practical cases involving complex bathymetry, irregular boundary conditions, and unsteady flows, the governing nonlinear partial differential equations cannot be solved analytically. Instead, computational fluid dynamics (CFD) methods are employed to obtain numerical solutions. CFD tackles the problem by discretizing the governing equations using techniques such as finite difference, finite volume, or finite element methods. This discretization divides the flow domain into small control volumes or cells. Each cell is then treated as an algebraic problem, typically solved iteratively, and the solution is obtained by solving the resulting system of equations across the grid of cells. This numerical approach allows for the simulation and analysis of a wide range of complex flow scenarios that lack analytical solutions.

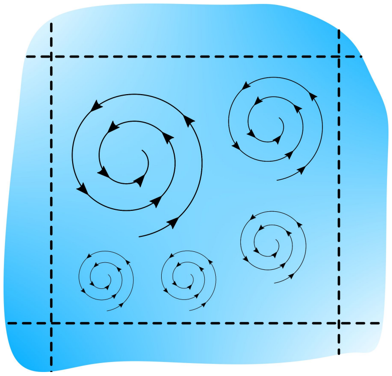

Figure 2.22 Small eddy size to resolve in a relatively large grid. To resolve this turbulence scale, the grid must be much smaller.

Undoubtedly, turbulent flows pose significant challenges due to the limitations of simplifications typically employed in laminar flows. The presence of eddies in turbulent flows requires the consideration of three-dimensional flow behavior, deviating from the two-dimensional assumptions often applied in laminar flows. Furthermore, the wide range of spatial and temporal scales present in turbulent flows adds complexity to the problem. As mentioned above, as the Reynolds number (Re) increases, smaller eddies form, leading to finer spatial and temporal scales that must be resolved to accurately capture the complete flow field. This requires utilizing a finer grid and smaller time steps to achieve a satisfactory solution (Figure 2.22). These computational requirements underscore the inherent computational challenges associated with simulating turbulent flows.

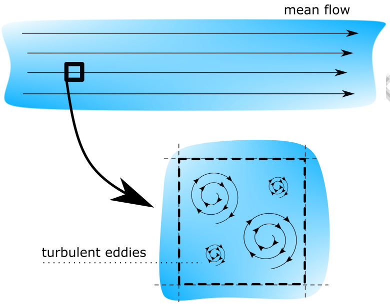

Figure 2.23 Mean flow that can be resolved and turbulence scales that need to be modeled.

Indeed, the smallest length scales in turbulent flows can be on the order of millimeters or even smaller. Consequently, the grid used to solve the flow field must be smaller than these smallest turbulence length scales. When the entire flow field is solved using a grid refined to be smaller than the smallest turbulence scales, it is termed a **Direct Numerical Simulation** (DNS). DNS involves directly simulating the flow by resolving all relevant scales of turbulence. However, the main drawback of DNS is its high computational cost. Even at low Reynolds numbers, the computational requirements are extremely demanding, exceeding the capacity of even the most powerful computers available today.

To address the computational challenges associated with resolving the entire range of turbulence scales, a commonly used approach is to separate the time-dependent turbulent velocity fluctuations from the mean flow velocity and assess the impact of these fluctuations on the flow. This technique is known as the **Reynolds Averaged Navier-Stokes equation (RANS)**. RANS allows for the estimation of the mean flow by considering only the mean flow components while accounting for the potential influence of turbulent velocity fluctuations on the mean flow. By performing algebraic manipulations of the Reynolds-averaged Navier-Stokes equation, we can analyze how the velocity fluctuations affect the mean flow. This analysis then serves as a basis for modeling the influence of turbulence on mean flow, enabling simulation of turbulent flows with reduced computational requirements compared to direct simulation methods.

The presence of a wide range of eddies in turbulent flows introduces additional spatial and temporal fluctuations, resulting in enhanced mixing and energy dissipation. The fluctuations of a generic quantity in a turbulent flow exhibit variations over space and time, and a significant portion of this variation is attributed to stochastic processes arising from the eddies. To analyze these fluctuations, the Reynolds decomposition technique is commonly employed. Through this decomposition, a quantity χ_i can be split into deterministic and stochastic components, such as:

$$\chi_i(x_i, t; \wp) = \bar{\chi}_i(x_i, t) + \chi_i'(x_i, t; \wp), \tag{2.59}$$

in which $\bar{\chi}_i(x_i, t)$ indicates the deterministic component of χ_i and χ_i' is the fluctuation due to stochastic processes of turbulence, a function of $\wp$ that belongs to the sample space B. The expected value of this random variable χ_i is intuitively given by the average of χ_i. Mathematically, we can write

$$\bar{\chi}_i(x_i, t) = \int_{\wp \in B} \chi_i(x_i, t; \wp)\, \mathrm{d}P(\wp) \tag{2.60}$$

in which P is the probability density function. Note that if the mean flow is steady, $\bar{\chi}_i$ is a constant over time (Figure **??**).

Now, by applying the Reynolds decomposition (Equation 2.59) to the averaged mass conservation and considering the property that the average of a sum of derivatives is equivalent to the sum of derivative of the averages, we can express the the mass conservation equation as follows:

$$\frac{\partial \overline{\rho}}{\partial t} + \frac{\partial \overline{\rho(\overline{u_i} + u_i')}}{\partial x_i} = 0.$$

Applying the product rule and considering ρ constant, we have

$$\frac{\partial \overline{\rho}}{\partial t} + \frac{\partial \overline{\rho(\overline{u_i} + u_i')}}{\partial x_i} = 0,$$

$$\frac{\partial \overline{\rho}}{\partial t} + \frac{\partial \rho \overline{\overline{u_i}}}{\partial x_i} + \cancelto{\overline{u_i'} = 0}{\frac{\partial \rho \overline{u_i'}}{\partial x_i}} = 0,$$

$$\frac{\partial \overline{\rho}}{\partial t} + \frac{\partial \rho \overline{u_i}}{\partial x_i} = 0,$$

$$\frac{D\rho}{Dt} + \rho\frac{\partial \overline{u_i}}{\partial x_i} = 0,$$

which since ρ is constant in time and space, we obtain a similar expression obtained for the non-averaged equation (equation 2.32),

☞ If you require further clarification on the mathematical manipulation between the averaged terms, please refer to exercise 2.7 for a detailed step-by-step explanation.

$$\frac{\partial \overline{u_i}}{\partial x_i} = 0. \tag{2.61}$$

The subsequent step involves applying the Reynolds decomposition to the averaged Navier-Stokes equation. To facilitate the analysis, it is advantageous to consider each term of the equation separately.

Firstly, the transient term can be simplified to

Large eddy simulations
An alternative approach to both RANS and DNS is the Large Eddy Simulation (LES). LES lies between RANS and DNS and is based on the concept of filtering. In LES, the method involves filtering out the larger eddies and directly resolving them using the governing equations, while the smaller turbulence length scales are modeled similarly to the RANS technique. In other words, while the LES method still requires a refined temporal and spatial grid to capture certain turbulence-length scales, the smaller scales can be effectively modeled, reducing the computational requirements compared to DNS. The LES method strikes a balance between accuracy and computational efficiency, making it a valuable tool for simulating turbulent flows.

Table 2.8 A Third optional to solve tubulence problems.

$$\frac{\overline{\partial \rho u_i}}{\partial t} = \frac{\partial \rho(\overline{\overline{u_i} + u_i'})}{\partial t} = \frac{\partial \rho\overline{\overline{u_i}}}{\partial t} + \cancelto{\overline{u_i'}=0}{\frac{\partial \rho \overline{u_i'}}{\partial t}} \quad .$$

Thus, we have

$$= \frac{\partial \rho \overline{u_i}}{\partial t}. \tag{2.62}$$

The second term is the convective and nonlinear term defined as

$$\frac{\overline{\partial \rho u_i u_j}}{\partial x_j} = \frac{\partial}{\partial x_j}\left(\overline{\rho(\overline{u_i} + u_i')(\overline{u_j} + u_j')}\right) =$$

$$= \frac{\partial}{\partial x_j}\left(\overline{\rho\overline{u_i}\,\overline{u_j}}\right) + \frac{\partial}{\partial x_j}\left(\cancelto{=0}{\overline{\rho\overline{u_i}u_j'}}\right) + \frac{\partial}{\partial x_j}\left(\cancelto{=0}{\overline{\rho u_i'\overline{u_j}}}\right) + \frac{\partial}{\partial x_j}\left(\overline{\rho u_i' u_j'}\right)$$

$$= \frac{\partial}{\partial x_j}\left(\rho\overline{u_i}\,\overline{u_j}\right) + \frac{\partial}{\partial x_j}\left(\rho\overline{u_i' u_j'}\right). \tag{2.63}$$

The pressure term is also decomposed by Reynolds decomposition. Thus, we obtain the following:

$$\frac{\overline{\partial P}}{\partial x_i} = \frac{\partial}{\partial x_j}\left(\overline{\overline{P} + P'}\right) = \frac{\partial \overline{P}}{\partial x_i} + \cancelto{=0}{\frac{\partial \overline{P'}}{\partial x_i}} \quad ,$$

that results in

$$= \frac{\partial \overline{P}}{\partial x_i}. \tag{2.64}$$

The gravitational term remains unchanged because it is not decomposed. Variables ρ and g are constants in our equation. The next term that requires the application of Reynolds decomposition is the viscous term. Hence, by referring to the Navier-Stokes equation, we obtain the following:

$$\overline{\frac{\partial}{\partial x_j}\left(\mu\frac{\partial}{\partial x_j}\left(\overline{u_i} + u_i'\right)\right)} = \frac{\partial}{\partial x_j}\left(\mu\frac{\partial}{\partial x_j}\overline{\left(\overline{u_i} + u_i'\right)}\right),$$

$$= \mu \frac{\partial^2 \overline{u_i}}{\partial x_j^2} + \mu \cancelto{=0}{\frac{\partial^2 \overline{u'_i}}{\partial x_j^2}} \quad ,$$

which, finally, we have

$$= \mu \frac{\partial^2 \overline{u_i}}{\partial x_j^2}. \tag{2.65}$$

Reassembling the terms of the Reynolds Averaged Navier-Stokes equation (equations 2.62, 2.63, 2.64, and 2.65) gives

$$\frac{\partial \rho \overline{u_i}}{\partial t} + \frac{\partial}{\partial x_j}\left(\rho \overline{u_i}\,\overline{u_j}\right) + \frac{\partial}{\partial x_j}\left(\rho \overline{u'_i u'_j}\right) = -\frac{\partial \overline{P}}{\partial x_i} + \rho g_i + \mu \frac{\partial^2 \overline{u_i}}{\partial x_j^2} \tag{2.66}$$

in which the second and last terms of equation 2.66 can be combined, leading to

$$\frac{\partial \rho \overline{u_i}}{\partial t} + \frac{\partial}{\partial x_j}\left(\rho \overline{u_i}\,\overline{u_j}\right) = -\frac{\partial \overline{P}}{\partial x_i} + \rho g_i + \frac{\partial}{\partial x_j}\left(\mu \frac{\partial \overline{u_i}}{\partial x_j} + \underbrace{\rho \overline{u'_i u'_j}}_{\text{Reynolds stress}}\right). \tag{2.67}$$

Please note that equation 2.67 resembles equation 2.49, with the exception of the **Reynolds stress** term. This term signifies the influence of turbulence on the alteration of mean flow. The **Reynolds stress** term represents the shear stress generated by turbulence. In the case of internal waves, which typically exhibit turbulent flows and therefore possess high Reynolds numbers (Re), they are significantly impacted by this turbulence-induced shear stress. Consequently, turbulent diffusion greatly exceeds molecular diffusion in this scenario,

$$\mu \frac{\partial \overline{u_i}}{\partial x_j} \ll \rho \overline{u'_i u'_j}, \tag{2.68}$$

and consequently the shear stress caused by the friction of molecules may be neglected.

The Reynolds tensor, R_{ij}, may be written similarly to the strain tensor, equation 2.48, as

$$R_{ij} = \begin{bmatrix} \rho \overline{u'^2} & \rho \overline{u'v'} & \rho \overline{u'w'} \\ \rho \overline{v'u'} & \rho \overline{v'^2} & \rho \overline{v'w'} \\ \rho \overline{w'u'} & \rho \overline{w'v'} & \rho \overline{w'^2} \end{bmatrix} \tag{2.69}$$

in which the main diagonal is the variances of the velocities fluctuation, whilst other terms represent the covariance of the velocities fluctuation.

Dividing the main diagonal by two yields **turbulent kinetic energy (TKE)** per unit mass:

$$k_e = \frac{\rho}{2}\left(\overline{u'^2} + \overline{v'^2} + \overline{w'^2}\right). \tag{2.70}$$

The challenge of turbulence lies in the need to accurately model the Reynolds stress, denoted as R_{ij}, in a similar manner to how we model the viscous stress

S_{ij} for Newtonian fluids. These effects are not directly resolved in simulations. The approach involves solving for the mean flow and incorporating a turbulence model to account for the turbulent term that emerges from the averaged governing equations (Figure 2.23). It is important to note that in this method, all turbulence length scales are modeled to capture the influence of turbulence on the mean flow, without explicitly solving for each individual scale.

Exercises

Exercises for 2.1 Stratified Fluids

P2.1 A researcher conducted an investigation into the relationship between water density and oxygen content in two distinct effluents. For each investigation, the investigator developed their own equations of state, which were derived from a series of laboratory experiments. The equations of state rely primarily on polynomial functions that estimate the water density of the effluents, with temperature being the main input parameter for these polynomial functions:

$$\begin{aligned} &\text{Effluent A:} \quad \rho = -0.0083\tau^2 + 0.0661\tau + 1000.9 \\ &\text{Effluent B:} \quad \rho = 6\ 10^{-5}\tau^3 - 0.0075\tau^2 + 0.0507\tau + 1000.4 \end{aligned}$$

Considering that the temperature-oxygen solubility relationship is given by

$$O_{\text{sol}} = 0.0057\tau^2 - 0.3823\tau + 14.586,$$

neglecting the interdependence between dissolved oxygen and salinity, we found the oxygen solubility in mg/l for the maximum water density in both cases. Also, what would you say about the difference between each effluent.

PS: Estimate the maximum water density using a polynomial function with two decimal places.

Exercises for 2.2 Theory of Stratified Flows

P2.2 Consider a typical scenario of incompressible flow occurring in a three-dimensional space (x, y, z), where fluid particles move in response to a steady velocity field (u, v, w). The velocity gradient,

$$\frac{\partial v}{\partial y},$$

is necessary approximately zero? Explain your answer.

P2.3 A hypothetical reservoir of surface area of 3.3 km² has a high concentration of methane (CH_4) and is thermally stratified during summer with a well-mixed hypolimnion. Given the strong variation in density, the thermocline presents a reduced vertical turbulent diffusion ($D = 0.14$ cm^2/s). The reservoir has an inlet stream and an outlet, with a flow rate of 1 m^3/s. The inflow does not contain methane. Assuming that the conditions shown in Figure 2.24 represent steady state, how much is the flux of methane to the atmosphere?

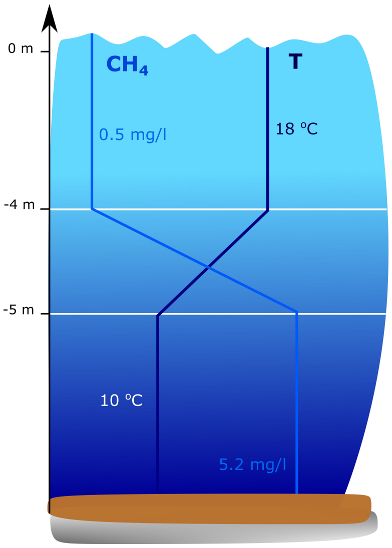

Figure 2.24 Stratified reservoir.

P2.4 In a two-dimensional, the fluid velocity components are given by:

$$u = -a\omega \exp^{-kz+i(kx-\omega t)} \quad \text{and} \quad w = -i a\omega \exp^{-kz+i(kx-\omega t)}.$$

Show that the flow satisfies the continuity equation and verify that the flow is irrotational. If the flow is irrotational, obtain also the expression for the velocity potential.

P2.5 Torricelli's theorem states that the speed, denoted by u, of a liquid flowing under the force of gravity out of an opening in a tank is jointly proportional to the square root of the vertical distance, represented by h.

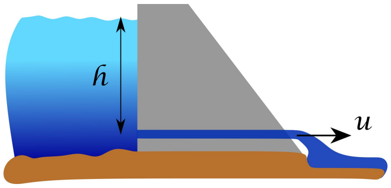

Figure 2.25 Stratified reservoir and Torricelli principle.

Now, consider a thermal stratified freshwater reservoir that extends over a significant distance, as shown in the accompanying figure. The reservoir is equipped with a dam that has a gate near its base, positioned at a distance of h from the surface of the reservoir. Assuming a stable stratification, apply the Navier-Stokes equation, with the gate fully open, to find the velocity of the exiting water. Discuss the contribution of stratification to water velocity and the limitations of this application.

P2.6 Show that for a Newtonian and incompressible fluid, the divergence of the stress tensor is

$$= \rho \nu_u \frac{\partial^2 u_i}{\partial x_j^2},$$

in which ν_u is the kinematic viscosity, ρ is the water density, and u_i is the vector velocity.

P2.7 Using equation 2.60 and considering $\overline{\phi_i} = [1,2,3]$, $\overline{\beta_i} = [5,4,3]$, $\overline{\phi_i \beta_j} = [[3,3,4][4,7,8][6,9,11]]$, find a solution for the following statements

$$\overline{\phi'_i \overline{\beta_j}},$$

and

$$\overline{\phi'_i \beta'_j},$$

in which ϕ_i and β_j are vectors that present stochastic and deterministic components.

P2.8 Find the expression to describe the hydrostatic pressure along the depth in a tank H deep, assuming an equilibrium position and a water density ρ. Assume that the water surface may vary from the equilibrium position followed by the function η.

P2.9 Considering the situation shown in figure **??**, find an expression to describe the distribution of hydrostatic pressure along the lower layer assuming that ζ is an interfacial perturbation between both fluids.

P2.10 Based on the hydrostatic pressure at the bottom of the tank from the previous exercise ($H = H_1 + H_2$), find the expression of the surface wave in a fluid-density unstratified system ρ_1 to have the same pressure at the bottom of the tank. Assume that the total depth of water is the same in both systems.

Chapter 3

Physical Limnology

Exercises

Chapter 4

Experimental Methods: Laboratory, numerical and Field Observations

Over several decades, numerous researchers have been working to study internal waves and explore their significant implications in various areas such as mixing, turbulence, water quality, and biogeochemical cycles within lakes and reservoirs. Research has been carried out in the main three branches: field measurements, laboratory experiments, and numerical modeling.

Field measurements have played a crucial role in unraveling the complex nature of internal waves. By directly observing and collecting data from lakes and reservoirs, researchers have been able to gain valuable insights into the behavior, characteristics, and propagation of internal waves in natural settings. These measurements often involve the use of high-resolution sensors such as thermistors' chains and Acoustic Doppler Velocimeters (ADVs). These data enable scientists to acquire detailed information about the vertical and horizontal movement of water, as well as their temporal and spatial variability.

In addition to field measurements, researchers have led experimental studies in stratified tanks under controlled conditions to examine basin-scale and high-frequency internal wave patterns. Laboratory experiments help overcome the difficulty in interpreting natural phenomena in the natural environment. Although experimental analyses contain an element of abstraction, they frequently allow us to examine a specific phenomenon that is often inaccessible through field observation due to the complexity and coast of the underwater measurements and the presence of uncontrolled natural perturbations. In these controlled settings, researchers can precisely manipulate parameters such as density stratification, wave amplitude, and reservoir size, allowing for a deeper understanding of the underlying physical processes.

Laboratory experiments also offer the opportunity to conduct detailed measurements using advanced imaging techniques and sensors, enabling researchers to explore intricate details of wave behavior that may be challenging to observe directly in the field.

Numerical modeling has emerged as a powerful tool in studying internal waves, allowing researchers to simulate and analyze complex wave phenomena in a computationally efficient manner. By employing mathematical equations that describe the fundamental principles governing fluid dynamics, numerical models can recreate realistic scenarios and provide quantitative predictions of the characteristics of internal waves. These models take into account various factors, such as bathymetry, stratification profiles, and external forcing, to simulate wave generation, propagation, and interactions. Numerical simulations not only aid in interpreting field measurements and laboratory results, but also enable researchers to investigate scenarios that are difficult to replicate in real-world settings, contributing to a comprehensive understanding of internal wave dynamics.

By combining insights from field measurements, laboratory experiments, and numerical modeling, researchers are gradually unraveling the intricate nature of internal waves and their far-reaching implications (). These interdisciplinary investigations serve as the foundation for advancing our understanding of mixing processes in thermally stratified lakes and reservoirs.

4.1 Laboratory experiments

However, before introducing the technique used to study internal waves in laboratory experiments, we devote the first subsection to exploring and reviewing the well-known theory of dimensional analysis, which is extremely useful to make comparisons between internal waves excited in small-scale experiments and real lakes.

4.1.1 Dimensional Analysis

Dimensional analysis offers a method to reduce the complexity of a physical problem, by looking at the relationships among the quantities that characterize the problem studied, reducing the number of experimental variables. In addition, the dimensional analysis provides the *scaling law*, which evaluates the equivalence between two phenomena that are actually different. Our goal here is not to provide all details about dimensional analysis but to draw attention to the importance of dimensional analysis on the study of internal wave propagation in controlled environments. For more details and a precise description of dimensional analysis and scaling law, the reader should refer to book by **?**.

Governed parameter

Suppose that we are interested in a governed parameter a_1 that can be determined by n governing parameters a_i, in which k is the number of independent dimensions. This means that parameters between a_1 and a_k cannot be expressed as a product of powers of dimensions of other members,

$$g(a_1, \cdots, a_k, \cdots, a_n) = 0. \tag{4.1}$$

However, the parameters of $n-k$ can be expressed in terms of the dimensions of the independent parameters, $a_1, \cdots, a_k$. Mathematically, the system of dimensions $(k \times (n-k))$ is given by

$$\begin{array}{ccccc} [a_{k+1}] & = & [a_1]^{p_{k+1}} & \cdots & [a_k]^{r_{k+1}} \\ \vdots & & \vdots & & \vdots \\ [a_{k+i}] & = & [a_1]^{p_{k+i}} & \cdots & [a_k]^{r_{k+i}} \\ \vdots & & \vdots & & \vdots \\ [a_n] & = & [a_1]^{p_n} & \cdots & [a_k]^{r_n} \end{array} \tag{4.2}$$

Dimensionless parameters

From system 4.2, we can define non-dimensional groups Π_i based on independent governing quantities:

$$\Pi_i = \frac{a_{k+i}}{a_1^{p_{k+i}} \cdots a_k^{r_{k+i}}}, \tag{4.3}$$

where i varies from 1 to $n-k$, which is the number of parameters that can be expressed as product of power of the dimension of the independent parameters, varying from a_{k+1} to a_n.

From equation 4.1 and 4.3, we have

$$f(a_1 \cdots a_k, \Pi_i a_1^{pk}) = 0 \tag{4.4}$$

Substitution of equation 4.4 into equation 4.1 gives the non-dimensional equation

$$\mathscr{G}(\Pi_1, \cdots, \Pi_{n-k}) = 0, \tag{4.5}$$

in which $\mathscr{G}$ is a general function of the non-dimensional parameters Π, that are constructed from a_i by $n-k$ dimensionless equations. Equation 4.5 may be expressed as

$$\Pi = a_1^{m_1} \cdots a_n^{m_n} \tag{4.6}$$

where the exponents m are rational numbers.

This equation lead to the Π-theorem, also known as Buckingham theorem. If there is a physical law that may be written as a relationship between dimensional variables and several dimensional governed parameters, the relation can be reduced through dimensionless products of quantities, in which the number of products is equal to the difference between the total number of governing parameters and those with independent dimensions (**?**).

Example

Consider a breakwater built at near the coast to protect a coastline from wave attack (Figure 4.1). The important variables to design the appropriate weight of the rip-rap armour, F_s, are: water density, ρ_l, wave amplitude, a, wave period, T, gravitational acceleration, g, slope of the breakwater, Θ, and density of the rubble-mound material, ρ_s.

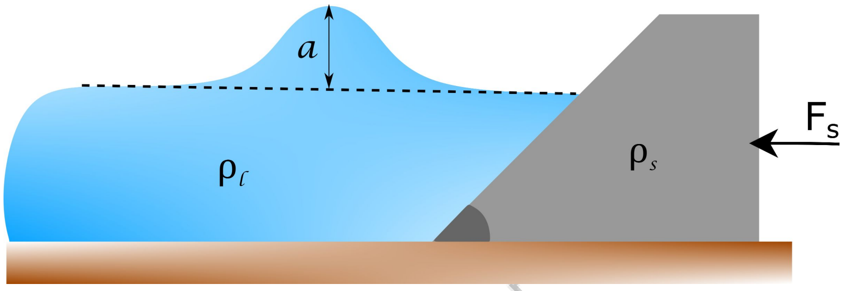

Figure 4.1 Breakwater near the coast to protect a coastline from the water attack.

Firstly, we can arrange the variables into a dimensional matrix given as

$$\begin{array}{c|cccccc} & \rho_l & a & T & g & \rho_s & F_s \\ \mathbf{M} & 1 & 0 & 0 & 0 & 1 & 1 \\ \mathbf{L} & -3 & 1 & 0 & 1 & -3 & 1 \\ \mathbf{T} & 0 & 0 & 1 & -2 & 0 & -2 \end{array} \tag{4.7}$$

note that the angle of the breakwater is already dimensionless. This dimensionless variable must be included into the non-dimensional products, even through it can be left out of the dimensional analysis. From 4.7 and using the definition expressed by equation 4.6, we have that

$$\Pi = \rho_l^{m_1} a^{m_2} T^{m_3} g^{m_4} \rho_s^{m_5} F_s^{m_6} \tag{4.8}$$

which shows that there are 6 governing parameters and just 3 independent dimensions. This means that there are 3 $(n-k=6-3)$ non-dimensional groups. The theorem allows different combinations of variables to form different dimensionless products, and does not provide any indication of importance between products and variables. Thus, for each Π group must have a number of variables equal to the number of dimensions. Table 4.1 presents some considerations to chose correctly variables to the non-dimensional products.

From 4.7 and 4.8 we have

$$\begin{array}{lrcl} \text{From M:} & m_1 + m_5 + m_6 & = & 0 \\ \text{From L:} & -3m_1 + m_2 + m_4 - 3m_5 + m_6 & = & 0 \\ \text{From T:} & m_3 - 2m_4 - 2m_6 & = & 0 \end{array} \tag{4.9}$$

Taking the advice from Table 4.1, we can define the first Π group as a function of the dependent variable F_s. We also can set $m_1 = 0$ and $m_5 = 0$. Thus, from

Selection of Π products

- The dependent variable should not appear in more than one non-dimensional product;
- Controllable variables should appear in only one dimensionless product to keep a reasonable experimental control;
- No two repeating variable can have the same dimension in a Π group (However, in the end of the analysis, these variables must be included as a Π product).
- Just keep in the analysis really important variables, ignoring those that has minor impact on the process over the range being examined;
- Standard dimensionless products are useful. Try to manipulate the exponents to obtain them in the Π products.

Table 4.1 Some considerations about the selection of Π products variables equation 4.8 and 4.9, the first non-dimensional product is defined as

$$\Pi_1 = \rho_l^0 a^{-3} T^0 g^{-1} \rho_s^{-1} F_s = \frac{F_s}{a^3 g \rho_s}. \tag{4.10}$$

The second group can include the wave period, since it has not appeared in the first group. Setting $m_1 = 0$ and $m_6 = 0$ (since the F_s should appear in only one product),

$$\Pi_2 = \rho_l^0 a^{-0.5} g^{0.5} \rho_s^0 F_s^0 T = \sqrt{\frac{g}{a}}\, T. \tag{4.11}$$

The third group is formed through the variables with the same dimension, water density and armor material density,

$$\Pi_3 = \rho_l^{-1} a^0 T^0 g^0 F_s^0 \rho_s^1 = \frac{\rho_s}{\rho_l}. \tag{4.12}$$

Finally, the non-dimensional representation of the problem has the form

$$\frac{F_s}{a^3 g \rho_s} = \mathscr{G}\left(\sqrt{\frac{g}{a}}\, T, \frac{\rho_s}{\rho_l}, \Theta\right) \tag{4.13}$$

in which Θ is an additional non-dimensional group.

Through equation 4.13, the relationship between all Π groups can be tested experimentally through laboratory experiments to predict how F_s varies due to the variation of the non-dimensional groups.

4.1.2 Setup and Wavemaker

Frequently investigation of internal waves under controlled conditions are conduced in Plexiglas rectangular tanks of different sizes. Normally this studies are carried out in tanks that vary from 3 to 21 m long. The tank height and width normally vary from 0.1 to 0.6 m. Although density gradients in nature are always continuous, greater amplitude internal waves normally arise near the region of rapidest change in water density, region called pycnocline. Thus, many studies have investigated the interfacial wave that propagates in a stable two-layer system, in which upper and lower layers are completely homogeneous and present small density difference (Figure 4.2). Many studies investigate experimentally the propagation of interfacial solitary waves in a two-layer system (**???**). Laboratory investigations also have studied the propagation of basin-scale internal waves in continuous stratified rectangular thanks (Boegman et al., 2005b).

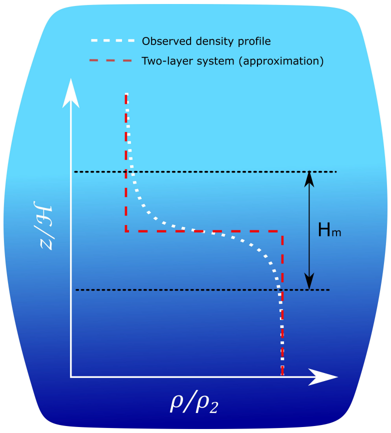

Figure 4.2 Hypothetical profile of water density and an approximation to a two-layer system.

There are a number of methods to create a two layer system in rectangular tank. Often, the tank is filled with liquids as carefully as possible to achieve small thickness of the intermediate transition layer H_m (**?**). A large H_m modify the internal wave structure and a simple two-layer model fails to reproduce greatly the system dynamic. To generate the two-layer stratified system with a small H_m, the lighter fluid is added in a first step, whilst the denser one is injected slowly underneath the upper layer in a subsequent stage. To a better visualization, a dye can be applied in the denser fluid before the injection. To minimize the thickness of the density layer transition (H_m), a low flow rate of the density fluid isa required. The flow rate can be increased just when the interface is completely formed and far from the injection region.

There are also other techniques used to create a two-layer system. The tank can be filled firstly with denser fluid, whilst the lighter fluid is injected slowly through a floater, just above the denser fluid (Hutter, 2011).

Watch the video How to build 3.1 available on the supplemental material to understand how to build a two layer system in a rectangular tank.

Video HTB 3.1

To simulate the hydrodynamic of shallow basin, which the metalimnion takes up a relatively larger proportion of the total lake depth, a two-layer system can be created through the lock-exchange procedure, explained in details in section **??**. The strong perturbation may create a thicker intermediate layer. Often, for experiments that tend to avoid a large interface thickness, $h_m/H < 0.15$.

Video HTB 3.2

Evidences have shown that, considering a system with finite intermediate layer ($h_m/H \approx 0.2$), after the interaction between internal solitary wave and submerged obstacle there are a excitation of higher mode of transmitted and reflected internal waves (**?**).

Through the advance of technologies to measure and visualize stratified flows, more complex studies have investigate internal waves in continuous stratified fluid, often through a linear stratification. A detailed historic review of laboratory experiments in continuous stratified fluid is given by **?**. A linear stratification is normally achieved through the *double-bucket method*. This technique have been described in details by **?** and basically consists of two large vessels at equal height, one filled with salt water and another with fresh water, connected with a U-tube, initially closed through a clamp. Using the Bernoulli principle, the two-buckets can be positioned in a determined height position in relation to the main tank, the one that we want to create the linear stratification. The pipe can be placed in the salt water bucket to conduce water into the main tank. To better control the flow rate, a pump can be used (Figure 4.3).

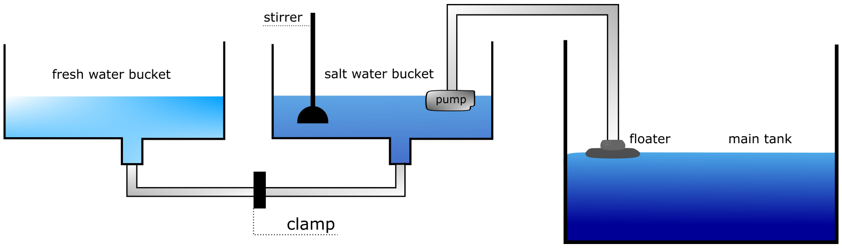

Figure 4.3 Schematic diagram of apparatus and set-up used to produce a linear stratification using the double-bucket technique.

The initial density of the seawater bucket is defined as our required maximum water density, the water density of the tank bottom. In addition, to avoid salt water rushing into the fresh water tank when we remove the clamp, for each gram of salt added on the salt water bucket, one gram of fresh water must be added to the fresh water bucket.

When the pump is switched on and the clamp is removed, pump draws salt water from the salt water bucket to the main tank. To keep the water levels in both vessels, part of the water flows through the U-tube to the salt water bucket, reducing the relative salt concentration. As the processes continues, the water flowing out into the tank gets gradually fresher, creating a linear stratification.

To avoid mixing and turbulence on the water surface, the fresher water should be spread out above the salter water by a sponge. inject the water in the main tank (Figure 4.3).

To provide a direct visualization of the stratified system and enhance the visibility of mixing events, colored dyes can be introduced periodically to the floater during the filling procedure. This technique provides a good qualitative visualization of the diapycnal mixing (**?**). However, the advancement in computer-controlled devices has allowed the development of new non-intrusive measurements, which provides a efficient quantitative analysis. The synthetic Schlieren technique is one of the most applied methods to analyze stratified-flows and described in details in section 4.1.3. The technique is based on automatic processing of optical distortion of images caused essentially by density difference (**?**).

4.1.3 Synthetic Schlieren Technique

Many laboratory experiment that studies the propagation of internal waves in stratified system have been conducted in laboratory tanks colored by dye, in which dye is applied in each interface, and the wave propagation is visualized easily (). However, according to **?**, the advancement in lasers and computer-controlled devices have created valuable new non-intrusive measurements such as particle image velocimetry (PIV), laser-induced fluorescence, shadowgraph, and the synthetic schlieren technique.

In this section we pay a particular attention to the technique based on traditional schilieren method to visualize stratified system. Internal waves and other motions that occurs in a stratified media made by the same fluid but with different properties (e.g. temperature, salinity, pressure), does not present an evident difference in color, however, due to the density difference, the refractive index of the media may vary, refracting or bending light rays differently. The difference in refraction is not easily detected by the human eyes and ordinary camera, but can be evidenced by simple optical techniques.

The technique described in this book is a low-cost version () of the traditional schilieren method which requires professional or DSLR cameras and has been used by many authors to investigate the dynamic of internal wave and other movements in continuous stratified fluids (). The simple technique described here has been proposed by () and generated background-oriented schlieren (BOS) images through Schlieren and shadowgraph techniques using simple smartphone imaging and basic accessories and materials.

Non-traditional schlieren technique limitations
Traditional schlieren methods project a light beam into the camera lens. Smartphone cameras has a tiny aperture which ....

Table 4.2 Limitations.

4.2 Field measurements

4.2.1 Measurement Devices

The study of the hydrodynamics of stratified lakes is often a challenging task, as it involves many different physical processes that can influence water masses, heat, and biogeochemical transport. The hydrodynamics of these observation motion in these environments is not possible through a dyed layer or the synthetic Schlieren technique, commonly used in controlled settings. In lakes and reservoirs, the prediction of water motion requires the utilization of different fast response sensors. Typically, the motion of stratified flows is predicted by analyzing the variations of temperature, pressure, and salinity, as these variables are responsible for the stratification of the water density. In addition, advances in technology have allowed for a better understanding of stratified flow patterns through the prediction of water velocity fields. Furthermore, modern fast response water quality sensors can be utilized to assess the impact of motion on water quality in stratified fluids.

Although nowadays many fast response sensor are available in the market, one of the simplest method to analyze the water quality and some important property is through the Van Dorn Water Samples **??**. The Van Dorn water sampler is a horizontal transparent acrylic tube with double releaser, which can be closed by the operator when it reaches the desired depth, insuring a representative water sample at required depth. Some Van Dorn water samplers models have sensors coupled to the device, such as thermometers and pressure sensors.

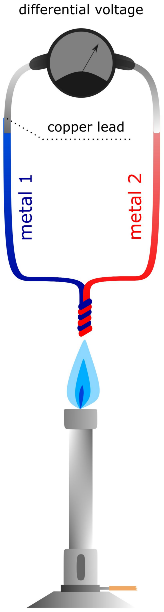

Figure 4.4 Thermocouples operating principles.

Although Van Dorn Water sampler is an efficient probe for sampling water at different levels depth, the submerging process may cause disturbance during the water sampling. Nowadays, there are many stationary instruments available in the market to predict the hydrodynamic os stratified fluid and evaluate their effect on the water quality. In the next section we present in more details some sensor capable to describe the motion of stratified fluids. To measure directly the field velocity of the water, one of the most used devices are: Acoustic Doppler velocimetry and Acoustic Doppler current profiler. There are also other alternatives since sensors based on Doppler principle are relatively expensive. To predict the dynamic of stratified fluid, many times we measure the variables that influence the stratification. As discussed earlier, temperature, pressure, and salinity. In this section we present some sensor used to measure some of this variables. In addition, we present a multi-parametric sensor extensively used in the study of stratified fluids and low-cost sensors, which can be easily developed to better understand the system dynamic.

Temperature Sensors

Temperature can be measured by many devices, such as infrared and liquid in glass thermometers, thermocouples, resistive temperature devices (RTDs), thermistors, and semiconductor IC. Trade-offs amongst devices include accuracy, sensitivity, cost, operating temperature range, and stability, which influence the output signal drift over time, and consequently the need for repeat calibrations.

Liquid-glass thermometer is the most popular device to measure temperature. Mercury thermometers, which was invented in 1714, consists of a bulb containing mercury attached to a narrow glass tube, in which depending on the temperature, the mercury expands or contracts. Based on thermal radiation principle, infrared thermometer is also an option to measure temperature. However, since this type of thermometer is based on the amount of infrared energy emitted by a determined object, it can only measure the surface water temperature.

Thermocouples are devices to measure temperature by measuring a change in voltage, a result of the Seebeck effect (Figure 4.4). Whenever there is a temperature difference along two wires, there is also an electric potential difference that generates a magnetic field, and consequently the compass is moved to indicate the temperature. The magnitude of this electric pressure depends on the wires material. The relationship between voltage created by the conductors and temperature is known for a large number of conductor pair, and have been largely documented (Taylor, 1997). Even though thermocouples have a very fast response to temperature changes, voltage signal in a majority of cases is nonlinear. They are susceptible to corrosion and have worse long-term stability and accuracy than the resistive devices.

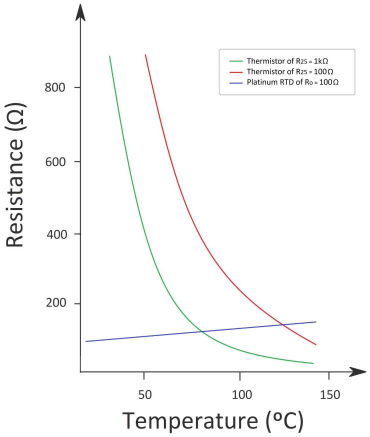

Figure 4.5 Resistance versus temperature for Platinum RTD and Thermistors.

Resistive temperature devices (RTDs), also called resistance thermometers, are devices to measure temperature based in resistance change, and have a positive temperature coefficient. Most RTDs devices consist of fine coiled wire wrapped around a ceramic core. Usually, the wire is made of pure metals such as nickel, platinum, and copper. These devices are classified according to metal that are used in their composition.

In the same way of thermocouples, RTDs have been largely documented according to a large range of wires. RTDs are typically protected by a sheathed probe since their elements are relatively fragile. RTDs provide an excellent long-term stability. In the similarly way of thermocouples, resistance thermometers can be affected by corrosion, converting the metal element from its pure form to a metal oxide, which will tend to increase the wire resistance. When RTDs are made with platinum, they are not susceptible to be affect by corrosion or oxidation. However, Platinum resistance thermometers may be really more expensive. In addition, although RTDs show an almost linear resistance-temperature relationship, the temperature coefficient is really low (Herman, 2011). As a result, it does exhibit a low change in resistance over a large change of temperature.

Another resistive device used to measure temperature is known as a thermistor (portmanteau of thermal and resistor). Thermistors are made of ceramic or polymer instead of metals, and have much higher temperature coefficients than RTDs. Their resistance varies dramatically over some temperature range, and are considered one of the most sensitive devices to measure temperature, with sensitivities in the range of 3 to 6% (Figure 4.5). Thermistors are ceramic semiconductors made from metal oxides which have an electrical resistance that decrease with temperature. Although thermistor can achieve great precision, the temperature range is limited.

The last type of sensor discussed here is the 1-Wire digital temperature sensors, which offer several valuable features such as linearity, high sensitivity with 9 to 12-bit precision, and small size. These devices are based on relationship between the base-emitter voltage and the collector current of a bipolar transistor. They are inexpensive, require no linearization, and can be interfaced directly on micro-controllers, such as an Arduino Uno. In section 4.4, we provide a guide of how measure continuous water temperature from a waterproof DS18B20 temperature sensor (≈ \$12) using a Arduino Uno R3 (≈ \$20) (Figure 4.6).

Figure 4.6 Waterproof DS18B20 temperature sensor and Arduino UNO R3.

Thermistor chain

In those early years after the observation of underwater temperature fluctuation (Watson, 1903), Wedderburn and collaborators[1] provided guidelines to spread the knowledge about internal seiches in stratified basins through the first simultaneous recording of water temperature (with just one single point in depth) using a underwater thermograph. However, even after continuous water temperature measurements in a single point, many limnologists disbelieved that internal wave could be important or even exist within thermal stratified lakes.

The phenomenon was doubted until 1952, when finally Mortimer (1952) demonstrated their universality and importance using a thermistor chain, a powerful device for continuous water temperature measurements at selected depths (Figure 4.7). Nowadays temperature measurements collected from thermistor chain are still the most common data analyzed through detect internal waves in stratified basins of fresh-water (Hutter, 2011).

The thermistor chain frequently is placed in buoy stations, also called moorings, which keep instruments in a specific submerged position. The surface buoy is usually equipped with a data logger, which is responsible to recover sensors data. To avoid movements and rotations due to internal and external forces, ball-bearing swivels, anchors and rope are often used on the surface and near the basin bottom. The thermistor chain is a long electrical cable containing temperature sensors and connected to batteries and a host logger systems (Figure 2.8). Since internal waves can be excited in different depths, a several quantity of temperature sensor along the vertical coordinate is essential. In spite of the fact that a good spatial resolution is crucial for internal waves investigation, for low-frequency waves of order of several hours, a low temporal resolution is not required. Since most of time basin-scale internal waves have order of several hours, generally data collection has order of minutes. **?** investigated basin-scale internal waves with period of ≈ 8 h in a small dendritic reservoir through a thermistor chain with temporal resolution of 15 min. On the other hand, to investigate high-frequency internal waves (~ 10^{-3} Hz), internal wave breaking, and shear instabilities (~ 10^{-2} Hz), high temporal resolution for temperature sensor is cru-

---

[1] Wedderburn, Williams (1911); Wedderburn (1912); Wedderburn, Young (1915)

cial to capture these high-frequency thermal oscillations (Boegman et al., 2003). Thus, the temporal resolution of the sensor must be in the same order of the phenomenon that is investigated. Generally, the sample frequency must be twice the maximum Brunt-Väisälä frequency, N_{max}, and 4 times the average of N for the vertical profile.

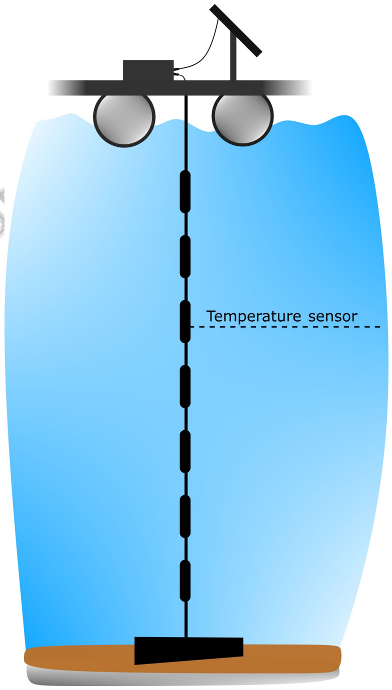

Figure 4.7 Thermistor chain.

Velocity measurements

Although isotherms analysis have been used extensively to identify internal waves and to predict the dynamic of thermal-stratified system (Mortimer, 1952; Münnich et al., 1992), nowadays internal wave is also identified through sensors capable to measure the local field velocity of the water. Acoustic Doppler Velocimetries, developed in the end of the 20th century, and the Acoustic Doppler Current Profile are much more expensive devices than those used to measure temperature. However, the field velocity may present a direct indication of the dynamic of stratified system, with no secondary disturbances.

For example, imagine a water surface submitted to a constant wind event. Daily variation of water temperature occurs essentially due to the daily heat flux at water surface and water movement, which can be associated to water cooling, internal waves, turbulence, among others.

Due to the surface heat flux, warmer isotherms are typically eroded near the midday, when the solar radiation is more intense. This variation does not represent a water motion, but just a change in water temperature. The wind that acts over the lake surface creates a mixing region that decrease the water temperature located right bellow the water surface. This variation in temperature can create a thermal instability that could promote a downward movement. This motion is associated due to the density difference between colder water generated by mixing at water surface. Figure **??** presents the isotherms and vertical velocity of this hypothetical system. Note that the isotherm analysis is not so intuitive to predict the motion of the system.

Acoustic Doppler Velocimeter

The Acoustic Doppler velocimeter was invented in the end of the 20th century. It is based on the Acoustic Doppler Shift principle and measure the water velocity in three dimension. The sensor has two main components: the acoustic sensor module and the signal conditioning module (Figure 4.8).

The acoustic module is composed by one acoustic transmitter beam and three receiver elements. The probe is submerged into the flow, where the transmitter beam sends pulse of short acoustic waves. The pulse propagates through the water. However, a fraction of the acoustic energy is scattered back by particulate matters present in the sampling volume. The sampling volume is located approximately 10 cm from the acoustic transmitter to avoid the flow interference. This distance may vary slightly from probe to probe.

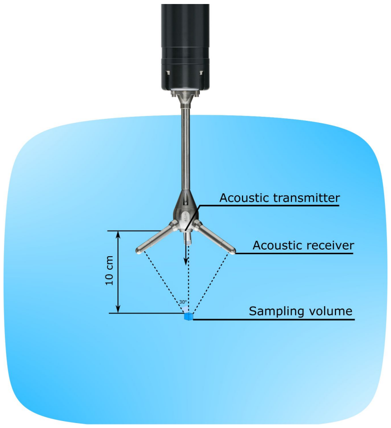

Figure 4.8 Acoustic Doppler velocimetry (ADV).

The three acoustic receiver detect the scatted acoustic waves originating from the sampling volume. Due to the Doppler shift principle, the emitted acoustic waves change in frequency. The Doppler shift observed at each acoustic receiver beam is proportional to the field velocity of the water (**?**).

The signal conditioning module is responsible to control

Acoustic Doppler Current Profiler

Multi-parametric sensor

One of the most famous instruments developed for determining water properties in lakes, reservoir, and oceans is known as CTD (an acronym for conductivity, temperature, and depth) (Figure 4.9). Often this device is built with a fast response Platinum RTD to measure temperature.

CTD device has a pressure sensor that measures the equivalent hydrostatic pressure of the water above the sensor to calculate the total water depth. It is also equipped with a conductivity sensor that measures true or specific conductivity. A profiling CTD measurement is made when this device travels vertically though the water. It is submerged until it hits the bottom. Many multi-parametric sensors can make an average between the travel up and down to measure the profile parameters.

CTDs have good spatial resolution, since are built with extremely fast response sensors. However, usually it is operated manually and the time resolution of the acquisition of each profile depends on the submerged time, what limits the usage of these devices to detect internal waves. However, CTD measurements are useful for calibrating the thermistor chain and providing information on density dynamic of the system, since the contribution to density are not only from temperature.

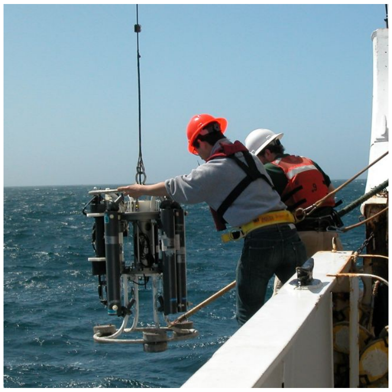

Figure 4.9 CTD - Crew of NOAA Ship Miller Freeman (Source: NOAA/Department of Commerce)

Salinity measurements

In most lakes and reservoirs, density stratification is dominated by thermal stratification, and consequently water density is controlled by water temperature. However, in most hydrodynamic experiments, the heat transport cannot be controlled. Thus, in most cases, experimental analysis of stratified flow is conducted in a channel where stratification is caused by salt concentration difference, also called salinity difference. In addition, it is worth pointing out that salinity may also influence the dynamic of internal waves in ocean, estuaries, and salt lakes.

Salinity could be defined as the total concentration of all dissolved salts in a solution. Since the number of dissolved ions per volume influence positively water conductivity, which express the ability of electrons to flow through the solution, frequently the salinity is directly correlated to conductivity. That is why seawater has high conductivity, and consequently higher density than the fresh water. Although the number of the ions increase in seawater, the system remains electrically neutral. This phenomenon occurs when electrolytes dissolve in water, they split into cations and anions, but the concentration of each atoms remain the same. For example, consider the electrolysis of water and sodium chloride solution (NaCl), one type of salt. When the NaCl is dissolved in water, they are separated into different ions, Na^+ and Cl^-. In addition, the water molecules undergo self-ionization, also called autodissociation, in which water molecule are split into hydroxide ion, OH^-, and hydrogen ion, H^+.

$$NaCl \longrightarrow Na^+ + Cl^- \tag{4.14}$$

$$H_2O \longrightarrow H^+ + OH^- \tag{4.15}$$

If the negative and positive pole of battery are connected through conducted wires (electrodes) and they are submerged in water as shown in Figure 4.10, electricity will pass through and between the electrodes. Thus, negative ions, anions, in the solution will be attracted to the positive pole, anode, and vice versa.

However, the ionization process produces two anions and two cations. There are two possibilities of semi-reaction of reduction (cathode side) and oxidation (anode side), which depends on the preferential discharge of ions. Firstly, since H^+ is more electropositive than Na^+, the semi-reaction that occurs in the cathode is

$$2\,H_2O + 2\,e^- \longrightarrow H_{2\,(g)} + 2\,OH^-, \tag{4.16}$$

whilst at anode, since Cl^- is more electronegative than OH^-, the semi-reaction that occurs is

$$2\,Cl^- \longrightarrow Cl_{2\,(g)} + 2\,e^-. \tag{4.17}$$

Equations 4.16 and 4.17 is a oxidation-reduction (redox) reaction that involves a transfer of electrons between two species, in this case, from catode to anode. In other words, reaction 4.17 shows that the chloride ion is oxidized to chlorine gas, transferring electrons to the anode. Whilst, hydrogen ions capture electrons from the cathode to form diatomic hydrogen molecule.

The global reaction is obtained through equations 4.14, 4.16, and 4.17,

$$2\,NaCl + 2\,H_2O \longrightarrow H_{2\,(g)} + Cl_{2\,(g)} + 2\,Na^+ + 2\,OH^-, \tag{4.18}$$

which H_2(g) and Cl_2(g) are produced at the cathode and anode, respectively. The 2 Na^+ and the 2 OH^- are combined to form 2 $NaOH^-$

This ability of electrons to flow is called conductance, expressed as G and frequently measured in Siemens, S. Since conductance is the inverse of resistance, which are measured in Ω, sometimes the conductance is expressed in a reciprocal form as $\mho$, that is equivalent to S. In this textbook we use the most common form, in which is expressed with ’S’. The conductance is not a specific measurement on its own, the measurement depends directly on the electrodes length, similar with resistance. Thus, a larger electrode increases the contact area with ions, and consequently rises the conductance.

The conductance is parameterized with the ratio between the conductors distance, d, and the surface of electrode, A. This parameterization gives the

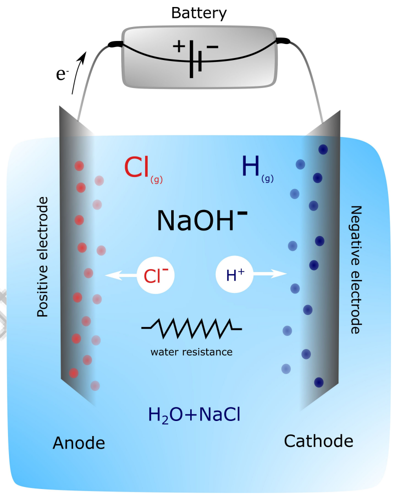

Figure 4.10 Principles of water electrolysis.

Pure water electrolysis
The electrolysis of pure water is a decomposition of water molecules into hydrogen and oxygen gases due to the passage of an electric current.

$$2\,H_2O + E \longrightarrow O_2 + 2\,H_2$$

Actually, since pure water has a very high resistivity (≈ 18 Ω/cm), it requires excess energy in the form of overpotential to speed up the electrolysis. In other words, the ions concentration of OH^- is extremely low to conduce rapidly electrons. This means that any applied potential is going to be converted into thermal energy. Note that tap water has higher concentration of electrolytes, such as sodium, potassium, and magnesium, than pure water. Their resistivity is ≈ 5 kΩ/cm, approximately 1000 greater than pure water.

Table 4.3 Electrolysis of water.

electrical conductivity, expressed as

$$\kappa = G \times \frac{d}{A}, \tag{4.19}$$

in which κ is the solution conductivity given in μS/cm, G is the conductance given in μS, and the ratio d/A is the cell constant, K_{cell}, expressed in 1/cm, Figure 4.11.

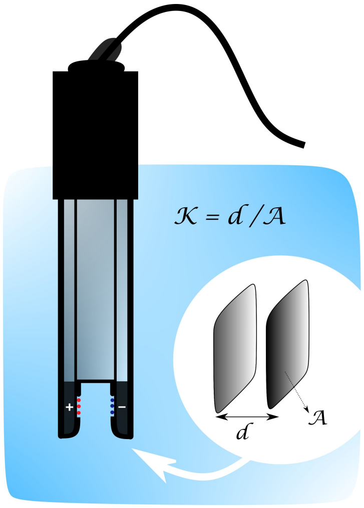

Figure 4.11 Sketch of a conductivity probe and how is defined the cell constant, K.

Conductivity meters are delivered with certified cell constants, K_{cell}. The choose of the best conductivity probe with a specific K_{cell} depends on the conductance readings, and consequently on ions concentration. For a sample with low conductivity, the electrodes can be placed closer or the surface area of electrodes can be raised, which is the definition of a conductivity meter of lower cell constant. The measurement accuracy is strongly influenced by the cell constant, which needs to be selected appropriately for each application. Figure 4.12 shows standard conductivity values for a set of samples and the range of recommended cell constants for a given conductivity meter.

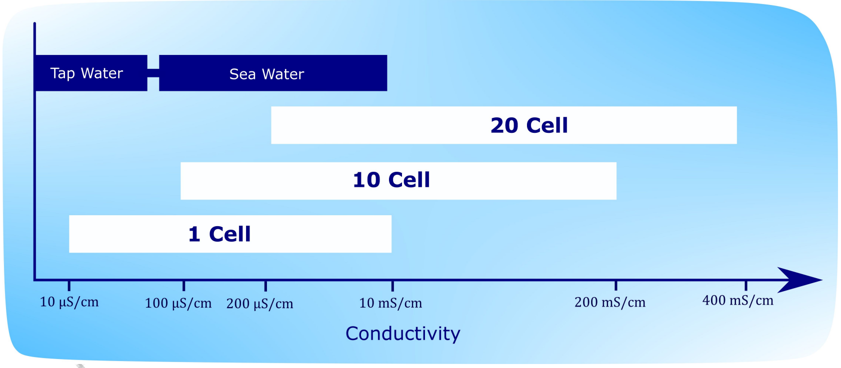

Figure 4.12 Range of conductivity for three different cell constant. Pure water has conductivity of approximately 0.1μS/cm.

The conductivity of a solution is measured through the potential difference between the positive and negative pole. This measurement uses equation 4.19, the principle of ohms law and the inverse relation between conductance and resistance. Thus, the conductivity is given by the expression

$$\kappa = \frac{K_{\text{cell}}}{R_{sol}} = \frac{K_{\text{cell}}\, i}{U_{sol}}, \tag{4.20}$$

in which R_{sol} is the solution resistance, i is the electric current, and U_{sol} is the electrical potential of the solution. Note that U_{sol} is similar to ΔU, the difference between the input and output voltage.

When the salinity is based on a direct comparison with the specific conductance of a solution (conductivity ratio), the salinity is called *practical salinity* and is expressed in psu (practical salinity units), which is dimensionless (Forch Knudsen Martin e, 1901). A useful summary of equations used to calculate salinity from electrical conductivity is presented by Fofonoff, Millard (1983). However the application is restricted to the range between 2 and 42 psu.

Recently, a new description to estimate salinity have been proposed, which introduced the term: *absolute salinity*. According to **?**, differently from the *specific salinity*, measured through conductivity cells, the *absolute salinity* uses the thermodynamic properties of seawater.

Described by Intergovernmental Oceanographic Commission, others (2015), the new description of salinity is based on a Gibbs function, which represents all properties of seawater in a consistent way with the thermodynamic state of the system. Unlike *specific salinity* which has a unit in PSU, *absolute salinity* has units of ppt (parts per thousand) or g/kg (mass fraction of salt in seawater).

4.3 Numerical models

4.3.1 Modeling of heat transport: Delft3D-FLOW

Although unidimensional internal wave models have been used to describe internal seiche patterns in thermally stratified lakes Lemmin, Mortimer (1986); Münnich et al. (1992); Roget et al. (1997); Vidal et al. (2005); Carvalho Bueno de, Bleninger (2018), they have several simplifications and cannot be used to describe the whole process of heat transport associated with the internal wave field. The simplified multilayer internal wave model neglects horizontal variability, including effects of inflows, outflows, heat transport, mixing, and interaction between internal wave and lake bathymetry. These limitations cause fundamental problems to describe the hydrodynamic of lakes and reservoirs, especially when we are concerned with the internal wave field, which has different spatial and temporal scales, and an intrinsic three-dimensional nature.

With an improvement in computational performance, three-dimensional models of heat transport have gained prominent research interest because they are capable of simulating processes in lakes by solving the full continuity, momentum, and transport equations. As with all numerical approaches, three-dimensional hydrostatic models also have several limitations, mainly related to the turbulence aspect. Due to numerical diffusion and dissipation Hodges et al. (2006) and the inability of hydrodynamic models to deal with nonlinear and non-hydrostatic mechanisms, the energy fluxes must be investigated carefully, especially the mechanism of internal seiche damping Shimizu, Imberger (2008). ELCOM and Delft3D are among the most well-known three-dimensional models to simulate the dynamics of shallow-water systems, such as coastal regions, reservoirs, estuaries, lakes, ponds, and rivers. The basin-scale internal wave affected by Earth's rotation has been greatly stimulated by ELCOM Hodges et al. (2000); Valerio et al. (2012) and Delft3D Dissanayake et al. (2019); Carvalho Bueno de, Bleninger (2019); Kranenburg et al. (2020); Baracchini et al. (2020). Recently, observation has shown that Delft3D and ELCOM are significantly trained in simulated large-scale internal seiches in lakes, which agrees well with field measurements

Impact of temperature on conductivity measurement
Conductivity depends on ions mobility and electrolytes concentration, which means that is affected not by salt concentration, but also by temperature. As temperature rises, the number of ions solution increases due to dissociation of molecules and also their mobility in the solution, favoring the transference of ions between electrodes, and consequently increasing the conductivity. As stated by Gray (2005), the relationship follows a extremely nonlinear behavior for natural waters, which implies that a nonlinear temperature compensation method must be used. Different methods of temperature correction have been developed. Generally, the conductivity is measured by using a temperature compensation at a reference temperature of 20 °C or 25 °C ,and can be measured by

$$\kappa_\epsilon = f_\epsilon \times \kappa_\tau, \qquad (4.21)$$

in which κ_ϵ is the conductivity at the reference temperature ϵ, κ_τ is the measured conductivity at temperature τ, and f_ϵ is the temperature correction factor for natural waters. A list of temperature correction factors is provided by **?**. **Attention:** Many current conductivity meters has a temperature sensor and, in this case, the correction is automatically applied and the conductivity is displayed at a reference temperature. Some conductivity meters also offer a specific temperature correction method.

Table 4.4 Temperature compensation.

in Upper Lake Constance Dissanayake et al. (2019).

Now we focus on the description of the three-dimensional Delft3D-FLOW model, which is the model used in this thesis to simulate the hydrodynamics of the lake. In the next section, we present the model description, paying special attention to numerical approaches that may limit the applicability of Delft3D to investigate the internal wave field, trying to make the connection with the physical description discussed in section **??**. A full description of the model is provided by deltares2003delft3d.

Delft3D is a multidimensional hydrodynamic numerical model based on Reynolds-Average Navier-Stokes (RANS) under the Boussinesq approximation and shallow-water assumption. The program calculates the unsteady flow and transport phenomena of heat and matter due to tidal and meteorological forces by solving the equations of mass conservation, transport, and horizontal momentum, using a turbulence closure model Delft Hydraulics (2003). The vertical velocity field is obtained implicitly from the continuity equation.

Governing equations

The depth-averaged mass conservation equation is obtained by integrating the equation **??** along the water column, taking into account the boundary conditions at the water surface and lake bottom:

$$\int_{-H}^{\eta} \frac{\partial u_i}{\partial x_i} \mathrm{d}z = \frac{\partial}{\partial x_i} \int_{-H}^{\eta} u_i \mathrm{d}z - u_i(z=\eta) \frac{\partial \eta}{\partial x_i} - u_i(z=-H) \frac{\partial H}{\partial x_i} = 0, \tag{4.22}$$

in which $\eta(x, y, t)$ and $H(x, y, t)$ are the water level (surface function) and bed horizontal plane of reference, respectively.

Assuming that the bathymetry does not vary with time, we may rewrite equation 4.22:

$$\frac{\partial}{\partial x_i} \int_{-H}^{\eta} u_i \mathrm{d}z - u_i(z=\eta) \frac{\partial \eta}{\partial x_i} = 0, \tag{4.23}$$

in which η and H are the water level above and the depth below a horizontal plane of reference, respectively.

The kinematic boundary condition at water surface ($z = \eta(x, y, t)$) is defined as

$$u_i = \left\{ \frac{x_2 - x_1}{\Delta t}, \frac{y_2 - y_1}{\Delta t}, \frac{\eta(x_2, y_2, t_2) - \eta(x_1, y_1, t_1)}{\Delta t} \right\} \tag{4.24}$$

Expanding $\eta(x_2, Y_2, t_2)$ in a Taylor series:

$$\eta(x_2, t_2) \approx \eta(x_1, t_2) + (x_2 - x_1) \frac{\partial \eta(x_1, t_2)}{\partial x} + (y_2 - y_1) \frac{\partial \eta(y_1, t_2)}{\partial y}, \tag{4.25}$$

and substituting equation 6.9 into the vertical component of equation 4.24, we obtain

$$w = \frac{\partial \eta}{\partial t} + u \frac{\partial \eta}{\partial x} + v \frac{\partial \eta}{\partial y}, \tag{4.26}$$

in which $u_i = \Delta x_i / \Delta t$, where Δx_i is the grid size of each component and Δt is the time step.

Finally, substitution of equation 4.26 into equation 4.23 gives

$$\frac{\partial \eta}{\partial t} + \frac{\partial}{\partial x_i}\left(u_i\ (\eta + H)\right) = 0. \tag{4.27}$$

In Delft3D an additional term of source and sink per unit of area is added to equation 4.27 to account for the contribution of inflows and outflows.

Delft3D solves the Reynolds Averaged Navier-Stokes equations (RANS) for an incompressible fluid considering the Boussinesq approximation and the hydrostatic assumption in the vertical direction. Dividing the contribution of vertical and horizontal eddy viscosities from equation **??**, and applying the conservation of mass and hydrostatic assumption:

$$\frac{\partial u_i}{\partial t} + u_j \frac{\partial u_i}{\partial x_j} - \overline{\omega_o} u_k = -\frac{1}{\rho}\frac{\partial p}{\partial x_i} + \nu_h \frac{\partial^2 u_i}{\partial x_j^2} + \frac{\partial}{\partial z}\left(\nu_v \frac{\partial u_i}{\partial z}\right), \tag{4.28}$$

in which u_i is the Reynolds' time-averaged velocity field, p is the pressure, $\overline{\omega_o}$ is the inertial frequency, used to account for the contribution of the Coriolis effect. ν_h and ν_v are the horizontal and vertical eddy kinematic viscosity (m^2/s), respectively. Recall that for the shallow water assumption, the momentum equation in z-direction is reduced to the hydrostatic form since the vertical velocity is neglected in the numerical procedure ($w = 0$). Once horizontal velocities have been found, the vertical velocity is estimated by integrating the mass conservation equation 4.27.

The transport of scalars and heat are governed by a multidimensional convection-diffusion equation, which can be defined, in the orthogonal coordinates as

$$\frac{\partial C}{\partial t} + \frac{\partial u_i\ C}{\partial x_i} = \frac{\partial}{\partial x_i}\left(D \frac{\partial C}{\partial x_i}\right) + S, \tag{4.29}$$

in which C is a scalar (e.g. heat, salinity, or constituents), S is sources and sinks due to discharges and withdrawals, and D is the eddy diffusivity coefficient. For the horizontal plane and the vertical direction, $D = D_h$ and $D = D_v$, respectively. The horizontal eddy diffusivity coefficient (D_h) is anisotropic along the horizontal plane x-y.

In order to solve equations 4.28 and 4.29, Delft3D estimates the eddy viscosity and diffusivity coefficients from the turbulence closure modules, discussed in Section 4.3.1.

Heat flux model

The total flux of heat energy across the water surface is modeled according to the heat balance illustrated in Figure 2.7. Delft3D-FLOW offers different heat flux models Delft Hydraulics (2003) depending on the available meteorological data, such as the Murakami heat flux model Murakami et al. (1985) and the Ocean flux heat model Lane (1989); Gill (2016). Observations in small thermally stratified reservoirs have shown that the Murakami heat flux model underestimates the energy loss by evaporation compared to the Ocean model Polli, Bleninger (2019). Although this difference has been identified, the Murakami model was capable of detecting Kelvin and Poicaré internal waves in Lake Constance Dissanayake et al. (2019). Ocean heat flux model has been used in the Delft3D model to simulate internal seiches Carvalho Bueno de, Bleninger (2019); Kranenburg et al. (2020). Since both models have been capable to simulate internal seiches in lakes, here we describe in detail only the Ocean heat flux model, which has been used in this thesis. The Ocean heat flux model takes into account the following components of heat:

$$Q_{\text{total}} = Q_{sw} + Q_{ir} + Q_{la} + Q_{se}, \tag{4.30}$$

in which Q_{sw} is the net heat flux from short wave, Q_{ir} is the infrared (long wave) heat flux, Q_{la} is the latent heat flux (phase change effect; e.g. evaporation), and Q_{se} sensible heat flux (temperature change effect; e.g. convection).

The net incident solar radiation (short wave) is the only term that is entirely prescribed by the Ocean heat flux model [2]. The absorption component of the net incident solar radiation into the water column is computed from the albedo coefficient $Ab_s = 0.06$, which reduces the magnitude of short wave that hits the water surface

$$Q_{sw} = Q_{iw}\ (1 - Ab_s)\ F_{cc}, \tag{4.31}$$

in which Q_{iw} is the incident solar radiation and $F_{cc} = 1 - 0.40\ C_c - 0.38\ C_c^2$ is a function to take into account the influence of absorption of solar radiation by clouds, where C_c is the user-specified fraction of sky covered by clouds. Equation 4.31 describes the balance between *short wave radiation* and *water surface radiation* illustrated in Figure 2.7.

The infrared radiation (Figure 2.7) is calculated by Ocean heat flux model as

$$Q_{ir} = 0.985\ K_{sb}\ \tau^2_{\text{water (K)}} (0.39 - 0.05\ \sqrt{e_a})(1 - 0.6\ C_c), \tag{4.32}$$

where $K_{sb} = 5.67\ 10^{-8}$ J/(m²sK^4) is the Stefan-Boltzmann's constant, $\tau_{\text{water (K)}}$ is the water surface temperature in Kelvin units, and e_a is the vapor pressure, which is defined as

$$e_a = RH\ 10^{\frac{0.7859+0.03477\ \tau_{\text{atm}(^\circ C)}}{1+0.00412\ \tau_{\text{water}(^\circ C)}}}, \tag{4.33}$$

where τ_{atm} is the air temperature, τ_{water} is the surface water temperature, and RH is the relative humidity (%), which can be specified by the user as a function of time and space.

The latent heat flux is calculated by dividing the contribution into two factors: wind-driven and buoyancy forces ($Q_{la} = Q_{la}^{\text{wind}} + Q_{la}^{\text{buoy}}$). The contribution due to wind is calculated through Danton's law of mass transfer Murakami et al. (1985):

$$Q_{la}^{\text{wind}} = L_v\ \rho_{\text{atm}}\ c_e\ U_{10}\Big(q_s - q_a\Big), \tag{4.34}$$

---

[2] Delft3D also provides an option that estimates the incoming shortwave radiation based on geographical position and the local time of the simulated system

in which L_v is the latent heat of vaporization (J/kg), $c_e = 0.0015$ is the Dalton number, U_{10} is the wind speed at 10 m height (m/s), and q_s and q_a are the specific humidity of saturated and remote air, respectively. ρ_{atm} is the user-specified air density $(\text{kg/m})^3$.

The contribution due to buoyancy forces to the evaporation rates Q_{la} is caused essentially by the temperature differences, and is calculated based on the principle of heat and mass transfer:

$$Q_{la}^{\text{buoy}} = \kappa_s L_v \overline{\rho_{\text{atm}}}\Big(q_s - q_a\Big), \tag{4.35}$$

where κ_s is the heat transfer coefficient (-) and $\overline{\rho_{\text{atm}}}$ is the average air density (kg/m³).

The sensible heat flux is computed similarly to the latent heat flux, being split into two contributions, wind forcing and buoyancy effect:

$$Q_{se} = cp_{\text{atm}}\Big(\tau_{\text{water}} - \tau_{\text{atm}}\Big)\Big(\rho_{\text{atm}}\ c_h\ U_{10} + \kappa_s \overline{\rho_{\text{atm}}}\Big), \tag{4.36}$$

in which $cp_{\text{atm}} = 1004$ J/(kg K) is the specific heat of air at constant pressure, $c_h = 0.00145$ is the Stanton number, κ_s is the heat transfer coefficient (-) and τ_{water} and τ_{atm} are the surface water and air temperature expressed in Kelvin unit, respectively.

Turbulence model

Since Delft3D is based on RANS concepts, which average all flow fluctuations, the influence of turbulent fluctuation on mean flow can be modeled through an implemented turbulence closure model, which determines ν_v and D_v. The Delft3D model has four different turbulence closure models, including the κ-ε and $k - L$ models.

The κ-ε model is a second-order turbulence closure scheme that is based on the balance between dissipation and production of turbulent energy, which implies an equilibrium hypothesis under the boundary condition, $P = \varepsilon$. Investigations have shown that the κ-ε turbulence closure model provides good applicability to detect internal seiches in stratified lakes **?**. However, vertical mixing induced by shear and break of high-frequency internal waves is not explicitly taken into account in the κ-ε turbulence closure model implemented in Delft3D Delft Hydraulics (2003). Furthermore, the energy of BSIW transferred to high-frequency waves through degeneration processes is underestimated by the Delft3D model Carvalho Bueno de, Bleninger (2019).

The vertical eddy viscosity (ν_v) is defined as the combination of the molecular viscosity and the maximum eddy viscosity coefficient comparing the result of the turbulence closure model and the background vertical mixing that accounts for all other forms of unresolved turbulence ν_v^{back}, which must be specified by the user. For a strong stratified system, ν_v is reduced to the molecular viscosity, which neglects the contribution of unresolved internal waves. To model the production of turbulence induced by the internal wave field, the vertical eddy viscosity must be amplified. In Delft3D, propagating internal waves, which are susceptible to being excited and breaking near the lakeshore, may not be explicitly taken into account depending on the wavelength scale. The effect of these internal waves can be taken into account through a constant background vertical eddy viscosity coefficient.

The vertical eddy diffusivity coefficient D_v is obtained similarly to the viscosity coefficient. In addition, for the 3D-turbulent closure model, the influence of internal wave breaking is also taken into account in a strong stratified system by the Ozmidov length scale (equation **??**):

$$D_v^{wave} = 0.2\, L_o^2\, N \tag{4.37}$$

in which L_o is the Ozmidov length scale and N is the buoyancy frequency (equation **??**). The vertical eddy diffusivity (D_v) is determined as the maximum of the vertical eddy diffusivity estimated by equation 4.37 and the 3D turbulence closure model Uittenbogaard et al. (1992), which is also combined with the molecular contribution. Note that the equation 4.37 defined in Delft3D uses a constant mixing efficiency $\gamma_{\text{mix}} = 0.2$ (equation **??**).

The horizontal components of the viscosity and diffusivity are calculated based on the contribution of the sub-grid scale horizontal eddy viscosity/diffusivity, background quantity, and the coefficients computed following the κ-ε turbulence closure model.

To find all eddy coefficients, the user must specify the background vertical eddy diffusivity (D_v^{back}) and the background vertical eddy viscosity (ν_v^{back}), which are specified to take into account the contribution of vertical mixing associated with internal wave breaking and shearing, and other mixing effects that are not resolved by the turbulence model. The background coefficient should be of the order of 10^{-4} to 10^{-5} m²/s for the diffusivity coefficient and 10^{-4} m²/s for the viscosity coefficient Delft Hydraulics (2003). For fine grids ($\mathcal{O}(< 100\text{ m})$), $D_h \approx 1$ to 10 m²/s, while for coarser grids, D_h may vary between 10 and 100 m²/s.

Numerical aspects

The full momentum, continuity, and transport equations in Delft3D are solved based on a finite difference approach with the implicit method in alternating direction Stelling, Duinmeijer (2003) using the Arakawa C-grid type of discretization Arakawa, Lamb (1977), in which the water level is defined in the center of the cell and the velocity components are specified perpendicular to the faces of the cells. Delft3D follows the Courant-Friedrichs-Lewis (CFL) condition to guarantee the stability of the model Smith et al. (1985)

$$C_r = 2\Delta t \sqrt{gH\left(\frac{1}{\Delta x^2} + \frac{1}{\Delta y^2}\right)} \leq 1, \tag{4.38}$$

in which g is the acceleration of gravity, H is the total water depth, Δt is the simulation time step, and Δx and Δy are the grid size in x and y direction, respectively.

It should be mentioned here that, since Delft3D uses an implicit scheme, even for $C_r > 1$, the simulation is not unstable. The recommended limit to guarantee a stable solution is $C_r < 11$ Delft Hydraulics (2003).

To keep small numerical diffusion, the horizontal advection term in the multidimensional convection-diffusion equation 4.29 is split into two second-order central discretizations and a third-order upwind scheme (cyclic method).

The horizontal eddy viscosity must be specified by the user under the following condition:

$$\nu_h < \frac{\Delta x^2\, \Delta y^2}{\Delta t(\Delta x^2 + \Delta y^2)}, \tag{4.39}$$

in which Δt is the time step, and Δx and Δy are the grid size of the simulation in x-direction and y-direction, respectively.

The model also requires a condition for the stability of baroclinic mode (internal wave propagation), which requires that

$$\Delta t \sqrt{\frac{\rho_b - \rho_o}{\rho_o} \frac{gH}{4} \left(\frac{1}{\Delta x^2} + \frac{1}{\Delta y^2}\right)} < 1, \tag{4.40}$$

in which ρ_b and ρ_o are the water density at the lake bottom and surface, respectively.

4.4 Application

Engineers often design sensors to fit their exact needs. Today, there are countless sensor devices to measure many types of physical, chemical, and biological parameters.

4.4.1 Using Arduino

4.4.2 Temperature probe

4.4.3 Conductivity probe

In this section it shows how to construct a simple resistive conductivity probe for continuous measurements, which fundamentally measure the water resistance to the electrons flow continuously. The fundamental concepts of conductivity meters have already been explained in section 4.2.1, here we present just the procedure to construct the conductivity and some brief details. This device should not be used to practical applications that requires high accuracy.

4.5 Interwave Analyzer

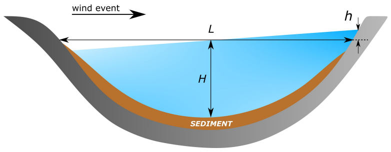

Figure 4.13 Wind-setup

Exercises

Exercises for 4.1.1 Dimensional Analysis

P4.1 The continuous action of a steady wind on the water surface of a lake causes a vertical displacement of the water level, h. This setup is influenced by the basin depth, H, the lake length parallel to the wind direction, L, the water density, ρ_l, the gravitational acceleration, g, and the shear stress of the wind, τ.

Applying the Buckingham theorem, find a relation for the setup.

Exercises for 4.1.1 Dimensional Analysis

P4.2 Would solid NaCl conduct electricity ?

L4.3 Measure the thing in P **??**.

Chapter 5

Signal and Data processing

5.1 Time series

5.2 Thermocline

The Schmidt stability (Equation 2.22), introduced in section 2.2.1, describes the lake's capacity to resist mixing because of density gradients and the water volume.

5.3 Spectral Analysis

Spectral analysis is a statistical technique commonly used for data analysis. In this method, a time series is decomposed into a sum of sine components, which reveals all the oscillatory components present in a given signal. By doing so, it unveils oscillatory motions that might have been hidden in time series measurements (Mortimer, 2004).

This technique transforms spatial and temporal patterns into frequency domains, allowing easy identification of dominant frequencies in periodic time series (Lin, 2012). When applied to the dynamic behavior of lakes, spectral analysis of measured data (such as temperature and horizontal current) demonstrates that lakes exhibit a complex mixture of oscillatory mechanisms. Some of these mechanisms are waves, such as seiches and high-frequency internal waves, while others may be purely random noises (Imboden, 2003).

To detect oscillatory responses in temperature and velocity data, spectral analysis becomes a valuable tool. Spectral analysis allows us to identify dominant periods in the oscillations of each component. Two spectral techniques that are commonly used for this purpose are the Fourier transform and the Wavelet transform. Using these spectral techniques, researchers gain insight into the behavior of internal waves and the complex interaction between wind and water dynamics in lakes and reservoirs. This comprehensive approach helps us better understand these phenomena and their implications for the aquatic environment.

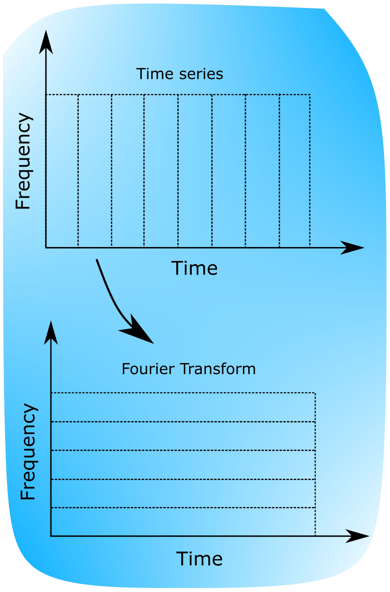

Figure 5.1 Transformation of time series to frequency components by the Fourier transform.

5.4 Fourier Analysis

The Fourier transform is a mathematical technique used to decompose a function of time into the sum of many sine or cosine components of different frequencies, phases, and amplitudes (Chu, 2008). It provides valuable information on frequencies, revealing dominant periodicities (Figure 5.1). The Fourier transform $\mathscr{F}$ of a function $f(n)$ is defined as (Greenberg, 2013)

$$\mathscr{F}\{f(n)\} = \hat{f}(\omega) \equiv \langle f, e^{-i2\pi f n}\rangle = \int_{-\infty}^{+\infty} f(n)\,\mathrm{e}^{-i\omega n}\,\mathrm{d}n, \tag{5.1}$$

in which n represents *time* and the transform variable ω represents the frequency.

Given that we are dealing with a time series of measurements, our focus is on the discrete view of the Fourier transform. The discrete Fourier transform (DFT) can be obtained easily from the continuous transformation. In the discrete transformation, we take N samples in the time domain and convert them into N complex values $\hat{n}(\omega)$ in the frequency domain. Thus, equation 5.1 can be rewritten as

$$\mathscr{F}\{f(n)\} = \hat{f}(\omega) \equiv \sum_{n=0}^{N-1} f(n)\,\mathrm{e}^{-i2\pi\omega n/N}. \tag{5.2}$$

Equations 5.1 and 5.2 demonstrate that the Fourier transform can be understood as a convolution between a time signal and a series of sine and cosine functions, or alternatively, as a matrix-vector multiplication of $f(n)$ (Figure 5.2):

$$\hat{f}(\omega) = \mathrm{e}^{-i2\pi\omega n/N} \cdot f(n).$$

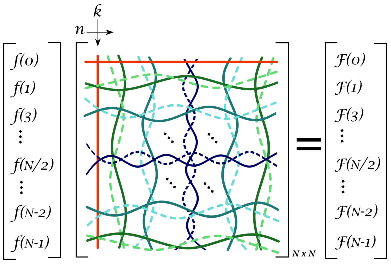

Figure 5.2 A N point DFT as a matrix multiplication, in which each curve is composed of real and complex values.

Equation 5.2 yields the amplitude of the signal under analysis for a given frequency ω. The combination of amplitudes for different frequencies provides us with the spectrum of the analyzed signal. The frequency resolution is given by

$$\Delta f = \frac{1}{T_s} \tag{5.3}$$

in which T_s is the total time sampling. Multiplying Δf by the length of the signal sample (N), we obtain the maximum frequency at which the DFT is defined ($f_{\max} = \Delta f\ N$).

However, due to the nature of the Fourier transform, equation 5.2 represents the result of two phase vectors rotating around the complex plane, where the real and imaginary components are orthogonal to each other. In fact, although the real and imaginary components are out of phase, they are exactly the same in magnitude, but with opposite signs, resulting in a conjugate symmetry around $f_{\max}/2$. Due to this symmetry, the signal produces data loss at frequencies higher than $f_{\max}/2$, which is a phenomenon known as aliasing. This occurs due to overlapping processes, and it can distort the information contained in the signal beyond the Nyquist frequency ($f_{\max}/2$). The lowest frequency that guarantees that no data is lost is called *Nyquist frequency*, which can be expressed as:

$$f_{\text{nyquist}} = \frac{f_{\max}}{2} = \frac{\Delta f N}{2}. \tag{5.4}$$

Listing 22 shows the implementation of the DFT based on equation5.2. Note that to obtain the total amplitude of each component, we should normalize the DFT by $2/N$.

In fact, due to the nature of convolution, which provides a sum of components, we must divide this sum by the number of samples (N). Additionally, since the Fourier transform is two-sided symmetrical and we are interested in the single-sided spectrum, we must multiply the Fourier transform by 2. This step is necessary to account for the contributions of the signal on the other side of the spectrum. By taking these factors into consideration, we obtain an accurate and normalized representation of the single-sided spectrum, eliminating redundancy and preserving the relevant information of the signal in the desired frequency range.

```python
import numpy as np

def dft_slow(t,y):
        dfx = []
        N = len(y)

        dt = t[1]-t[0]          # time resolution
        Ts = N*dt               # total period
        frq = np.arange(N)/Ts   # spectrum (frequency axis)

        for k in range(N):
                df = 0
                for n in range(N):
                        M   = np.exp(-2j*np.pi*k*n/N)
                        df += y[n]*M
                dfx.append(df)
        return dfx,frq

ffx, freq = dft_slow(t,y)
dft = [2*i/N for i in ffx]  # normalization
```

Listing 5.1 Algorithm to compute the discrete Fourier transform (DFT).

For example, consider a stationary time series lasting 770.5 h (approximately 32 days). The signal represents the unit length and is given in meters. It has a mean value of 15 m and consists of two cosine functions with strong random noise, leading to a maximum displacement of ±5 m. The time series is sampled every 1800 sec (see Figure 5.3a). The two main fluctuations in the signal have periods of 2 h and 5 h, and both oscillatory components have an amplitude of 1 m. Due to the presence of strong noise, it is challenging to distinguish the existence of harmonic components in the time series. To reveal these components, we need to apply a spectral method. One way to obtain the time-series spectrum is by using the discrete Fourier transform algorithm (Listing 22).

The right part of the spectrum lacks valuable information due to the conjugate symmetry of the Fourier transform. It essentially mirrors the spectral energies present in the left part. To avoid redundancy, this side of the spectrum is ignored and to compensate for the omitted data, the Fourier transform is multiplied by a factor of 2 (Figure 5.3b).

Additionally, when plotting the amplitude, we use the modulus to focus solely on the magnitude of the harmonics without concern for their phase differences. Consequently, in the DFT plot of the signal shown in Figure 5.3b, we observe two positive peaks, representing the cosine functions that were added to the original signal. It is important to note that the noise introduced into the signal does not contribute to any periodic component. Instead, it only adds noise to the spectrum, without showing any discernible pattern.

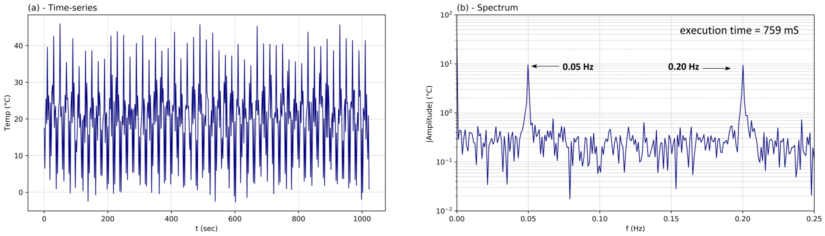

Figure 5.3 a) Time series of a hypothetical signal and b) spectrum associated with this signal, obtained by listing 22.

Recall that the two cosine functions added to the signal had an amplitude of 1 m. However, in Figure 5.3b, we can observe a slight difference for each component. This effect is attributed to two significant factors: spectral leakage and the noise present in the data.

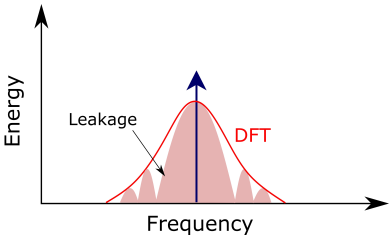

Figure 5.4 Example of the spectral leakage.

In the discrete Fourier transform, both the time and frequency domains are circular topologies, meaning that the two endpoints of time are connected together. Spectral leakage occurs when the frequency does not exactly match the corresponding bin, resulting in a misalignment. In other words, when the integer number of periods does not fit within the acquisition time interval. As a consequence, energy from the signal leaks into other frequencies, leading to an increase in spectral energy at neighboring frequencies around the main peak. The primary peak is often referred to as the **main lobe**, while the energized frequencies surrounding it are known as **side lobes**. It is important to note that spectral leakage always reduces the spectral energy of the main peak, as a portion of the energy gets distributed to the side lobes.

Another effect that can reduce the accuracy of spectral peaks is noise. Noise may introduce inaccuracies in the spectral peaks due to its contribution to harmonics during the convolution performed by the Fourier transform. To address this issue, we introduce in Section 5.4.3 the concept of the windowed Fourier transform, a technique used to average segments of the Fourier transform. Although this technique is effective in mitigating noise-induced inaccuracies, it can also lead to increased spectral leakage.

In Section 5.4.3, we dive into the windowed Fourier transform and discuss how to handle the issue of spectral leakage that arises when performing this type of transform.

By now, we shift our focus to the conjugate symmetry of the Discrete Fourier Transform (DFT) to accelerate the algorithm. As we know, the right part of the spectrum, which was obtained using Listing 22 and shown in Figure 5.3, was completely ignored. However, any additional information regarding the spectral energy can be valuable for its calculation, making the computation of this neglected portion of the spectrum unnecessary. Taking advantage of the inherent symmetry of DFT, Cooley, Tukey (1965) proposed a faster algorithm to calculate the spectral energy of a signal.

Spectral leakage and the effect on frequency band
Peaks located close to the highest and lowest frequencies may exhibit greater spectral leakage due to the abrupt transition at the signal's end. This sudden discontinuity generates high-bandwidth frequency content, leading to a broad-band spectrum, and causing some of the energy to leak. As seen in our example, this effect is evident in the 5 h^{-} frequency oscillation, where a more pronounced and energetic side lobe is observed, consequently reducing the amplitude of the main peak.

Table 5.1 Spectral leakage.

5.4.1 Fast Fourier Transform

The Fast Fourier Transform (FFT), initially proposed by Cooley, Tukey (1965), takes advantage of the inherent symmetry of the DFT to eliminate redundant calculations. This technique substantially reduces storage requirements and computation time, operating on the order of $N\log_2 N$ instead of N^2 complex multiplications. The FFT accomplishes this by breaking down the calculation into two discrete Fourier transforms of length $N/2$, one with even and the other with odd subscripts:

$$n = \begin{cases} 2r & \text{for } n \text{ even} \\ 2r+1 & \text{for } n \text{ odd} \end{cases}$$

in which $0 < r < N/2$. The fast Fourier transform $\mathscr{F}$ of the function $f(n)$ is defined as

$$\mathscr{F}\{f(n)\}_k = \sum_{r=0}^{(N/2)-1} f(2r)\,\mathrm{e}^{-2i\pi k(2r)/N} + \sum_{r=0}^{(N/2)-1} f(2r+1)\,\mathrm{e}^{-2i\pi k(2r+1)/N}.$$

$$= \underbrace{\boxed{\sum_{r=0}^{(N/2)-1} f(2r)\,\mathrm{e}^{-4i\pi kr/N}}}_{\text{even-indexed}} + \mathrm{e}^{-2i\pi k/N} \underbrace{\boxed{\sum_{r=0}^{(N/2)-1} f(2r+1)\,\mathrm{e}^{-4i\pi kr/N}}}_{\text{odd-indexed}}. \tag{5.5}$$

The FFT operates on the principle that the DFT of a sequence with N data points can be obtained by combining the DFTs of its two halves. By splitting the DFT into two parts, as shown in Equation 5.5, we can compute the DFT of two shorter signals, effectively reducing the computation to $N^2/4$. However, we can achieve even greater computational efficiency by applying this technique iteratively as long as the Fourier transforms have an even value R, leading to a significant reduction in computational cost to $N\ \log_2 N$. The reduction in computational cost compared to the standard DFT is proportional to the length of the signal, as illustrated in Figure 5.5.

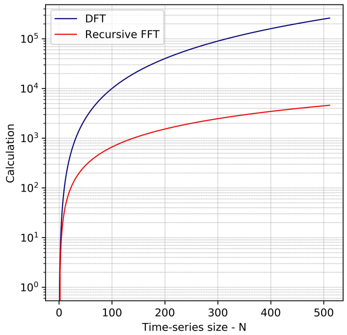

Figure 5.5 Comparison between the computational cost of DFT and FFT, implemented in the listing 22 and 5.4.1, respectively.

In this case, where the DFT is split into two interleaved DFTs, we refer to the FFT as *radix-2*. Radix-2 FFT requires that the time series length be of a power of two, as it computes the DFT in $\log_2 N$ stages. In Listing 5.4.1, we present a simple and efficient implementation of a radix-2 FFT based on Equation 5.5. Although radix-2 is the most common type of FFT, there are other radices, such as radix-4, where the DFT is divided into four parts, which require fewer calculations stages than radix-2. However, the limitation with radix-4 is more stringent, as the length of the signal must be a power of four.

```


def fft_recursive(y):

    N = len(y)

    if N == 1:
        return y
    else:
      Feven = fft_recursive([y[i] for i in range(0, N, 2)])
      Fodd  = fft_recursive([y[i] for i in range(1, N, 2)])

      ff = [0] * N
      for m in range(0,int(N/2)):
          ff[m] = Feven[m] + np.exp(-2j*np.pi*m/N) * Fodd[m]
          ff[int(m + N/2)] = Feven[m] - np.exp(-2j*np.pi*m/N) * Fodd[m]

      return ff
```

Listing 5.2 Fast Fourier transform

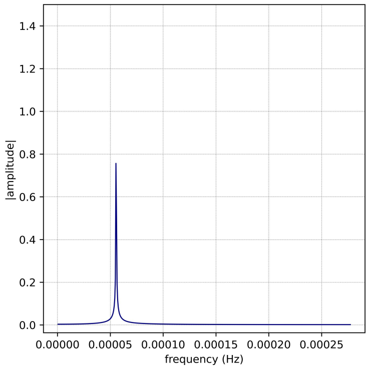

Figure 5.6 The spectrum of time series of temperature obtained through the radix-2 FFT, implemented in the listing 5.4.1.

In our previous example, we applied the signal to the FFT implemented as shown in Listing 5.4.1. Since the signal must now have a length that is a power of two, we reduced the time series to only the first 512 h (≈ 21 days). As observed, the resulting spectrum is exactly the same as that calculated by the standard DFT, which was implemented in Listing 22. However, the execution time of the algorithm is significantly faster (approximately 150 times faster than the DFT; Figure 5.6). The Fast Fourier Transform completed the calculation in 0.042 sec, while the previous DFT implementation took around 6 sec to complete the process. It is important to note that as the signal becomes shorter, the difference in time consumption between DFT and FFT becomes less pronounced (Figure 5.5).

Indeed, while the FFT implemented in Listing 5.4.1 provides notable advantages and is faster than the standard DFT, many computing packages in various programming languages offer their own pre-implemented functions for FFT, which can be significantly faster than the radix-2 implementation shown here. These optimized FFT packages not only exploit the symmetry of DFT, but also utilize techniques like sub-computation reuse, resulting in substantial improvements in FFT performance. Moreover, some of these packages employ general factorization methods, enabling them to compute FFT even when the length of the data is not a power of two. In Python, for instance, the Numpy package provides the fft function, which is highly efficient and capable of performing FFT computations on various input lengths.

When applying the FFT implemented in Listing 5.4.1, we encountered the need to shorten the signal length to reach a power of two, resulting in some data loss. However, a technique is commonly employed to extend the length of the data without introducing any new spectral information, known as **zero padding**. This technique involves adding zeros to the end of the signal, effectively increasing its length to the nearest power of two, while preserving the existing data and avoiding any loss.

5.4.2 Zero-padding

Zero padding involves the addition of extra zeros to a data sample. Its primary purpose is to increase the signal length to the nearest power of two, which can significantly improve the performance of the FFT based on the algorithm proposed by Cooley, Tukey (1965). However, the benefits of zero padding extend beyond simply reaching the next power of two signal lengths. Zero padding can also be advantageous in reducing spectral leakage. By appending zeros to the signal, you effectively interpolate the data and increase the frequency resolution, resulting in a narrower main lobe and lower sidelobes in the frequency domain. This, in turn, reduces spectral leakage and improves the accuracy of spectral peaks in the FFT output. Therefore, zero padding is a valuable technique not only for achieving the desired signal length for efficient FFT computation but also for enhancing the frequency resolution and mitigating spectral leakage, leading to more accurate frequency domain analysis.

This approach can lead to an increase in the number of frequency bins, resulting in a more closely spaced spectrum. The sharper fluctuations in Figure 5.7b illustrate this effect. Although zero padding does not directly enhance frequency resolution, it can yield a smoother spectrum, making it easier to visually identify isolated dominant frequencies. Additionally, since zero padding can alter the interval between frequency domain samples, the energy may be better aligned with an FFT bin, reducing spectral leakage and enhancing the accuracy of energy estimation. In particular, in Figure 5.7, the application of the zero-padding technique is evident by the much sharper peak in the moving average of the PSD, indicating a reduction in spectral leakage.

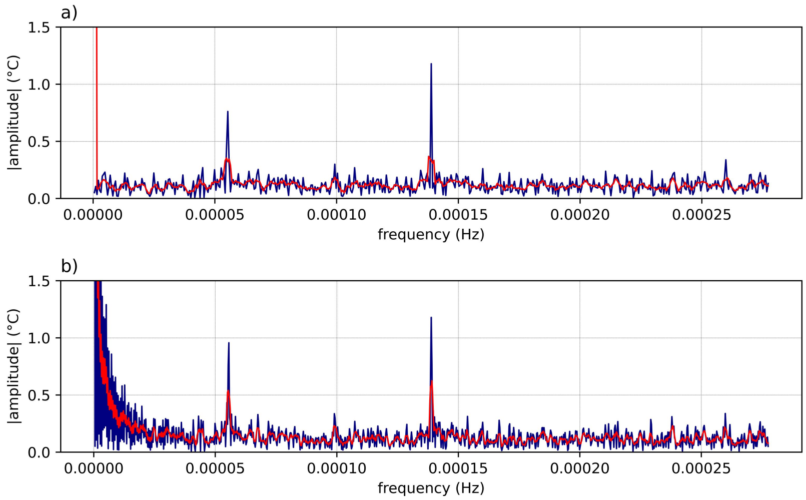

Figure 5.7 a) Signal spectrum assuming the shortened data and b) Signal spectrum of the signal zero-padded to the next power of two. The red line indicates the moving average of the amplitude.

As mentioned earlier, when dealing with noise in spectral power estimation, a common technique used is the **Windowed Fourier Transform**.

5.4.3 Windowed Fourier Transform

The windowed Fourier transform (WFT), also known as the short-time Fourier transform (STFT), serves to decrease the variance of power spectral estimations. To achieve this, the WFT divides the signal into multiple equal segments and applies a window function to each segment. This windowing assumes stationarity within the segments. Consequently, the window function, denoted g, is shifted by ς along the timeline, and a Fourier transform is computed for each segment, revealing the Fourier spectrum in each segment. Finally, the global spectrum of the signal is obtained by averaging all individual segment spectra. This technique allows for a more reliable and accurate representation of the signal's frequency content, particularly in the presence of noise or time-varying characteristics. This technique decreases spectral variance and is expressed as a simple convolution between signal and window,

$$\mathscr{F}\{f(n)\} = \langle f, g_{n,\omega}\rangle = \int_{-\infty}^{+\infty} f(n)\, g(n-\varsigma)\, \mathrm{e}^{-i2\pi\omega n} \mathrm{d}n. \tag{5.6}$$

The STFT can be computed using the code provided in Listing **??**, which includes the STFT function and the rectangular window function used for signal convolution. Rectangular window is a commonly used window type in STFT computations and is the most general case. It can be represented as a normalized boxcar function that zeros out the signal data outside the window. In this way, the FFT is performed in segments of the total signal, as illustrated in Figure 5.8. The rectangular window serves as a straightforward approach for STFT computation and is often used for its simplicity and ease of implementation.

In Figure 5.8, the signal is divided into three short segments (A to C), and the FFT is performed on each segment independently. Each individual periodogram exhibits two peaks followed by noise fluctuations. The noise arises due to random signals and does not represent any meaningful harmonic component.

By taking the average of all the individual periodograms, we obtain a smoother periodogram. This averaging process effectively filters out noise fluctuations, providing a more reliable representation of the underlying signal's frequency content. The peaks in the averaged periodogram are more pronounced and accurate, as they reflect the true harmonic components present in the original signal, while the noise is diminished through the averaging process. This process enhances the quality of spectral estimation and allows for a clearer and more accurate analysis of the signal's spectral characteristics.

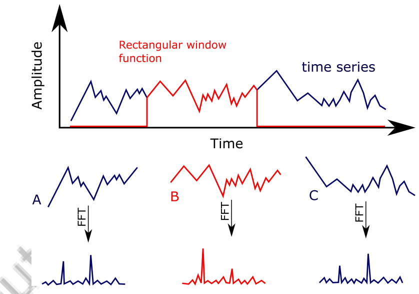

Figure 5.8 Example of the convolution of the window function and the signal to the STFT computation for a segment of the time series (using a rectangular window).

```python
def stft_square(y,r,dt):

    size = int(len(y)/r)

    f_new  = []
    ff_new = []

    for i in range(r):


        y_new = y[int(i*size):int((i+1)*size)]

        N  = len(y_new)
        Ts = N*dt

        ff   = 2*abs(np.fft.fft(y_new))/N
        f    = np.arange(N)/Ts

        ff_new.append(ff)
        f_new.append(f)



    return f_new, ff_new
```

Listing 5.3 Short-time Fourier Transform

Indeed, when we divide the time series into multiple segments for STFT computation, each segment's signal length becomes shorter. This can increase the influence of sudden transitions or discontinuities at the end of the signal. As a consequence, spectral leakage is more likely to occur, leading to an increase in the energy that leaks into neighboring frequencies.

When applying the STFT with a window size of $N/3$ to the time series of the previous example, we observe three periodograms, each representing a period in which the FFT was applied (Figure 5.9a). It should be noted that decreasing the size of the window results in the signal being divided into a larger number of segments, potentially producing more periodograms in Figure 5.9a.

Figure 5.9 b shows that the averaging technique aids in reducing spectrum variance, resulting in a reduction in noise fluctuation. However, this technique may increase the degree of spectral leakage due to discontinuities that arise from sudden transitions at the signal endpoints.

To mitigate the effect of discontinuities and reduce spectral leakage, it is possible to employ a smoothing method that gradually reduces the energy near the endpoints. This approach helps to decrease the amplitude of discontinuities, and consequently decreases the spectral leakage. One common technique involves convolution with a window function that exhibits a lower amplitude near the signal's endpoints. For example, performing a convolution between the signal and a Gaussian function can achieve the desired smoothing effect, resulting in improved spectral estimation and a more accurate representation of the underlying signal's frequency content.

Figure 5.9 a) Periodograms from three segments were obtained from a rectangular function of size $N/3$. b) Global periodogram (averaged periodogram) for different window sizes. The red line indicates the FFT performed without a window, whilst the light and dark blue lines show the WFT performed with a signal split into 10 and 5 segments, respectively.

There are several types of window function available and each is suited to different types of application. The most common windows used are the Hamming and Hanning (also called Hann) window functions (Figure 5.10).

Hamming and Hanning are families of window functions known as raised cosine, both featuring sinusoidal shapes with low side lobes that effectively address the energy leakage effect in the Fourier transform. Some studies have suggested that the Hamming and Hanning window functions are more suitable for narrowband signals (Gao, Yan, 2010).

The main difference between the two lies in the handling of discontinuities. The Hanning window removes all discontinuities, resulting in a faster side-lobe roll-off decay rate. Consequently, it may not handle the nearest side lobes well, but it performs better with other lobes that are not too close to the main lobe. However, the Hamming window has a slower side-lobe roll-off decay rate, leading to higher spectral leakage. However, it excels in dealing with closely spaced peaks, making it more appropriate for closely spaced internal waves (internal waves with closed periods). The Hamming window can effectively cancel the closest side lobe in such scenarios (Figure 5.10).

Often, the Hanning window is adequate for identifying internal wave activities in most cases, as it strikes a good balance between spectral energy and frequency accuracy. While many internal wave studies employ these cosine windows, there is no consensus on the best windows to identify internal waves. Certain applications in internal wave studies have utilized different windows to discern the response of the periodic oscillation.

Often, windowing techniques are used to smooth the signal near the endpoints, reducing discontinuities. However, this smoothing process can also lead to data loss, resulting in an underestimation of the spectral energy. To address this distortion and correct the amplitude and energy, we need to apply the window correction factor, which is determined by the specific window type that was applied. The amplitude correction factor (k^a_{window}) is defined as:

$$k^a_{\text{window}} = \frac{N_{\text{window}}}{\sum g(n)}, \tag{5.7}$$

in which N_{window} is the window size (number of points) and g is the window function. For the Hamming window, $k^a_{\text{window}} \approx 1.85$.

Figure 5.10 depicts the Short-Time Fourier transform applied to the previous signal using various window functions. For clarity, we remove the noise from the signal to facilitate interpretation of the results. Notice that the Hamming window function effectively reduced spectral leakage. However, it also led to some data loss caused by the convolution with the window, resulting in a lower spectral energy than the expected value. To compensate for this discrepancy, the entire spectrum should be multiplied by the amplitude correction factor. This correction factor ensures that the energy estimation accurately reflects the true spectral energy in the signal.

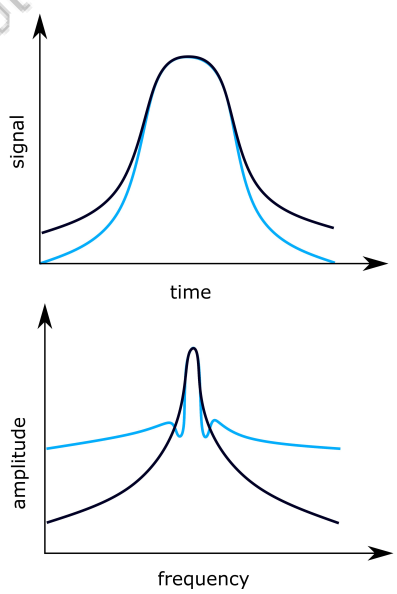

Figure 5.10 Example of Hamming and Hanning window functions and how they deal with spectral leakage.

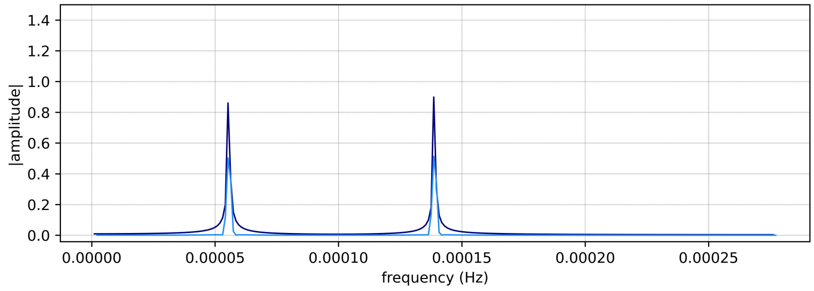

Figure 5.11 Short-time Fourier Transform windowed by the rectangular and Hamming functions (window size of $N/4$ points) without correction factor.

Although many internal wave studies use cosine windows, there is no consensus on the best windows to identify internal waves. Specific applications of internal wave studies have employed different windows to analyze the period oscillation response. For example, Ostrovsky et al. (1996) utilized a short flat-top window in temperature measurements to study internal waves on a small scale, while Stocker et al. (1987) applied a split cosine bell window to analyze long internal seiches in lakes. Carvalho Bueno de et al. (2020) compared the use of two different window functions (Flattop and Hamming windows) to identify internal seiches in a small thermally stratified reservoir from a thermistor chain.

It should be noted that the flat-top window preserves the amplitude of the signal but squeezes the data, necessitating the analysis of a larger amount of data

(Smith, 2013). As such, the flat-top window is more recommended for analyzing high-frequency internal waves when periodic data last for long periods. The choice of the window function depends on the specific characteristics and goals of the analysis, and it is essential to carefully consider the trade-offs between resolution and data requirements for a particular study.

5.4.4 Overlapping process

Since convolution between a window function and a signal can lead to data loss, the **overlapping sliding window method** is a common technique used in STFT to mitigate this issue. It is important to note that the overlapping technique does not correct the spectral energy lost as a result of convolution. However, it ensures that the energetic harmonics, which may be present at the endpoints of a segment, are not neglected (Figure 5.12).

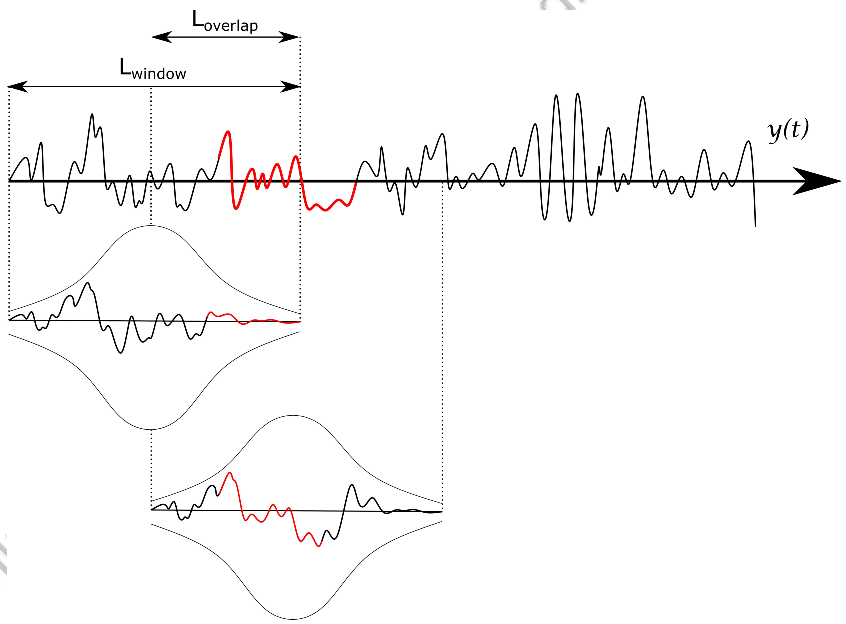

Figure 5.12 Data segmentation and overlapping sliding window technique. Note that the oscillatory energy associated with the red solid curve would be neglected if the overlapping technique was not applied.

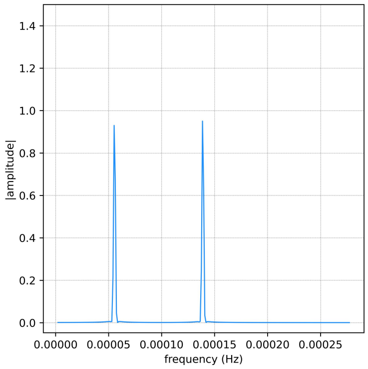

Figure 5.13 Corrected short-time Fourier transform windowed by the Hamming window function with size of $N/4$ and 50%-overlapped.

The overlapping sliding window method involves dividing the signal into overlapping segments for analysis (Figure 5.12). The optimal overlap percentage (L_{overlap}) is determined by the chosen window function. For wide windows, such as Hamming and Hanning windows, a commonly recommended overlap percentage is 50%. Conversely, narrower window functions often require a higher percentage of overlap. The recommended overlap percentages for each window function are well documented in the literature (Heinzel et al., 2002). This technique ensures that important information at segment boundaries is not overlooked and contributes to more accurate and reliable spectral analysis.

5.4.5 Non-stationary Signals

The Fourier transform commonly assumes that the analyzed signal is stationary, meaning that the spectral components persist with the same frequencies and amplitudes throughout the analysis period. However, many natural time series exhibit non-stationary behavior, which includes most of the natural physical processes, such as internal waves. The internal wave field may vary over time, leading to the generation and dissipation of waves with different time scales depending on the analysis period. Consequently, even numerical and experimental studies investigating the generation and dissipation of internal waves excited from a single wind event (Carvalho Bueno de et al., 2023; **?**; Horn et al., 1998; Boegman et al., 2005a) may not fully adhere to this assumption, as internal waves dissipate over time.

For example, a study conducted on Lake Arendsee (Germany) analyzed six months of data to identify different types of internal waves, including internal seiches with higher vertical modes Bernhardt, Kirillin (2013). In another case, within 9 days, the internal wave field identified in Lake Bala was reenergized three times, causing significant fluctuations in the internal wave amplitude over time (Simpson et al., 2011a). Consequently, the spectral content of non-stationary signals may evolve and fluctuate, challenging the traditional stationary analysis methods.

Due to the convolution in the Fourier transform, the spectral energy may be underestimated when the harmonic components do not have consistent amplitudes throughout the entire analysis period. This leads to an inaccurate estimation of the spectral energy. When the Fourier transform is normalized by the number of samples, it assumes that the spectral energy is equally distributed throughout the period, resulting in lower-amplitude oscillations (Figure 5.14). This phenomenon is particularly evident in non-stationary signals where the spectral content changes over time, leading to fluctuations in the spectral energy. As a result, traditional stationary analysis methods may not accurately capture the dynamic nature of such signals.

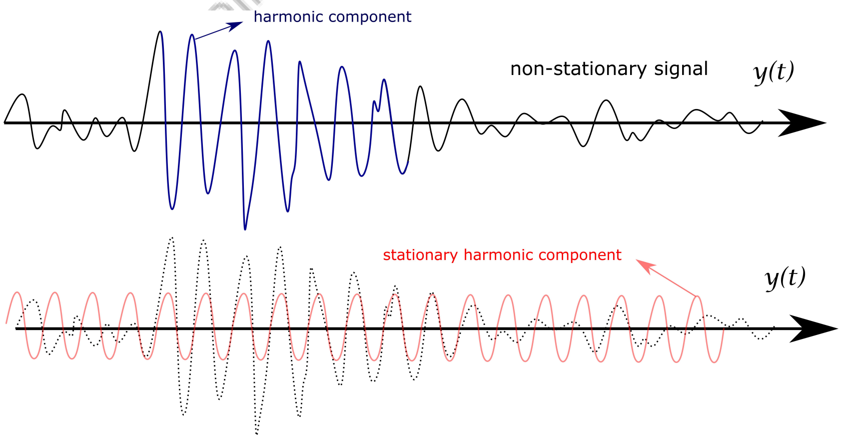

Figure 5.14 The effect of Fourier transform in a non-stationary signal.

The simplest approach to analyze non-stationary signals is to compute the mean and variance for different time periods and examine if the statistics significantly differ. One commonly used method is the short-time Fourier transform (STFT), which assumes that the signal is stationary within each segment where the FFT is performed. Unlike Listing 5.4.3, the spectrum of each segment in STFT is not averaged to obtain a global spectrum. Instead, this non-averaged representation provides valuable information on both time and frequency and is referred to as a spectrogram. Each spectrum in the spectrogram represents the spectral energy associated with the specific subperiod in which the FFT was performed. This enables us to observe how the spectral characteristics of the signal change over time, making the spectrogram a powerful tool for analyzing non-stationary signals.

In our previous examples, the noisy signal consisted of two periodic functions with an amplitude of 1 m, persisting throughout the analysis period. Now, we consider a different scenario where the signal is composed of a dominant oscillatory response lasting for 10 h during the last 10 days, and a transient harmonic component varying from 2 h to 4 h during the initial part of the period (Figure 5.15a). Figure 5.15 b shows the global spectrum of the signal, corrected with the amplitude correction factor of 1.85. Despite the correction factor, the amplitude of the 10 h peak is still underestimated due to the non-stationary nature of the time-series. When segments are averaged, it leads to a global reduction in spectral energy, as illustrated in Figure 5.14.

In fact, transient oscillations are challenging to detect in the global spectrum. However, Figure 5.15c presents the STFT for each individual segment, providing valuable insight into when each harmonic component exhibits higher energy. The periodogram clearly reveals the transient component varying from 0.00012 Hz to 0.00004 Hz, as well as the 10 h component occurring during the final 10 days of the analysis period. The STFT's time-frequency representation effectively highlights the variations in spectral energy over time, allowing for more precise identification of different harmonic components present in the non-stationary signal.

The STFT technique effectively addresses the time localization problem by identifying periods in which harmonic components are excited. However, a significant challenge with STFT is the inconsistent treatment of different frequencies, which is commonly referred to as Heisenberg's uncertainty principle. This principle states that there is a fundamental trade-off between time and frequency resolution in signal analysis. When trying to achieve better time localization, frequency resolution is compromised, and vice versa. As a result, STFT may not offer an optimal balance between time and frequency precision, making it less suitable for certain applications where both high time and frequency resolution are crucial.

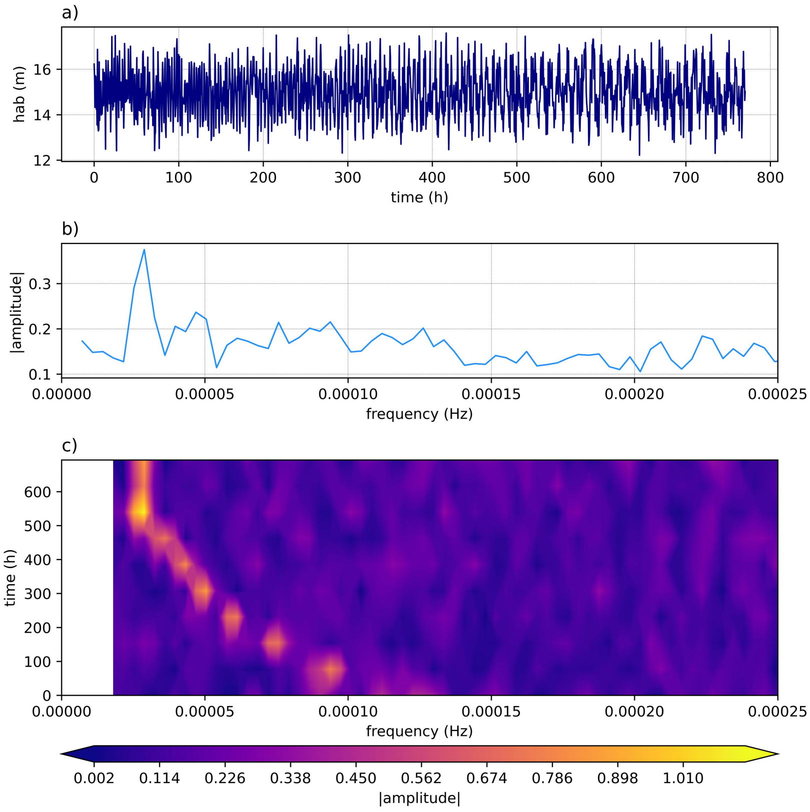

Figure 5.15 Spectral analysis of a noised non-stationary signal. a) Time-series of the non-stationary signal, b) the spectrum of the signal-based windowed Fourier transform (10 averaged windows), and c) the spectrum of the signal for each window along time.

The uncertainty principle is closely related to the time-frequency resolution (Millette, 2011). This challenge arises from the presence of an aliased spectrum that falls outside the frequency range of the selected window (Gubbins, 2004). When the window size and type are chosen, the time-frequency resolution remains constant, meaning that satisfactory resolution can only be achieved in either the time domain or the frequency domain, but not both. When the window size is kept fixed, the time-frequency resolution depends solely on the window size and type. Consequently, a key aspect of the problem lies in the fact that at high periods, there are few oscillations within the window, resulting in a loss of frequency localization. On the contrary, at low periods, there are many oscillations, leading to a loss of time localization.

An alternative approach to overcome Heisenberg's uncertainty principle is to use the **Wavelet transform**, which offers improved capabilities in analyzing different frequencies. The wavelet transform incorporates a scaling parameter that allows for varying the window size to analyze each frequency component effectively. This flexibility in window size enables wavelet analysis to achieve a better balance between time and frequency resolution.

5.5 Advancing processing

5.5.1 Power Spectral Density

As mentioned above, the harmonic amplitudes estimated by the Fourier transform rely heavily on the frequency resolution of the signal. This implies that they will vary depending on the size of the signal. Although this can pose a challenge when analyzing a single signal, it becomes even more problematic when comparing two or more signals of different sizes (Figure 5.16). To address this issue, we introduce the **Power Spectral Density**, a widely used technique to investigate internal waves (Gloor et al., 1994; Vidal et al., 2013; Rozas et al., 2013; Bouffard et al., 2016; Carvalho Bueno de et al., 2023; **?**, 2020).

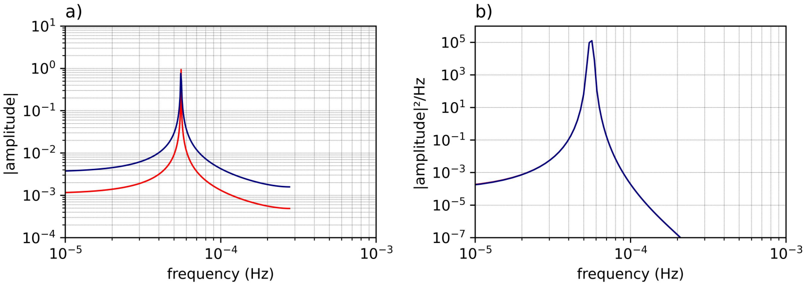

Figure 5.16 Fast Fourier transform and power spectral density of two signals with the same harmonic component but different size. a) Fast Fourier transform for 1024 (blue) and 2048 (red) data points. b) Power spectral density for the same two signals.

The key aspect of the Power Spectral Density (PSD) lies in the normalization of the energy value to the width of the frequency bin. This normalization enables a meaningful comparison between time series of different lengths. Additionally, each frequency bin is multiplied by its complex conjugate. The power spectral density is expressed as energy (square amplitude) per frequency (width).

One significant advantage of this process is the reduction of differences in spectral energy. Formally, PSD can be obtained by calculating the ratio of the sampling frequency to the mean square power spectrum. The mean-square power spectrum, in turn, is obtained through the Fourier transform of the auto-covariance function,

$$\phi_{ff}(\omega) = \phi^*_{ff} \times T_s \equiv \frac{T_s}{N}|\mathscr{F}\{f(n)\}|^2. \tag{5.8}$$

in which $\phi_{ff}(\omega)$ is the PSD of the function $f(n)$, ϕ^*_{ff} is mean-square power spectrum of the function $f(n)$, T_s is the sampling period, and N is the length of the signal.

In their work, Welch (1967) introduced an improved estimator of the Power Spectral Density (PSD) known as the Welch method. This method incorporates all of the techniques described above. By combining Short-Time Fourier Transform (STFT) with PSD estimation, the Welch method reduces the variance of the spectral density, albeit at the expense of a lower frequency resolution in the resulting estimate.

The technique involves the following steps: first, the time-series data is divided into segments. Then, window convolutions and overlapping techniques are applied to these segments. The segments are then averaged to obtain a smoothed estimate. To compute the power spectral density of the signal, the averaged segment is squared and then normalized by the frequency bandwidth. This process results in an improved estimation of the PSD.

To calculate the energy content within a specific frequency band (spectral variance), we integrate the spectrum over the corresponding frequency bandwidth. This integration process involves summing up the spectral values within the designated frequency range. By doing so, we can determine the total energy associated with those frequencies. This approach allows us to quantify the strength or intensity of the signal within the specified frequency band, providing valuable insights into its characteristics and behavior:

$$E_{\mathrm{PSD}}(f) = \int_{f_o}^{f} \phi_{ff}(\omega)\mathrm{d}f. \tag{5.9}$$

5.5.2 Phase and Coherence Analysis

Another significant analysis commonly utilized to examine internal waves is coherence and phase analysis. Coherence analysis is a method designed to measure the correlation between two or more signals in terms of frequency. Provides correlation values for each frequency (Figure 5.17).

Coherence analysis is a common method used to assess whether two or more isotherms are influenced by an internal wave (Vidal et al., 2013). It also serves to identify periods with potential resonance between internal waves and wind forcing. For example, in the tropical Andean reservoir, high coherence was observed over a 24-hour period between internal seiche activity and wind forcing, suggesting the occurrence of wave-wind resonance with potential wave amplification (Posada-Bedoya et al., 2019).

The phase is often obtained for higher coherence harmonics, allowing for the determination of the phase lag between two signals in radians for each frequency. This analysis offers valuable insights into the relationships and synchronization between different signals, helping to understand their interactions and behavior.

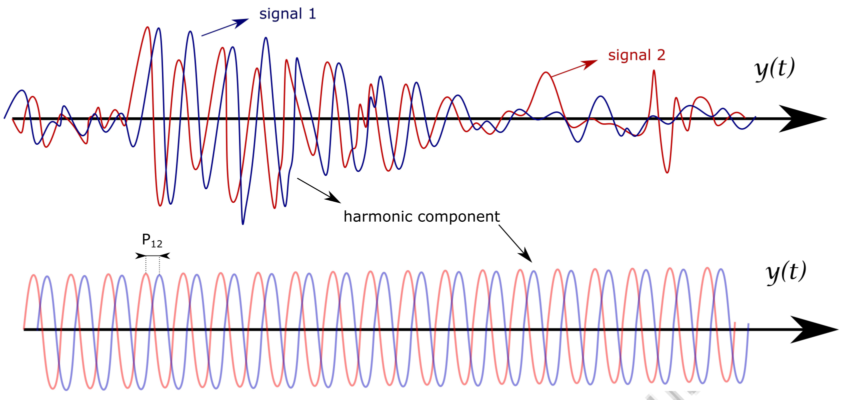

Figure 5.17 Sketch of phase and coherence analysis between two signals. The coherence is high when both signals present high energy in the same harmonic component. The phase indicates a 90 ° out-phase response between signals 1 and 2.

Coherence can be obtained using the mean-square power spectrum of two signals and the cross-power spectrum, ϕ^*_{fg}. The cross-power spectrum is the Fourier transform of the cross-covariance function, given by

$$\phi^*_{fg}(\omega) = \sum_{k=-\infty}^{\infty} \frac{1}{N-1} \sum_{n=1}^{N} (f_n - \bar{\mu_f}) \times (g_n - \bar{\mu_g})\, \mathrm{e}^{-i\omega k} \qquad \omega \in [-1/2, 1/2], \qquad (5.10)$$

where $\bar{\mu_f}$ and $\bar{\mu_g}$ are the means of each signal. The coherence, or mean square coherence, between two signals f and g is given by

$$C_{fg}(\omega) = \left| \frac{\phi^*_{fg}(\omega)}{\sqrt{\phi^*_{ff}(\omega)\, \phi^*_{gg}(\omega)}} \right|^2 \quad \in [0,1], \qquad (5.11)$$

in which ϕ_{fg} is the cross-power spectral density (CPSD) of the signal $f(n)$ and $g(n)$, and ϕ^*_{ff} and ϕ^*_{gg} are the mean-square power spectrum of functions $f(n)$ and $g(n)$, respectively.

The coherence function provides correlation values ranging from 0 to 1, with a value of 1 indicating a perfect linear relationship between the signals. This feature is particularly valuable for establishing correlations between internal waves and other variables that may be periodically influenced by internal wave activity. Numerous studies have used coherence analysis to investigate the relationship between underwater temperature and wind speed, revealing the presence of resonance between baroclinic motion and the wind blowing above the lake surface (Münnich et al., 1992; Posada-Bedoya et al., 2019).

Using coherence analysis, researchers have shown that the amplitude growth of basin-scale internal waves in lakes, resulting from resonance with wind events, can exhibit different growth behaviors depending on the mode of the internal wave and the basins where baroclinic activity is observed (**?**). This analysis technique has proven to be a valuable tool in understanding the interactions and influences of internal waves on various environmental factors, shedding light on the dynamics of these phenomena in different settings.

When combined with coherence analysis, phase-shift analysis becomes a powerful tool for detecting higher vertical baroclinic modes and determining the longitudinal extension of internal waves. Phase analysis is frequently employed to identify the occurrence of internal seiches with higher vertical modes, as these modes are characterized by different layers flowing in opposite directions, leading to an out-of-phase response in thermal fluctuations. For example, studies conducted at Mono Lake identified a high coherence between temperature data across the water column at a frequency of 22 h^{-1} (Vidal et al., 2013). This finding suggests the presence of internal seiches with higher vertical modes in the lake.

Phase-shift analysis calculates the phase lag between two signals (f and g) in radians for each frequency and is defined as follows:

$$P_{fg}(\omega) = \frac{\mathrm{Re}\left\{\phi^*_{fg}\right\}}{\mathrm{Im}\left\{\phi^*_{fg}\right\}} \quad \in [\pi, -\pi]. \tag{5.12}$$

In this equation, the numerator represents the cross-spectral density between signals f and g, while the denominators represent the spectral densities of signals f and g, respectively. Phase-shift analysis allows us to understand the temporal relationship between the two signals at different frequencies.

Figure 5.18 displays the coherence and phase shift between two noisy time series, both exhibiting dominant periods of 5 and 2 h. The 5 h component oscillates in-phase, while the 2 h component is 90° out-of-phase. As expected, coherence indicates a higher spectral correlation for frequencies 5 and 2 h; however, due to the presence of noise in our data, several higher coherence peaks appear in the spectrum.

To appropriately address the significance of spectral peaks and coherence, we calculate the phase shift only for harmonic components with coherence greater than 80%. Phase shift analysis reveals that the oscillatory response of the 1/2 h^{-} frequency is approximately 90° out of phase, whereas the 1/5 h^{-} frequency component oscillates almost in-phase between the two signals.

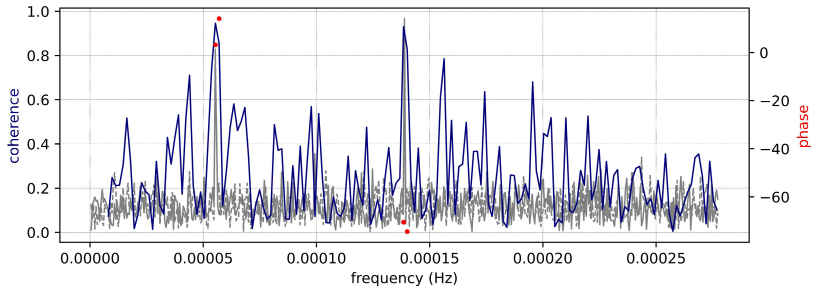

Figure 5.18 Coherence (blue) and phase shift (red) between two time series.

5.5.3 Significance level

In many cases, when performing spectral analysis in various natural time series, the peaks may not be as distinct as those depicted in Figure 5.3. Often, significant peaks could be only slightly higher than the background spectrum noise, making it challenging to discern them clearly. To ensure a consistent approach to determine which peaks are truly significant, it is essential to base our analysis on statistical methods that can quantify the significance of spectral quantities.

The significance of spectral peaks can be estimated by performing a chi-square test on the mean red noise spectrum of the time series (Bernhardt, Kirillin, 2013). This test allows us to determine whether the observed spectral peaks deviate significantly from what would be expected under the assumption of red noise. By comparing the observed spectrum to the mean red noise spectrum, we can objectively identify which peaks are statistically significant. This approach provides a robust and reliable method to assess the presence of significant periodicities or frequencies in time-series data and is frequently adopted in the wide literature (Vidal et al., 2013; Ahmed et al., 2014; **?**; Carvalho Bueno de et al., 2020, 2023).

First, we need to calculate the one-lag autoregressive coefficient of the analyzed signal ($f(t)$) (**?**):

$$\rho_{\text{lag}} = \frac{\sum_{N-1}^{i=1}\left(\bar{f}_i\,\bar{f}_{i+1}\right)}{\sum_{N}^{i=1}\left(\bar{f}_i^2\right)}, \tag{5.13}$$

in which $\bar{f}_i = f_i - \bar{f}$ and N is the length of the signal.

Why do we use the red noise ?
The red noise has zero mean and constant variance, presenting a low-power spectrum weighted toward low frequencies, without dominant periodicity.
The red noise can be generated by a temporal integration of white noise:

$$\text{red}(t) = \rho_{\text{lag}}\,\text{red}(t-1) + \text{w}', \tag{5.14}$$

where w' is the white noise and given by $R\sqrt{1-\rho_{\text{lag}}}$, in which R is a sample from the standard normal distribution.

Table 5.2 Red noise.

From equation 5.13, we can derive the power spectral density of a red noise function. It is important to note that the power spectral density of the red noise must be normalized with the spectral energy of the signal:

$$\phi_{\text{red}}^{f} = \phi_{\text{red}} \frac{\overline{\phi_{ff}}}{\overline{\phi_{\text{red}}}}, \tag{5.15}$$

in which ϕ_{red}^{f} is the normalized power spectral density of the red noise.

Finally, we can calculate the confidence level with respect to the amount of red noise in the signal based on the chi-square test.

First, we calculate the finite Fourier transform of the lag correlation function:

$$R_{\text{spectra}} = \frac{1-\rho_{\text{lag}}^2}{1-2\rho_{\text{lag}}\,\cos\!\left(2\pi\omega/f_{\text{nyquist}}\right)+\rho_{\text{lag}}^2}, \tag{5.16}$$

in which ρ_{lag} is the one-lag autocorrelation, ω is the frequency that varies from 0 to 0.5 f_{nyquist}, where f_{nyquist} is the Nyquist frequency. R_{spectra} must be normalized by taking into account the total power spectral energy of the signal, similar to equation 5.15.

The normalized R_{spectra} represents the power spectral density of theoretical red noise (Figure 5.19). To estimate the confidence levels, we perform the Chi-square test, where we define the probability of error and the degrees of freedom

(Thomson, Emery, 2014):

$$\mathrm{dof} = 2\,k_{\mathrm{over}}\left(\frac{2.5164\;N_{\mathrm{zero}}}{N_{\mathrm{window}}}\right), \tag{5.17}$$

in which N_{window} is the window size, N_{zero} is the window size considering zero-padding, and k_{over} is a correction factor to compensate for the overlapping and windowing processes (Thomson, Emery, 2014). $k_{\mathrm{over}} = 1.2$ is recommended for the 50% overlapping Hamming window(Bernhardt, Kirillin, 2013). Note that k_{over} is different from k^{a}_{window}, the correction factor used to account for the influence of the window function on WFT (Equation 5.7).

Applying the Power Spectral Density (PSD) to a signal composed of three fundamental harmonic components (2 h, 5 h, and 10h), we can readily identify the first two peaks (5 h and 10 h). However, the 2 h component is barely detectable as a significant peak. It can only be considered valid on the basis of the analysis of the mean red noise spectrum using the chi-square test (see Figure 5.19).

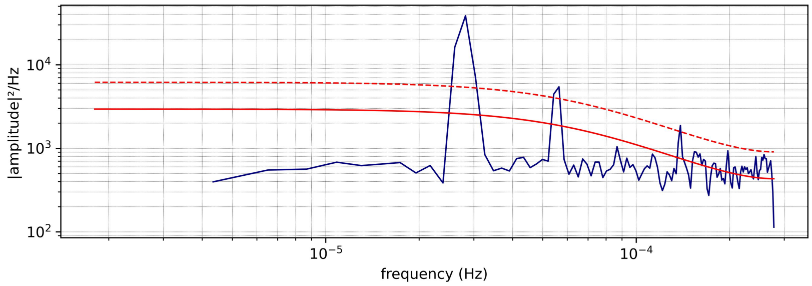

Figure 5.19 The power spectral density (PSD) plot shows the synthetic signal with three harmonic components. The solid red line represents the theoretical Fourier transform of the lag-correlation function. Additionally, the red dashed lines depict the mean red noise spectrum for the time series at a confidence level of 95%.

5.5.4 Wavelet Analysis

To overcome Heisenberg's uncertainty principle, an alternative approach to conducting spectral analysis is wavelet analysis. Unlike traditional methods, the wavelet transform utilizes multi-resolution techniques, allowing the simultaneous decomposition of a signal into both time and frequency domains. This feature proves especially valuable when analyzing long periods of data. In essence, the wavelet transform employs a variable aspect ratio, as demonstrated in Figure 5.20, providing a higher time resolution at higher frequencies. As a result, this technique becomes more powerful for time series that consist of both lower- and higher-frequency harmonic components.

Numerous studies have employed wavelet analysis to detect internal wave activity. For example, Stevens (1999) correlated the spectral power of the wavelet within the high-frequency internal wave range with the maximum shear between layers over time, indicating that propagating internal waves might be excited by shear stress between layers. Additionally, Bernhardt, Kirillin (2013) used wavelet analysis to identify the seasonal variability of rotation-affected internal seiches in Lake Arendsee (Germany).

Although wavelet analysis overcomes Heisenberg's uncertainty principle in studying internal waves, most studies in the scientific community still rely on the Fourier transform to analyze harmonic components in temperature time series (Boegman et al., 2003; **?**; Antenucci, Imberger, 2001; Dissanayake et al., 2019). This preference for Fourier analysis can be attributed to its well-established status and widespread use. However, it is important to note that the Short-Time Fourier Transform (STFT) has also proven useful for detecting internal waves in various situations.

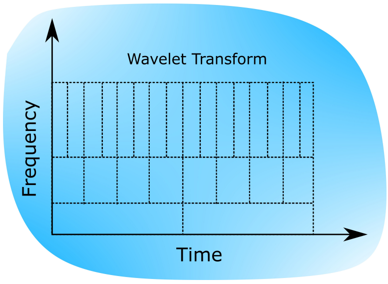

Figure 5.20 Wavelet transformation with variable aspect ratio.

Wavelet Transform

The wavelet transform, denoted as W_x, involves the inner convolution between a wavelet function ψ_w and a signal f, where $f \in L^2(\mathbb{R})$. Unlike the Fourier transform, the wavelet function is not fixed; instead, it adapts its size or scale depending on the analyzed harmonic component:

$$W_f(v,s) \equiv \langle f, \psi_{w(v,s)} \rangle = \int_{-\infty}^{+\infty} \frac{f(t)}{\sqrt{s}} \psi_w^* \left(\frac{t-v}{s} \right) \mathrm{d}t. \tag{5.18}$$

The wavelet function is derived from the mother wavelet through translation and scaling (window size). The parameter v controls the position of the wavelet function as it shifts through the signal, akin to the window shift in STFT. On the other hand, the parameter s governs the wavelet scaling and determines the resolution of time and frequency. When s is large, the signal is dilated, providing more information on low frequencies. In contrast, small s values compress the signal, offering more insight into the high frequencies.

The scaling parameter s plays a crucial role in overcoming Heisenberg's uncertainty principle, making wavelet analysis more powerful than Fourier analysis. By appropriately adjusting s, wavelet analysis achieves a better balance between time and frequency resolution, allowing the study of signals with varying characteristics and frequency content.

In theory, equation 5.18 quantifies the fluctuation of the signal in the vicinity of v, and the extent of this neighborhood is proportional to the scaling parameter (s). The asterisk in the equation represents the complex conjugation of the base wavelet function ($\psi_w(n)$). This wavelet analysis allows us to examine the signal at different scales and positions, providing valuable insights into its time and frequency characteristics with improved resolution compared to traditional Fourier analysis.

In wavelet analysis, the size of the wavelet function does not need to be explicitly chosen, as it adapts to the scale of the analyzed signal. However, there are numerous types of wavelet function available, and the appropriate selection depends on the characteristics of the signal under study. Several factors must be considered during the wavelet function selection process, including the orthogonality of the wavelet function, its width, the shape of the time series being analyzed, and whether the wavelet function codomain is real or complex (Farge, 1992).

Wavelet functions can be broadly categorized into orthogonal and non-orthogonal wavelets. The orthogonal wavelet transform has a convolution number at each scale that is proportional to the wavelet width. This property facilitates efficient and invertible wavelet transforms, making it suitable for various applications in signal and image processing, compression, and denoising. On the other hand, non-orthogonal wavelets offer more flexibility but may not guarantee perfect reconstruction. The choice between orthogonal and non-orthogonal wavelets depends on the specific requirements and trade-offs in each analysis scenario. Careful consideration of these factors helps to ensure that the wavelet analysis yields meaningful and accurate results for the given data.

Wavelet functions are selected on the basis of their codomain, whether they are real or complex wavelet functions. A complex wavelet is more adept at capturing the oscillatory behavior of a signal, making it suitable for analyzing signals with multiple components or varying frequencies. It effectively represents both magnitude and phase information, making it useful for denoising and feature extraction tasks.

The choice of the wavelet function is also influenced by the *e*-folding time, a parameter exclusively used for continuous transforms. The resolution of the wavelet transform directly depends on the *e*-folding time, which strikes a balance between the width space and the Fourier space. Measures the width of the wavelet relative to the scaling parameter (s). A larger *e*-folding time results in a broader spread of the wavelet power, leading to poorer time resolution but improved frequency resolution.

Another critical parameter considered in determining the wavelet function is the shape of the signal. The selected wavelet function should match the type of features present in the signal. For example, studies have suggested the use of a rectangular function like the Harr function for sharp signals with jumps and steps (Torrence, Compo, 1998). Conversely, for smooth signals, a smoother function, like a damped cosine, is more suitable.

By appropriately adjusting these parameters and selecting an appropriate wavelet function, researchers can effectively tailor the wavelet analysis to the specific characteristics of the signal, obtaining valuable insights and accurate results. Figure 5.21 shows a comparison between the wavelet analysis and the periodogram obtained from the STFT.

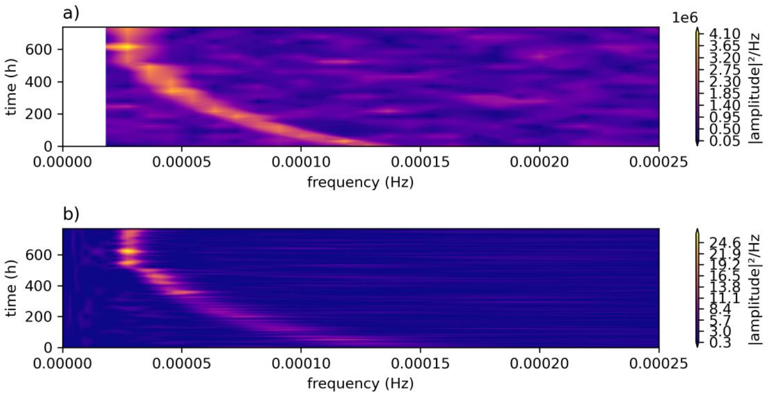

Figure 5.21 Spectral analysis of a noised non-stationary signal (same presented in Figure 5.15).

Another application of wavelet analysis is related to the global wavelet spectrum. The global wavelet spectrum is an averaged power spectrum based upon a set of wavelet functions, which is similar to the averaged spectrum obtained from the STFT. The global wavelet spectrum is a smoothed version of the global STFT and is an efficient estimator of the true power of a signal (Fernando, 2012). The global wavelet spectrum can be obtained by averaging all the local wavelet spectra, equation 5.18:

$$\bar{W_f}^2(v,s) = \frac{1}{N}\sum_{f=0}^{N-1} |W_f(v,s)|^2. \tag{5.19}$$

Despite this method being extremely useful to estimate the true power of a time series, it can generate the bias problem. This issue is related to the difference between the global wavelet spectrum and the true Fourier spectrum in terms of energy. At high frequencies, the global wavelet is very broad in frequency, and consequently all peaks in the spectrum are smoothed. On the other hand, at low frequencies, the wavelet is narrow; therefore, the peaks are sharp, and they present higher energy. Studies have revealed that in some occasions the low-frequency energy is amplified and, consequently, the global wavelet does not work efficiently (Wu, Liu, 2005).

5.6 Applications in physical limnology perspective

Time series of underwater temperatures are widely utilized as a prominent variable for identifying baroclinic motions in thermally stratified water bodies. Many times, temperature fluctuations are not directly applied to the power spectral density, since this analysis would only give an idea of how the temperature varies in a specific water depth. Instead, time series of isotherms are commonly used to highlight the temperature fluctuation of a specific interface, providing the amplitude of those physical waves. For example, in Mono Lake, a 14 °C isotherm was used to identify the occurrence of a 22 h basin-scale internal wave through spectral analysis (Vidal et al., 2013). The time-series of isotherms were obtained by using a thermistor chain. To gain a better understanding of the internal seiche characteristics, the study evaluated time-series of isotherms at different stations along the lake. The application of linear interpolation to obtain isotherms does not disrupt the integrity of the spectral analysis (Lemmin, 1987).

Studies conducted in Lake Villarrica (Chile), using two-thermistor chains, identified three different modes of internal oscillations through spectral analysis of isotherm series (Rozas et al., 2013). These modes include the fundamental Kelvin internal wave with a period of 24 h, the 12 h Kelvin internal wave with the second vertical mode, and a Poincare wave with a period of 8 h. Note that to reveal the occurrence of internal waves with higher vertical modes, a phase analysis (Section 5.5.2) should be performed on different isotherms to reveal the intrinsic nature of this type of internal seiche, which is characterized by water masses flowing in opposite directions. A further discussion of this topic can be found in Chapter 7.1.

In the context of identifying internal waves with different vertical modes, the first mode is typically determined by using the isotherm situated in the pycnocline region (thermocline when stratification is mainly induced by temperature variations). On the other hand, higher vertical modes generally require consideration of multiple isotherms at various depths (Lemmin et al., 2005). However, it is essential to recognize that higher vertical modes might exhibit a relatively low level of energy. Consequently, they can sometimes evade easy detection through spectral analysis because of their weak signal strength.

When using spectral analysis to identify internal seiches and higher horizontal modes in a reservoir, the response of the analysis can be influenced by the location of the temperature sensor within the reservoir. Temperature measurements conducted in Baldeggersee showed a minimal vertical temperature displacement near the center of the stratified basin, suggesting the presence of a fundamental internal seiche with the nodal point located near the center of the basin (Lemmin, 1987). Stations located in the middle of the reservoir, which could potentially serve as nodal points for internal seiches, may demonstrate a limited response to the effects of internal seiches. However, they show a strong response to higher horizontal modes.

During the past several decades, extensive research has focused on studying the dynamics of lakes and reservoirs by monitoring the water temperature (Mortimer, 1952). Today, as a result of significant technological advances, water velocity measurements have also become valuable tools for understanding the dynamics of stratified lakes. Studies conducted in Lake Alpnach have revealed, using spectral analysis of the bottom current and isotherms, that the current of the bottom boundary layer is strongly induced by oscillatory motion induced by internal seiche activity (Gloor et al., 1994). These measurements provide additional information and complement the information derived from the temperature data. As a result, researchers now have a more complete understanding of the intricate processes that govern the behavior of stratified water bodies.

It is important to note that the measurements utilized for identifying internal waves (e.g. temperature, underwater velocity field) are not solely influenced by internal wave motions. Other factors such as variations in solar radiation and wind intensity oscillations can also impact, for example, temperature measurements. Therefore, it becomes essential to carefully investigate the spectrum, specifically isolating and distinguishing oscillations caused by internal waves from those that are unrelated to baroclinic motion. This distinction is crucial for accurately interpreting the spectral analysis results and gaining a comprehensive understanding of the dynamics present in the reservoir.

Exercises

Exercises for 5.4 Fourier Analysis

P5.1

Exercises for 5.5 Advancing processing

P5.2

Chapter 6

Interfacial Wave

Waves can be generated between two or more layers of fluids of different densities and are not limited only to the water-air interface. The sea waves excited by the wind and the circular surface waves generated by a stone thrown onto a smooth surface of water (Figure 6.2) are examples of free surface waves. By definition, a surface wave propagates in a "one-layer system", presenting a high density difference between interfacial fluids. For example, considering sea waves, the water is approximately 1000% heavier than the air. Waves formed between oil and air are also considered free surface waves, since oil is still much heavier than air, approximately 900% heavier. However, waves can be generated by any perturbation in a system composed of fluid layers with a density difference.

Figure 6.1 Oil-water interface.

Figure 6.2 Circular dispersive waves fronts radiating from a localized source.

A "two-layer system" is formed by two fluids that present a small fraction of the density of either layer. For example, oil and water (Figure 6.1), where water is only 11% heavier than oil. Although apparently there is no difference between free surface waves and interfacial waves, the mathematical description can be strongly simplified when we have two fluids with a strong density difference.

Considering free surface waves, we can neglect the contribution of the air layer, since the water density is much higher than the air density. This simplification leads to a final solution that does not consider the properties of the air, leading to a particular solution of the interfacial wave equation.

6.1 Free surface wave

Free surface waves have been described in great detail in many textbooks (see, for instance, **?**). Here, we present just relevant features of free surface waves to help in understanding internal waves and its analogy with free surface waves.

This section is divided into three main topics. Firstly, we present a mathematical description to find the dispersion relation for free surface waves, the solution of wave equations. Most of this solution is applied to find the dispersion relation of internal waves; however, in the internal wave case the upper layer fluid is not neglected.

Even after this generalization, the dispersion relation can be divided into two cases depending on another simplification, which classifies the wave in more than two different categories: deep and shallow waves. We explore this classification since it is useful to treat these simplifications for internal waves, which tend to have a more complex solution.

Finally, we discuss the energy transport of free surface waves and the definition of group waves, phase, and group velocities. This last topic may be important for drawing a comparison between the energy of internal waves and surface waves and for making an analogy between the physical description in a surface and for a continuous stratified fluid, where internal waves, without interfacial ones, are susceptible to be excited.

6.1.1 Small-amplitude solution

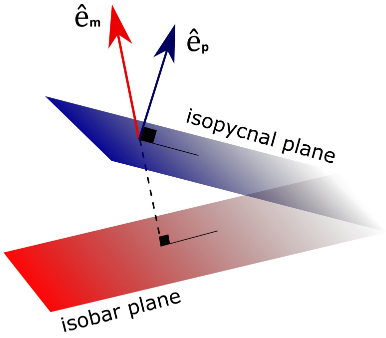

Figure 6.3 Baroclinic torque.

As we have previously shown in equation 2.56, vorticity is created essentially by baroclinic torque and viscous shear. When an inviscid flow is considered, the baroclinic term is the only source of vorticity.

From Equation 2.56, the baroclinic term can be expressed using vector notation as

$$\frac{1}{\varrho^2}\epsilon_{pmk}\frac{\partial\varrho}{\partial x_p}\frac{\partial P}{\partial x_m}=\frac{1}{\varrho^2}\vec{\nabla}\varrho\times\vec{\nabla}P, \tag{6.1}$$

in which $\vec{\nabla}\varrho\times\vec{\nabla}P$ is non-zero for any non-parallel planes. For example, in baroclinic activity, the isopycnals and isobars are inclined toward each other (Figure 6.3). In this case, the lighter fluid is accelerated faster than the heavier one, resulting in a shear layer that causes vorticity generation.

On the other hand, considering that the isopycnal and isobars are parallel to each other, the flow is considered barotropic and vorticity is not generated. This is the case for an unstratified system where free surface waves are the only wave that can be generated. This also leads to an important conclusion: surface waves are irrotational, whilst the internal wave is not. In addition, as we will explore in the next section, ignoring turbulent motions, interfacial waves can also be considered irrotational.

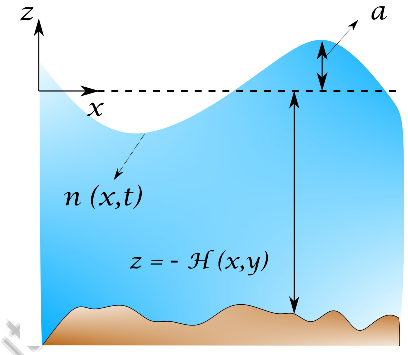

Figure 6.4 Surface wave.

Let us now focus on a free surface wave as shown in Figure 6.4. The superficial variation of the water due to wave evolution is represented by $\eta(x, y, t)$, a is the wave amplitude, and the mean depth of the water is expressed by $z = -H(x, y)$, in which z can vary spatially along the coordinates x and y. Note that z can also vary in time when topography variation is not neglected.

Since these waves are irrotational and inviscid, they can be described by potential theory. Therefore, as discussed in Section 2.2, the velocity field can be reduced to one scalar function, given by Equation 2.42. Thus, the simplified mass conservation equation (equation 2.34) reduces to **Laplace equation**:

$$\frac{\partial}{\partial x_i}\left(\frac{\partial \phi}{\partial x_i}\right) = \frac{\partial^2 \phi}{\partial x_i^2} = 0, \tag{6.2}$$

in which ϕ is the potential velocity function.

In Cartesian space, the Laplace equation for a three-dimensional wave (Figure 6.4) may be expressed in a complete form as

$$\frac{\partial^2 \phi}{\partial x^2} + \frac{\partial^2 \phi}{\partial y^2} + \frac{\partial^2 \phi}{\partial z^2} = 0. \tag{6.3}$$

The Laplace equation is an elliptic-type partial differential equation. Although this equation is linear, it can be used to describe large-amplitude waves. Considering the presence of large-amplitude waves, it introduces nonlinear terms on surface boundary condition. This equation requires boundary conditions in the six surrounding boundaries, two in $x-$direction, two in $y-$direction, and two in $z-$direction.

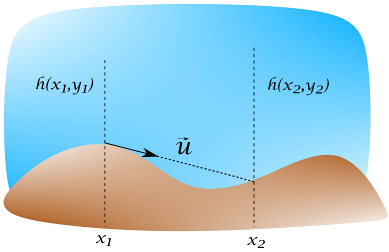

Figure 6.5 Particle motion on the system bottom.

In $z-$direction we have two boundary conditions, one at the water surface and another at the bottom of the system. Taking into account an impermeable bottom (rigid), the vector velocity is aligned parallel to the bottom topography and, consequently, the normal fluid velocity must be zero at $z = -H(x, y)$. Mathematically, $\mathbf{n} \cdot \nabla\phi = 0$. Note that in this case, the vertical and horizontal components of the velocity field are not necessarily zero.

First, consider the flow velocity vector in the bottom topography for a period of time, as illustrated in Figure 6.5. Fluid particles move with velocity u_i from point 1 to point 2. Thus, we have the following.

$$\left\{x_2 - x_1, y_2 - y_1, -H(x_2, y_2) + H(x_1, y_1)\right\} = \Delta t\,\{u, v, w\}, \tag{6.4}$$

in which the vertical function $H(x, y)$ can be expanded in a Taylor series for two variables as

$$H(x_2, y_2) \approx H(x_1, y_1) + (x_2 - x_1)\frac{\partial H_1}{\partial x} + (y_2 - y_1)\frac{\partial H_1}{\partial y}. \tag{6.5}$$

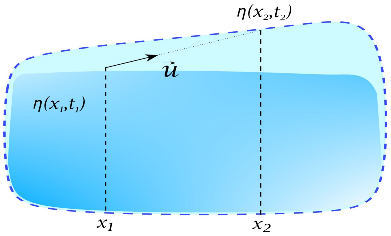

Figure 6.6 Particle motion on the bottom of the system.

Substitution of equation 6.5 into $z-$direction of equation 6.4 and dividing the whole term by Δt, give us

$$\frac{\Delta x}{\Delta t}\frac{\partial H}{\partial x} + \frac{\Delta y}{\Delta t}\frac{\partial H}{\partial y} = w,$$

in which $\Delta x/\Delta t = u$ and $\Delta y/\Delta t = v$. Note that if we set the bottom conditions as a plane surface, H is constant along the system, not varying along x and $y-$direction, and consequently the bottom conditions become $w = 0$. Using the definition of potential theory, we find that

$$\left.\frac{\partial \phi}{\partial z}\right|_{z=-H} = 0. \tag{6.6}$$

Equation 6.6 is known as the kinematic boundary condition for a rigid and plane bottom.

When considering the free surface, once a particle is on the water-free surface, it stays there always. Thus, the dot product between the velocity vector field and the outward-pointing normal vector is not necessarily zero, as previously observed with the bottom condition. In this case, the fluid particles move with the water surface.

In analogy to bed conditions, Figure 6.6 shows the surface displacement during the time interval Δt, in which the particle velocity vector is defined as

$$\left\{x_2 - x_1, 0, \eta(x_2,t_2) - \eta(x_1,t_1)\right\} = \Delta t\{u, v, w\} \tag{6.8}$$

in which, since we consider the surface to be just displaced by wave motion, η is the wave function. As the phase speed is aligned with x-direction, the velocity of the particles in y-direction may be neglected.

Expanding $\eta(x_2,t_2)$ into a Taylor series, we obtain the following.

$$\eta(x_2,t_2) \approx \eta(x_1,t_2) + (x_2 - x_1)\frac{\partial \eta(x_1,t_2)}{\partial x}. \tag{6.9}$$

Introducing Equation 6.9 into the vertical component of Equation 6.8 and dividing each term by Δt, we obtain the following:

$$\frac{\eta(x_1,t_2) - \eta(x_1,t_1)}{\Delta t} + \frac{\Delta x}{\Delta t}\frac{\partial \eta}{\partial x} = w,$$

in which $\Delta x/\Delta t = u$ and $t_2 \to t_1$. Thus, we have the following.

$$\frac{\partial \eta}{\partial t} + u\frac{\partial \eta}{\partial x} = \frac{\partial \phi}{\partial z} \quad \text{on } z = \eta(x,t). \tag{6.10}$$

Equation 6.10 is the kinematic boundary condition on the surface of free water. However, we can simplify the conditions one step further. Note that the point of application is $\eta(x,t)$ which varies along x and t. We can extend equation

Eulerian form
Another way to obtain the kinematic boundary condition is to analyze the material derivative of the resulting plane displacement.

$$\frac{DZ}{Dt} = \frac{\partial Z}{\partial t} + u_i\frac{\partial Z}{\partial x_i}, \tag{6.7}$$

in which

$$Z = \begin{cases} z + H(x,y) & \text{for } z = -H \\ \eta(x,t) - z & \text{for } z = \eta \end{cases}$$

Applying the condition z to the derivative form of the material (Equation 6.7), we obtain the bottom and surface conditions exactly equal to the expressions 6.6 and 6.10, respectively.

Table 6.1 Kinematic boundary conditions .

6.10 in a Taylor's series at $z = 0$ (Figure 6.7). Thus, considering just the first two terms of Taylor's expansion (first-order approximation), we have the following.

$$\frac{\partial\eta}{\partial t} + \eta\frac{\partial}{\partial z}\frac{\partial\eta}{\partial t} + u\frac{\partial\eta}{\partial x} + \eta\frac{\partial}{\partial z}\left(u\frac{\partial\eta}{\partial x}\right) \approx \frac{\partial\phi}{\partial z} + \eta\frac{\partial^2\phi}{\partial z^2} \quad \text{on } z = 0. \tag{6.11}$$

To simplify equation 6.11 we can write it in a non-dimensional form using transformation variables.

$$\eta = a\eta^* \qquad t = Tt^*, \tag{6.12a}$$
$$u = a/T\ u^* \qquad v = a/T\ v^* \qquad w = a/T\ w^*, \tag{6.12b}$$
$$x = \lambda x^* \qquad y = \lambda y^* \qquad z = \lambda\ z^*, \tag{6.12c}$$

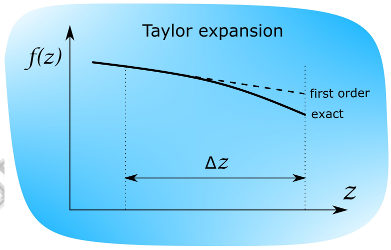

Figure 6.7 Taylor expansion.

in which T is the wave period, a is the wave amplitude, and λ is the wavelength. Variables donated by * are dimensionless. Substitution of equations 6.12 into the expanded kinematic boundary condition at the water surface (equation 6.11) gives us

☞ For shallow waters, the total depth of the water H can be used to parameterize the dimensional variables instead of λ.

$$\frac{a}{T}\frac{\partial\eta^*}{\partial t^*} + \frac{a^2}{\lambda T}\eta^*\frac{\partial}{\partial z^*}\frac{\partial\eta^*}{\partial t^*} + \frac{a^2}{\lambda T}u^*\frac{\partial\eta^*}{\partial x^*} + \frac{a^3}{\lambda^2 T}\eta^*\frac{\partial}{\partial z^*}\left(u^*\frac{\partial\eta^*}{\partial x^*}\right) \approx \frac{a}{T}\frac{\partial\phi^*}{\partial z^*} + \frac{a^2}{\lambda T}\eta^*\frac{\partial^2\phi*}{\partial z*^2}. \tag{6.13}$$

Dividing equation 6.13 by a/T, we obtain the following.

$$\frac{\partial\eta^*}{\partial t^*} + \frac{a}{\lambda}\eta^*\frac{\partial}{\partial z^*}\frac{\partial\eta^*}{\partial t^*} + \frac{a}{\lambda}u^*\frac{\partial\eta^*}{\partial x^*} + \left(\frac{a}{\lambda}\right)^2\eta^*\frac{\partial}{\partial z^*}\left(u^*\frac{\partial\eta^*}{\partial x^*}\right) \approx \frac{\partial\phi^*}{\partial z^*} + \frac{a}{\lambda}\eta^*\frac{\partial^2\phi*}{\partial z*^2}, \tag{6.14}$$

where for small-amplitude waves ($a << \lambda$), the terms of order $\mathcal{O}(a/\lambda)$ in equation 6.14 can be neglected. Thus, considering the dimensional form, equation 6.14 becomes

$$\frac{\partial\eta}{\partial t} = \left.\frac{\partial\phi}{\partial z}\right|_{z=0}, \tag{6.15}$$

which means that the vertical velocity of fluid particles on the water surface moves vertically with the water surface and cannot be measured horizontally by u and v. Note that for large-amplitude waves, the nonlinear convective terms also move the particle laterally (Figure 6.6).

The last boundary condition comes from the equations of motion and is called the dynamic boundary condition, which is applied exactly to the water surface on the streamline ($z = \eta$). Dividing all terms of 2.50 by ϱ, the Euler equation can be written.

$$\frac{\partial u_i}{\partial t} + u_j\frac{\partial u_i}{\partial x_j} = -\frac{1}{\varrho}\frac{\partial P}{\partial x_i} + g_i. \tag{6.16}$$

Small-amplitude wave and linearization
Another way to simplify the kinematic boundary condition for the small-amplitude wave is the direct linearization of equation 6.11. We showed through dimension analysis that there are terms in equation 6.11 that have order $\mathcal{O}(a/\lambda)$, which may be neglected when $a \ll \lambda$. However, inspecting equation 6.14, we can see that all terms of order $\mathcal{O}(a/\lambda)$ are nonlinear. So, by neglecting non-linear terms, we actually adopt the condition $a \ll \lambda$. Therefore, the linearization of equation 6.14 implies that we restrict our solution to small-amplitude waves.

Table 6.2 Linearization of the kinematic boundary condition at water surface.

The second term of Equation 6.16 can be explored to obtain the Bernoulli unsteady equation under some simplifications. The second term can be written as

$$u_j \frac{\partial u_i}{\partial x_j} = u_j \frac{\partial u_i}{\partial x_j} + u_j \frac{\partial u_j}{\partial x_i} - u_j \frac{\partial u_j}{\partial x_i} = u_j \left(\frac{\partial u_i}{\partial x_j} - \frac{\partial u_j}{\partial x_i} \right) + u_j \frac{\partial u_j}{\partial x_i}. \tag{6.17}$$

Note that, for an irrotational flow, we have the following.

$$\frac{\partial u_i}{\partial x_j} - \frac{\partial u_j}{\partial x_i} = 0,$$

and, consequently, Equation 6.17 reduces to

$$u_j \frac{\partial u_i}{\partial x_j} = u_j \frac{\partial u_j}{\partial x_i} = \frac{1}{2} \frac{\partial u_j u_j}{\partial x_i},$$

and equation 6.16 can be written as

$$\frac{\partial u_i}{\partial t} + \frac{\partial u_j^2/2}{\partial x_i} + u_j \left(\frac{\partial u_i}{\partial x_j} - \frac{\partial u_j}{\partial x_i} \right) = -\frac{1}{\varrho} \frac{\partial P}{\partial x_i} + g_i.$$

Although we have already applied a simplification based on irrotational flow, the potential theory (restricted to irrotational flows) can be applied to the transient term. Considering that ϱ does not change along a streamline, we have the following.

$$\frac{\partial}{\partial t} \left(\frac{\partial \phi}{\partial x_i} \right) + \frac{\partial (u_j)^2/2}{\partial x_i} + \frac{\partial P/\varrho}{\partial x_i} - g_i = 0 \quad \text{on } z = \eta, \tag{6.18}$$

in which $g_i = \{0, 0, -g\}$. Therefore, Equation 6.18 can be written in a convenient form as

$$\frac{\partial}{\partial t} \left(\frac{\partial \phi}{\partial x_i} \right) + \frac{\partial (u_j)^2/2}{\partial x_i} + \frac{\partial P/\varrho}{\partial x_i} + \frac{\partial g z}{\partial z} = 0 \quad \text{on } z = \eta. \tag{6.19}$$

Taking into account only the vertical component (z direction) of the system of equations 6.19 and that ϕ is a smooth function, equation 6.19 becomes

$$\frac{\partial}{\partial z} \left(\frac{\partial \phi}{\partial t} + \frac{(u_j)^2}{2} + \frac{P}{\varrho} + g z \right) = 0 \quad \text{on } z = \eta. \tag{6.20}$$

We can now integrate the equation 6.20 with respect to z to obtain the following result.

$$\frac{\partial \phi}{\partial t} + \frac{(u_j)^2}{2} + \frac{P}{\varrho} + g z = F(t) \quad \text{on } z = \eta, \tag{6.21}$$

in which $F(t)$ is the integration constant with respect to z, an arbitrary function of time alone. Since $F(t)$ is arbitrary, we can choose a suitable constant that fits our needs. In a convenient form, assuming that $F(t) = P(\eta)$, the equation 6.21 reduces to **unsteady Bernoulli equation**, given by

$$\frac{\partial \phi}{\partial t} + \frac{u_j^2}{2} + g z = 0 \quad \text{on } z = \eta(x, t). \tag{6.22}$$

Now we can expand the equation6.22 in a Taylor's series at $z = 0$

$$\frac{\partial \phi}{\partial t} + \eta \frac{\partial}{\partial z}\frac{\partial \phi}{\partial t} + \frac{u_j^2}{2} + \eta \frac{\partial}{\partial z}\left(\frac{u_j^2}{2}\right) + gz + \eta \frac{\partial gz}{\partial z} = 0 \qquad \text{on } z = 0,$$

$$\frac{\partial \phi}{\partial t} + \eta \frac{\partial}{\partial z}\frac{\partial \phi}{\partial t} + \frac{u_j^2}{2} + \eta \frac{\partial}{\partial z}\left(\frac{u_j^2}{2}\right) + \eta g = 0. \tag{6.23}$$

Equation 6.23 can be written in a non-dimensional form using the same transformation variables used before (equations 6.12). Thus, we have

$$\frac{a\lambda}{T}\frac{\partial \phi^*}{\partial t^*} + \frac{a^2}{T^2}\eta^* \frac{\partial}{\partial z^*}\frac{\partial \phi^*}{\partial t^*} + \frac{a^2}{T^2}\frac{u_j^{*2}}{2} + \frac{a^3}{\lambda T^2}\eta^* \frac{\partial}{\partial z^*}\left(\frac{u_j^{*2}}{2}\right) + a\eta^* g = 0,$$

$$\frac{\partial \phi^*}{\partial t^*} + \frac{a}{\lambda}\eta^* \frac{\partial}{\partial z^*}\frac{\partial \phi^*}{\partial t^*} + \frac{a}{\lambda}\frac{u_j^{*2}}{2} + \frac{a^2}{\lambda^2}\eta^*, \frac{\partial}{\partial z^*}\left(\frac{u_j^{*2}}{2}\right) + \frac{T^2}{\lambda g}\eta^* g^* = 0. \tag{6.24}$$

in which the last term cannot be adimensionalized with respect to fundamental quantities of our problem. Thus, we cannot compare the order of this term with others ($\mathcal{O}(T^2/(g\lambda))$), and consequently we cannot neglect this term by dimensional analysis. However, for small-amplitude waves, the terms of order $\mathcal{O}(a/\lambda)$ can be neglected, since $a \ll \lambda$. Thus, the equation 6.24 can be written in dimensional form as

$$\frac{\partial \phi}{\partial t} = -\eta g. \tag{6.25}$$

Equation 6.25 is known as **the dynamic boundary condition at the water surface**. This equation specifies that the boundary condition at the water surface cannot have an arbitrary periodicity in space and time.

Now, before proceeding, let us analyze the motion function of the interface, η. Since we are interested only in a simple harmonic motion, it is convenient to specify the wave as a sinusoidal wave,

☜ For a hydrostatic solution, we can find the dispersion relation through the wave equation, which is obtained from a system of equations formed by conservation of the mass and momentum equations. For more details, see Table 6.3.

$$\eta(x_i, t) = a\cos(k_i x_i - \omega t), \tag{6.26}$$

where a is the wave amplitude and k_i and ω are the wave number and frequency, respectively. Since the crests and troughs are parallel to each other, this type of wave is called **plane wave**.

Equation 6.26 is one way to represent a plane wave which can also be prescribed, for example, by

$$\eta(x_i, t) = a\ \sin(k_i x_i - \omega t), \tag{6.27a}$$

$$\eta(x_i, t) = A\ \mathrm{e}^{\mathrm{i}(k_i x_i - \omega t)}, \tag{6.27b}$$

in which A is a complex number that expresses the amplitude and phase of the wave.

The sinusoidal representation of the interface displacement is not just convenient because these functions assume a basic wave form, but they can be expanded in a linear series. Since the Laplace equation (Equation 6.2) is a linear function, all the terms of an expanded representation of η can be a solution of the problem.

The dispersion relation is obtained by solving the Laplace equation. Note that the momentum equation in this situation is used just as in the dynamic boundary conditions.

Since we assume the generation of only small-amplitude waves, linearizing the boundary conditions, we can assume that the system response must have the same periodicity. In this case, the solution of the Laplace equation (equation 6.2) has the following form:

$$\phi(x,z,t) = f(z)\sin(kx - \omega t). \tag{6.28}$$

Subtracting equation 6.28 from the Laplace equation (equation 6.2), we obtain a second-order linear homogeneous differential equation with constant coefficients,

$$-k^2 f(z)\sin(kx-\omega t) + \frac{\partial^2 f(z)}{\partial z^2}\sin(kx-\omega t) = 0,$$

$$\frac{\partial^2 f(z)}{\partial z^2} - k^2 f(z) = 0, \tag{6.29}$$

in which we have two linearly independent solutions.

Hydrostatic solution
The hydrostatic solution provides results for shallow water waves, which considers that the horizontal scales (wavelength) are larger than the vertical scales (water depth). The non-hydrostatic solution (6.36), is a generalization of this solution.
By combining the momentum equations in $x-$ and $z-$direction, and the mass conservation equation, we can obtain the wave equation:

$$\frac{\partial^2\eta}{\partial t^2} - c_p^2\frac{\partial^2\eta}{\partial x^2} = 0, \tag{6.30}$$

in which $c_p = \sqrt{gH}$ is the phase velocity. The solution of shallow water can be obtained assuming $\eta = A\ \exp^{i(kx-\omega t)}$, and is exactly the same as from 6.40.

Table 6.3 Shallow water free-surface wave.

The general solution is given by

$$f(z) = C_1\ \mathrm{e}^{k_1 z} + C_2\ \mathrm{e}^{k_2 z}, \tag{6.31}$$

where k_1 and k_2 are roots of $f^2 - k^2 = 0$. Thus, Equation 6.31 reduces to

$$f(z) = C_1\ \mathrm{e}^{kz} + C_2\ \mathrm{e}^{-kz}, \tag{6.32}$$

in which C_1 and C_2 are coefficients of the equation 6.32 that can be found by boundary conditions.

From the kinetic boundary condition at the bottom of the basin ($z = -H$) defined by equation 6.6 and the general solution of $\phi(x,z,t)$ and $f(z)$, defined by equations 6.28 and 6.32, respectively, we have

$$\left.\frac{\partial\phi}{\partial z}\right|_{z=-H} = \left(kC_1\ \mathrm{e}^{-kH} - kC_2\ \mathrm{e}^{kH}\right)\sin(kx-\omega t) = 0,$$

in which we can easily find that

$$C_1 = C_2\ \mathrm{e}^{2kH}.$$

The general solution now can be written as

$$\phi(x,z,t) = C_2\left(\mathrm{e}^{2kH}\ \mathrm{e}^{kz} + \mathrm{e}^{-kz}\right)\sin(kx-\omega t). \tag{6.33}$$

Applying the dynamic boundary condition on the water surface for a small-amplitude wave (Equation 6.25) to equation 6.28, we obtain the expression of C_2:

$$\frac{\partial}{\partial t}\left(C_2\left(\mathrm{e}^{2kH}\,\mathrm{e}^{kz}+\mathrm{e}^{-kz}\right)\sin(kx-\omega t)\right)\bigg|_{z=0} = -ag\cos(k_i x_i-\omega t)$$

$$C_2 = \frac{ag}{\omega}\,\frac{1}{\mathrm{e}^{2kH}+1} = \frac{ag}{\omega}\left(\frac{\mathrm{e}^{-kH}}{\mathrm{e}^{kH}+\mathrm{e}^{-kH}}\right),$$

in which $\mathrm{e}^{kH}+\mathrm{e}^{-kH} = 2\cosh(kH)$. Thus, we have

$$C_2 = \frac{ag}{2\omega}\,\frac{\mathrm{e}^{-kH}}{\cosh(kH)}. \tag{6.34}$$

Finally, substituting equation 6.34 into the general solution (6.33) gives us the following.

$$\begin{aligned}\phi(x,z,t) &= \frac{ag}{2\omega}\,\frac{\mathrm{e}^{-kH}}{\cosh(kH)}\left(\mathrm{e}^{2kH}\,\mathrm{e}^{kz}+\mathrm{e}^{-kz}\right)\sin(kx-\omega t),\\ &= \frac{ag}{2\omega\cosh(kH)}\left(\mathrm{e}^{k(z+H)}+\mathrm{e}^{-k(z+H)}\right)\sin(kx-\omega t),\end{aligned}$$

$$\phi(x,z,t) = \frac{ag}{\omega}\,\frac{\cosh(k(z+H))}{\cosh(kH)}\sin(kx-\omega t). \tag{6.35}$$

The dispersion relation is obtained by the last boundary condition, the kinematic boundary condition on the surface of the water (equation 6.15).

$$\frac{\partial\eta}{\partial t}-\frac{\partial\phi}{\partial z}\bigg|_{z=0} = 0,$$

$$\omega-\frac{kg}{\omega}\,\frac{\sinh(kH)}{\cosh(kH)} = 0,$$

$$\omega^2 = kg\tanh(kH), \tag{6.36}$$

in which this expression is called **dispersion relation** since it describes the relationship between wave frequencies (ω) and wave numbers (k). Actually, the expression shows that, for some conditions, waves of different wavelengths propagate at different phase speeds (Figure 6.8).

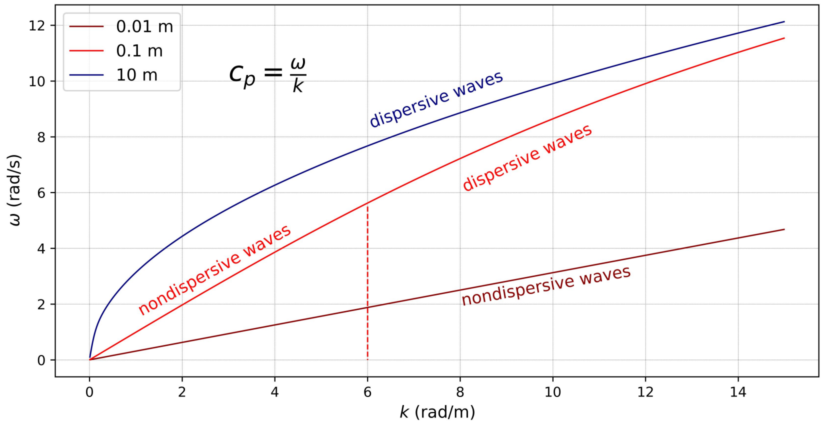

Figure 6.8 Comparison of the dispersion curves for three different depths ($H = 0.01, 0.1,$and 10 m).

Note that when the wavelength is much higher than the depth of the water, the phase velocity is constant, and consequently the wave is non-dispersive. The dark red curve may contain non-dispersive waves only for low wavelength, when $k \gg 600$. The red curve shows that for $k > 6$, the larger the wavelength, the faster the phase velocity of the free surface wave. Figures 6.2 show dispersive circular surface waves generated by a stone thrown into deep water.

From Equation 6.35 we can also compute the velocity fields. Taking the derivatives of the potential velocity, the horizontal and vertical velocities are, respectively,

$$u(x,z,t) = \frac{akg}{\omega}\frac{\cosh(k(z+H))}{\cosh(kH)}\cos(kx-\omega t), \tag{6.37a}$$

$$v(x,z,t) = \frac{akg}{\omega}\frac{\sinh(k(z+H))}{\cosh(kH)}\sin(kx-\omega t), \tag{6.37b}$$

in which the wave crest moves at phase speed,

$$c_p = \frac{\omega}{k} = \sqrt{\frac{g}{k}\tanh(kH)}. \tag{6.38}$$

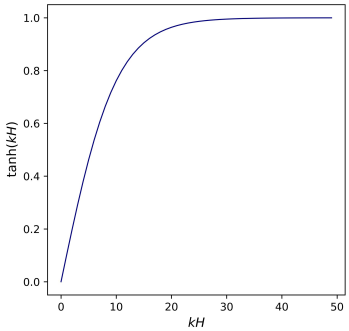

Figure 6.9 Tangent hyperbolic function ($H = 0.1$ m).

Figure 6.10 shows the solution to the problem of waves on the free surface. As we can analyze, the maximum horizontal velocity occurs in the wave crest and in the opposite direction at the wave trough. Maximum vertical velocities occur between the wave crest and the trough. Furthermore, we can also observe that the velocities are stronger at the surface of the water than at deeper regions. Note that although Figure 6.10 uses the general solution of surface wave propagation, since η is a monochromatic wave (has a single wavelength and frequency), the wave evolution does not show wave dispersion, which characterizes the propagation of waves in deep waters.

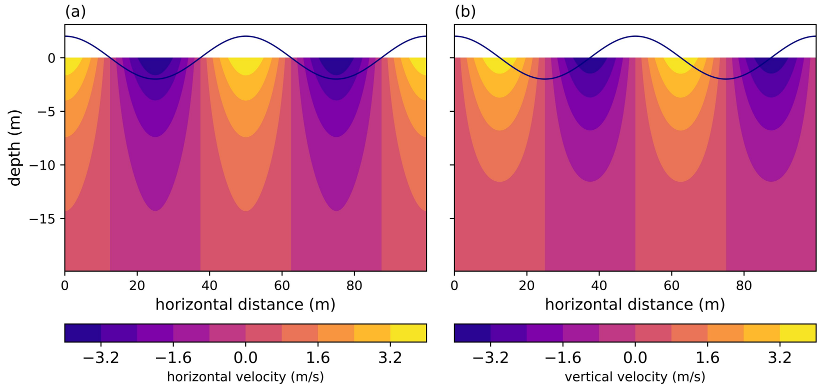

Figure 6.10 Free-surface wave solution for an internal wave of 2 m amplitude (with wavelength 50 m and wave period of 10 sec) propagating in an unstratified basin of depth 20 m: (a) shows the horizontal velocity component and (b) the vertical velocity component. The blue curve represents the interfacial displacement given by 6.26.

6.1.2 Special cases

As we noted in Figure 6.8, if the depth of the water H is more grating than the wavelength λ, the wave is called dispersive. Essentially, this occurs since the phase velocity of the wave can vary as a function of λ. Based on this classification, we now investigate the behavior of wave propagation for special cases: shallow and deep waters.

In the limit of deep water, which can be expressed mathematically as $kH \gg 1$, $kH \to \infty$, and $\tanh(kH) \to 1$ (Figure 6.9), we find that

$$\omega^2 = gk, \tag{6.39}$$

and $c_p = \sqrt{g/k}$. Note that in this case c_p is a function of the wavenumber k, which characterizes the propagation of a dispersive wave.

On the other hand, in the limit of shallow water waves ($kH \to 0$), $\tanh(kH)$ can be approximated to kH through Taylor expansion, resulting in

$$\omega^2 = gHk^2. \tag{6.40}$$

The phase velocity in the deep water limit is given by $c_p = \sqrt{gH}$, which means that the phase velocity does not depend on the wavelength.

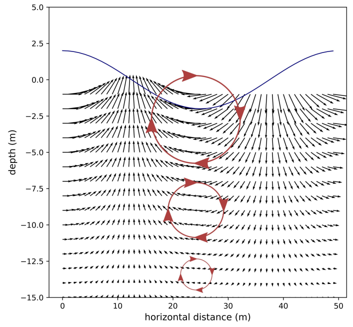

Figure 6.11 Velocity field for a surface wave ($H = 100$ m).

6.1.3 Energy transport and Group velocity

As a surface wave travels horizontally at the water surface, the water particles move in a circular motion, returning to its original position. This behavior can be observed in Figure 6.11, which is a vectorization of the velocities presented in Figure 6.10. Clearly, the vector velocities do not form a circular motion, since wave propagation is not a steady flow, and Figure 6.11 shows only a moment of wave propagation. Following the evolution of the wave, we may observe that the pathline is circular and that as deeper the location, the smaller the circular motion.

☞ The particle returns to its original position according to linear theory. Due to nonlinearity, a small net forward movement is observed.

When water particles move up/down toward the surface wave crest/trough, the kinetic energy is converted to the potential energy, and consequently the water level is displaced from the equilibrium position. However, the tilted interface flows back toward equilibrium, transforming the potential energy into kinetic energy during wave propagation. Thus, the surface wave travels, exchanging kinetic energy with potential energy and vice versa. In this case, since we neglected the contribution of viscosity and mixing, we assume that the wave propagates infinitely and that the total energy is not dissipated by viscosity or turbulence.

Since the motion is dominated by kinetic and potential energy, we consider that the total wave energy is given by the sum of its contributions.

$$E_t = E_K + E_P, \tag{6.41}$$

in which E_K is the kinetic energy and E_P is the potential energy.

The kinetic energy of the wave per unit of surface area during a wave period is given by

$$\overline{E_K} = \frac{1}{T}\int_0^T \int_{-H}^{\eta} \frac{\rho}{2}(u^2 + w^2)\mathrm{d}z\,\mathrm{d}t, \tag{6.42}$$

in which T is the wave period.

Note that we can modify the integration limit from η to 0, just assuming that the kinetic energy neglected at the crest is equal to the overestimation at the trough. Thus, we have

$$\overline{E_K} \approx \frac{\rho}{2T}\int_0^T \int_{-H}^{0} \frac{a^2 g^2}{c^2\cosh^2(kH)}\Big(\cosh^2(k(z+H))\cos^2(kx-\omega t)+ \sinh^2(k(z+H))\sin^2(kx-\omega t)\Big)\,\mathrm{d}z\,\mathrm{d}t. \tag{6.43}$$

Taking the time average defined by Equation 6.44, we obtain the following.

$$\overline{E_K} \approx \frac{\rho}{4}\int_{-H}^{0} \frac{a^2 g^2}{c^2\cosh^2(kH)}\underbrace{\Big(\cosh^2(k(z+H)) + \sinh^2(k(z+H))\Big)}_{\text{(I)}}\,\mathrm{d}z. \tag{6.45}$$

Term (I) can be written in an exponential form as

$$\begin{aligned}\text{(I)} &= \left(\frac{e^{k(z+H)} + e^{k(z+H)}}{2}\right)^2 + \left(\frac{e^{k(z+H)} - e^{k(z+H)}}{2}\right)^2,\\ &= 2\frac{e^{2k(z+H)} + e^{2k(z+H)}}{4},\\ &= \cosh(2k(z+H)),\end{aligned}$$

Time average
Even through the time average of a powered trigonometric functions that can be found through the integration of the Pythagorean identity, we may find the solution through a simpler form. If T is large enough, the time average of $\sin^2(t)$ is the same as the time average of $\cos^2(t)$, so we know that:

$$\sin^2(t) + \cos^2(t) = 1,$$

in which the time average is defined as

$$\overline{\sin^2(t)} = 1/2. \tag{6.44}$$

Table 6.4 Time average of powered trigonometric function.

which results

$$\overline{E_K} = \frac{a^2\rho g^2}{4\cosh^2(kH)c^2}\int_{-H}^{0}\cosh(2k(z+H))\,\mathrm{d}z,$$

$$= \frac{a^2g^2}{4c^2}\frac{\rho}{\cosh^2(kH)}\left(\frac{\sinh(2k(z+H))}{2k}\right)\bigg|_{-H}^{0},$$

$$= \frac{\rho}{8}\frac{a^2g^2k}{\omega^2}\frac{\sinh(2kH)}{\cosh^2(kH)},$$

Applying the solution 6.36, we have

$$\overline{E_K} = \frac{\rho}{8}\frac{a^2g}{\sinh(kH)}\frac{\sinh(2kH)}{\cosh(kH)},$$

$$= \frac{\rho a^2 g}{8}\frac{\sinh(2kH)}{\cosh(kH)\sinh(kH)},$$

$$= \frac{\rho a^2 g}{8}\frac{2\sinh(2kH)}{\sinh(2kH)},$$

$$\overline{E_K} = \frac{\rho a^2 g}{4}. \tag{6.46}$$

Now, the potential energy per unit of surface area during a wave period may be expressed as

$$\overline{E_P} = \frac{1}{T}\int_0^T\int_0^\eta \rho g z \mathrm{d}z\,\mathrm{d}t. \tag{6.47}$$

By the integration equation 6.47 with respect to z and using the expression of η (equation 6.26), we find that

$$\overline{E_P} = \frac{1}{T}\int_0^T \frac{\rho g z^2}{2}\bigg|_0^\eta \mathrm{d}t,$$

$$= \frac{1}{T}\int_0^T \frac{\rho g \eta^2}{2}\,\mathrm{d}t,$$

$$= \frac{1}{T}\int_0^T \frac{\rho g a^2}{2}\,\cos^2(k_i x_i - \omega t)\,\mathrm{d}t$$

Applying the time average (Equation 6.44) and solving the integral, similar to the case when obtaining equation 6.45, the potential energy is

$$\overline{E_P} = \frac{1}{T}\left(\frac{\rho g a^2}{2}\right)\frac{T}{2} = \frac{\rho g a^2}{4}. \tag{6.48}$$

As observed, assuming that the wave is not damped, the mean wave energy along one wave period is equally partitioned between potential and kinetic energies.

Combining the equations 6.46 and 6.48, the mean total energy per unit area (J/m^2) is given by

$$\overline{E_t} = \frac{\rho g a^2}{2}. \tag{6.49}$$

As the wave propagates, its energy is transported. Thus, the wave energy flux through a vertical plane of units of width perpendicular to the wave direction can be obtained through the energy equation. Now we leave it as an exercise to show that the rate of flux energy is given by

$$\mathscr{F}_E = \underbrace{\frac{\rho g a^2}{2}}_{\text{wave energy}} \underbrace{\frac{c}{2}\left(\frac{2kH}{\sinh(2kH)}+1\right)}_{\text{wave energy velocity}}. \tag{6.50}$$

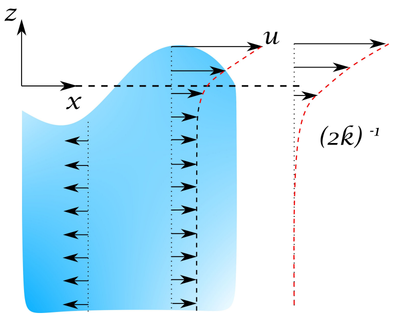

Figure 6.12 Mean horizontal flow associated to stokes drift under a periodic surface wave.

The field velocity obtained in 6.37 predicts that the particle path is closed (Figure 6.11), which means that the particles return to their original position after wave evolution, and consequently the wave does not transport mass, just energy (Equation 6.50). This is observed since we linearized our problem and assumed that $\eta \approx 0$. However, water particles in the wave crest travel faster than at great depths, so we observe a small net forward movement, which is called Stokes drift.

6.1.4 Stokes drift

The strokes drift is a small forward net movement induced by wave propagation, which decreases exponentially with higher depths (Figure 6.12). Since we linearized the governing equations in Section 6.1.1 ($a/H \ll 1$), we neglected the contribution of the horizontal velocity near the wave crest. Taking into account a small displacement of the fluid parcel from the mean position due to the Stokes drift, the magnitude of the net drift can easily be estimated. Applying a Taylor expansion around the mean position of the horizontal velocity component (equation 6.37a), we have the following.

$$u_s(x+x_s, z+z_s) \approx u(x,z) + x_s \left.\frac{\partial u}{\partial x}\right|_{x,z} + z_s \left.\frac{\partial u}{\partial z}\right|_{x,z}, \tag{6.51}$$

in which x_s and z_s are the small net displacements in the horizontal and vertical directions as a result of the Stokes drift, respectively. Both displacements can be obtained through the integration in time of equations 6.37:

$$x_s(x,z,t) = -\frac{akg}{\omega^2}\frac{\cosh(k(z+H))}{\cosh(kH)}\sin(kx-\omega t), \tag{6.52a}$$

$$z_s(x,z,t) = \frac{akg}{\omega^2}\frac{\sinh(k(z+H))}{\cosh(kH)}\cos(kx-\omega t), \tag{6.52b}$$

assuming that ω^2 is defined by the dispersion relation 6.36, the system 6.52 reduces to

$$x_s(x,z,t) = -a\frac{\cosh(k(z+H))}{\sinh(kH)}\sin(kx-\omega t), \tag{6.53a}$$

$$z_s(x,z,t) = a\frac{\sinh(k(z+H))}{\sinh(kH)}\cos(kx-\omega t). \tag{6.53b}$$

Applying the horizontal velocity 6.37a to the expansion defined in equation 6.51 and the horizontal and vertical displacement determined in 6.53, we may obtain the following.

$$u_s = \frac{agk}{\omega}\frac{\cosh(k(z+H))}{\cosh(kH)}\cos(kx-\omega t) + \frac{a^2k^2g}{\omega}\frac{1}{\cosh(kH)\sinh(kH)}$$
$$\left(\cosh^2(k(z+H))\sin^2(kx-\omega t) + \sinh^2(k(z+H))\cos^2(kx-\omega t)\right)$$

Taking the average over a wave period, we find that

$$u_s = \frac{a^2k^2g}{\omega}\frac{1}{\sinh(2kH)}\left(\cosh^2(k(z+H)) + \sinh^2(k(z+H))\right)$$

$$u_s = \frac{a^2k^2g}{\omega}\frac{\cosh(2k(z+H))}{\sinh(2kH)}, \tag{6.54}$$

in which u_s expresses the Stokes drift velocity (Figure 6.12).

6.1.5 Kelvin waves

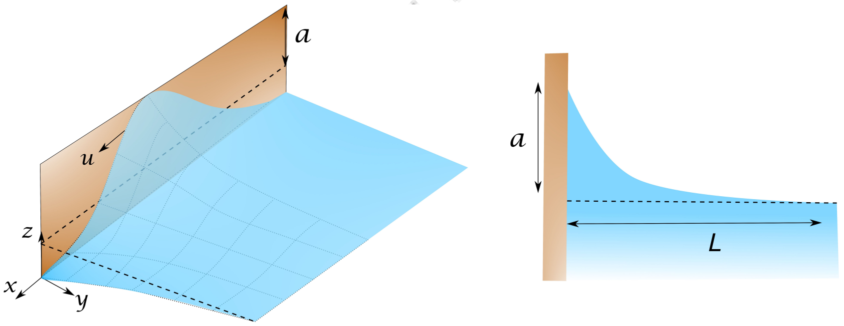

Figure 6.14 Kelvin wave.

Kelvin wave is a large-scale (low-frequency) trapped gravity wave affected by Earth's rotation that propagates in a shallow-water system, presenting an exponential decay away from the boundaries (Figure 6.14). The Kelvin wave balances the Coriolis force against a topographic boundary, moving equatorward and poleward along the western and eastern boundaries, respectively (Figure 6.13). In a closed basin, the Kelvin wave propagates cyclonically with a typical amphidromic structure.

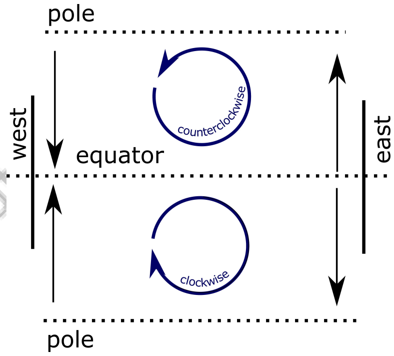

Figure 6.13 Amphidromic system

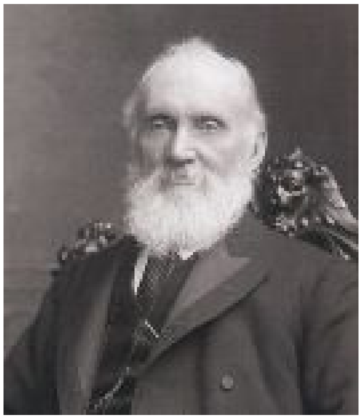

William Thomson (Baron Kelvin) (1824–1907, British) was born in Belfast. He was a mathematical physicist and engineer. Due to his achievements in thermodynamics and of his opposition to Irish Home Rule, he became Baron Kelvin. He was the pioneer of vortex dynamic (Kelvin-Helmholtz instabilities) and has also determined the correct value of absolute zero (the lower limit to temperature). This absolute scale is known today as the Kelvin thermodynamic temperature scale in honor of him. Baron Kelvin was the first to identify the large-scale trapped gravity wave affected by Earth's rotation (now known as Kelvin waves).

The water is deflected by the rotation of the Earth through the Coriolis force, which deflects the wave. However, due to the topography boundaries, the water portion is piled up on the boundary.

Mathematically, we can obtain the solution of Kelvin waves taking into account the Coriolis force from 2.46.

$$\varrho\left(\frac{\partial u_i}{\partial t}+u_j\frac{\partial u_i}{\partial x_j}\right)=-\frac{\partial P}{\partial x_i}+\varrho g_i-2\varrho\varepsilon_{ijk}\overline{\omega_j}u_k. \tag{6.55}$$

Recall that the second term of 6.55 can be neglected by a linearization procedure, assuming that the wavelength is much larger than the amplitude of the wave ($a \ll \lambda$). This simplification reduces equation 6.55 to

Kelvin waves in the equator
There is a special type of Kelvin wave, defined as the equatorial Kelvin wave, that is trapped close to the equator. The balances of Coriolis forces from both hemispheres act analogously as a topographic boundary.
The mathematical solution is similar to that derived from the Kelvin waves (coastal Kelvin wave). However, since the Coriolis frequency is zero ($f = 0$) in the equator, equation 6.109 must be parameterized by an artificial coefficient.

Table 6.5 Equatorial Kelvin wave.

$$\frac{\partial u_i}{\partial t}=-\frac{1}{\varrho}\frac{\partial P}{\partial x_i}+g_i-2\varepsilon_{ijk}\overline{\omega_j}u_k. \tag{6.56}$$

Assuming the coordinate system as shown in Figure 6.14, we see that 6.56 can be simplified as

$$\frac{\partial u}{\partial t}=-\frac{1}{\varrho}\frac{\partial P}{\partial x}+\cancelto{=0}{g_x}+f\cancelto{=0}{v}, \tag{6.57a}$$

$$\cancelto{=0}{\frac{\partial v}{\partial t}}=-\frac{1}{\varrho}\frac{\partial P}{\partial y}+\cancelto{=0}{g_y}-f\,u, \tag{6.57b}$$

$$\cancelto{=0}{\frac{\partial w}{\partial t}}=-\frac{1}{\varrho}\frac{\partial P}{\partial z}-g. \tag{6.57c}$$

Note that the velocity in $y-$direction is zero at the boundaries and the acceleration in z direction is neglected.

Assuming a general solution of $\eta = a(y)\ \exp^{-i(kx-\omega t)}$, from 6.57cc, we have

$$\frac{\partial P}{\partial z}=-\varrho g \qquad \int_{\text{surface}}^{\text{bottom}}\mathrm{d}P=-\varrho g(-H-\eta)=\varrho g(H+\eta) \tag{6.58}$$

From 6.58, 6.57a can be reduced to

$$\frac{\partial u}{\partial t}=-g\frac{\partial \eta}{\partial x} \tag{6.59}$$

Poicaré wave
Another type of wave affected by the Coriolis effect is Poicaré waves. Unlike the Kelvin wave, the Poicaré wave is dispersive and has a phase velocity different from the waves that are not affected by Coriolis.
To obtain the solution for Poicaré waves, assume conditions similar to Kelvin waves, but assume that the deflection due to the Coriolis force induces a velocity in y-direction.

Table 6.6 Poicaré waves.

Taking 6.57b in time and applying 6.59 and 6.58 to it and assuming the general solution of η, give us

$$\frac{\partial}{\partial t}\frac{\partial P}{\partial y}=-\varrho f\frac{\partial u}{\partial t}$$

$$\frac{\partial}{\partial y}\frac{\partial \eta}{\partial t}=f\frac{\partial \eta}{\partial x}$$

$$i\omega\frac{\partial a(y)}{\partial y}=-ikf\,a(y)$$

$$\frac{\partial a(y)}{\partial y} + \frac{f}{c_p} a(y) = 0,$$

in which $c_p = \omega / k$. This equation is a differential equation that can be solved by separation, which results in

$$\eta = a_o \exp^{-\frac{f}{c_p} y} \exp^{-i(kx - \omega t)} \tag{6.60}$$

Applying 6.59 to the mass conservation equation and assuming that the vertical velocity w is approximated by the surface velocity of the water pointing upward, we can find the wave equation, similar to that found in table 6.3, considering the shallow water solution:

$$\int_{\text{surface}}^{\text{bottom}} \mathrm{d}w = \int_{\eta\approx 0}^{\text{-H}} \frac{\partial u}{\partial x} \mathrm{d}z$$

$$-w_{\text{surface}} = -\frac{\partial u}{\partial x}\Big(-H\Big)$$

$$\frac{\partial \eta}{\partial t} + H\frac{\partial u}{\partial x} = 0$$

$$\frac{\partial^2 \eta}{\partial t^2} - gH\frac{\partial^2 \eta}{\partial x^2} = 0. \tag{6.61}$$

The partial differential equation 6.61 can be solved by applying the general solution of 6.60. Note that the partial differential equation is independent of the variable y, indicating that the phase velocity of the Kelvin waves is the same as that for the non-rotating case.

The influence of rotation is limited to the new term 6.60 ($\exp^{-\frac{f}{c_p} y}$). The f/c_p is known as the Rossby radius of deformation L_R and describes the length scale at which the Coriolis effect becomes important in wave motion. In the ocean, L_R is strongly affected by latitude and depth of water, varying from 10 km in high-latitude regions to more than 2000 km in the deep sea near the equator.

6.2 Interfacial wave in a two-layer system

Interfacial waves are generalizations of free surface waves that have been studied in the previous section. Instead of free surface waves, where the upper layer is air (or any lighter fluid compared to the fluid above), we now consider that both fluids have comparable densities.

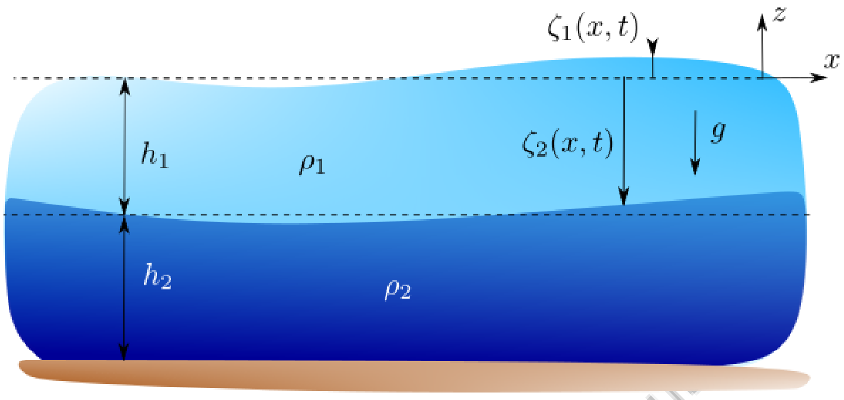

Figure 6.15 Interfacial wave in a bounded system.

Although interfacial waves do not represent the continuous stratification of a natural environment, they remain a good approximation of density structure in many situations. We start our analysis by considering a two-layer system made up of two immiscible fluids (Figure 6.15). As a first example, we consider the hydrostatic approximation, valid only when the horizontal scale is large compared to depth, characterizing a shallow-water solution (similar solution discussed in Table 6.3).

6.2.1 Solution for shallow water

Based on the situation depicted in figure 6.15, our first step is to derive for each layer the governing equations for nonrotating shallow-water flow:

$$\frac{\partial u_s}{\partial t} = -\frac{1}{\varrho_s}\frac{\partial P_s}{\partial x}, \tag{6.62a}$$

$$\cancel{\frac{\partial w_s}{\partial t}} = -\frac{1}{\varrho_s}\frac{\partial P_s}{\partial z} - g, \tag{6.62b}$$

$$\frac{\partial u_s}{\partial x} + \frac{\partial w_s}{\partial z} = 0, \tag{6.62c}$$

where the subscript s indicates the layer, where $s = 1$ and $s = 2$ represent the upper and lower layer, respectively. We neglect w_s from the momentum equation for z-direction, which results in a hydrostatic approximation.

The displacement of the interface between fluids 1 and 2 is given by the sinusoidal wave shape with wave number k_2 and angular frequency ω_2 (similar to the one used to describe surface waves in 6.27):

$$\zeta_2(x,t) = a_i\, \mathrm{e}^{\mathrm{i}(k_2 x - \omega_2 t)}, \tag{6.63}$$

in which a_i is the amplitude of the interfacial wave. Note that the water surface is also free to oscillate. Therefore, we can also represent the surface displacement by a sinusoidal function η_1:

$$\zeta_1(x,t) = a_o\, \mathrm{e}^{\mathrm{i}(k_1 x - \omega_1 t)}, \tag{6.64}$$

in which a_o is the amplitude of the surface wave.

Since the dynamic does not influence the pressure in z − direction ($w = 0$), we obtain from equation 6.62b that the pressure distribution in each layer is given by the hydrostatic pressure for each layer:

$$P_1(x,z,t) = \rho_1 g(\zeta_1 - z) \qquad \zeta_2 \leq z \leq \zeta_1, \tag{6.65}$$

$$P_2(x,z,t) = \rho_1 g(\zeta_1 - \zeta_2) + \rho_2 g(-z + \zeta_2) \qquad -H \leq z \leq \zeta_2, \tag{6.66}$$

in which $H = H_1 + H_2$ is the total water depth.

Applying equations 6.65 and 6.66 to 6.62a, give

$$\frac{\partial u_1}{\partial t} = -g\frac{\partial \zeta_1}{\partial x} \tag{6.67a}$$

$$\frac{\partial u_2}{\partial t} = -\frac{\rho_1}{\rho_2} g \frac{\partial \zeta_1 - \zeta_2}{\partial x} - g\frac{\partial \zeta_2}{\partial x}. \tag{6.67b}$$

Combining the two equations, assuming $\hat{u} = u_2 - u_1$ and neglecting surface displacement ($\zeta_1 = 0$), we have the following.

$$\frac{\partial \hat{u}}{\partial t} = -g\frac{\Delta\rho}{\rho_2}\frac{\partial \zeta}{\partial x} = -g'\frac{\partial \zeta}{\partial x}. \tag{6.68}$$

The second equation can be found by combining the mass conservation equations of each layer. Thus, assuming that $\hat{u} = u_2 - u_1$ and $\zeta_1 = 0$, we find the following.

$$\int_0^{-h_1} \mathrm{d}w_1 = -\int_0^{-h_1} \frac{\partial u_1}{\partial x}\mathrm{d}z \tag{6.69a}$$

$$\int_{-h_1}^{-H} \mathrm{d}w_2 = -\int_{-h_1}^{-H} \frac{\partial u_2}{\partial x}\mathrm{d}z \tag{6.69b}$$

$$\frac{\partial \zeta_1}{\partial t} - \frac{\partial \zeta_2}{\partial t} = -h_1\frac{\partial u_1}{\partial x} \tag{6.70a}$$

$$-\frac{\partial \zeta_2}{\partial t} = -(-H + h_1)\frac{\partial u_2}{\partial x} = h_2\frac{\partial u_2}{\partial x} \tag{6.70b}$$

$$\frac{\partial \hat{u}}{\partial x} = -\left(\frac{h_1 + h_2}{h_1\ h_2}\right)\frac{\partial \zeta_2}{\partial t} \tag{6.71}$$

Combining equations 6.71 and 6.68, we have the partial differential equation for a shallow-water interfacial wave:

$$\frac{\partial^2 \zeta_2}{\partial t^2} - g'\overline{H}\frac{\partial^2 \zeta_2}{\partial x^2} = 0, \tag{6.72}$$

in which $g' = \Delta\rho/\rho_2$ is the reduced gravity and $\overline{H} = h_1\ h_2/H$ is the relative depth of the water.

Note that the interfacial displacement $\zeta_2(x,t)$ used here is a function defined from the upper boundary, where $x=0$. However, to define the interfacial displacement as described by 6.64, we must consider $\zeta_{z=0}=\zeta_{z=-h_1}-h_1$. Applying ζ_2 to the partial differential equation 6.72 and deriving it from t and x, we find that

$$c_p=\sqrt{g'\frac{h_1\,h_2}{h_1+h_2}}, \tag{6.73}$$

where c_p is the phase speed of propagation of the baroclinic mode in a shallow water system. This result is a generalization of the result from the free surface wave (Equation 6.40). Because $g' \ll g$, interfacial waves are much slower than surface waves, resulting in much longer periods.

We may derive the phase velocity 6.73 to obtain the period of the interfacial wave T. Assuming that $c_p=\omega/k$, we may find that

$$\begin{aligned} c_p=\frac{\omega}{k}=\frac{2\pi\, f\,\lambda}{2\pi}=f\,\lambda=\frac{\lambda}{T}; \\ T=\frac{\lambda}{c_p} \end{aligned} \tag{6.74}$$

One of the first observation of internal waves was noted by Benjamin Franklin during an expedition to Madeira in 1761. He noted that when his boat began to roll, waves formed in his Italian lamp made in an empty glass jar filled with oil and water (Figure 6.16). However, the waves were not on top; the surface of the oil was quiet. He noted that waves formed between the water and the oil.

The first scientific observations of internal waves in the natural environment were made by Nansen (1897) during an expedition to the North Pole in 1893. Nansen felt an extra drag on his boat due to internal waves, which slowed his boat to a quarter of its normal speed.

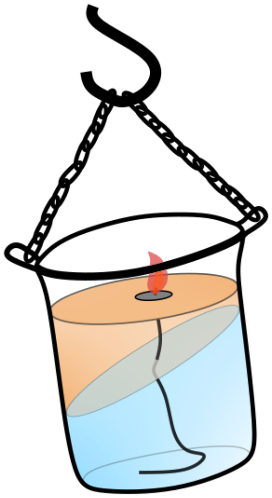

Figure 6.16 Italian lamp made in an empty glass jar, filled with oil and water

> *"Fram appeared to be held back, as if by some mysterious force,*
> *and she did not always answer the helm. In calm weather,*
> *with a light cargo, Fram was capable of* 6 *to* 7 *knots.*
> *When in dead water she was unable*
> *to make* 1.5 *knots*[1]*."*
> F. Nansen (1897)

Ekman (1904) was the first to provide a reasonable interpretation of the phenomenon. In the preface to Ekman's paper, Bjerknes said:

> *"The present investigation of "Dead-Water" was occasioned by a letter in November 1898 from Prof. NANSEN asking my opinion on the subject. In my reply to Prof. NANSEN I remarked that in the case of a layer of fresh water resting on the top of salt water, a ship will not only produce the ordinary visible waves at the boundary*

---

[1] The knot is a unit of speed equal to one nautical mile per hour, 1 knot ≡ 1.852 km/h

> *between the water and the air, but will also generate invisible waves at the salt-water fresh-water boundary below; I suggested that the great resistance experienced by the ship was due to the work done in generating these invisible waves."*
>
> Vagn Walfrid Ekman (1904)

He explained that energy from the ship is transmitted to internal waves, which occur between layers of different densities. The boat experiences an important loss of steering power and consequently the speed of the ship decreases dramatically. He supported this claim with several laboratory experiments.

Equation 6.73 has been derived from the hydrostatic condition, which considers that the pressure is given only by the hydrostatic contribution. This approximation neglects the vertical momentum by taking the contribution of the vertical velocity. This results in a non-dispersive solution, which is valid only for shallow-water waves, when $\lambda \gg H$. Although this is a good approximation in many large-scale motions (large internal waves), those waves may also be susceptible to non-hydrostatic effects, which usually rise at a minimum grid scale (Wadzuk, Hodges, 2004), where the nonlinear effect could also be important. Often, the hydrostatic approximation fails at open boundaries (), at steep slopes (), and when linear motions degenerate into high-frequency waves (Horn et al., 1998, 2001). Although non-hydrostatic flows often behave also non-linearly, in the next section we ignore non-linear effects and take into account just the non-hydrostatic contribution.

6.2.2 Non-hydrostatic solution

Now we solve the previous problem assuming a non-hydrostatic solution, which is similar to the approach used to find the solution for surface waves in Section 6.1.1.

According to Kelvin's circulation theorem, since we assume that each layer has a homogeneous density (Figure 6.15), the viscous effects are ignored and the Coriolis force neglected. Considering that the result motion for each layer is irrotational, an independent velocity potential (equation 2.42) can be defined in each layer. Rewrite the mass conservation equation 6.62c for the direction $x-z$ as **Laplace equation** for each layer, which gives us

$$\frac{\partial^2 \phi_1}{\partial x^2} + \frac{\partial^2 \phi_1}{\partial z^2} = 0, \tag{6.75a}$$

$$\frac{\partial^2 \phi_2}{\partial x^2} + \frac{\partial^2 \phi_2}{\partial z^2} = 0, \tag{6.75b}$$

in which equations 6.75 refer to mass conservation in the upper and lower layers, respectively. For a cosine dependence, the potential velocities ϕ_1 and ϕ_2 that satisfy the Laplace equations 6.75 are, respectively, of the form

$$\phi_1(x,z,t) = f_1(z)\, \mathrm{e}^{i(kx-\omega t)}, \tag{6.76a}$$

$$\phi_2(x,z,t) = f_2(z)\, \mathrm{e}^{i(kx-\omega t)}. \tag{6.76b}$$

Substituting equations 6.76 into the Laplace equation gives us a second-order linear homogeneous differential equation with two linearly independent solutions. The general solution assumes the following form:

$$f_1(z) = C_1\,\mathrm{e}^{kz} + C_2\,\mathrm{e}^{-kz}, \tag{6.77a}$$

$$f_2(z) = C_3\,\mathrm{e}^{kz} + C_4\,\mathrm{e}^{-kz}, \tag{6.77b}$$

in which the constants C_1, C_2, C_3, and C_4 can be determined from the boundary conditions.

Assuming that the coordinate system is referenced ($z = 0$) at the upper layer boundary, we have the following:

$$\underset{\sim}{\nabla}\phi_1 \cdot \underset{\sim}{\hat{n}}|_{z=0} = 0, \tag{6.78a}$$

$$\underset{\sim}{\nabla}\phi_2 \cdot \underset{\sim}{\hat{n}}|_{z=-H} = 0, \tag{6.78b}$$

in which $H = h_1 + h_2$.

Applying the general solution 6.76a in the rigid upper condition 6.78a gives $C_1 = C_2$, in which C_3 can be obtained from the boundary condition at the bottom 6.78b:

$$\left.\frac{\partial \phi_2}{\partial z}\right|_{z=-H} = 0 \qquad C_3 = C_4\,\mathrm{e}^{2kz}. \tag{6.79}$$

We can obtain a new relation between coefficient C_1 and C_2 using the kinematic boundary condition at the interface for the upper layer. The boundary condition at the interface between the two fluids must be satisfied for such a wave to move (similarly to that obtained from surface waves 6.10), so in this case we have the following.

$$\{x_2 - x_1, 0, \zeta(x_2, t_2) - \zeta(x_1, t_1)\} = \Delta t\,\{u_s, v_s, w_s\}, \tag{6.80}$$

in which η is the interfacial wave function and s indicates the layer number.

Expanding $\zeta(x_2, t_2)$ in a Taylor series, we have the following.

$$\zeta(x_2, t_2) \approx \zeta(x_1, t_2) + (x_2 - x_1)\frac{\partial \zeta(x_1, t_2)}{\partial x}, \tag{6.81}$$

which can be easily applied to equation 6.80. From z component, we have

$$\frac{\zeta(x_1, t_2) - \zeta(x_1, t_1)}{\Delta t} + \frac{\Delta x}{\Delta t}\frac{\partial \zeta}{\partial x} = w_s,$$

in which $\Delta x/\Delta t = u_s$ and $t_2 \to t_1$, with the result that

$$\frac{\partial \zeta}{\partial t} + u_s\frac{\partial \zeta_s}{\partial x} = \frac{\partial \phi}{\partial z} \qquad \text{on } z = \zeta(x, t). \tag{6.82}$$

Now we apply a linearization procedure, which assumes that the interfacial wave has a small amplitude compared to the wavelength ($b \ll \lambda$). Here, we do not show that nonlinear terms have $\mathcal{O}(b/\lambda)$. A detailed procedure can be performed by dimensional analysis, similar to that applied to surface waves in section 6.12. The linearization procedure leads to a linear form of the equation 6.82 by neglecting the second term on the left side.

Note that the equation is evaluated at $z = \zeta(x,t)$. So, assuming a linearization, we can simplify the term expanding in a Taylor series around $z = -h_1$ and neglecting the higher-order terms. Thus, the kinematic boundary condition for both layers at the interface becomes the following.

$$\left.\frac{\partial \phi_s}{\partial z}\right|_{z=-h_1} \approx \frac{\partial \zeta}{\partial t}. \tag{6.83}$$

Assuming that the interfacial displacement is represented by the sinusoidal wave form 6.64, and applying the general solution 6.76a in the kinematic boundary conditions 6.83 for the upper and lower layers, give us the following.

$$C_1 = C_2 = -\frac{ib\omega}{k}\frac{1}{e^{-kh_1} - e^{kh_1}}, \tag{6.84a}$$

$$C_4 = -\frac{ib\omega}{k}\frac{1}{e^{2kH}\,e^{-kh_1} - e^{kh_1}}, \tag{6.84b}$$

where C_3 can be obtained from 6.79,

$$C_3 = -\frac{ib\omega}{k}\frac{e^{2kH}}{e^{2kH}\,e^{-kh_1} - e^{kh_1}} \tag{6.85}$$

The last two boundary conditions come from the momentum equation in z-direction and are known as the dynamic boundary condition. Assuming an inviscid and irrotational flow, we obtain the unsteady Bernoulli equation.

$$\rho_s\frac{\partial \phi_s}{\partial t} + \rho\left(\frac{u_s^2 + w_s^2}{2}\right) + P_s + \rho_s g z_s = F(t), \tag{6.86}$$

which is constant along a streamline. $F(t)$ can be absorbed by the potential velocity, since it is just a function of t. Equation 6.86 can be applied to the interfacial wave function ($z = \zeta$).

Assuming small-amplitude surface waves ($b \ll \lambda$), the nonlinear kinetic energy term can be neglected in equation 6.86. Since we are assuming that the wave has a small amplitude, we can expand the equation in a Taylor series around $z = -h_1$ (equilibrium position) and neglect higher-order terms. Finally, we have

$$\rho_s\left.\frac{\partial \phi_s}{\partial t}\right|_{z=-h_1} + \rho_s g\zeta \approx F(t). \tag{6.87}$$

Selecting the fluid interface as the streamline and applying the unsteady Bernoulli equation to it gives the following.

$$\rho_1\left.\frac{\partial \phi_1}{\partial t}\right|_{z=-h_1} = \rho_2\left.\frac{\partial \phi_2}{\partial t}\right|_{z=-h_1} + \Delta\rho g\zeta. \tag{6.88}$$

Substitution of equations 6.84, 6.85, 6.76, and 6.77 into equation 6.88 gives us the dispersion relation:

$$\rho_1\left(\frac{e^{-kh_1}+e^{kh_1}}{e^{kh_1}-e^{-kh_1}}\right)+\rho_2\left(\frac{e^{kh_2}+e^{-kh_2}}{e^{kh_2}-e^{kh_2}}\right)=\frac{kg\Delta\rho}{\omega^2}$$

$$\omega^2=\Delta\rho g k\frac{\tanh(kh_1)\ \tanh(kh_2)}{\rho_2\ \tanh(kh_1)+\rho_1\ \tanh(kh_2)} \tag{6.89}$$

The dispersion relation 6.89 describes the propagation of a small-amplitude interfacial wave, in which the second order in ω indicates that the wave travels with a single speed but in two directions. The difference from that obtained for shallow waters (equation 6.73) is that the dispersion relation 6.89 is a generalization of the hydrostatic solution, which describes the evolution of just non-dispersive interfacial waves.

Often large-amplitude propagating internal waves are accompanied by surface waves or ripple patterns at the water surface due to the nonlinear effects of internal waves (Hutter et al., 2011). In oceans and large lakes, these ripple patterns increase the roughness of the surface of the water, allowing detection by SAR images 6.17. Due to the alternating pattern of quasiperiodic bright and dark bands against a gray background caused by the ripple patters created on the water surface, SAR images can detect the surface variation, which is directly correlated to the propagation of internal waves. In medium to small lakes, the small image resolution prevents the detection of high-frequency internal waves by SAR images. In large closed basins, standing internal waves (discussed in more detail in Section 7.1) can be detected by oscillations at the water surface. Lemmin et al. (2005) analyzed large-internal waves in lakes through surface-level variation; often surface waves associated with internal waves are typically 100 to 1000 times smaller than internal waves, depending on the density gradient.

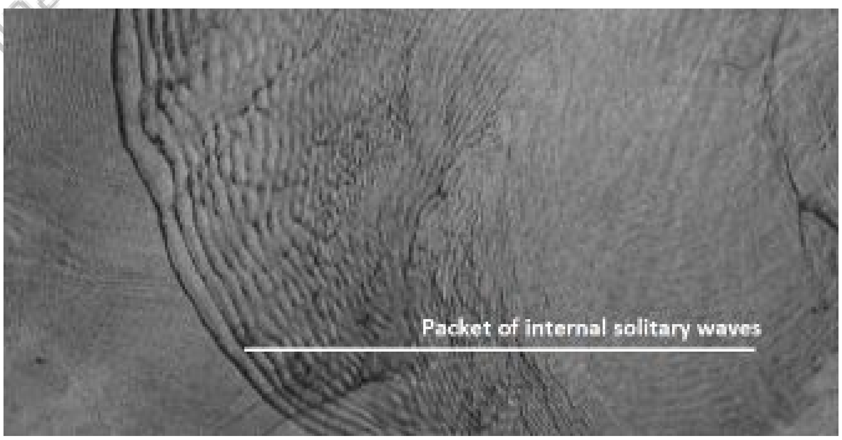

Figure 6.17 SAR image from the Gulf of Maine west of Cape Cod on 3 July 2008, at 22:26. The image shows the signatures of the internal wave packets. Assembled from (**?**)

A nonhydrostatic solution for an open upper boundary can be obtained similar to the one obtained previously for interfacial waves in section **??**.

☞ These solution is left for reader to solve. See exercises 6.7 and 6.8.

The solution of this problem is left to the reader to solve. After working through the algebra and assuming the non-hydrostatic case, the dispersion relation for an open boundary condition is given by

$$\omega^2 = \frac{g}{2(\beta_\rho\,\Gamma+1)}\left((\Gamma_1+\Gamma_2) \pm \sqrt{(\Gamma_1+\Gamma_2)^2 + 4\Gamma(\beta_\rho\,\Gamma-1)(\beta_\rho-1)}\right), \qquad (6.90)$$

in which $\beta_\rho = \varrho_1/\varrho_2$, $\Gamma_1 = \tanh(k\,h_1)$, $\Gamma_2 = \tanh(k\,h_2)$, and $\Gamma = \Gamma_1\,\Gamma_2$.

Note that the dispersion relation 6.90 provides four solutions of four orders in ω. The solution can be grouped into two modes, each group allowing the wave to travel in two directions. The wave modes are distinguished by the wave period but have many other differences in the wave property. The solution of a shorter period describes the barotropic mode, where the wave on the surface of the water is greater than the interfacial wave (Figure 6.18). Because the density difference in the interior of the water is very small compared to the water-air density difference, the internal waves have lower velocities and longer periods than the surface waves. Due to the effect of reduced gravity across the water body, surface waves travel more than 50 times faster than the speed of internal waves.

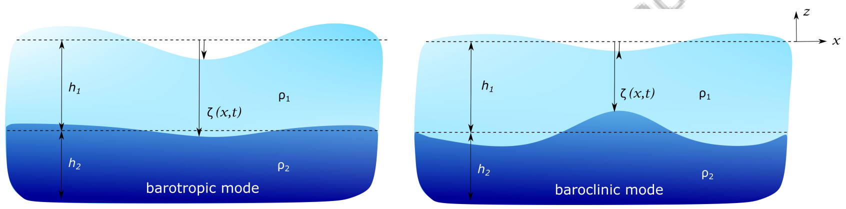

Figure 6.18 Surface and internal waves in barotropic and baroclinic mode.

The barotropic mode, also called the external, fast, and sinuous mode, has isobars parallel to isopycnals, lines of equal water density. The motion of the water behaves as if the water body is not stratified, presenting an in-phase response between the internal and surface waves (Figure 6.18).

The longer-period solution describes the baroclinic mode, which is also called the internal, slow, and varicose mode. The baroclinic mode has internal waves with amplitudes larger than those of surface waves (Figure 6.18). In this case, the isopycnals and isobars are inclined to each other, and the angle of this inclination depends on the stratification profile.

6.2.3 Interfacial wave energy

We may estimate the energy of internal seiches similarly to what we estimated in section **??** for surface waves, combining the contribution of kinetic and potential energies.

Assuming that the wave energy is equally partitioned between potential and kinetic energies along one wave cycle, the averaged kinetic energy of the internal wave can be defined as

$$E_{\mathrm{K}} = \frac{1}{T_{\mathrm{V1H1}}} \int_0^T \int_0^{\forall} \frac{\rho\, u^2}{2}\, \mathrm{d}\forall\, \mathrm{d}t, \tag{6.91}$$

in which

6.2.4 Interfacial seiche

In stratified closed basins, the wind that acts on the surface of the water favors the formation not only of a standing surface wave, but also a standing interfacial wave, which often has a wavelength comparable to the length of the lake (Mortimer, 1952). The wind introduces kinetic energy to the surface of the water. The transfer of momentum caused by wind stress pushes the surface water to the leeward shore, causing a surface displacement, called wind set-up. If wind stress is applied for a sufficient time, the horizontal pressure gradient increases and hypolimnion water accelerates in the upwind direction. Consequently, the hypolimnion and epilimnion layers are tilted, as shown in Figure 6.19. When the wind stops, the tilted layers flow back towards equilibrium. However, the momentum is considerable, and the equilibrium is overshot, resulting in a rocking motion about nodal points.

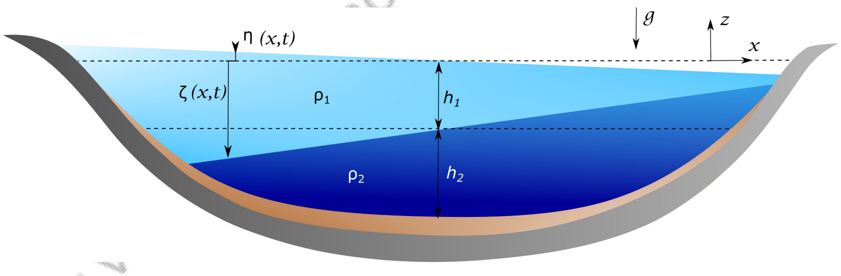

Figure 6.19 Sketch of a standing interfacial wave for the baroclininc mode formed a two-layer system.

Similarly to propagating waves, seiche can be classified as barotropic or baroclinic depending on the most dominant wave excited (Figure 6.20). The modes have properties similar to those described for propagating waves. The baroclinic mode has a higher internal amplitude compared to the surface amplitude, presenting an out-of-phase response.

Internal seiche in lakes has been observed primarily by (Thoulet, 1894) who observed a temperature oscillation with higher amplitude at middle depths. However, the first right interpretation was provided by Watson (1903) during a field campaign in Lake Loch Ness, which reported:

> *"I concluded from these observations, and others taken at different parts of the loch, that is an internal oscillation in the water – an internal seiche (...)"*
> E.R. Watson (1903).

Watson (1903) gave the first correct interpretation of internal waves, concluding that this temperature oscillation was caused by a uninodal baroclinc internal

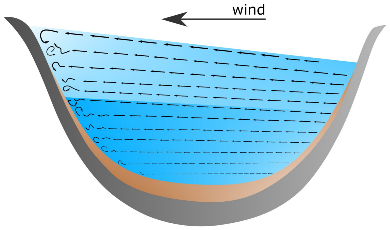

barotropic mode

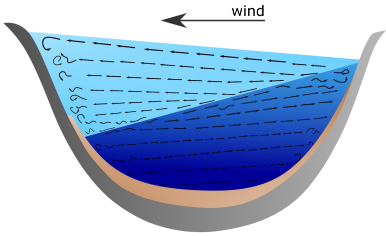

baroclinic mode

Figure 6.20 Barotropic and baroclininc modes for seiche waves in a closed basin.

wave in Lake Loch Ness. Motivated by his earlier observations, Watson (1904) developed the first equation to determine the internal wave period, a hydrostatic solution for a rectangular basin, known as Watson's equation (adapted Merian's equation). He observed that the periods of these oscillations found fair agreement between the observed and calculated periods. In those early years, Wedderburn and colleagues (Wedderburn, Williams, 1911; Wedderburn, 1912; Wedderburn, Young, 1915) provided guidelines to spread the knowledge about internal seiches in stratified basins that he called internal as "temperature seiches".

Although Wedderburn has notable improvements in theory and observations of internal seiches in closed basins, many limnologists disbelieved that internal waves could be important or even exist within thermal stratified lakes. The phenomenon was doubted until 1952, when finally Mortimer (1952) demonstrated its universality and importance in detail. He investigated the formation of large internal seiches generated by wind forcing in Lake Windermere analyzing a long time series of measurements with moored thermistor chains. In the isotherm analysis, Mortimer (1952) observed an internal seiche with periods of 18 h to 19 h that was well represented by the Watson's formula (deviation lower than 5%). He concluded that one of the main effects of the wind action in stratified basins is to generate internal seiches.

Mortimer had worked extensively on internal waves, providing many information about the physical processes of internal waves in lakes and reservoirs (Mortimer, 1950; **?**, 1952, 1953, 1955, 1971, 1979, 2004).

The evolution of internal seiches has been detected through temperature measurements () and field velocity data sets (). The oscillatory motion due to internal seiche, which most of the time is hidden by other fluctuations, is often reveled through the power spectral density obtained from Welch's methods (Welch, 1967), explained in detail in Chapter 5.5.1.

Due to the out-of-phase response between surface and internal waves during baroclininc modes, studies have detected large internal waves in lakes through surface level variation (Lemmin et al., 2005). Lemmin, D'Adamo (1997) Winds from the northeast were responsible for the generation of a large internal seiche with an amplitude of approximately 20 meters.

The mathematical solution for internal seiches is quite similar to that described in Sections 6.2.1 and 6.2.2 for propagating interfacial waves, with the exception that in a close basin, a new boundary condition is applied to describe wave reflection on the basin shore. Since the end wall of the basin allows the wave to move freely in the vertical direction, the wave is reflected pointing in the same direction, which means that an upward displaced pulse will also generate a reflected wave pointing upward (Figure 6.21).

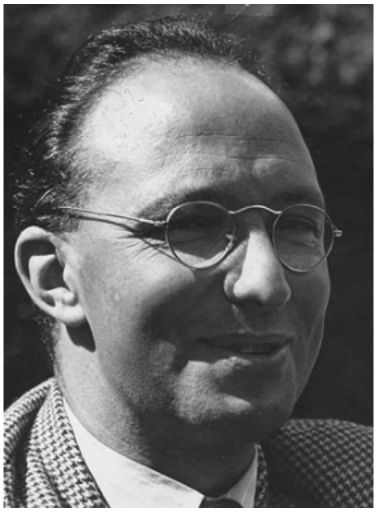

Clifford H. Mortimer (1911–2010, British) was born in Bristol (England). He was a zoologist and geneticist. During the Second World War, he was recruited to work in the Oceanographic Group of the Admiralty Research Laboratory, where we have gained sufficient knowledge in dynamic oceanography. Mortimer was elected to *Royal Society, London* and lifetime membership of the American Society of Limnology and Oceanography (ASLO). He worked extensively to interpret the physical processes that lie behind the lakes' data. His papers and books are landmarks in the understanding of the dynamics of internal waves.

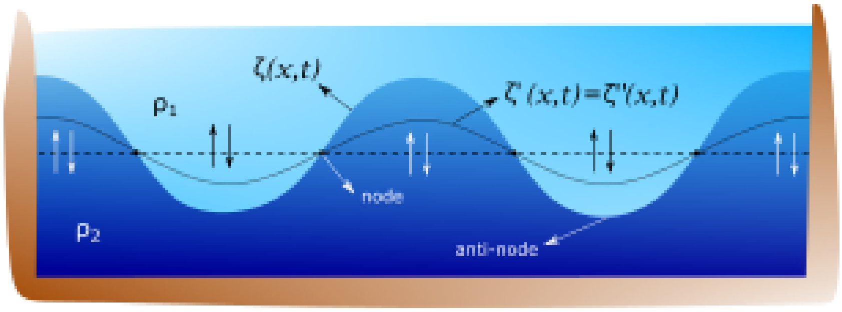

Figure 6.21 Standing interfacial wave formed by a superposition between interfacial waves ζ' and ζ''. Unlike Figure 6.19, the standing wave formed here has four nodes formed by two waves traveling on the right side of the tank and two reflected waves traveling in the opposite direction. Although fundamental internal seiche is often observed in lakes and reservoirs (Figure 6.19), higher horizontal baroclinic modes are also susceptible to being excited in stratified basins. Note that the superposition doubles the wave amplitude a_i.

The wave superposition modify the sinusoidal wave form 6.64. For a finite-sized longitudinal region, the wave is confined within the system, and the wave form must be described by a superposition of wave modes. This occurs only at certain frequencies and can be obtained from the trigonometric functions as

$$\zeta(x,t) = \zeta' + \zeta'' = a_i\, \mathrm{e}^{\mathrm{i}(kx-\omega t)} + a_i\, \mathrm{e}^{\mathrm{i}(-kx-\omega t)},$$

$$\zeta(x,t) = a_i\, (\mathrm{e}^{\mathrm{i}kx} + \mathrm{e}^{-\mathrm{i}kx})\, \mathrm{e}^{-\mathrm{i}\omega t} = 2a_i\, \mathrm{e}^{\mathrm{i}(kx-\omega t)}, \tag{6.92}$$

in which ζ' and ζ'' are waves traveling in opposite directions. a_i is the wave amplitude of ζ' and ζ''. Note that the constructive superposition between waves ζ' and ζ'' displaces an amount equal to twice the wave amplitude, $A_i = 2\, a_i$.

Taking into account the effect of lateral boundaries, the interfacial wave has maximum vertical displacement when

$$\zeta(x=0,t) = \zeta(x=L,t) = A_i, \tag{6.95}$$

in which L is the basin length and A_i is the wave amplitude (maximum vertical displacement assuming the wave form 6.92. From the wave form 6.92, the boundary conditions 6.95, and considering that the wave number is defined as $k = 2\pi/\lambda$, where λ is the wavelength, we obtain the condition for the standing wave:

$$\cos\frac{2\pi x}{\lambda}\, \mathrm{e}^{-i\omega t}\bigg|_{x=0,L} = 1. \tag{6.96}$$

Note that the only way to satisfy always the condition 6.96 is when

$$\frac{2\pi x}{\lambda}\bigg|_{x=0,L} = m\,\pi, \tag{6.97}$$

in which $m = 1,2,3,4,\ldots$ $(\pi, 2\pi, 3\pi, 4\pi, \ldots)$.

Trigonometric and Hyperbolic functions
The trigonometric and hyperbolic functions can be obtained assuming the following relations:

$$\mathrm{e}^{ix} = \cos x + i \sin x, \tag{6.93a}$$

$$\mathrm{e}^{x} = \cosh x + i \sinh x, \tag{6.93b}$$

resulting in

$$\sin x = \frac{\mathrm{e}^{ix} - \mathrm{e}^{-ix}}{2i}, \tag{6.94a}$$

$$\cos x = \frac{\mathrm{e}^{ix} + \mathrm{e}^{-ix}}{2}, \tag{6.94b}$$

$$\sinh x = \frac{\mathrm{e}^{x} - \mathrm{e}^{-x}}{2}, \tag{6.94c}$$

$$\cosh x = \frac{\mathrm{e}^{x} + \mathrm{e}^{-x}}{2}. \tag{6.94d}$$

Table 6.7 Trigonometric functions in terms of exponential functions.

Finally, by rearranging, we find that

$$\lambda = \frac{2L}{m}, \tag{6.98}$$

in which fundamental interfacial seiche (Figure 6.19) is always generated for $m = 1$. For higher horizontal modes, the wave length is shorter, resulting in higher m values. Figure 6.21 has $m = 4$ (four nodes).

Applying condition 6.98 to some general solution of the propagating wave, we get the solution for standing internal waves. For example, assuming the interfacial period obtained from the hydrostatic solution 6.74 (T) and applying the condition 6.98 gives us the following.

$$T = \frac{\lambda}{c_p} = \frac{2L}{m\, c_p}, \tag{6.99}$$

in which L is the basin length and c_p is the phase speed of the internal seiche. Note that the length of the basin for the internal seiche L depicted in Figure 6.21 is easily represented by the length of the basin at the water surface. However, increasing the complexity of the bathymetry (Figure 6.19), the basin length is not easily defined. In this case, the basin length L must be defined taking into account the depth in which the interfacial seiche is excited.

6.2.5 Fundamental internal seiche amplitude

The wave amplitude of the fundamental internal seiche may be estimated for the idealized two-layer rectangular box tank through the governing equation of motion, more specifically using the momentum equation for x-direction in a non-rotating frame of reference assuming shallow waters. We assume that the basin has only two layers and that the system is forced by an instantaneous wind shear stress (Figure 6.22). This model scheme is similar to the model derived in Section 6.2.1, but here we take into account the contribution of the wind stress u_* to the water surface.

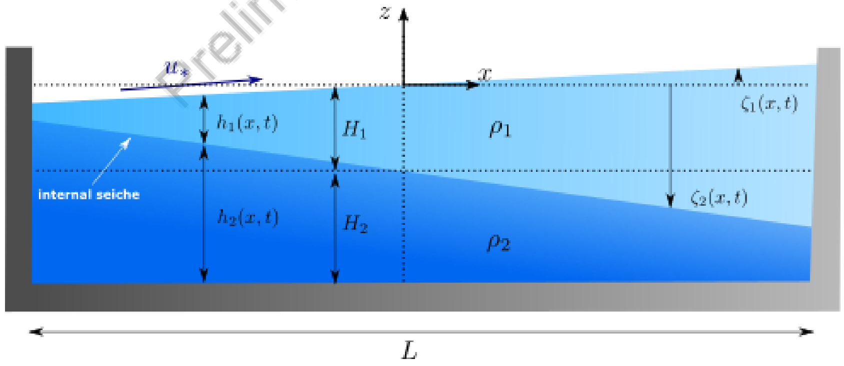

Figure 6.22 Stable two-layer system ($\rho_2 > \rho_1$) in a rectangular basin. The vertical coordinate is positive above the water surface. H is the thickness of the equilibrium layer, while h is the thickness of the local layer. η and ζ describe the interfacial movement between two fluids with different densities (referenced from $z = 0$).

Firstly we must derive the momentum equation in a non-rotating frame of reference for shallow-water waves. Basically, the solution is derived from the two-layer model.

The pressure distribution along the water column within each layer is as follows:

$$P_1(x,z,t) = \rho_1 g(-z+\eta), \tag{6.100a}$$

$$P_2(x,z,t) = \rho_1 g(\eta-\zeta) + \rho_2 g(-z+\zeta), \tag{6.100b}$$

in which P is the hydrostatic pressure, ρ is the fluid density, g is the acceleration of gravity, and η and ζ are the interfacial displacement of the surface and internal wave, respectively.

The momentum equation for x-direction can be applied for each layer (equation 6.62a). Unlike Equation 6.62a, an additional term is added on the right side accounting for the contribution of the wind stress u_* to the water surface.

$$\frac{\partial u_1}{\partial t} = -\frac{1}{\rho_1}\frac{\partial P_1}{\partial x} + \frac{u_*^2}{H_1}, \tag{6.101a}$$

$$\frac{\partial u_2}{\partial t} = -\frac{1}{\rho_2}\frac{\partial P_2}{\partial x}, \tag{6.101b}$$

where u is the horizontal velocity and H_1 is the thickness of the equilibrium upper layer.

Substituting equations 6.100 into 6.101 gives:

$$\frac{\partial u_1}{\partial t} = -g\frac{\partial \eta}{\partial x} + \frac{u_*^2}{H_1}, \tag{6.102a}$$

$$\frac{\partial u_2}{\partial t} = -\frac{\rho_1}{\rho_2} g\frac{\partial \eta}{\partial x} - \frac{\rho_2-\rho_1}{\rho_2} g\frac{\partial \zeta}{\partial x}. \tag{6.102b}$$

Let us write equation 6.102 in a more compact form, assuming that $\eta = \zeta_o$:

$$\frac{\partial u_i}{\partial t} = -g\ A_{i,j}\ \frac{\partial \zeta_j}{\partial x} + \frac{u_*^2}{H_1}\ \delta_{i1}, \tag{6.103}$$

in which $\delta_{i1} = 1$ only for $i = 1$, in all other cases $\delta_{i1} = 0$. The matrix $A_{i,j}$ is defined as:

$$A_{i,j} = \begin{pmatrix} 1 & 0 \\ \rho_1/\rho_2 & \Delta\rho/\rho_2 \end{pmatrix} \tag{6.104}$$

We can also apply the mass conservation equation 6.62c for each layer:

$$\frac{\partial}{\partial t}\Big(\eta-\zeta\Big) = -H_1\frac{\partial u_1}{\partial x}, \tag{6.105a}$$

$$\frac{\partial}{\partial t}\Big(\zeta - H\Big) = -H_2\frac{\partial u_2}{\partial x}. \tag{6.105b}$$

Rearranging the equations 6.105a and 6.105b, we find the following.

$$\frac{\partial u_1}{\partial x} = -\frac{1}{H_1}\frac{\partial \eta}{\partial t} + \frac{1}{H_1}\frac{\partial \zeta}{\partial t}, \tag{6.106a}$$

$$\frac{\partial u_2}{\partial x} = -\frac{1}{H_2}\frac{\partial \zeta}{\partial t}, \tag{6.106b}$$

which can also be written in a more compact form, as

$$\frac{\partial u_i}{\partial x} = -B_{i,j}\,\frac{\partial \zeta_j}{\partial t}, \tag{6.107}$$

where $\eta = \zeta_o$ and $B_{i,j}$ is:

$$B_{i,j} = \begin{pmatrix} 1/H_1 & -1/H_1 \\ 0 & -1/H_2 \end{pmatrix} \tag{6.108}$$

Note that the derivation of equations 6.103 in x and 6.107 in time and the combination of both solutions give us the following result.

$$\frac{\partial^2 \zeta_j}{\partial t^2} - g\,\frac{A_{i,j}}{B_{i,j}}\,\frac{\partial^2 \zeta_j}{\partial x^2} = 0, \tag{6.109}$$

which is similar to Equation 6.72. It is important to note that since wind stress does not vary along the horizontal plane direction, wind does not play any role in the internal wave speed. Shear stress only influences internal seiche growth.

Assuming that the horizontal velocity is zero when the interface present maximum vertical displacement, the expressions for the first two layers are as follows.

$$\frac{\partial \eta}{\partial x} = \frac{u_*^2}{g\,H_1}, \tag{6.110a}$$

$$\rho_1\,\frac{\partial \eta}{\partial x} = -(\rho_2 - \rho_1)\,g\,\frac{\partial \zeta}{\partial x}. \tag{6.110b}$$

Combining the equations 6.110a and 6.110b, we find

$$\frac{\partial \eta}{\partial x} = -\frac{\Delta\rho}{\rho_1}\,\frac{\partial \zeta}{\partial x} = \frac{u_*^2}{g\,H_1}$$

$$\frac{\partial \zeta}{\partial x} = -\frac{\rho_1}{g\Delta\rho}\,\frac{u_*^2}{H_1} = -\frac{u_*^2}{g'\,H_1}, \tag{6.111}$$

in which ζ is the internal seiche displacement (assuming the internal seiche mode of V1H1), g' is the reduced gravity, u_* is the wind stress and H_1 is the thickness of the equilibrium upper layer. Note that the negative sign in equation 6.111 is related to the sign convention.

Integrating equation 6.111 and applying the lateral boundary conditions:

$$\Delta\zeta(x = L/2) = a_2 \tag{6.112a}$$

$$\Delta\zeta(x = 0) = 0, \tag{6.112b}$$

in which a_2 is the initial internal seiche amplitude and L is the lake length ($L = 0$ is located in the lake center), we find that

$$\partial\zeta = -\int_0^{L/2} \frac{u_*^2}{g'\,H_1}\,\mathrm{d}x$$

$$a_2 = 0.5\,\frac{u_*^2\,L}{g'\,H_1}. \tag{6.113}$$

Multiplying both sides of 6.113 by $1/H_1$, we get

$$\frac{a_2}{H_1} = \frac{1}{2}W^{-1}, \tag{6.114}$$

in which W is the Wedderburn number. By compassion, we may state that for $W = 1$, $a_2 = H_1$, which indicates that metalimnetic water will increase to the surface. For higher values of W (in the literature, we may consider $W > 30$), the system is too stable to generate a large vertical displacement. We may observe that assuming $W = 30$, the vertical displacement would be of the order of 1% of the thickness of the epilimnion.

6.2.6 Interfacial seiche affected by Earth's rotation

Similarly to surface waves (Section 6.1.5), interfacial waves may also be affected by Earth's rotation, generating internal Kelvin and Poincaré waves. The geostrophic force is balanced by the adjustment of the pressure and velocity fields. When the system has lateral boundaries, the flow is trapped by the lateral boundaries, which strongly influence the velocity fields.

The Coriolis force is proportional to the speed of Earth's rotation, which may vary depending on the latitude due to circumference of the Earth. At the equator, the velocity is higher than near the poles, indicating a lower influence of the Coriolis force. In the Arctic, even shorter waves may be influenced by Earth's rotation, which indicates that even small lakes are susceptible to being affected by Coriolis forces.

Interfacial waves have another interesting behavior compared to surface waves affected by the Coriolis force. Since they have a much smaller velocity (higher period wave), the internal wave is more susceptible to be influenced by Earth's rotation (Bäuerle, 1994). Studies in Lake Uberlingen, which has a length of just a few kilometers, have identified the evolution of Poicaré internal waves (Bäuerle, 1994), one type of interfacial wave that is affected by Earth's rotation.

To identify when the Coriolis force can affect the propagation of internal waves, the Burger number Bu is often calculated (Antenucci, Imberger, 2003). The Burger number is defined as the ratio of the internal Rossby radius of deformation to a length scale L, which is often assumed to be the length of the basin. The Bu can be written as

$$Bu = \frac{R_\mathrm{R}}{L} \equiv \frac{c_p}{\omega_o L_p}, \tag{6.115}$$

Table 6.9 Burger numbers, Bu, for some lakes and reservoirs.

Basin	Latitude	Bu	Source
Lake Mono	38° 01’ N	2.07	MacIntyre et al. (2009)
Lake Babine	54° 45’ N	0.53	Farmer (1978)
Lake Kinneret	32° 50’ N	0.56	Antenucci et al. (2000)
Lake Zurich	47° 13’ N	0.14	Horn et al. (1986)
Alpnacher See	46° 57’ N	0.22	Münnich et al. (1992)
Sau Reservoir	41° 58’ N	2.64	Vidal et al. (2005)

in which $R_{\mathrm{R}} = c_p/\omega_o$ is the Rossby deformation radius, c_p is the non-rotating internal wave velocity, and $\omega_o = 2\Omega \sin\alpha$ is the inertial frequency, where $\Omega = 7.2921\ 10^{-5}$ rad/s is the rotation rate of the Earth (equation 6.116) and α is the latitude. In some cases, we approximate $\omega_o = 10^{-4}$ Hz

Rotation rate of the Earth
The rotation rate of Earth Ω, which is given in Hz, can be calculated as

$$\Omega = \frac{2\pi}{T_{\mathrm{rot}}}, \tag{6.116}$$

in which T_{rot} is one sidereal day (23 hours, 56 minutes, and 4.1 seconds), which represents the Earth rotation relative to the star position rather than the Sun.

Table 6.8 Rotation rate of the Earth.

For a Burger number larger than unity, gravity force dominates, and the modal models described previously are fully applicable. For Burger numbers smaller than unity, the internal waves are affected by Earth’s rotation, changing the internal wave velocity and the lateral distribution of the wave energy (Forcat et al., 2011). As observed, the influence of earth rotation does not depend only on the basin spatial scale, but also on the internal wave temporal evolution. In Table 6.9 we summarize some different values of Bu for internal waves obtained from different lakes and reservoirs where basin-scale internal waves have been detected.

Interfacial Kelvin wave

Internal Kelvin waves are large-scale waves that are affected by Earth’s rotation and have higher amplitude at the boundary, decaying exponentially with distance from the lakeshore, where the wave is trapped. As a result, this motion normally presents higher velocities close to the shore and lower ones in the interior of the basin. Another general behavior of Kelvin waves is that they can travel along the coast in one direction only. The pressure balances the Coriolis force, driving the wave along the horizontal boundaries, clockwise in the Southern Hemisphere, exactly as described by the surface wave in Section 6.1.5.

Studies have observed the formation of a fundamental internal Kelvin wave with a period of 78 h in Lake Geneva (Bauerle, 1985). The amphidromic system showed a clearly counterclockwise rotation (Figure **??**), indicating a Kelvin-type wave for the north hemisphere. Higher horizontal modes with opposite amphidromic phase, indicating mixed behaviors between Kelvin and Poicaré waves, have also been observed ().

Interfacial Poicaré wave

Poincaré waves are also large-scale waves, but they are not trapped at boundaries. This type of wave develops from cross-wise seiching, which becomes deflected by the Coriolis force (Wüest, Lorke, 2003). They are often observed in a counter-clockwise direction in the south hemisphere and by greater transverse velocities.

Exercises

Exercises for 6.1 Free surface wave

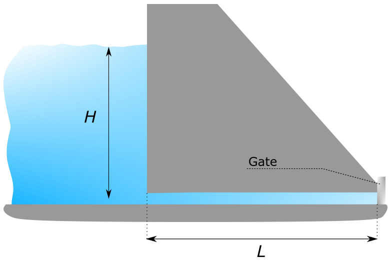

Figure 6.23 Reservoir.

P6.1 Torricelli's equation is derived from steady Bernoulli's principle and is expressed as

$$u = \sqrt{2gH},$$

in which g is the acceleration of gravity and H is the total depth of the water (Figure 6.23). However, the steady Bernoulli principle neglects the initial flow rate variation. Now consider the analysis of the initial transient flow applying the unsteady Bernoulli principle (equation 6.22) and find an expression of $u(t, H)$ for an initial transient flow.

P6.2 Multiplying the Navier-Stokes equation (equation 2.49) by velocity and using the polarization relations for surface waves show that the energy flux of surface waves is given by equation 6.50.

P6.3 Based on solution for shallow water waves, presented in table 6.3, shows the detailed simplification to obtain equation 6.30 and apply the general solution to obtain the dispersion relation for shallow water waves. Finally, compare the solution with the general solution (equation 6.36)

P6.4 Find the dispersion relation for Poicaré waves, looking for plane waves. Start with the linear shallow-water equation and assume that the Coriolis frequency f and the water depth H are constants. TIP: align $y-$axis with the wave crest, so $\frac{\partial .}{\partial y} = 0$

Exercises for 6.2 Interfacial wave in a two-layer system

P6.5 The phase speed of the interfacial wave under a shallow water system is given by

$$c_p = \sqrt{g' \frac{H_1 \, H_2}{H_1 + H_2}},$$

where g' is the reduced gravity and H_1 and H_2 are the thicknesses of the upper and lower layers. Based on this generalization, find the phase speed of the free surface wave assuming that the upper layer (layer 1) is the air layer above the water surface.

P6.6 From the dispersion relation for interfacial waves (nonhydrostatic solution), find the dispersion relation for surface waves by assuming that the upper layer is formed by an "air layer".

P6.7 Based on the hydrostatic solution for the interfacial wave presented in Section 6.2.1, solve the same problem assuming that the surface waves, represented by a sinusoidal function $\eta(x,t)$, propagate at the water surface.

P6.8 Based on the non-hydrostatic solution for the interfacial wave presented in section 6.2.2, solve the same problem assuming that the surface waves, represented by a sinusoidal function $\eta(x,t)$, propagate at the water surface.

P6.9 Considering a 10 m deep and 2 km long two-layer stratified lake, with a epilimnion located approximately 5 m above the water surface, what is the highest horizontal baroclininc mode (internal seiche) supported by the lake ? Explain why above this limit we may not expect the formation of standing internal waves?

P6.10 Assuming a 27 m deep stratified lake of two layers ($\Delta\rho/\rho = 0.0025$), in which the thermocline is 7 m above the surface of the water, find the Rossby deformation radius. Explain what this value means.

Chapter 7

Internal Wave in Continuous Stratified Fluid

7.1 Internal Seiche

Oceans, lakes, and reservoirs are often continuously stratified. In these environments, stratification can be represented by a collection of homogeneous layers, separated by multiple density jumps (Maas, 2005). Exactly as in a two-layer system, discussed in Section 6.2, all density jumps are able to support the evolution of internal waves, in which each layer will not flow separately. An internal wave propagating to the right side of the upper layer pushes the lower layer in the same direction, creating a cascading effect (Hazewinkel, 2010). The wave propagates obliquely into the system rather than forward along the density interface. In this case, internal waves can propagate horizontally and vertically along the water column. Thus, the phase velocity is not necessarily aligned with the group velocity, implying that the wave crests may move upward while its energy modes downward.

According to Pannard et al. (2011), standing internal waves in closed basins can be classified by nodal points on the vertical (V) and horizontal (H) components, VnHm[1], in which n and m are the number of nodes of each component. Internal waves with higher vertical modes are only excited when the density stratification patterns promote a higher number of layers with different density differences. However, even in a continuous stratification condition, the fundamental internal wave may be dominant or even be the only mode generated. The occurrence of higher vertical modes is related, in addition to the unequal differences in density between layers, resonance with wind forcing () and sloping topography (). The fundamental internal seiche mode (V1) is characterized by the epilimnion and hypolimnion layers moving in opposite directions, with shear concentrated in the pycnocline. The second vertical mode (V2) is associated

---

[1] This nomenclature can be presented in different forms. For example, a V3H2 internal wave is called by Sutherland (2010) as the 2-3 mode. Hutter et al. (2011) call this same internal wave pattern as vertical mode 3 and horizontal mode 2.

with a change in the thickness of the metalimnion, a strong tilt of the epilimnion interface, a large shear across the base of the epilimnion, and an undisturbed hypolimnion.

Second-vertical-mode internal seiches are characterized by the epilimnion and hypolimnion moving in the same direction, with a balancing flow in the metalimnion flowing in the opposite direction, creating shear stress at both the top and bottom of the metalimnion. Although higher vertical modes were rarely reported until the end of the 18th century, nowadays it is accepted that high vertical modes are often excited in lentic water bodies. Data from Mortimer (1971) based exclusively on large lakes concluded that higher vertical modes were not frequently observed. However, Roget et al. (1997) stated that the formation of higher vertical modes is more evident in small lakes where the metalinstake occupies a relatively higher proportion of the total lake depth than in large closed basins.

Hutter et al. (2011) showed that the second vertical baroclinic modes are caused not just by diffusive metalimnion but also by the presence of a second pycnocline. Furthermore, Wiegand, Chamberlain (1987) observed that after a strong wind event, the first vertical mode generated was typically followed by excitation and dominance of a second vertical mode baroclinic wave. Boehrer et al. (2000) reported higher vertical mode due to strong wind events in Lake Constance, where the V1H1 mode is dominant. Münnich et al. (1992) pointed out that wind oscillations also contribute to excite higher vertical baroclinc waves. Although higher internal wave modes have been extensively studied in recent years, the influence of temperature profiles, mean depth, shape, morphology, meteorological conditions, and its resonances on the excitation of higher vertical modes is not yet well understood.

An interesting observation of higher vertical modes is related to the structure of each baroclinic wave. As shown by Salvadè et al. (1988), the nodal lines of each baroclinic wave are frequently shifted due to the fact that each baroclinic mode has different vertical boundaries defined by the shore of the basin. Thus, different baroclinic modes present different nodal positions. As a result, the effect of internal waves may be different along the reservoir, depending on the depth of each layer.

Another interesting observation is that a higher vertical mode normally requires less energy compared to the fundamental baroclinic mode (V1). This can be interpreted by a process called WKB normalization, an initialism for Wentzel, Kramers, and Brillouin that was first used for a semi-classical calculation in quantum mechanics. According to Sutherland (2010), WKB renormalization is a coordinate change procedure that allows for the transformation of the structure of internal waves in a uniformly stratified fluid to those in a non-uniformly stratified fluid. Actually, the WKB is an approximate solution to a time-independent differential equation. This analysis shows that the energy of hydrostatic baroclinic modes at any depth is proportional to the Brunt-Väisälä frequency. Thus, although higher vertical modes present longer periods and higher amplitudes compared to fundamental modes, higher modes normally suggest lower internal wave energy due to the density structure.

Large thermal oscillations at depths much deeper than the pycnocline have already been observed by Mortimer (1950). This may explain the eddy diffusion of heat and nutrient content in the benthic boundary layer. The vertical and horizontal modes are completely independent, internal waves can be generated with a wide range of modes, and some combinations are shown in Figure 7.1.

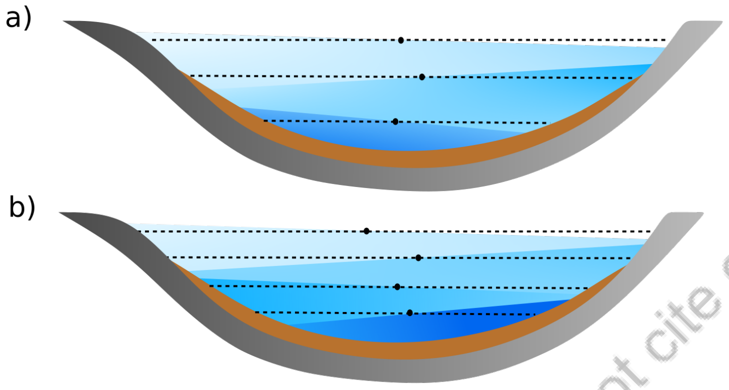

Figure 7.1 Schematic view of two types of higher internal wave modes in a closed basin: a) V2H1 and b) V3H1 with free surface. Black dots represent nodal points.

7.1.1 Hydrostatic three-layer model

Before creating internal waves in a multilayer system, which allow the formation of infinite numbers of internal waves with higher vertical mode internal (for example, the mode V3H1 illustrated in Figure 7.1b), we will demonstrate how we can extend the solution for a two-layer system, presented in Section 6.2.1, to three layers (Figure 7.1a).

Basically, the solution is obtained by solving the system of governing equations for shallow water flow, the same system of equations 6.62. However, differently from the two-layer cases, s now can vary from 1 to 3.

The pressure distribution in each layer is similar to the pressure distribution of the two-layer system, which was given by equations 6.65 and 6.66. The only difference is that now we must define an additional function for the third layer:

$$P_3(x,z,t) = \rho_1 g(\zeta_1 - \zeta_2) + \rho_2 g(\zeta_2 - \zeta_3) + \rho_3 g(\zeta_3 - z) \qquad -H \leq z \leq \zeta_3, \tag{7.1}$$

in which $H = H_1 + H_2 + H_3$ is the total water depth.

Applying the pressure functions to the momentum equations 6.62a for all the three layer, gives

$$\frac{\partial u_1}{\partial t} = -g\frac{\partial \zeta_1}{\partial x} \tag{7.2a}$$

$$\frac{\partial u_2}{\partial t} = -\frac{\rho_1}{\rho_2}\,g\frac{\partial \zeta_1}{\partial x} - \frac{\rho_2-\rho_1}{\rho_2}\,g\frac{\partial \zeta_2}{\partial x} \tag{7.2b}$$

$$\frac{\partial u_3}{\partial t} = -\frac{\rho_1}{\rho_3}\,g\frac{\partial \zeta_1}{\partial x} - \frac{\rho_2-\rho_1}{\rho_3}\,g\frac{\partial \zeta_2}{\partial x} - \frac{\rho_3-\rho_2}{\rho_3}\,g\frac{\partial \zeta_3}{\partial x}. \tag{7.2c}$$

The second equation is derived from the mass conservation equation for all the three layers (equation 6.62c) can be obtained similarly to found in the two-layer case (equation 6.69), except now we have three-layers:

$$\int_0^{-h_1} \mathrm{d}\frac{\partial \zeta}{\partial t} = -\frac{\partial u_1}{\partial x}\int_0^{-h_1} \mathrm{d}z \tag{7.3a}$$

$$\int_{-h_1}^{-(h_1+h_2)} \mathrm{d}\frac{\partial \zeta}{\partial t} = -\frac{\partial u_2}{\partial x}\int_{-h_1}^{-(h_1+h_2)} \mathrm{d}z \tag{7.3b}$$

$$\int_{-(h_1+h_2)}^{-H} \mathrm{d}\frac{\partial \zeta}{\partial t} = -\frac{\partial u_3}{\partial x}\int_{-(h_1+h_2)}^{-H} \mathrm{d}z \tag{7.3c}$$

$$\frac{\partial u_1}{\partial x} = \frac{1}{h_1}\left(\frac{\partial \zeta_2}{\partial t} - \frac{\partial \zeta_1}{\partial t}\right) \tag{7.4a}$$

$$\frac{\partial u_2}{\partial x} = \frac{1}{h_2}\left(\frac{\partial \zeta_3}{\partial t} - \frac{\partial \zeta_2}{\partial t}\right) \tag{7.4b}$$

$$\frac{\partial u_3}{\partial x} = -\frac{1}{h_3}\frac{\partial \zeta_3}{\partial t} \tag{7.4c}$$

7.1.2 Hydrostatic multi-layer model

Motivated by the case of the three-layer system, we can extend the number of layers to have a solution for a $N-$layred system.

Expanding the linearized momentum equation 6.62b to N-layers, we have for layer i

$$\frac{\partial u_i}{\partial t} = -\frac{1}{\rho_i}\frac{\partial P_i}{\partial x}, \tag{7.5}$$

which the subscript $i = 1,\ldots,N$ describes each layer of the N-layered multi-layer system, u_i is the horizontal velocity in the layer i, ρ_i is the density of water in the layer i, and P_i is the hydrostatic pressure in the layer i.

The hydrostatic pressure P_i is described by

$$P_i(z,x,t) = P_o + \underbrace{\boxed{g\sum_{j=1}^{i-1}\rho_j(\zeta_j-\zeta_{j+1})}}_{\text{above layer } i} + \underbrace{\boxed{g\rho_i(\zeta_i - z)}}_{\text{in layer } i}, \tag{7.6}$$

in which P_o is the atmospheric pressure. Note that i is a fixed index (which stays at i-layer), while j describes the contribution of other layers to the dynamic of i-layer.

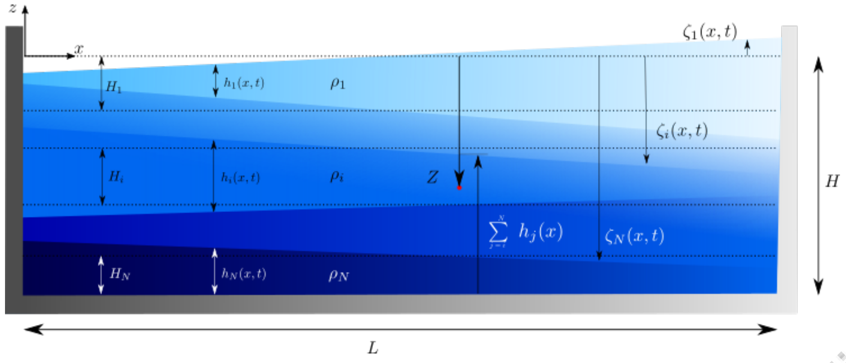

Figure 7.2 Stable N-layer system in a rectangular basin ($\rho_1 < \rho_j < \rho_N$). The vertical coordinate is positive above the water surface. H is the thickness of the equilibrium layer, while h is the thickness of the local layer. ζ describes interfaces between two fluids with different densities (referenced from $z = 0$). The index i indicates the analyzed layer (as an example, we defined the position of the red dot as our point of interest). The index j represents all the layers that affect the pressure in the layer i, which are all the layers above i.

Substitution of equation 7.6 into 7.5 and assuming that P_o is constant throughout the lake give us

$$\frac{\partial u_i}{\partial t} = -\frac{g}{\rho_i}\left(\sum_{j=1}^{i}(\rho_j - \rho_{j-1})\,\frac{\partial \zeta_j}{\partial x}\right). \tag{7.7}$$

in which $\rho_0 \approx 0$.

The second equation is obtained from the mass conservation. Using the three-layer case is easy to find a relationship to N layers:

$$\frac{\partial u_i}{\partial x} = \frac{1}{h_i}\frac{\partial}{\partial t}\left(\zeta_{i+1} - \zeta_i\right), \tag{7.8}$$

in which when $i + 1 > N$, $\zeta_{i+1} = 0$.

Deriving equation 7.7 in x and equation 7.8 in time and combining both equations to eliminate horizontal velocity, we find the following equation

$$\frac{\partial^2}{\partial t^2}\left(\zeta_{i+1} - \zeta_i\right) + \frac{g\,H_i}{\rho_i}\sum_{j=1}^{i}\left((\rho_j - \rho_{j-1})\,\frac{\partial^2 \zeta_j}{\partial x^2}\right), \tag{7.9}$$

in which depending on the number of layers, a set number of governing equation will be available to define all solutions.

7.1.3 Continuous stratification non-hydrostatic model

Our first step is to derive the governing equation for non-rotating and non-viscous shallow water flow. Unlike our previous solution for multi-layer system, presented in Section 7.1.2, now we do not apply the governing equation separately for each layer. Thus, from the conservation equations 6.62a to 6.62c in Cartesian coordinates, we have the following.

$$\overline{\rho}\frac{\partial u}{\partial t} = -\frac{\partial p}{\partial x}, \tag{7.10a}$$

$$\overline{\rho}\frac{\partial v}{\partial t} = -\frac{\partial p}{\partial y}, \tag{7.10b}$$

$$\overline{\rho}\frac{\partial w}{\partial t} = -\frac{\partial p}{\partial z} - g\rho, \tag{7.10c}$$

$$\frac{\partial u}{\partial x} + \frac{\partial v}{\partial y} + \frac{\partial w}{\partial z} = 0, \tag{7.10d}$$

in which $\mathbf{u} = (u, v, w)$ is the velocity field, p is the pressure, and g is the gravitational acceleration. It is important to note that we already have linearized the governing equations, which assumes just small-amplitude internal waves. As discussed before, the linearization procedure neglects the non-linear term from the governing equations by expanding the equation in Taylor's series and assuming that wave amplitude is much smaller than the wavelength ($a \ll \lambda$). The linearization procedure can be done formally in a way similar to what we have done in Section 6.1.1 for surface waves.

First, we can derive the equations 7.10a and 7.10b from x and y, respectively:

$$\overline{\rho}\frac{\partial}{\partial x}\frac{\partial u}{\partial t} = -\frac{\partial^2 p}{\partial x^2}, \tag{7.11a}$$

$$\overline{\rho}\frac{\partial}{\partial y}\frac{\partial v}{\partial t} = -\frac{\partial^2 p}{\partial y^2},, \tag{7.11b}$$

assuming that u and v are characterized by a smooth function, we may combine the equations 7.11a and 7.11b as

$$\overline{\rho}\frac{\partial}{\partial t}\left(\frac{\partial u}{\partial x} + \frac{\partial v}{\partial y}\right) = -\left(\frac{\partial^2 p}{\partial x^2} + \frac{\partial^2 p}{\partial y^2}\right). \tag{7.12}$$

Substitution of the mass conservation equation 7.10d into equation 7.12 and deriving consecutively in z and time give us

$$-\overline{\rho}\frac{\partial}{\partial t}\left(\frac{\partial w}{\partial z}\right) = -\left(\frac{\partial^2 p}{\partial x^2} + \frac{\partial^2 p}{\partial y^2}\right).$$

$$\overline{\rho}\frac{\partial^2}{\partial t^2}\left(\frac{\partial^2 w}{\partial z^2}\right) = \frac{\partial}{\partial t}\frac{\partial}{\partial z}\left(\frac{\partial^2 p}{\partial x^2} + \frac{\partial^2 p}{\partial y^2}\right). \tag{7.13}$$

Deriving in time the momentum equation in z-direction, we have

$$\overline{\rho}\frac{\partial^2 w}{\partial t^2} = -\frac{\partial}{\partial t}\frac{\partial p}{\partial z} - g\frac{\partial \rho}{\partial t}. \tag{7.14}$$

Recall that $\overline{\rho}$ is a function of z only, different from $\rho(\mathbf{x}, t)$. The last term of the equation 7.14 can be obtained from the mass conservation equation. From the

Reynolds decomposition, we can split the contribution of fluid density into mean and perturbation components ($\varrho(\mathbf{x},t) = \overline{\rho} + \rho$), and we find the following.

$$\frac{\partial \varrho}{\partial t} + u_i \frac{\partial \varrho}{\partial x_i} = 0,$$

$$\frac{\partial \rho}{\partial t} + u_i \frac{\partial \rho}{\partial x_i} = -w \frac{\partial \overline{\rho}}{\partial z}, \tag{7.15}$$

in which ρ is the density perturbation and $\overline{\rho}$ is the density in hydrostatic equilibrium.

Equation 7.15 can be linearized similarly to that described in Section 6.1.1 for a surface wave. First, equation 7.15 can be presented in non-dimensional form using the following transformation variables.

$$\rho = \tilde{\rho}\,\rho^* \qquad \overline{\rho} = \rho_o\,\overline{\rho}^*, \tag{7.16a}$$

$$u_i = a/T\,u_i^* \qquad x_i = \lambda x_i^* \qquad t = T t^*, \tag{7.16b}$$

in which T is the wave period, a is the wave amplitude, λ is the wavelength, and ρ_o and $\tilde{\rho}$ are the density of the fluid unperturbed and perturbed, respectively. The variables denoted by * are dimensionless. Substituting equations 7.16 into 7.15 gives us

$$\frac{\tilde{\rho}}{T}\frac{\partial \rho^*}{\partial t^*} + \frac{a\,\tilde{\rho}}{T\lambda} u_i^* \frac{\partial \rho^*}{\partial x_i^*} = -\frac{a\rho_o}{T\lambda} w^* \frac{\partial \overline{\rho}^*}{\partial z^*},$$

$$\frac{\partial \rho^*}{\partial t^*} + \overset{a \ll \lambda}{\cancel{\frac{a}{\lambda}}}\; u_i^* \frac{\partial \rho^*}{\partial x_i^*} = -\frac{a\,\rho_o}{\lambda\,\tilde{\rho}} w^* \frac{\partial \overline{\rho}^*}{\partial z^*}, \tag{7.17}$$

in which the term of order $\mathcal{O}(a/\lambda)$ can be neglected for small-amplitude waves (a/λ). Note that we cannot neglect the last term of 7.18 because even though $a \ll \lambda$, $\rho_o \gg \tilde{\rho}$.

Considering the linearization procedure and rewriting equation 7.18 in terms of dimensional variables, we obtain the following.

$$\frac{\partial \rho}{\partial t} = -w \frac{\partial \overline{\rho}}{\partial z}, \tag{7.18}$$

Substituting equation 7.18 into 7.14, we have

$$\overline{\rho}\frac{\partial^2 w}{\partial t^2} = -\frac{\partial}{\partial t}\frac{\partial p}{\partial z} + g w \frac{\partial \overline{\rho}}{\partial z}, \tag{7.19}$$

Rearranging equation 7.19, we find that

$$\frac{\partial^2 w}{\partial t^2} - w \underbrace{\frac{g}{\overline{\rho}}\frac{\partial \overline{\rho}}{\partial z}}_{-N^2} = -\frac{1}{\overline{\rho}}\frac{\partial}{\partial t}\frac{\partial p}{\partial z}, \tag{7.20}$$

in which N is the buoyancy frequency, defined by 2.15.

Substituting equation 7.20 into 7.13 gives us

$$\frac{\partial^2}{\partial t^2}\left(\frac{\partial^2 w}{\partial z^2}\right) = \frac{1}{\rho}\frac{\partial}{\partial t}\frac{\partial}{\partial z}\left(\frac{\partial^2 p}{\partial x^2} + \frac{\partial^2 p}{\partial y^2}\right),$$

$$= \frac{1}{\rho}\left(\frac{\partial^2}{\partial x^2}\left(\frac{\partial}{\partial t}\frac{\partial p}{\partial z}\right) + \frac{\partial^2}{\partial y^2}\left(\frac{\partial}{\partial t}\frac{\partial p}{\partial z}\right)\right),$$

$$= \underbrace{\frac{1}{\rho}\frac{\partial}{\partial t}\frac{\partial p}{\partial z}}_{\text{equation 7.20}}\left(\frac{\partial^2}{\partial x^2} + \frac{\partial^2}{\partial y^2}\right),$$

Some manipulations, such as the change in derivative order, are not trivial and are only possible for a smooth velocity field function. Rearranging this equation, we may find that

$$\frac{\partial^2}{\partial z^2}\left(\frac{\partial^2 w}{\partial t^2}\right) = -\left(\frac{\partial^2 w}{\partial t^2} + N^2 w\right)\left(\frac{\partial^2}{\partial x^2} + \frac{\partial^2}{\partial y^2}\right),$$

$$\frac{\partial^2}{\partial t^2}\underbrace{\frac{\partial^2 w}{\partial x_i^2}}_{\text{total laplacian}} + N^2\underbrace{\left(\frac{\partial^2 w}{\partial x^2} + \frac{\partial^2 w}{\partial y^2}\right)}_{\text{horizontal laplacian}} = 0, \tag{7.21}$$

in which $x_i = (x, y, z)$. When the system is unstratified ($N = 0$), the laplacian $\nabla^2 w = 0$ (irrotational motion), which indicates the formation of surface gravity waves only.

Taking into account only the x-z plane, we can obtain the bidimensional form of the internal wave equation (Equation 7.21)

$$\frac{\partial^2}{\partial t^2}\frac{\partial^2 w}{\partial x_i^2} + N^2\frac{\partial^2 w}{\partial x^2} = 0. \tag{7.22}$$

The general solution of 7.22 can have the form of a plane wave.

$$w(x, z, t) = W(z)\,\mathrm{e}^{-i(kx-\omega t)}, \tag{7.23}$$

in which w is the vertical velocity, k is the waver number in x-direction, and ω is the wave frequency. The solution of the three-dimensional equation can have a different wave number for all directions x, y, and z. Furthermore, it is important to note that the solution is a composition of several components of various frequencies ω_j.

Substitution of the general solution 7.23 into equation 7.22 leads to the ordinary differential equation of the internal wave, also known as modified **Taylor-Goldstein equation**:

$$\frac{\partial^2}{\partial t^2}\left(\frac{\partial^2 w}{\partial x^2} + \frac{\partial^2 w}{\partial z^2}\right) + N^2\frac{\partial^2 w}{\partial x^2} = 0$$

Internal wave equation

Table 7.1 Non-Boussinesq internal wave.

$$\frac{\partial^2}{\partial t^2}\left(i^2\, k^2 W(z)\,\mathrm{e}^{-i(kx-\omega t)} + \frac{\partial^2 W}{\partial z^2}\mathrm{e}^{-i(kx-\omega t)}\right) + N^2 i^2 k^2 W(z)\,\mathrm{e}^{-i(kx-\omega t)} = 0$$

$$-k^2 W(z)\, i^2\omega^2 + i^2\omega^2\frac{\partial^2 W}{\partial z^2} - N^2 k^2 W(z) = 0$$

$$k^2 W(z) - \frac{\partial^2 W}{\partial z^2} - \frac{N^2}{\omega^2}k^2 W(z) = 0$$

$$\frac{\partial^2 W}{\partial z^2} + \left(\frac{N^2}{\omega^2} - 1\right)k^2 W(z) = 0$$

$$\frac{\partial^2 W}{\partial z^2} + \left(\frac{N^2-\omega^2}{\omega^2}\right)k^2 W(z) = 0. \tag{7.24}$$

Taking into account the boundary condition in the vertical direction,

$$w(x, z=0, t) = W(z=0)\; e^{-i(kx-\omega t)} = 0 \quad W(z=0) = 0, \tag{7.25a}$$

$$w(x, z=-H, t) = W(z=-H)\; e^{-i(kx-\omega t)} = 0 \quad W(z=-H) = 0, \tag{7.25b}$$

and combining with equation 7.24, the differential equation results in a Sturm-Liouville problem, similar to the solution for the hydrostatic multi-layer system, equation 7.9. For some special cases, equation 7.24 has an analytical solution; however, for an arbitrary N^2 profile, the solution should be found numerically.

In both equations, the solution is formed by a set of eigenvalues k_n and eigenfunctions W_n. The eigenfunctions W_n of the Sturm-Liouville system, corresponding to different eigenvalues k_n, in which W_n''s must be orthogonal to each other:

$$\int_{-H}^{0} W_1(z)\, W_2(z)\,\mathrm{d}z = 0. \tag{7.26}$$

Orthogonality

To prove the orthogonality, we may consider two different solutions of equation 7.24:

$$\frac{\partial^2 W_j}{\partial z^2} + \left(\frac{N^2-\omega_j^2}{\omega_j^2}\right)k^2 W_j = 0. \tag{7.27}$$

Multiplying the equation 7.27 by W_i and integrating into z-direction along the water column gives us

$$\underbrace{\int_{-H}^{0}\frac{\partial^2 W_j}{\partial z^2}\, W_i\,\mathrm{d}z}_{\text{integration by parts}} + \int_{-H}^{0}\left(\frac{N^2-\omega_j^2}{\omega_j^2}\right)k^2\, W_j\, W_i\,\mathrm{d}z = 0. \tag{7.28}$$

The first term on the left-hand side of equation 7.28 can be rearranged by integration by parts and assuming boundary conditions 7.25:

$$\int_{-H}^{0} \frac{\partial^2 W_j}{\partial z^2} W_i \,\mathrm{d}z = \frac{\partial W_j}{\partial z} W_i \Big|_{-H}^{0} - \int_{-H}^{0} \frac{\partial W_j}{\partial z} \frac{\partial W_i}{\partial z} \,\mathrm{d}z$$

$$= \cancelto{=0}{\frac{\partial W_j}{\partial z} W_i \Big|_{-H}^{0}} - \left(\cancelto{=0}{W_j \frac{\partial W_i}{\partial z} \Big|_{-H}^{0}} - \int_{-H}^{0} W_j \frac{\partial^2 W_i}{\partial z^2} \,\mathrm{d}z \right)$$

$$\int_{-H}^{0} \frac{\partial^2 W_j}{\partial z^2} W_i \,\mathrm{d}z = \int_{-H}^{0} W_j \frac{\partial^2 W_i}{\partial z^2} \,\mathrm{d}z$$

Substituting into the equation 7.28, we have

$$\int_{-H}^{0} W_j \frac{\partial^2 W_i}{\partial z^2} \,\mathrm{d}z + \int_{-H}^{0} \left(\frac{N^2 - \omega_j^2}{\omega_j^2} \right) k^2 \, W_j \, W_i \,\mathrm{d}z = 0. \tag{7.29}$$

Similarly, we can change the indexes i to j and vice versa, leading to

$$\int_{-H}^{0} W_i \frac{\partial^2 W_j}{\partial z^2} \,\mathrm{d}z + \int_{-H}^{0} \left(\frac{N^2 - \omega_i^2}{\omega_i^2} \right) k^2 \, W_i \, W_j \,\mathrm{d}z = 0. \tag{7.30}$$

Subtracting equation 7.29 from equation 7.30, we get

$$\int_{-H}^{0} \left(\frac{N^2}{\omega_j^2} - \frac{N^2}{\omega_i^2} \right) k^2 W_i W_j \,\mathrm{d}z = 0,$$

$$\left(\frac{1}{\omega_j^2} - \frac{1}{\omega_i^2} \right) k^2 \int_{-H}^{0} N^2 \underbrace{W_i \, W_j}_{\text{orthogonal}} \,\mathrm{d}z = 0, \tag{7.31}$$

which indicates an orthogonality relation modulated by the buoyancy frequency $N(z)$, which can be included in the eigenvectors W_n.

Boundary condition
Note that the solution of the vertical velocity converges to zero for each mode at the bottom boundary. However, because of the discrete value of the wave period, the solution does not exactly match the zero condition. Thus, one approach is to find the place where the solution at the bottom crosses the y-axis.

Table 7.2 Numerical approach.

Internal wave modes and orthogonal decomposition

The internal wave modes provide a valuable tool for describing the energy content of each mode, which may help to describe the vertical and horizontal structure of the response of lakes to wind forcing. The solution of 7.24 describes the nature of the oscillatory motion in water flow. From the velocity profiles, the solution decomposes the profile into normal modes, providing vertical and horizontal velocity profiles associated with different vertical baroclinic modes. The decomposition is defined by the projection of the point onto the coordinate axis in the space in which the vertical velocity at the boundary conditions for all vertical modes is equal to zero.

To find the numerical solution of W, we first discretize the differential equation 7.24,

$$\frac{W_i - 2W_{i-1} + W_{i-2}}{\Delta z^2} + k^2\left(\frac{N_{i-1}^2}{\omega^2} - 1\right) W_{i-1} = 0$$

$$W_i = -W_{i-2} + \left(2 - \Delta z^2 k^2\left(\frac{N_{i-1}^2}{\omega^2} - 1\right)\right) W_{i-1} = 0, \tag{7.32}$$

in which Δz is the vertical resolution of the model, $k = 2\pi/\lambda$ is the wave number, N is the buoyancy frequency, and $\omega = 2\pi/T$ is the angular frequency of the wave, where λ and T are the wavelength and wave period, respectively.

To find the solution of equation 7.32 for each vertical mode, we must consider the initial and boundary conditions 7.25a ($W_{z=0} = 0$). For a first approximation, we assume $W_{z=\Delta z} = 1$ and a small internal wave period.

As the solution progresses to the next iteration step based on the increase in the wave period, the profile of W becomes closer to the solution. The final solution of the first mode is obtained when the last value of W satisfies the boundary condition at the bottom 7.25b, in which $W_{z=-H} = 0$ (Figure 7.3).

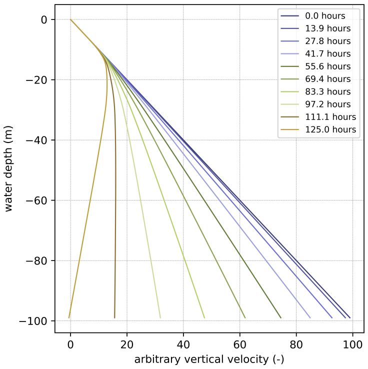

Figure 7.3 Steps to obtain the numerical solution for the fundamental vertical mode. The solution indicates a period of 125 hours for the first vertical mode.

After finding the solution for the first mode, the solution is recalculated to compute the solution for the second mode. The value at the bottom boundary converges again to zero after more iterations, approximating the vertical velocity profile from the first to the second mode (Figure 7.5). This procedure is repeated to find higher vertical modes.

Using the mass conservation equation 7.10d, we can also estimate the horizontal component in arbitrary units. Note that at the wave node, the horizontal velocity is higher than the vertical component. Figure 7.4 illustrates the velocity pattern for each mode and component.

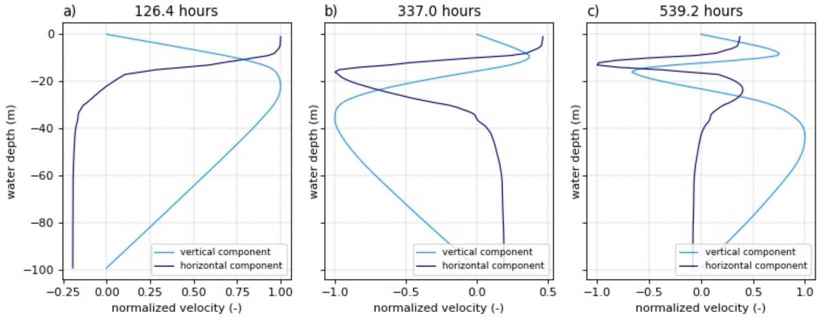

Figure 7.4 Solutions of the Taylor-Goldstein equation for a temperature profile. a) Present the temperature and buoyancy frequency estimated from the temperature profile. The numerical solution of internal seiches obtained from 7.24 for each mode normalized by the maximum velocity for each component is presented in b), c), and d). The light and dark blue lines represent the vertical and horizontal components of the velocity, respectively. Each graph shows the solution for a determined vertical mode: b) first mode ($T_{\mathrm{V1H1}} = 126.4$ h), c) second mode ($T_{\mathrm{V2H1}} = 337.0$ h), and d) third mode ($T_{\mathrm{V3H1}} = 539.2$ h)

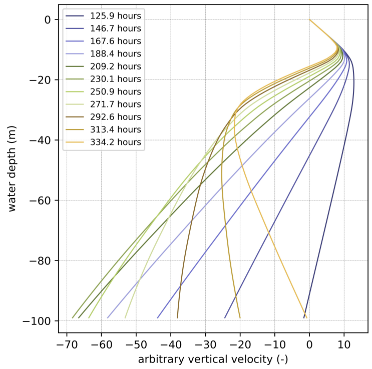

Figure 7.5 Steps to obtain the numerical solution for the second vertical mode. The solution indicates a period of 334.2 hours for the second vertical mode.

To obtain a fair relation between the existing modes, we should orthogonalize the solution through a normalization to obtain the weighted modes. The normalization of W is performed by taking the square root of the orthogonality relation, which was found in equation 7.31:

$$w = \frac{W}{w_{\text{norm}}} = \frac{W}{\sqrt{W\ N^2\ W^{\text{T}}}}, \tag{7.33}$$

in which W^{T} represents the transpose of $W(z,m)$, which is a function of the vertical axis z pointing to the lake bottom and the vertical mode m. Note from Equation 7.34 that normalization $w_{\text{norm}}(m)$ is a function only of the mode.

To obtain the arbitrary horizontal component of the horizontal velocity, we must consider the bidimensional form of the mass conservation equation 7.10d, which gives us the following:

$$u = \frac{W_{z+1} - W_z}{w_{\text{norm}}}. \tag{7.34}$$

Note that Equation 7.34 does not yet provide the horizontal velocity profile for each vertical mode. To decompose a velocity profile into different vertical modes, we must combine the integration of the original horizontal velocity profile with the weighted normal eigenvectors, as explained in Table 7.3. This procedure is described by Boehrer et al. (2000) for Lake Constance.

This method has been extended to the variable bottom cases for multilayer stratification (Shimizu, 2011) and for continuous stratification (Shimizu, 2019). Studies have applied this model to compute the total energy of each vertical mode for internal seiches generated in a rectangular-shaped box tank with flat bottom (). For the cases of variable bottoms, Imam et al. (2020) has studied the energy assigned to different vertical modes through an extended version of the modal decomposition (Shimizu, 2011).

Interwave Analyzer
The software processes only temperature data, but is coupled to the internal wave model that estimates the weighted normal eigenvectors for the horizontal profile, helping to calculate mode decomposition. Based on results from the Taylor-Goldstein equation, a simple convolution between the eigenvectors and the integration of the original horizontal velocity profile gives the horizontal velocity profile associated with each vertical mode:

$$u_z^m = \sum \left(W_{\text{int}} N^2 w u^{\text{T}} \right), \tag{7.35}$$

in which u^{T} represents the transpose of u, and W_{int} is the "measured" integrated horizontal velocity.

Table 7.3 Interwave Analyzer and mode decomposition.

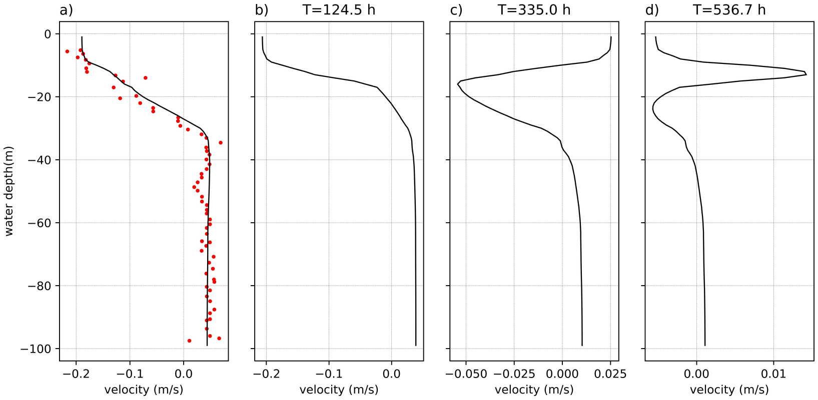

Figure 7.6 Mode decomposition Numerical solution of internal seiches obtained from equation 7.24 for each mode normalized by the maximum velocity for each component. The light and dark blue lines represent the vertical and horizontal components of the velocity, respectively. Each graph shows the solution for a determined vertical mode: a) first mode ($T_{\mathrm{V1H1}} = 126.4$ h), a) second mode ($T_{\mathrm{V2H1}} = 337.0$ h), and a) third mode ($T_{\mathrm{V3H1}} = 539.2$ h)

Dispersion relation

From equation 7.22 and considering the insert wave of the form:

$$w = w_o \mathrm{e}^{-i(K_x\, x + k_z\, z - \omega t)}, \tag{7.36}$$

yields the dispersion relation:

$$\frac{\partial^2}{\partial t^2}\left(\frac{\partial^2 w}{\partial x^2} + \frac{\partial^2 w}{\partial z^2}\right) + N^2\, \frac{\partial^2 w}{\partial x^2} = 0.$$

$$-\left(k_x^2 + k_z^2\right)\frac{\partial^2}{\partial t^2}\left(w_o \mathrm{e}^{-i(K_x\, x + k_z\, z - \omega t)}\right) - N^2\, k_x^2 w_o \mathrm{e}^{-i(K_x\, x + k_z\, z - \omega t)} = 0$$

$$\left(k_x^2 + k_z^2\right)\omega^2\, w_o \mathrm{e}^{-i(K_x\, x + k_z\, z - \omega t)} - N^2\, k_x^2 w_o \mathrm{e}^{-i(K_x\, x + k_z\, z - \omega t)} = 0$$

$$\left(k_x^2 + k_z^2\right)\omega^2 - N^2\, k_x^2 = 0$$

$$\omega^2 = N^2\, \frac{k_x^2}{k_x^2 + k_z^2} \tag{7.37}$$

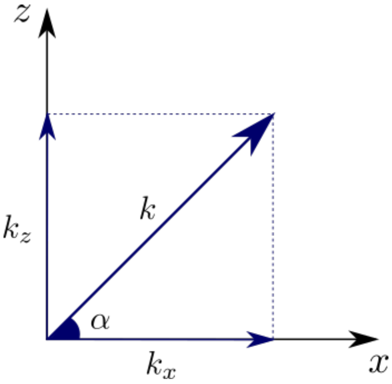

Figure 7.7 Components of the wave number.

Rearranging equation 7.37, we may find

$$\frac{\omega}{N} = \sqrt{\frac{k_x^2}{k_x^2 + k_z^2}} = \frac{k_x}{k} = \cos\alpha, \tag{7.38}$$

in which k is the resultant wavenumber and α is the angle between the resultant wavenumber and x-component (Figure 7.7).

Equation 7.38 states that ω/N varies between 0 and 1, implying that the excitation frequency ω must be less than or equal to the buoyancy frequency N. This relation indicates that internal waves cannot exist when $\omega > N$, since density stratification cannot support the forcing frequency ω, which breaks stratification right after the initialization of the perturbation.

Three-dimensional form
The dispersion relation obtained for a two-dimensional case can be easily obtained for a three-dimensional case, assuming a wavenumber $\mathbf{k} = (k_x, k_y, k_z)$. In this case, the wave would have the form:

$$w = w_o \mathrm{e}^{-i(K_x\ x+K_y\ y+k_z\ z-\omega t)},$$

which yields the dispersion relation

$$\omega^2 = N^2 \frac{k_x^2 + k_y^2}{k_x^2 + k_y^2 + k_z^2} \qquad (7.39)$$

Table 7.4 Wave in a stratification (3D).

From the two-dimensional form of the mass conservation equation 7.10d and assuming the general solution of a plane wave (equation 7.36), we may find the horizontal components u of the velocity vector:

$$u = -\int \frac{\partial w}{\partial z}\,\mathrm{d}x = i\,w_o\,k_z \int \mathrm{e}^{-i(K_x\ x+K_y\ y+k_z\ z-\omega t)}\,\mathrm{d}x$$

$$u = -w_o\,\frac{k_z}{k_x}\mathrm{e}^{-i(K_x\ x+K_y\ y+k_z\ z-\omega t)}, \qquad (7.40)$$

in which the vertical component w is defined by the general solution (equation 7.36).

Finally, the vector velocity may be defined as

$$\mathbf{v}(u,w) = w_o\,\mathrm{e}^{-i(K_x\ x+K_y\ y+k_z\ z-\omega t)}\left(-\frac{k_z}{k_x}, 1\right)$$

$$\mathbf{v}(u,w) = k_z\ w_o\ \mathrm{e}^{-i(K_x\ x+K_y\ y+k_z\ z-\omega t)}\left(-\frac{1}{k_x}, \frac{1}{k_z}\right) \qquad (7.41)$$

Phase and group velocity

Phase velocity can be calculated from the dispersion relation 7.38

$$\mathbf{c_p} = \frac{\omega}{|k|}\frac{\mathbf{k}}{|k|} = \frac{N\,k_x}{\sqrt{k_x^2+k_z^2}}\frac{\mathbf{k}}{|k|\,|k|},$$

$$\mathbf{c_p} = \frac{N\,k_x}{\sqrt{k_x^2+k_z^2}}\,\frac{1}{\sqrt{k_x^2+k_z^2}}\,\frac{1}{\sqrt{k_x^2+k_z^2}}\left(k_x, k_z\right),$$

$$\mathbf{c_p} = \frac{N\,k_x}{(k_x^2+k_z^2)^{3/2}}\left(k_x, k_z\right). \qquad (7.42)$$

Rearranging equation 7.42, we may find

$$\mathbf{c_p} = \frac{N\,k_x^2\,k_z}{(k_x^2+k_z^2)^{3/2}}\left(\frac{1}{k_z}, \frac{1}{k_x}\right). \qquad (7.43)$$

The group velocity is defined as:

$$\mathbf{c_g} = \left(\frac{\partial\omega}{\partial k_x}, \frac{\partial\omega}{\partial k_z}\right), \qquad (7.44)$$

in which $\omega = N\,k_x\,(k_x^2 + k_z^2)^{-1/2}$ (equation 7.38).

The horizontal component of the group velocity can be found by substituting equation 7.38 into 7.44:

$$c_g^x = \frac{\partial \omega}{\partial k_x} = N\left((k_x^2 + k_z^2)^{-1/2} - k_x^2\,(k_x^2 + k_z^2)^{-3/2}\right),$$

$$c_g^x = N(k_x^2 + k_z^2)^{-3/2}\left(\frac{(k_x^2 + k_z^2)^{-1/2}}{(k_x^2 + k_z^2)^{-3/2}} - k_x^2\right),$$

$$c_g^x = N(k_x^2 + k_z^2)^{-3/2}\,k_z^2. \tag{7.45}$$

The vertical component of the group velocity may be found in a similar way.

$$c_g^z = \frac{\partial \omega}{\partial k_z} = -\frac{N\,k_x}{2}(k_x^2 + k_z^2)^{-3/2}\,(-2k_z)$$

$$c_g^z = -N(k_x^2 + k_z^2)^{-3/2}\,k_x\,k_z. \tag{7.46}$$

Substituting equations 7.45 and 7.45 into 7.44 gives the following

$$\mathbf{c_g} = N\,k_z\,(k_x^2 + k_z^2)^{-3/2}\left(k_z, -k_x\right). \tag{7.47}$$

Rearranging equation 7.47 to have the same form of phase velocity (Equation 7.43), we obtain the following.

$$\mathbf{c_g} = N\,k_z^2\,(k_x^2 + k_z^2)^{-3/2}\left(1, -\frac{k_x}{k_z}\right)$$

$$\mathbf{c_g} = N\,k_z^2\,k_x\,(k_x^2 + k_z^2)^{-3/2}\left(\frac{1}{k_x}, -\frac{1}{k_z}\right). \tag{7.48}$$

Considering that two vectors are perpendicular when their dot product equals zero, from equations 7.43 and 7.48 we can easily demonstrate that the phase velocity is perpendicular to the group velocity:

$$\frac{N^2\,k_z^3\,k_x^3}{(k_x^2 + k_z^2)^3}\underbrace{\left(\frac{1}{k_x\,k_z} - \frac{1}{k_z\,k_x}\right)}_{=0} = 0. \tag{7.49}$$

Internal wave attractor

From the tendency of the internal wave energy to propagate vertically along the water column, the internal wave rays may converge in a confined stratified basin to trajectories called **wave attractors** (Fig. **??**). To examine the formation of internal wave beams and wave attractors, scientists have performed a classic laboratory experiment on the generation of internal waves from a vertically oscillating cylinder in a continuous density stratified fluid (Mowbray, Rarity, 1967; Sutherland et al., 2014; Sutherland, Linden, 2002). To visualize the internal wave beams, scientists often have employed a non-intrusive technique called synthetic schlieren. This technique is a non-intrusive method based on density refraction and has been used to investigate the hydrodynamics of stratified flows (ref). This technique has been described in detail in chapter (ref).

As the cylinder moves up and down, four beams are formed around the cylinder, two propagating upward and two downward (Fig. **??**). The energy propagates along the wave beam, while the phase velocity moves perpendicular to the energy direction, verifying the orthogonality of the group and the phase velocity demonstrated mathematically by Equation 7.49. Note that the angle between the resultant wavenumber k and x-component k_x is our α defined in Equation 7.38.

As the wave beam propagates vertically along the water column, the beams propagating upward are susceptible to be absorbed at the free surface. The ones propagating downward are susceptible to reflect

Although these experiments do not provide a complete picture to describe the internal waves generated over topography, the experiments provide a useful starting point for investigating the interaction between internal waves and boundary layers.

Generation of turbulence
The generation of turbulence is proportional to the shear velocity of the wind u_* (mechanical stirring), which is a function of the speed of the wind and the roughness of the surface of the water, and convective overturns (convective stirring), which can be defined as

$$u_f = -\left(\frac{\alpha g Q h_{\mathrm{sbl}}}{\rho_{\mathrm{sbl}} C_p}\right)^{1/3},$$

in which α is the thermal compressibility of water, g is the acceleration of gravity, $h_{\mathrm{sbl}} = H_1$ is the thickness of the upper well-mixed layer, Q is the net heat flux with the atmosphere, ρ_{sbl} is the density of water in the well-mixed layer, and C_p is the specific heat of the water. Finally, the turbulent velocity scale can be defined as

$$q^3 \propto \eta^3\, u_*^3 + u_f^3, \tag{7.50}$$

in which η is a coefficient of order unity.

Table 7.5 turbulent velocity scale.

7.2 Lake mixing

Although wind speed contributes to the formation of higher amplitude internal seiches, as evidenced by the equation 6.114, the dynamics of lakes has more complex mechanisms that should be considered when we want to describe the dominance of internal seiche activity. Time scales of different mechanisms, such as wave damping and thermocline erosion due to mixing, can be evaluated to describe different lake regimes (Spigel, Imberger, 1980).

7.2.1 Internal seiche

In the absence of entrainment and considering that only internal seiche can influence the motion of thermally stratified lakes, a model similar to that described in Section 6.2.5 can be used to obtain the time scale associated with the motion of internal seiche.

The model is based on an idealized rectangular two-layer box tank (Figure 6.22), in which a surface stress applied in the upper layer is exerted by a constant wind stress (u_*). Integrating in time the governing equations of motion 6.102a described in Section 6.2.5 and considering that the vertical displacement is negligible in the center of the basin $\eta = 0$:

$$u_1(t) = \frac{u_*^2\, t}{H_1}. \tag{7.51}$$

However, note that the upper layer does not accelerate infinitely during the wind event, and the increase in velocity u_1 in the center of the lake is limited by the extension of the lake. As the wave propagates toward the center of the lake, the upper layer accelerates until $t = T_{\mathrm{V1H1}}/4$ (Figure 7.11), when the velocity associated with the wave motion is maximum:

$$u_1^{\max}(t = T_{\mathrm{V1H1}}/4) = \frac{u_*^2\, T_{\mathrm{V1H1}}}{4H_1}. \tag{7.52}$$

After this moment, the pressure gradient increases as a result of the presence of the end wall, decelerating the upper layer. As the wave propagates back and forth, the shear is not completely cut off at $t = T_{\mathrm{V1H1}}/4$.

7.2.2 internal wave damping

Another limiting factor for internal seiche formation is the time-scale of wave damping, which describes the time spent for the internal seiche energy to be completely dissipated. Heaps, Ramsbottom (1966) suggested that the wave would be damped mainly due to shear stress at the bottom of the lake. However, recent observations also demonstrate that internal seiches are susceptible to degenerate into higher-frequency internal waves(Boegman et al., 2005a; Horn et al., 2001) and break at sloping boundaries and irregularities **?**. For simplicity, we assume here that the internal wave is only dampened by bottom shear. Thus, internal seiche wave damping can be estimated through the balance between the wave energy (Eq. 6.91) and the energy dissipated on solid boundaries. Assuming a rectangular-shaped basin, the energy dissipated at solid boundaries is given by (Horn et al., 2001):

$$\frac{\mathrm{d}E_{\mathrm{bot}}}{\mathrm{d}t} = -\underbrace{\int_{A_1} \frac{\mu\, u_1^2}{2\,\delta_b}\mathrm{d}A}_{\text{surface shear}} - \underbrace{\int_{A_2} \frac{\mu\, u_2^2}{2\,\delta_b}\mathrm{d}A}_{\text{bottom shear}} - \underbrace{\int_{A_\rho} \frac{\mu\, \Delta u^2}{2\,\delta_\rho}\mathrm{d}A}_{\text{interfacial shear}}, \tag{7.53}$$

in which μ is the kinetic viscosity, u is the horizontal velocity, δ_b is the thickness of the laminar boundary layer, δ_ρ is the thickness of the interfacial layer, and A is the surface area in which shear occurs (Figure 7.8). Note that in this model, we neglected the shear that occurs in the end wall of the tank and also assumed a two-layer rig-lid model, in which the surface is closed and made with the same material of the tank bottom, indicating that the thickness of the laminar boundary layer is the same for surface and bottom shear. Another simplification is that μ is a mean kinematic viscosity and does not differentiate from the upper and lower fluids.

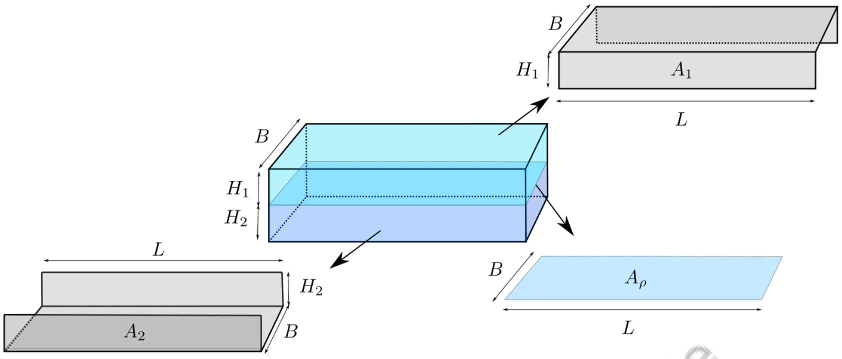

Figure 7.8 Schematic illustration of the rectangular tank and surface areas where shear occurs

Figure 7.9 Velocity of each layer in $t = T_{V1}/2$ along the longitudinal extension of the rectangular-shaped box.

Applying the surface areas A to equation 7.53 and rearranging the result, we find the following

$$\frac{\mathrm{d}E_{\text{bot}}}{\mathrm{d}t} = -\frac{\mu}{2\delta_b}\left((2H_1 + B)\int_{x=L} u_1(x)^2 \, \mathrm{d}x + \right.$$
$$\left.(2H_2 + B)\int_{x=L} u_2(x)^2 \, \mathrm{d}x\right) - \frac{\mu B}{2\delta_\rho}\int_{x=L} \Delta u(x)^2 \, \mathrm{d}x, \quad (7.54)$$

in which the horizontal velocity profile of each layer can be approximated by a linear variation along the longitudinal extension (Figure 7.9).

As we cannot mathematically represent the velocity profile continuously along the basin length, we may assume that the energy is equally partitioned between both sides of the rectangular-shaped box, computing only the energy for one side of the basin and duplicating the final solution. Thus, we have the following:

$$\frac{\mathrm{d}E_{\text{bot}}}{\mathrm{d}t} = -\frac{\mu}{\delta_b}\left((2H_1 + B)\int_{x=L/2} \frac{4u_1^2}{L^2}\, x^2 \, \mathrm{d}x + \right.$$
$$\left.(2H_2 + B)\int_{x=L/2} \frac{4u_2^2}{L^2}\, x^2 \, \mathrm{d}x\right) - \frac{\mu B}{\delta_\rho}\int_{x=L/2} \frac{4\Delta u^2}{L^2}\, x^2 \, \mathrm{d}x. \quad (7.55)$$

Integrating 7.55 along the longitudinal direction of the rectangular-shaped box, we find

$$\frac{\mathrm{d}E_{\text{bot}}}{\mathrm{d}t} = -\frac{4\mu}{\delta_b L^2}\Big((2H_1 + B) + (2H_2 + B)\Big)\frac{x^3}{3}\bigg|_{x=L/2} - \frac{4\mu B \Delta u^2}{\delta_\rho L^2}\frac{x^3}{3}\bigg|_{x=L/2},$$

$$\frac{\mathrm{d}E_{\text{bot}}}{\mathrm{d}t} = -\frac{\mu L}{6\delta_b}\Big(u_1^2(2H_1 + B) + u_2^2(2H_2 + B)\Big) - \frac{\mu B \Delta u^2 L}{6\delta_\rho}. \quad (7.56)$$

Applying the mass conservation into 7.56, give us

$$\frac{\mathrm{d}E_{\text{bot}}}{\mathrm{d}t} = -\frac{\mu L}{6\delta_b}\left(\frac{H_2^2}{H_1^2}(2H_1 + B) + (2H_2 + B)\right) - \frac{\mu B \Delta u^2 L}{6\delta_\rho}, \quad (7.57)$$

which describes the rate of energy decay due to shear stress at solid boundaries. Integrating this equation along one wave period gives a loss of energy during a single complete oscillation.

The total kinetic energy (equation 6.91) along the upper and lower layers is defined as

$$E_{\mathrm{K}} = \frac{1}{T}\int_0^T \int_{x=L} \left(\int_{z=H_1} \frac{\rho\, u_1(x)^2}{2}\,\mathrm{d}z + \int_{z=H_2} \frac{\rho\, u_2(x)^2}{2}\,\mathrm{d}z \right) \mathrm{d}x\, B\, \mathrm{d}t, \tag{7.58}$$

in which T is the fundamental internal seiche period, ρ is the mean density of water, B is the width of the basin, and u_1 and u_2 are the velocities of the upper and lower layers, respectively.

Assuming that the horizontal velocity profile along the extension of the basin can be approximated by a linear function between $x = 0$ and $x = L/2$ (Figure 7.9) and that the energy is equally partitioned between the sides of the basin, equation 7.58 can be rewritten as

$$\begin{aligned}
E_{\mathrm{K}} &= 2\int_{x=L/2} \left(\frac{\rho\, H_1}{2}\left(\frac{2\,x\,u_1}{L}\right)^2 + \frac{\rho\, H_2}{2}\left(\frac{2\,x\,u_2}{L}\right)^2 \right) \mathrm{d}x\, B,\\
E_{\mathrm{K}} &= \frac{4\rho}{L^2}\left(H_1\, u_1^2 + H_2\, u_2^2\right) \left.\frac{x^3}{3}\right|_{x=L/2} B,\\
E_{\mathrm{K}} &= \frac{\rho\, L\, B}{6}\left(H_1\, u_1^2 + H_2\, u_2^2\right).
\end{aligned} \tag{7.59}$$

Applying the mass conservation equation to 7.59, we find that

$$E_{\mathrm{K}} = \frac{\rho\, L\, B\, u_2^2}{6}\,\frac{H_2}{H_1}\, H, \tag{7.60}$$

where H is the total water depth.

Balancing the energy dissipation in the solid boundaries during a single complete oscillation (Equation 7.57) and the energy locked in the internal seiche motion (Equation 7.60), we have

$$\begin{aligned}
\frac{\mathrm{d}E_{\mathrm{bot}}}{E_{\mathrm{K}}} = \Bigg(&-\frac{\mu L T_{\mathrm{V1H1}}\, u_2^2}{6\delta_b}\left(\frac{H_2^2}{H_1^2}(2H_1 + B) + (2H_2 + B)\right)\\
&- \frac{\mu B \Delta u^2 L T_{\mathrm{V1H1}}}{6\delta_\rho}\Bigg)\left(\frac{6}{\rho\, L\, B\, u_2^2}\,\frac{H_1}{H\, H_2}\right),
\end{aligned} \tag{7.61}$$

in which 7.57 was first integrated in time along a wave period.

Rearranging 7.61 gives us

$$\frac{\mathrm{d}E_{\mathrm{bot}}}{E_{\mathrm{K}}} = -\frac{\nu T_{\mathrm{V1H1}}}{B\delta_b}\,\frac{H_1}{H\, H_2}\left(\frac{H_2^2}{H_1^2}(2H_1 + B) + (2H_2 + B)\right) - \frac{\nu T_{\mathrm{V1H1}}}{\delta_\rho}\,\underbrace{\frac{\Delta u^2}{u_2^2}}_{\text{(A)}}\,\frac{H_1}{H\, H_2}, \tag{7.62}$$

where the term (A), considering the mass conservation law, is defined as

$$\frac{\Delta u^2}{u_2^2} = 1 - 2\frac{u_1}{u_2} + \left(\frac{u_1}{u_2}\right)^2 = \left(\frac{H}{H_1}\right)^2$$

Rearranging 7.62 and assuming that the thickness of the laminar boundary layer is oscillatory, defined by $\delta_b = \sqrt{\nu\ T_{\mathrm{V1H1}}/\pi}$, we find

$$\frac{\mathrm{d}E_{\mathrm{bot}}}{E_{\mathrm{K}}} = -\frac{\pi\ \delta_b}{\forall}\left(2HL + B\left(\frac{H_1}{H_2} + \frac{H_2}{H_1}\right)\right) - \frac{\nu T_{\mathrm{V1H1}}}{\delta_\rho}\frac{H}{H_1\ H_2}, \tag{7.63}$$

in which $\forall = L\ H\ B$ is the volume of the rectangular-shaped box. Equation 7.63 is similar to that developed by Horn et al. (2001), which apparently assumed $H_1 \approx H_2$. Note that, different from Horn et al. (2001), we kept the minus sign on equation 7.63 to demonstrate that the wave energy decays with time $(E_2 - E_1 < 1)$

To determine the damping timescale for field data, studies recommend an alternative form of equation 7.63 Horn et al. (2001), in which the interfacial shear effect is neglected and the first term of equation 7.63 is counterbalanced:

$$\frac{\mathrm{d}E_{\mathrm{bot}}}{E_{\mathrm{K}}} \approx -\frac{\delta_b\ A_{\mathrm{solid}}}{\forall}, \tag{7.65}$$

in which $A_{\mathrm{solid}} = A_1 + A_2$ is the total area of the solid boundary (Figure 7.8). Since the horizontal extension of the lake is much greater than its vertical extension, the solid boundary area A_{solid} can be approximated to the surface area of the lake A_o (Spigel, Imberger, 1980). The δ_b can be approximated by

$$\delta = \frac{U_{\max}\ \sqrt{T_{\mathrm{V1H1}}}\ e}{471\ \sqrt{\nu}}, \tag{7.66}$$

where $U_{\max}$ is the maximum velocity due to oscillatory motions, ν is the kinetic molecular viscosity, e is the sand grain roughness (e.g., for a smooth river channel, $e = 6$ mm).

Comparing equation 7.65 with the ratio of time scales, we obtain the time scale for wave damping:

$$\frac{\mathrm{d}E_{\mathrm{BBL}}}{E_K} = \frac{T_{V1H1}}{T_{\mathrm{damp}}}$$

$$\frac{T_{V1H1}}{T_{\mathrm{damp}}} = \frac{\rho_o\ A_o\ u^2\delta}{2}\left(\frac{2}{\rho_o\ \forall\ u^2}\right)$$

$$T_{\mathrm{damp}} = \frac{\forall}{A_o\ \delta_b}\ T_{\mathrm{V1H1}}, \tag{7.67}$$

where T_{damp} represents the time in which all wave energy is dissipated through the bottom friction. Note that equation 7.67 can also be obtained through equation7.65, which results in a different equation based on the thickness of the turbulent oscillatory boundary layer (equation 7.66).

Energy dissipation
Another way of estimating the kinetic energy dissipated in the bottom boundary layer has been proposed by Gloor et al. (2000):

$$\frac{\partial E_K}{\partial t} = -c_h\ \rho_o\ A_o\ |u_h|^3, \tag{7.64}$$

in which A_o is the interior surface area of the basin, and c_h and u_h are the drag coefficient and the horizontal velocity at h meters above the bottom, respectively. Many authors have estimated the drag coefficient for different lakes (Ravens et al., 2000) by comparing the dissipation of turbulent energy near the bottom boundary layer with the cubed horizontal velocity at the same location (Fig. **??**). Observations on Lake Baikal estimated values of $c_{1\ \mathrm{m}} = 2\ 10^{-3}$ (Ravens et al., 2000), while values in a lake ....

Table 7.6 Dissipation based on drag coefficient

When T_{damp} is less than the period spent on internal seiche formation ($T_{\text{damp}} < T_{V1H1}/4$), the internal seiche is damped before complete vertical displacement, and consequently the internal seiche is not generated.

Note that the condition described by equation 7.67 considers only the dissipation due to the bottom friction. However, as mentioned earlier, energy can be dissipated from the internal seiche as a result of wave breaking and degeneration mechanisms. For more information on the internal seiche degeneration mechanism, see Section 7.5. In Figure 7.10 we present a summary of all regimes discussed in this section.

Figure 7.10 Regime of lake mixing as a function of Wedderburn number W.

7.2.3 Entrainment

During the evolution of internal seiches and with the damping mechanism, the well-mixed surface layer erodes to the bottom of the basin; this phenomenon is called deepening and can contribute to inhibiting the formation of internal seiches. This mechanism occurs primarily as a result of the shear and stirring effect. The stirring mechanism contributes to the production of the kinetic energy of turbulence in the surface boundary layer due to wave break and surface cooling (Wells, Sherman, 2001). The shear mechanism occurs at the interface between both fluids as a result of the interaction between the mean large flow and Reynolds stresses, which favors the production of turbulent kinetic energy. This mechanism occurs during the evolution of the internal wave as a result of shear in the interface region.

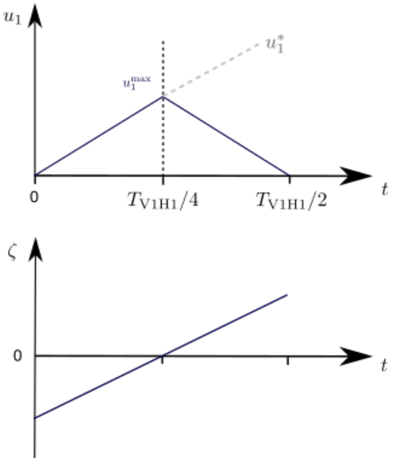

Figure 7.11 Velocity of the upper layer in the center of the basin. u_1^* describes equation 7.51 for the period in which the equation is not valid due to the presence of end walls. The lower figure illustrates the interfacial displacement ζ at the bottom end of the basin during the same period of analysis.

To evaluate the deepening of the mixed surface layer, the turbulent kinetic energy (TKE) equation can be integrated throughout the well-mixed upper layer (Niiler, 1975; Spigel, Imberger, 1980; Sherman et al., 1978). The TKE budget in the thermocline region is characterized by the balance of the energy rate required to erode the mixed surface layer with the energy rate available for mixing, which includes the energy coming from the surface boundary layer (Q_{st}) and shear production in the thermocline due to the formation and evolution of internal seiches (Q_{sh}), in which the shear flow can become unstable and turbulent (Gloor et al., 2000). At the same time, TKE is lost by the radiation of internal waves (Q_{iw}). In other words, part of the TKE is used to generate high-frequency waves at the base of the thermocline.

The energy rate available for mixing is illustrated in Figure 7.12 and is mathematically represented by Niiler (1975) and Sherman et al. (1978) as

$$\frac{\partial E}{\partial t} = \underbrace{\frac{C_K\, q^3}{2}}_{Q_{\text{st}}} + \underbrace{\frac{C_S\,(\mathbf{u}\cdot\mathbf{u})}{2}\frac{\mathrm{d}H_1}{\mathrm{d}t}}_{Q_{\text{sh}}} - \underbrace{\frac{C_L\, a^2\, N^3\, H_1}{2}}_{Q_{\text{iw}}}, \tag{7.68}$$

in which C_K and C_S are constants that represent the convective stirring efficiency and the non-equilibrium effect due to changes in turbulence input, respectively.

Both constants have the order $\mathcal{O}(1)$. H_1 is the thickness of the epilimnion, N is the buoyancy frequency, $\mathbf{u}$ is the vector of the mean velocity, q is the turbulent velocity scale, defined in Table 7.5, and a is the amplitude of the internal wave, which has been estimated by Sherman et al. (1978) as follows:

$$a = \frac{q^2}{q\,N + g\Delta\tau\alpha}, \tag{7.69}$$

where $\Delta\tau$ is the increase in temperature on the interface front and α is the thermal compressibility of the water.

From Equation 7.69, the leakage of energy due to the excitation of high-frequency internal waves can be rewritten as

$$Q_{\text{iw}} = \frac{C_L\,N^3\,H_1\,q^4}{2(q\,N + g\Delta\tau\alpha)^2}. \tag{7.70}$$

Multiplying both sides of equation 7.70 by H_1^2/q^4 and assuming that $R_S = NH_1/q$ and $Ri = g\,\Delta\tau\,\alpha\,H_1/q^2$, we finally find that

$$\begin{aligned} Q_{\text{iw}} &= \frac{C_L\,N^3\,H_1^3\,q^4}{2\,(q^2\,N^2\,H_1^2 + 2\,N\,q\,g\,\Delta\tau\,\alpha\,H_1^2 + g^2\Delta\tau^2\alpha^2\,H_1^2)}, \\ &= \frac{C_L\,N^3\,H_1^3}{2\left(N^2\,H_1^2/q^2 + 2\,N\,q\,g\,\Delta\tau\,\alpha\,H_1^2/q^4 + g^2\Delta\tau^2\alpha^2\,H_1^2/q^4\right)}, \\ &= \frac{C_L\,N^3\,H_1^3}{2\left(N\,H_1/q + g\,\Delta\tau\,\alpha\,H_1/q^2\right)^2}, \\ Q_{\text{iw}} &= \frac{C_L\,q^3\,R_S^3}{2(R_S + Ri)^2}. \end{aligned} \tag{7.71}$$

Finally, equation 7.68 can be rewritten as

$$\frac{\partial E}{\partial t} = \frac{C_K\,q^3}{2} + \frac{C_S\,(\mathbf{u}\cdot\mathbf{u})}{2}\frac{\mathrm{d}H_1}{\mathrm{d}t} - \frac{C_L\,q^3\,R_S^3}{2(R_S + Ri)^2}. \tag{7.72}$$

Equation 7.72 is balanced by the rate of energy required for deepening:

$$\underbrace{\frac{C_T\,q^2}{2}\frac{\mathrm{d}H_1}{\mathrm{d}t}}_{\text{(I)}} + \underbrace{\frac{\Delta\tau\,\alpha\,g H_1}{2}\frac{\mathrm{d}H_1}{\mathrm{d}t}}_{\text{(II)}} = Q_{\text{st}} + Q_{\text{sh}} - Q_{\text{iw}}, \tag{7.73}$$

in which term (I) represents the rate of change of TKE in the water column and the second term (II) indicates the contribution of buoyancy. The first term can be neglected in most cases in lakes, since the energy required for the deepening mechanism is most of the time controlled by buoyancy (Spigel, Imberger, 1980).

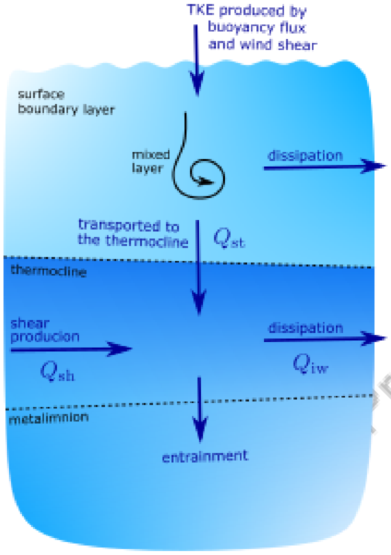

Figure 7.12 Schematic of turbulent energy flux path assumed the model proposed by Sherman et al. (1978).

Substituting equations 7.73 into equation 7.72 gives the following equation:

$$\frac{1}{2}\frac{\mathrm{d}H_1}{\mathrm{d}t}(C_T\, q^2+\Delta\tau\ \alpha\ g\ H_1)=\frac{C_K\, q^3}{2}+\frac{C_S\,(\mathbf{u}\cdot\mathbf{u})}{2}\frac{\mathrm{d}H_1}{\mathrm{d}t}-\frac{C_L\, q^3\, R_S^3}{2(R_S+Ri)^2},$$

$$\frac{1}{q^3}\frac{\mathrm{d}H_1}{\mathrm{d}t}(C_T\, q^2+\Delta\tau\ \alpha\ g\ H_1-C_S\,(\mathbf{u}\cdot\mathbf{u}))=C_K-\frac{C_L\, R_S^3}{(R_S+Ri)^2},$$

$$\frac{1}{q}\frac{\mathrm{d}H_1}{\mathrm{d}t}\left(C_T+\underbrace{\frac{\Delta\tau\ \alpha\ g\ H_1}{q^2}}_{Ri}-\frac{C_S\,(\mathbf{u}\cdot\mathbf{u})}{q^2}\right)=C_K-\frac{C_L\, R_S^3}{(R_S+Ri)^2}. \tag{7.74}$$

Assuming that $\mathbf{u}$ is the shear velocity between layers and $\Delta\tau\ \alpha\ g\ H_1 = g'\ H_1$, equation 7.74 can be rewritten as

$$\frac{1}{q}\frac{\mathrm{d}H_1}{\mathrm{d}t}\left(C_T+Ri-C_S\, Ri\ \frac{\Delta U^2}{g'\ H_1}\right)=C_K-\frac{C_L\, R_S^3}{(R_S+Ri)^2},$$

$$\frac{1}{q}\frac{\mathrm{d}H_1}{\mathrm{d}t}=\frac{C_K-C_L\, R_S^3/(R_S+Ri)^2}{C_T+Ri-C_S\, Ri\ \Delta U^2/(g'\ H_1)}, \tag{7.75}$$

in which ΔU is the velocity jump across the interface front. Most of the time ΔU can be approximated by the velocity of the upper well-mixed layer (u_1).

Equation 7.75 describes the speed of entrainment. Note that the higher the Richardson number, the slower the entrainment velocity in most cases. Shear production also contributes to the entrainment velocity by increasing the turbulent kinetic energy at the thermocline interface. This production is balanced by the change in TKE and the buoyancy effect. Furthermore, the energy available as a result of stirring, which speeds up the entrainment velocity, is counterbalanced by the losses of TKE as a result of radiation of the internal wave, which slows down the entrainment velocity. However, studies have suggested that the loss of TKE due to internal wave radiation can already be incorporated into the coefficient C_K, which is characterized by the energy that reaches the thermocline region (Spigel, Imberger, 1980). Assuming this simplification, Equation 7.75 is reduced to

$$\frac{v_{\text{ent}}}{u_*}=\frac{C_K}{C_T+Ri-C_S\, Ri\ \Delta U^2/(g' H_1)}. \tag{7.76}$$

Note that in equation 7.76, we also approximated the turbulent velocity scale q to the wind shear velocity u_*, neglecting the contribution of convective stirring (Table 7.5). Furthermore, the velocity entrainment, which was represented in equation 7.75 by the time derivative of the thickness of the epilimnion, in equation 7.76 is simply defined as v_{ent}.

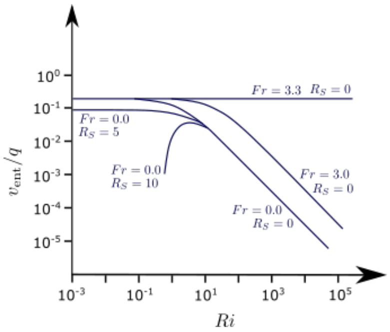

Figure 7.13 Entrainment velocity predicted by equation 7.75.

For a small Richardson number (Ri), the entrainment velocity can be approximated to

$$v_{\text{ent}}=\frac{C_K\, u_*}{C_T}. \tag{7.77}$$

Since the coefficients C_K/C_T are of order unity, $v_{\text{ent}} \approx u_*$. Many studies have been conducted to predict the exact value of C_K and C_T. Observations have suggested that C_K can vary from 0.13 to 1.0 (Niiler, 1975; Mahrt, Lenschow, 1976; List et al., 1979), while the coefficient C_T is equal to zero for most observations in lakes with a large Ri number (Niiler, 1975; Mahrt, Lenschow, 1976; Imberger et al., 1978). However, for most lakes with a low Ri, C_T is roughly 0.5.

For a large Richardson number ($Ri \gg 1$), which is a common condition observed in lakes and reservoirs, the entrainment velocity is given by

$$\frac{v_{\text{ent}}}{u_*} = \frac{C_K}{Ri - C_S\, Ri\, \Delta U^2/(g' H_1)}, \tag{7.78}$$

where the second term of the denominator indicates the contribution of shear stress to the deepening mechanism due to the production of turbulent kinetic energy. Shear stress is limited by two mechanisms. The first is related to the finite extension of the lake, whilst the second is related to the entrainment mechanism itself, which is counterbalanced by the stability condition of the system (see the denominator term of equation 7.78).

The first mechanism dominates the shear velocity when the internal seiche is reflected on the end wall of the basin. In this scenario, the horizontal velocity in the center of the lake is slowed, significantly reducing the shear velocity. Exactly as discussed above and illustrated in Figure 7.11.

To evaluate the contribution of the finite extension of the lake, we may consider momentum conservation for the upper layer (equation 6.102a) and neglect surface displacement, since the analyzed position is defined at the node of the wave:

$$\frac{\partial u_1}{\partial t} \approx \frac{u_*^2}{H_1}. \tag{7.79}$$

Froude number
The condition prescribed by equation 7.86 can also be interpreted using the concept of the Froude number. Assuming that U_{basin} is defined by the limit of shear velocity at $t = T_{V1H1}/4$ due to the finite extension of the lake, we find that

$$Fr_s = \frac{U_{\text{basin}}}{\sqrt{g' H_1}},$$

in which $Fr_s < 1/\sqrt{C_S}$ satisfies the condition defined by Equation 7.86.

In this case, the maximum shear velocity (u_1) is defined by the limit when the flow feels the finite extension of the lake, which occurs when $t = T_{V1H1}/4$. From Equation 7.79, we may find the following.

$$u_1^{\max} = u_1(t = T_{V1H1}/4) = \frac{u_*^2\, T_{V1H1}}{4\, H_1}. \tag{7.80}$$

However, the shear velocity is limited not only by the extension of the basin. v_{ent} will be the maximum when the shear stress increases proportionally to the stability condition. Mathematically, we may describe the maximum entrainment velocity as

Table 7.7 Regime based on Froude number

$$\lim_{\beta \to 1} \frac{C_K}{Ri\,(1-\beta)} = \infty, \tag{7.81}$$

in which $\beta = C_S\, u_1^2/(g' H_1)$.

From Equation 7.81, we find the maximum shear stress velocity:

$$u_1^{\max} = \sqrt{\frac{g' H_1}{C_S}}, \tag{7.82}$$

where the Froude number of the shear flow is defined as $Fr = C_S^{-1/2}$. Since C_S is a constant, the Froude number should also be a constant. Usually, C_S are of order unity.

Therefore, the maximum shear velocity is limited by the effects of finite lake extension (Equation 7.80) and the entrainment mechanism (Equation 7.82):

$$u_1^{\max} = \min\left(\frac{u_*^2\ T_{V1H1}}{4\ H_1}, \sqrt{\frac{g' H_1}{C_S}}\right). \tag{7.83}$$

Each mechanism contributes differently to the entrainment velocity. Assuming the shear velocity $\Delta U = u_1 - u_2 \approx u_1$, the substitution of equation 7.79 into 7.78 gives the following result.

$$\frac{v_{\text{ent}}}{u_*} = \frac{C_K}{Ri - C_S\ Ri\ u_1^2/(g' H_1)},$$

$$\frac{v_{\text{ent}}}{u_*} = \frac{C_K}{Ri - C_S\ u_*^2\ t^2/H_1^2}. \tag{7.84}$$

If shear does not contribute significantly to entrainment, $u_1^{\max}$ will never increase to the order of $\sqrt{g' H_1/C_S}$, as before the flow felt the presence of the finite extension of the lake. In this scenario, there is a lower TKE production, resulting in slower entrainment. In this case, equation 7.84 reduces to

$$v_{\text{ent}} = \frac{C_K\ u_*}{Ri}. \tag{7.85}$$

Mathematically, this condition can be obtained by balancing the two components defined in Equation 7.83 and the theoretical period of internal seiche for shallow waters. Another way to represent this condition is put in terms of the Wedderburn number (W):

$$\frac{T_{V1H1}}{4} > \frac{H}{u_*},$$

$$W > \frac{1}{2}\sqrt{\frac{H\ C_S}{H_2}}, \tag{7.86}$$

in which H is the total depth of the water and W is the Wedderburn number. Here, we assume $S_C = 1$ (Pollard et al., 1973). For this condition, the shear velocity may be neglected and the entrainment velocity can be predicted by equation 7.85, in which v_{int} is proportional to Ri^{-1}.

On the other hand, if W is lower than the condition defined by equation 7.86, shear contributes significantly to entrainment. In this case, $u_1^{\max}$ should be of the order of $\sqrt{g' H_1/C_S}$ before it could be felt by the end wall of the lake. Consequently, this mechanism favors the production of turbulent kinetic energy and consequently the deepening mechanism.

In this second case, the entrainment velocity can be predicted by the balance between the stability and shear stress mechanisms (equation 7.84). Thus, the entrainment velocity is given by

$$Ri = C_S\ u_*^2\ t^2/H_1^2$$

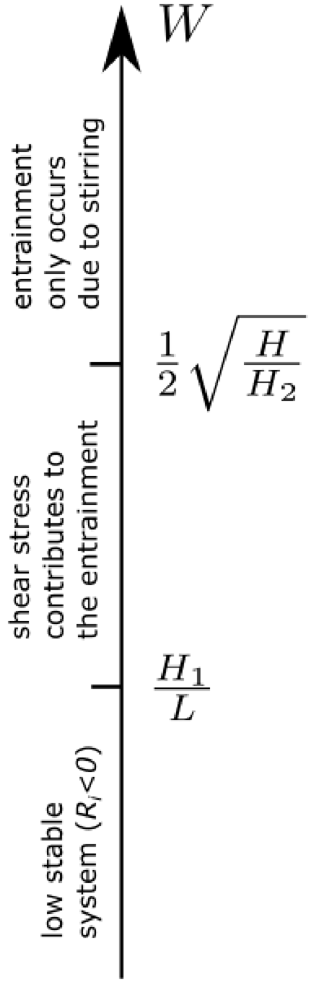

Figure 7.14 Lake classification based on Wedderburn number (W) according to equation 7.86 and the low stratification criteria ($Ri < 1$).

$$v_{\text{ent}} = u_* \sqrt{\frac{C_S}{Ri}}. \tag{7.87}$$

In conclusion, this criterion creates two different regimes. When the shear velocity does not exceed the limit described in Equation 7.82, the shear stress does not contribute to the production of TKE, leading to slower deepening ($v_{\text{ent}} = \mathcal{O}(Ri^{-1})$). On the other hand, if shear stress contributes to entrainment, the deepening mechanism occurs with velocity $v_{\text{ent}} = \mathcal{O}(Ri^{-1/2})$ (Figures 7.15 and 7.14). However, note that if W is lower than H_1/L ($Ri < 1$), the system has a negligible stratification condition. In this case, the entrainment velocity can be estimated using the equation 7.77 (Figure 7.14), and the internal seiche is not susceptible to being generated, as the system cannot support oscillations in the weak stratified system without a stratification break.

Note that even though we have only considered the flow for a time-scale lower than the wave period $t < T_{V1H1}/4$, the shear velocity may be induced by internal seiche and present a periodic pattern, with a local maximum value for each wave cycle (Figure 7.15). Depending on the intensity of the shear velocity induced by the internal seiche, this mechanism may contribute to the deepening phenomenon, which will depend on the maximum shear velocity per wave cycle $u_1^{\max} \geq \sqrt{g' H_1/C_S}$. A more realistic model should take into account wave damping, which can reduce the shear dominance period (Figure 7.15)

During the internal seiche activity illustrated in Figure 7.15, even for a shear speed that does not exceed the limit described in Equation 7.82, we can observe the appearance of a deepening of the epilimnion. The motion of the internal seiche will not be affected by entrainment only if the turbulent front generated by wind shear ($T_T = H_1/u_*$) reaches the thermocline in a time greater than one-fourth of the internal seiche, the period required for the vertical interfacial displacement ($T_T > 0.25 T_{V1H1}$):

$$\frac{T_{V1H1}}{4} > \frac{H_1}{u_*},$$

$$W > \frac{L\,H}{4\,H_1\,H_2}, \tag{7.88}$$

in which L is the length of the basin, H is the total water depth, and H_1 and H_2 are the thicknesses of the epilimnion and hypolimnion, respectively.

Now compare the magnitude of this regime with the limits presented in Figure 7.14. As you will see, this regime will always fall into the regime of highest value W, when entrainment occurs only due to stirring.

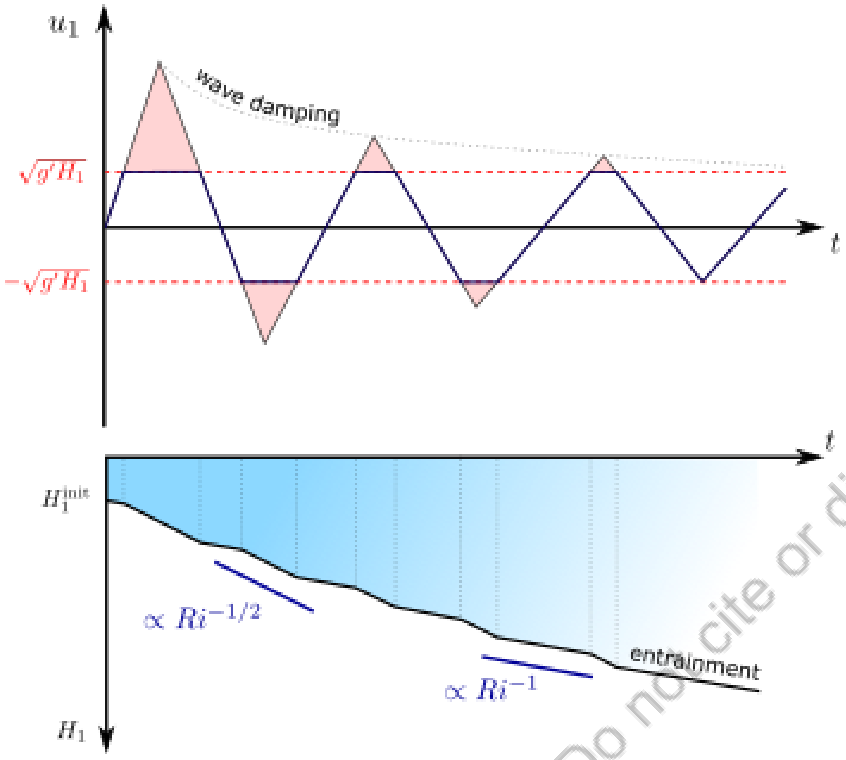

Figure 7.15 The contribution of shear to the deepening of the upper well-mixed layer. The upper figure indicates the shear oscillation as a result of the internal seiche motion, considering the damping mechanism. The lower figure illustrates the erosion of the surface boundary layer, in which a higher entrainment velocity ($\propto 1/\sqrt{Ri}$) is observed when the shear of the velocity exceeds the value proposed by Equation 7.82.

We can also consider the case where the thermocline is eroded to the bottom before the setup time ($T_{V1H1}/4$). In this case, we will not observe the evolution of the internal wave, since the thermocline will erode to the bottom of the lake before the interface is tilted. Mathematically, this condition would be observed when

$$\frac{T_{V1H1}}{4} > \underbrace{\frac{H_1\sqrt{g'\,H_1}}{u_*^2}}_{\text{Term 1}} + \underbrace{\frac{H_2\sqrt{g'\,H_1}}{u_*^2}}_{\text{Term 2}}, \tag{7.89}$$

in which the right-hand site describes the time of the turbulent front that last reached the lake bottom, where H is the total depth of the water and u_* is the wind shear velocity. Term 1 shows the time it takes for the layer to accelerate to reach the wave phase speed ($\sqrt{g'H_1}$), while term 2 describes the time it takes for the layer to deepen to the bottom by shear. Note now that the velocity is parameterized by the Richardson number, taking into account the phase velocity of the wave, since it is the maximum velocity that the layer could reach.

Substituting the theoretical period of interfacial waves for shallow waters into equation 7.89 and rearranging gives

$$W < \frac{H_1}{2\sqrt{H\,H_2}}, \tag{7.90}$$

which indicates that internal waves are not susceptible to be excited, since before the interface could be tilted, the thermocline is eroded to the bottom of the lake. However, even for values of W higher than those prescribed by Equation 7.90, we can expect a strong influence of entrainment on the formation of internal seiches.

7.3 Lake number

The Lake number (L_N) describes the ratio of moments about the centroid of the lake (Figure 7.16), characterizing the dynamic stability of the water column:

$$L_N = \frac{M_{\text{strat}}}{M_{\text{wind}}}, \tag{7.91}$$

where the wind shear applied to the water surface acts to promote a vertical displacement, contributing to lake mixing. While the gravity force resulting from density stratification tends to force the system to return to equilibrium, inhibiting mixing between layers.

The momentum around the centroid of the lake applied by the wind on the water's surface is described as

$$M_{\text{wind}} = z_v \int \sigma_{\text{wind}}\, \mathrm{d}A_o, \tag{7.92}$$

in which $\sigma_{\text{wind}} = \rho_o\ u_*$ is the shear stress of the wind, ρ_o density of the water surface, u_* is the wind shear velocity, z_v is depth of the centroid of the lake, and A_o is the lake surface area (Figure 7.16).

The stabilizing moment promoted by the force of gravity can be defined as

$$M_{\text{strat}} = \int F_x(z)\ \sin\theta \mathrm{d}z, \tag{7.93}$$

in which the F_x is the force of the water mass of each layer to return to equilibrium position from a vertical deflection θ.

Taking the definition of F_x, equation 7.93 can be reduced to

$$M_{\text{strat}} = \int (\rho_z - \overline{\rho})(z - z_*) g A_z \sin\theta \mathrm{d}z, \tag{7.94}$$

Considering that the Schmidt stability (W_s) can be written as equation 2.19 and the horizontal extension of the vertical displacement is much higher than the vertical deflection, equation 7.94 becomes

$$M_{\text{strat}} = A_o\ W_s\ \theta, \tag{7.95}$$

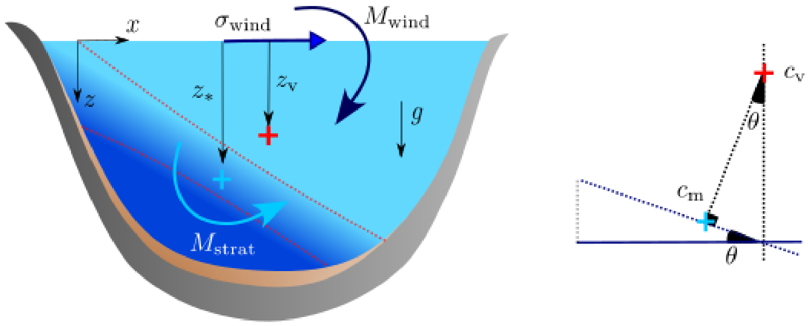

Figure 7.16 Schematic representation of the moment balance of a stratified lake when the wind induces a thermocline upwelling. σ_{wind} is the shear stress of the wind, g is the acceleration of gravity, z_* is the distance between the center of mass (approximated as the center of the metalimnion), and the water surface, z_v is the distance between the centroid of the lake (center of volume) and the water surface. M_{wind} and M_{strat} show the orientation of the moment about the centroid for wind and the mass of water, respectively. c_m and c_v are the center of mass and the centroid of the lake, respectively. θ is the angle formed between the vertical line aligned with the centroid of the lake and the center of mass.

in which A_o is the area of the lake surface and W_s is the Schmidt stability (equation 2.19).

Finally, combining equations 7.91, 7.92, and 7.94, we find that

$$L_N = \frac{A_o\ W_s\ \theta}{\rho_o\ u_*^2\ A_o\ z_v}. \tag{7.96}$$

The angle of the vertical displacement θ can be approximated as

$$\theta \approx \frac{z_*}{\sqrt{A_o}}, \tag{7.97}$$

note that we have scaled the fetch with the square root of the surface area of the lake (Imberger, Patterson, 1989).

Applying equation 7.97 into equation 7.96, we find the formal definition of the Lake number (L_N):

$$L_N = \frac{W_s\ z_*}{\rho_o\ u_*^2\ A_o^{1/2}\ z_v}. \tag{7.98}$$

The Lake number has been widely used as an indicator of the thermal stability of lakes and upwelling events (Coman, Wells, 2012; Lin et al., 2021; Dorostkar, Boegman, 2013). and also in combination with the Wedderburn number to predict the internal seiche activity of higher vertical modes (Imberger, Patterson, 1989). The microstructure taken in the Canning Reservoir showed that even during low Wedderburn number conditions, high Lake number led to stronger mixing in the surface layer and small response of the metalimnion (Imberger, Patterson, 1989). Measurements made on Lake Opengo indicated that small values of Lake number correlated well with temperature inversions in the nearshore benthic boundary layer, indicating a higher thermocline tilt (Coman, Wells, 2012).

7.3.1 Relationship between Wedderburn number and Lake number

The Wedderbun number and the Lake number are dimensionless numbers often used to predict the occurrence of internal seiche, and upwelling events, and to describe the mixing of stratified lakes. They are obtained from a different methodology. Although the Wedderburn number is derived from the ratio of the stabilizing buoyancy gradient to the velocity shear that can cause turbulent mixing, the Lake number is derived from the ratio of moments about the centroid of the lake. Although both quantities describe the stability of the system based on stratification and wind shear, the lake number takes into account the variability induced by the bathymetry of the lake. Note that this does not mean that the method captures the destabilization of upwelling events when the upwelling interface propagates to the shore in a reservoir-shaped lake (Lorke et al., 2008; Carvalho Bueno de et al., 2023). The method only considers the contribution of bathymetry induced by the distance between the centroid and the center of mass.

To analyze the difference between Wedderburn number and Lake number in a more simplified environment, consider a reservoir-shaped lake (Figure 7.17), the Schmidt stability W_s can be reduced to:

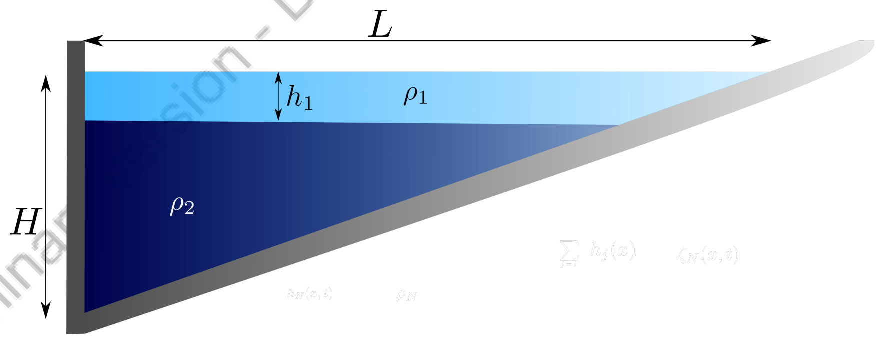

Figure 7.17 Schematic representation of a reservoir-shaped lake with surface area of $A_o = B\,L$, in which L is the lake length and B is the lake width.

$$W_s = \frac{g}{A_o}\int_0^H \rho_z\, A_z\,(z - z_v)\,\mathrm{d}z = \frac{g}{A_o}\int_0^H \rho_z\, A_z\left(z - \frac{H}{3}\right)\mathrm{d}z, \tag{7.99}$$

in which g is the acceleration fo gravity, A_o is the area of the reservoir surface, H is the maximum depth of the reservoir, and z_v is the depth of the centroid of the reservoir. Note that, unlike the rectangular-shaped box tank, the surface area of the layer z (A_z) is not constant but varies with the layer z, according to the bottom slope (H/L). This relation can be easily found through a linear regression:

$$A_z = -\frac{LB}{H}\,z + L\,B, \tag{7.100}$$

in which B is the reservoir width.

Thus, considering the model illustrated in Figure 7.17, equation 7.99 can be rewritten as

$$W_s = \frac{g}{A_o}\left(\int_0^{h_1} \rho_1 \left(-\frac{LB}{H}\,z^2 + \frac{4\,L\,B\,z}{3} - \frac{LBH}{3}\right)\mathrm{d}z + \int_{h_1}^{H} \rho_2 \left(-\frac{LB}{H}\,z^2 + \frac{4\,L\,B\,z}{3} - \frac{LBH}{3}\right)\mathrm{d}z\right),$$

$$W_s = g\,\Delta\rho\,h_1 \left(\frac{h_1^2}{3H} - \frac{4\,h_1}{6} + \frac{H}{3}\right). \tag{7.101}$$

7.4 Wind resonance

Generally, the resonance between internal seiche and wind-forced oscillations contributes to enhancing the amplitude of internal seiche and has been previously reported by a variety of studies in different thermally stratified lakes (Antenucci, Imberger, 2003; Simpson et al., 2011b; Vidal et al., 2007). This mechanism is usually observed when periodic wind fluctuations over the stratified basin coincide with an internal seiche period. Wind forcing that blows at the water's surface is typically periodic because of the periodicity of weather patterns, such as local differences in temperature and pressure that may occur over a period of days and nights (Figure **??**). Although diurnal and semi-diurnal frequency components are often observed in the wind spectrum, a different location may present a completely different persistent wind frequency. The wind pattern on Lake Kinneret presents dominant periods of 24 h and 50 h (**?**), while on Kootnay Lake the fluctuations in the wind force oscillate between 96 h and 216 h (Stevens et al., 1996).

Many studies have investigated the resonant amplification of waves in periodically forced basins numerically and experimentally (). For basins where the amplitude response is nonlinear, the resonant response is strongly dependent on the ratio of the total water depth to the lake length (H/L). However, considering the internal wave response of periodically forced lakes under shallow water conditions ($L \approx 100\ H_1$), three different regimes can be found. For large-amplitude internal waves, when the period of wind forcing that blows over the stratified basin coincides with the natural frequency of the fundamental internal seiche, the resonant fundamental internal seiche is excited, which is followed by the degeneration of internal surge to nonlinear internal waves. In addition, amplification is not restricted only to basin-scale internal waves. In this case, the non-linear and dispersive energy fluxes are also amplified (Boegman, Ivey, 2012), resulting in progressive nonlinear internal waves formed upon the fundamental internal seiche mode, as well as amplification of the nonlinear internal surges. If non-linear internal waves are large enough, Kelvin-Helmholtz instabilities may form, significantly increasing diapycnal mixing within the lake interior (Boegman, Ivey, 2012).

When the period of wind forcing is greater than the natural frequency of the fundamental internal seiche, forced internal seiche response can be excited. Usually this type of wave.....

When the period of wind forcing is lower than the natural frequency of the fundamental internal seiche, in addition to the fundamental internal seiche mode, internal seiche with higher horizontal modes can be generated.

In all cases, experimental results indicate that the degree of resonant amplification is inversely proportional to the strength of the forcing frequency. Although this could be....

The phenomenon of wind-wave resonance is also effective in amplifying internal seiches of higher vertical modes, which are not commonly energized by the surface wind (Boegman, Ivey, 2012). Similarly to the fundamental mode, when the wind force frequency matches one of the higher vertical mode frequencies, this mode can be amplified.

7.5 Internal seiche degeneration and Internal wave spectra

Field studies have shown that long-standing internal waves decay at a rate greater than what internal dissipation can account for (Imberger, 1994), which means that internal seiche is not only susceptible to being damped by bottom friction. The energy deposited into such long internal waves is eventually transformed through a down-scale energy cascade across the spectrum of internal waves into dissipative motions over the reservoir topography. Energy from internal seiches can be transferred to higher-frequency internal waves, exciting other internal waves with much shorter wavelengths, before dissipation. Figure **??** shows two mechanisms of internal seiche damping. The first one is controlled essentially by bottom friction, whilst the second is controlled by the transference of energy from basin-scale internal waves to high-frequency internal waves, which are susceptible to propagate to the lake shore and break in on the sloping boundary. Recent studies have also revealed that internal seiches also shoal near the lakeshore due to the bathymetry slope (ref). In addition, due to the tendency of internal wave energy to propagate vertically along the water column, the wave can be trapped into slope boundaries, generating internal wave attractors, paths in which internal wave converge or diverge in a confined basin after multi reflections from lateral boundaries. This mechanism is better discussed in Section **??**. Depending on the components of the wavevector and the bottom boundary slope, internal waves can be completely dissipated right after generation.

To understand different regimes of internal seiche degeneration, we must first discuss the different mechanisms responsible for extracting energy from long internal seiches. We start by presenting a simple model scheme. In this first analysis, we only consider a two-layer stratification. We will see in Section **??** that continuous stratification may generate different mechanisms responsible for the internal seiche dissipation (e.g. internal wave attractors).

Using the model scheme described by the governing equation of motion 6.102 and applying the Boussinesq approximation and neglecting the shear stress at the water surface, we have

$$\frac{\partial u_1}{\partial t} = -g\frac{\partial \zeta_1}{\partial x}, \tag{7.102a}$$

$$\frac{\partial u_2}{\partial t} = -g\frac{\partial \zeta_1}{\partial x} - g'\frac{\partial \zeta_2}{\partial x}. \tag{7.102b}$$

Unlike the model scheme described in Equation 6.102, we now take into account the fluctuation of surface water. Thus, solving equations 7.102 with a finite difference procedure along the extension of the rectangular shaped-box tank, from $\zeta_1(x=0) = -a_1$ to $\zeta_1(x=L/2) = 0$ and from $\zeta_2(x=0) = \zeta_{2(x=0)}$ to $\zeta_2(x=L/2) = \zeta_{2(x=L/2)}$, we find the following:

$$\frac{\partial u_1}{\partial t} = -\frac{2\,g\,a_1}{L}, \tag{7.103a}$$

$$\frac{\partial u_2}{\partial t} = -\frac{2\,g\,a_1}{L} + g'\frac{2\,\Delta\zeta_2}{L}. \tag{7.103b}$$

where $\Delta\zeta_2 = a_2$, in which a_2 is the internal seiche amplitude.

Substituting equation 7.103a into 7.103b gives

$$\frac{\partial}{\partial t}\left(u_2 - u_1\right) = \frac{2\,a_2\,g'}{L} \tag{7.104}$$

Finally, applying mass conservation ($u_1\,H_1 + u_2\,H_2 = 0$), we can write both velocities as a function of internal seiche amplitude only. The velocity of the lower layer is given by

$$\frac{\partial}{\partial t}\left(u_2\left(1+\frac{H_2}{H_1}\right)\right) = \frac{H}{H_1}\frac{\partial u_2}{\partial t} = \frac{2\,a_2\,g'}{L}$$

Following the same procedure for both layers, we obtain the velocities u_1 and u_2:

$$u_1 = -\frac{2\,a_2\,g'}{L}\frac{H_2}{H}\,t, \tag{7.105a}$$

$$u_2 = \frac{2\,a_2\,g'}{L}\frac{H_1}{H}\,t. \tag{7.105b}$$

Shear velocity
Note that the shear velocity between layers can be described by the difference between the upper (7.105a) and lower layer (7.105b), thus,

$$\Delta u = \frac{2\,a_2\,g'\,t}{L}. \tag{7.106}$$

Table 7.8 Shear velocity across layers.

7.5.1 Internal wave damping

Viscous losses occur at the hypolimnion-epilimnion interface and in the benthic boundary layer. This viscous damping is quantified by the time scale associated with the internal seiche energy and the rate of energy dissipation. The viscous effects can reduce the amplitude of internal seiches by energy dissipation induced by shear stress at solid boundaries and between layers that flow in opposite directions (see section 7.2). The time scale of wave damping (Eq. 7.67) can be easily obtained considering the balance between the wave energy and the energy dissipated on the solid boundaries:

$$T_{\text{damp}} = \frac{\forall}{A_o\,\delta}\;T_{\text{V1H1}} \tag{7.107}$$

Recall that in equation 7.107 we neglected the dissipation along the fluid interface. According to studies, energy dissipation in the interior of real lakes is sometimes neglected because energy dissipation in the benthic boundary layer is much greater than in the hypolimnion-epilimnion interface MacIntyre (2010). This assumption is not necessarily true for experiments performed in laboratory tanks, in which the time scale of wave damping should be estimated by equation 7.63.

7.5.2 Instability

The formation of these billows can occur in a stratified fluid when the shear velocity of each layer causes shear stress at the interface layer. As a result, the flow becomes unstable, leading to mixing or Kelvin-Helmholtz billow formations, which is characterized by a partial spiral almost crashing stationary wave (Figure **??**). The mixing process contributes to the destruction of pycnocline and the transport of species into the hypolimnion. When Kelvin-Helmholtz billows develop, a considerable interfacial shear has a maximum value at the nodal point. This type of instability can be analyzed using the local Richardson number. For a Boussinesq fluid, the perturbation increases exponentially if the Richardson number is less than 0.25 Miles (1961):

$$Ri = \frac{g'\,\Delta h_\rho}{\Delta u_{\text{KH}}^2} = \frac{1}{4}, \tag{7.108}$$

in which g' is the reduced gravity, Δu_{KH} is the shear velocity between layers, and Δh is the thickness of the metalimnion, which is not the difference between H_2 and H_1.

Rearranging equation 7.108, the critical shear velocity u_{KH} is defined as:

$$\frac{g'\,\Delta h}{\Delta u_{\text{KH}}^2} = \frac{1}{4},$$

$$\Delta u_{\text{KH}} = 2\sqrt{g'\,\Delta h_\rho}, \tag{7.109}$$

which characterizes the maximum shear velocity necessary to generate Kelvin-Helmholtz billows.

Applying 7.106 to equation 7.110, we find the timescale in which the flow starts to generate Kelvin-Helmholtz instabilities:

$$\frac{2\,a_2\,g'\,T_{\text{KH}}}{L} = 2\sqrt{g'\,\Delta h_\rho},$$

$$T_{\mathrm{KH}} = \frac{L}{a_2}\sqrt{\frac{\Delta h}{g'}}. \tag{7.110}$$

Using the fundamental wave period obtained from the shallow water equations, we can find equation 7.110 as a function of the fundamental internal wave period:

$$T_{\mathrm{KH}} = \frac{1}{2\,a_2}\sqrt{\frac{H_1\,H_2\,\Delta h_\rho}{H}}\,T_{\mathrm{V1H1}}. \tag{7.111}$$

Note that this Ri defined in the equation 7.108 is related to the velocity of the water flow and is not directly associated with the shear created by the action of the wind, as defined in Section 7.2. When the internal wave creates a strong shear across the pycnocline, Ri falls below 0.25. In this criterion, if the system is not completely mixed, Kelvin-Helmholtz billows form at the node of the internal seiche. Although equation 7.110 only describes the criteria for long internal seiches becoming unstable, the higher frequency waves can also induce local billowing separately. Kelvin-Helmholtz billows can be generated before the formation of internal seiches, according to the criteria discussed in Section 7.2.

7.5.3 Nonlinear mechanisms

Another mechanism that promotes the degeneration of basin-scale internal waves is those associated with nonlinear processes, which can be described by the *extended Korteweg-de Vries equation (eKdV)*. The *KdV equation* describes the balance between nonlinear wave steering and linear wave dispersion and can be applied to a wide range of weakly nonlinear long wave problems, including nonlinear surface and internal waves. The extended version of *Korteweg-de Vries (KdV) equation* describes the propagation of unidirectional internal solitary waves of weak to moderate amplitude (Grimshaw, 2002).

Assuming that the wave propagates along a basin of constant depth and neglects surface waves by the rigid-lid approximation, we have the following.

$$\frac{\partial \zeta_2}{\partial t} + c_p\,\frac{\partial \zeta_2}{\partial x} + \underbrace{\left(\alpha_1\,\zeta_2 + \alpha_2\,\zeta_2^2\right)\frac{\partial \zeta_2}{\partial x}}_{\text{Nonlinear terms}} + \underbrace{\beta\,\frac{\partial^3 \zeta_2}{\partial x^3}}_{\text{Dispersive term}} = 0, \tag{7.112}$$

in which ζ_2 is the amplitude of the internal wave, c_p is the phase speed of the linear internal wave, and α_1 and α_2 are non-linear parameters related to wave steepening:

$$\alpha_1 = \frac{3\,c_p}{2}\left(\frac{H_1 - H_2}{H_1\,H_2}\right), \tag{7.113a}$$

$$\alpha_2 = -\frac{3\,c_p}{8}\left(\frac{1}{H_2^2} + \frac{1}{H_1^2} + \frac{1}{H_1\,H_2}\right). \tag{7.113b}$$

Nonlinear steepening
Note that for a thin thickness of the epilimnion ($H_1 < H_2$), an internal wave of depression form will be generated.

Table 7.9 Nonlinear steepening

The coefficient β is the wave dispersion coefficient, given by

$$\beta = \frac{c_p\,H_1\,H_2}{6}. \tag{7.114}$$

Nonlinear steepening

Generally, for non-linear internal waves, the non-linear term is responsible for wave steepening. The wave solution steepens ahead of the crest, and a hydraulic jump or shock wave is generated. The initial steepening due to nonlinear effects of a nondispersive internal wave (Fig. **??**) can be described by equation 7.112 considering $\beta = 0$. To facilitate the solution of the problem, we may consider a steepening mechanism of first order only ($\alpha_2 = 0$). Balancing the unsteady and the first-order nonlinear terms leads to a timescale of wave steepening:

$$\frac{\partial \zeta_2}{\partial t} + \left(\alpha_1\, \zeta_2\right) \frac{\partial \zeta_2}{\partial x} = 0$$

$$T_{\text{steep}} = \frac{L}{\alpha_1\, a_2} = \frac{2\, L}{3 c_p\, a_2} \left(\frac{H_1\, H_2}{H_1 - H_2}\right), \tag{7.115}$$

Since c_p is the phase speed of the linear fundamental internal seiche, applying equation 6.99 into 7.115 gives us:

$$T_{\text{steep}} = \frac{1}{3\, a_2} \left(\frac{H_1\, H_2}{H_1 - H_2}\right) T_{\text{V1H1}}, \tag{7.116}$$

which notes that the higher the wave amplitude, the faster the internal seiche feels non-linear effects and the internal seiche is susceptible to degenerating into non-linear internal waves. In addition, note that the nonlinear effect can be neglected when $H_1 \approx H_2$.

Nonlinear dispersion

As the wave steepens, its horizontal length scales drop due to dispersive effects. Therefore, eventually high-frequency waves develop. The timescale associated with the dispersion mechanism is described by the balance between the unstable and dispersion terms of *Korteweg-de Vries (KdV) equation* (Eq. 7.112):

$$\frac{\partial \zeta_2}{\partial t} + \beta\, \frac{\partial^3 \zeta_2}{\partial x^3} = 0,$$

$$T_{\text{disp}} = \frac{L^3}{\beta} = \frac{6\, L^3}{c_2\, H_1\, H_2}. \tag{7.117}$$

Similar to the procedure before, considering that c_p is the phase speed of the linear fundamental internal seiche defined by equation 6.99, equation 7.117 reduces to:

$$T_{\text{disp}} = \frac{3\, L^2}{H_1\, H_2}\, T_{\text{V1H1}}. \tag{7.118}$$

Analyzing equation 7.118 we may conclude that the dispersion effect can be neglected for most lakes since $L^2 \gg H_1\, H_2$. However, as the wave starts to steepen its horizontal length λ decreases until the dispersive term cannot be neglected anymore. Often the nonlinear effect combined with the dispersion mechanism

Wave steepening domination
When $T_{\text{steep}} \ll T_{\text{disp}}$, the steep wave dominates the wave degeneration over dispersion, which occurs when:

$$\frac{\partial \zeta_2}{\partial t} + \beta\, \frac{\partial^3 \zeta_2}{\partial x^3} = 0,$$

Table 7.10 Nonlinear steepening

leads to a non-linear process that transfers energy from basin-scale internal waves to solitary internal waves, high-frequency internal waves that propagate with constant phase speed. Studies have identified that internal waves formed after storm passage contained higher energy levels than expected on the internal seiche field (Saggio, Imberger, 1998a). They pointed out that higher-frequency waves, identified as non-linear internal waves, were responsible for the increase in energy. The decay times and the time-varying spectra suggest that energy is quickly transferred within the internal wave spectrum from the internal seiches to high-frequency waves. The degeneration of internal seiches occurs primarily as a result of turbulence production in the benthic boundary layer. Although higher-frequency waves tend to be nonlinear, their amplitude and wavelength are variable and must be considered to better explain the nonlinear behavior. According to field measurements conducted in long lakes, high-frequency waves tend to disappear as a result of dissipation and dispersion (Mysak, 1984). However, in shorter lakes, short waves are seen to travel back and forth along the basin several times. Although fundamental internal seiche often contains more than 98% of the wave energy field, the transfer of energy from long waves to shorter waves has important consequences for mixing in stratified closed water bodies, since high-frequency waves can shoal and break at the basin boundaries, dissipating more than 70% of their energy at first interaction with the basin shore (Boegman et al., 2005a). The degeneration of internal seiche into high-frequency internal waves is often observed in most lakes and reservoirs (Horn et al., 2001; Lorke et al., 2006; Lorke, 2007).

7.5.4 Supercritical Flow

Many studies have identified internal bores in thermally stratified lakes (Hunkins, Fliegel, 1973; Farmer, 1978; Wiegand, Chamberlain, 1987). Nonlinear bores are typically hydraulic jumps that represent a transition of the flow regime from subcritical to supercritical flows (Cossu, Wells, 2013). Internal bores (Figure **??**) have often been observed due to the interaction between basin-scale internal waves and the bottom of the lakeshore (Saggio, Imberger, 1998b), large-amplitude internal seiches (), and supercritical conditions . The degeneration of internal seiche, even in rectangular shaped-box tanks can favor the formation of internal bores.

Although this kind of flow is frequently observed in oceans as a result of tidal flow over topographic features and has been identified in some lakes, this frequency is too high to support thermal stratification in many lakes. Generally, since internal bores are generated when the Wedderburn number (W) drops below 1 (MacIntyre et al., 2009), the system is mixed before internal bores can develop (Carvalho Bueno de et al., 2020).

Internal seiches produce higher vertical velocities in the center of the basin and lower on the lakeshore. If the wave amplitude is relatively high (low Wedderbun number W), the flow may be supercritical in the center of the lake and subcritical in the coastal areas of the lake. This transition of the flow regime gen-

Internal bore Vs Internal surge
Unlike internal bore, which is a hydraulic jump generated by supercritical conditions, internal surge

Table 7.11 Internal bore and internal surge erates an internal hydraulic jump, also called an internal bore. Thus, considering a two-layer system, the flow in the epilimnion becomes critical when

$$Fr^2 = \frac{u_1^2}{g'\,H_1} + \frac{u_2^2}{g'\,H_2} = 1 \tag{7.119}$$

Using the velocities defined by equation 7.105, equation 7.119 is reduced to

$$\begin{aligned} Fr &= \frac{T_{\text{bore}}^2}{g'\,H_1}\left(\frac{2\,g'\,a_2\,H_2}{H\,L}\right)^2 + \frac{T_{\text{bore}}^2}{g'\,H_2}\left(\frac{2\,g'\,a_2\,H_1}{H\,L}\right)^2 = 1 \\ T_{\text{bore}} &= \frac{1}{2}\,\frac{H\,L}{a_2}\,\sqrt{\frac{1}{g'}\left(\frac{H_1\,H_2}{H_1^3 + H_2^3}\right)} \qquad (7.120) \end{aligned}$$

Substituting the fundamental internal seiche period for shallow water into the equation7.120, gives us

$$T_{\text{bore}} = \frac{T_{\text{V1H1}}}{4\,a_2}\sqrt{\frac{H\,H_1^2\,H_2^2}{H_1^3 + H_2^3}}, \tag{7.121}$$

where an internal bore can be developed when the velocity of the surface layer exceeds the internal seiche speed.

7.5.5 Degeneration diagram

The time scales of each mechanism described previously can easily be compared with each other. A simple relationship can be obtained using the thickness of the epilimnion and the amplitude of the internal seiche, a_2. Therefore, as demonstrated by equation **??**, the ratio of the initial amplitude of the internal seiche to the thermocline depth can be written as the inverse form of the Wedderburn number. Comparison of the time scales with the relationship between the Wedderburn number and the normalized thermocline depth can demonstrate which mechanism will dominate the degeneration process during the internal seiche evolution. These regimes have been confirmed by many experimental and numerical results (Horn et al., 1998, 2001; Boegman et al., 2005a,b)

The first regime is evaluated by comparing the time scale of wave damping (Equation 7.107) with the time required for nonlinear effects to become significant on the degeneration process (Equation 7.116):

$$\begin{aligned} \frac{\forall}{A_o\,\delta} &= \frac{1}{3\,a_2}\left(\frac{H_1\,H_2}{H_1 - H_2}\right), \\ \frac{a_2}{H_1} &= \frac{A_o\,\delta\,(H - H_1)}{3\,\forall\,(H - 2H_1)}, \\ W^{-1} &= \frac{A_o\,\delta\,(1 - H_1/H)}{3\,\forall\,(1 - 2H_1/H)}. \qquad (7.122) \end{aligned}$$

The other two mechanisms of internal seiche degeneration are compared independently with one-fourth of the fundamental internal seiche period. Comparing equation 7.111 with the fundamental internal seiche period, we may observe the limit when the shear layer causes a flow destabilization, leading to Kelvin-Helmholtz billow formations, which helps in internal seiche degeneration. This mechanism occurs when

$$\begin{aligned} \frac{1}{2\,a_2}\sqrt{\frac{H_1\;H_2\;\Delta h_\rho}{H}} &< \frac{1}{4}, \\ \frac{a_2}{H_1} &> \frac{1}{2}\sqrt{\frac{(H\;H_1)\Delta h_\rho}{H_1\;H}}, \\ W^{-1} &> \frac{2}{H^2}\sqrt{\frac{(1-H/H_1)\Delta h_\rho}{H_1/H}}. \end{aligned} \tag{7.123}$$

Considering that the velocity is too high in the basin center, we may consider that there will be a transition between supercritial to subcritical flow, which the energy from basin-scale internal wave will be transferred to an internal hydraulic jump (also called internal bore). Using the same analogy and equation 7.121, we may find that internal seiches are more susceptible to degenerating as an internal bore when

$$\begin{aligned} \frac{1}{4\,a_2}\sqrt{\frac{H\;H_1^2\;H_2^2}{H_1^3+H_2^3}} &< \frac{1}{4}, \\ \frac{a_2}{H_1} &> \sqrt{\frac{(H-H_1)^2}{(H-H_1)^3/H+H_1^3/H}}, \\ W^{-1} &> \sqrt{\frac{(1-H_1/H)^2}{(1-H_1/H)^3+(H_1/H)^3}}. \end{aligned} \tag{7.124}$$

Note that when Equations 7.123 and 7.124 are satisfied, both mechanisms of internal seiche degeneration may occur, which means that the internal seiche is susceptible to degenerate into internal bore and Kelvin-Helmholtz billows.

Equations 7.122, 7.123, and 7.124 can be used to draw a diagram that shows all different degeneration regimes (Figure 7.18). When the lake is under strong winds or has weak stratification conditions, the ratio a_2/H_1 decreases, and consequently, internal seiches are more susceptible to being damped by viscosity. Generally, for basins of moderate size, the viscous damping time scale varies from 28 hours to 12 days. However, large-amplitude waves steepen and evolve into high-frequency waves before its could be damped by viscosity. This criterion is satisfied for most lakes and reservoirs in moderate to strong winds when the wave amplitude is relatively high (Stevens, 1999). The steepening time scale varies strongly depending on the amplitude of the internal wave. For a lake with $H_1 = 5$ m and $H_2 = 25$ m, $T_{\text{steep}} \approx 0.8\;T_{\text{V1H1}}$ when the wave amplitude is maximum ($a_2 = H_1$). This indicates that internal seiches transfer energy into small-scale waves in a period shorter than the fundamental wave period. In this situation, we may conclude that the wave will transfer a significant amount of energy to high-frequency internal waves, and less energy will be directly dissipated on interfacial and solid boundaries.

When T_{KH} is lower than the period of internal seiche formation ($T_{\mathrm{V1H1}}/4$), Kelvin-Helmholtz billows may form. The frequency of the most unstable mode is just below the Brunt-Väisälä frequency of the thermocline Likens (2010). After this value, the system is susceptible to evolve into a billow and collapse into turbulence. In most lakes T_{KH} is around x hour.

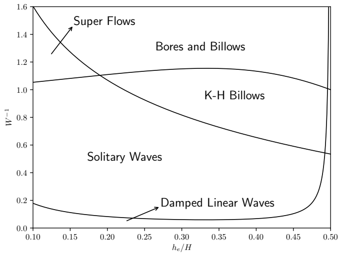

Figure 7.18 Analytical regime diagram showing a schematic structure of internal wave degeneration in lakes and reservoirs according to frequency scales.

7.5.6 Internal wave spectra

Although we have introduced the idea of turbulence spectra in Section 2.3 and discussed in detail the fundamental concepts of spectral analysis in Chapter 5.3, here we focus our analysis on the physical interpretation of the internal wave spectrum. Until now, the power spectral density of the isotherms could be used to provide information about the possible internal seiche period within the system. However, energy cascading may tell us important information about the mechanisms of internal seiche degeneration.

The energy in the internal wave field can be described by the Garrett-Munk spectrum (Garrett, Munk, 1972), which reconstructs the complete three-dimensional internal wave spectrum from the one-dimensional underwater temperature observation, providing an indication of the presence of internal waves within the system. The concepts of the Garrett-Munk spectrum are similar to those described in Section 5.3, which describes the lake as a complex mixture of fluctuations, in which some of them are waves, while others are of pure random nature (**?**). The power spectral density of the isotherms shows the oscillation response at each frequency (Thorpe, 2005). The isotherm spectrum suggests the existence of a universal spectrum that describes the decay of energy from basin-scale internal waves to small-scale turbulence (Figure 7.19). The energy cascade may characterize internal mixing in thermally stratified lakes and has been widely studied Horn et al. (1998); Imberger (2013); Horn et al. (2001); Boegman et al. (2005b,a).

The spectrum is divided into four regions. The first one is bounded at the low frequency band and comprises a large-scale motion that is often excited due to the wind stress acting at the water surface. Large-scale motion is often characterized by the evolution of internal seiches.

The second part of the internal wave spectrum ($100\ N < f < 10\ N$) describes a down-scale energy cascade that decays according to the ω^{-2}-power law, where ω is the angular frequency of the internal wave (Garrett, Munk, 1972). The energy cascade represents a transference of energy from large-scale motion to small-scale turbulence, which is characterized by the formation and evolution of high-frequency internal waves (HFIW), a mechanism described in section 7.5.3. High-frequency internal waves can be observed in the third part of the spectrum, where the frequency varies from $10\ N$ to N, and is characterized by an increase in spectral energy. Often, this pronounced peak is followed by a sharp reduction (Boegman et al., 2003; Huber et al., 2011). Evidence has also demonstrated

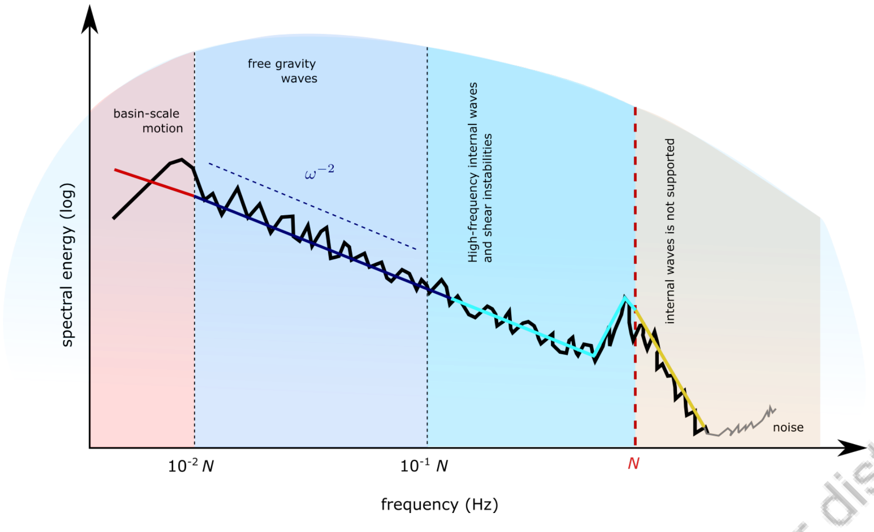

Figure 7.19 Internal wave spectra. N is the buoyancy frequency and ω is the angular frequency.

through field observations that the HFIW can also be observed in the spectrum as a simple plateau with elevated power spectral density compared to the ω^{-2}-power law (Lorke, 2007). Often, the peaks related to high-frequency internal waves are followed by a rapid decay (faster than a rate of -2) toward higher frequencies.

Research has shown that internal waves with these frequencies are not continuous, they occur in groups (Saggio, Imberger, 1998a). Although it is associated with vertical advection of high-frequency internal waves and continuous stratification, studies have shown that these waves belong to a complex field of multimodal internal waves that can be distorted by other waves with different frequencies (Saggio, Imberger, 1998a). These high-frequency internal waves may be generated from many sources, such as the interaction of horizontal flows with lake bathymetry, shear instabilities, and, most likely, due to internal seiche degeneration (Horn et al., 1998; Boegman et al., 2005a). Below the buoyancy frequency (equation **??**), the system is weakly stable to support the evolution and formation of internal waves.

Internal waves can also be detected through the power spectral density of other variables affected by internal wave motion, such as horizontal current speed (Figure 7.20a). Unlike isothermal analysis, the influence of surface waves is usually better analyzed by current speed because of resolution limitation. Temperature fluctuations at really fast motion are unlikely to be detected because the fluctuation is too small, and the spectral energy is comparable to noise fluctuations. In Figure 7.20b we can observe a distinct peak between 10 N and 100 N, followed by a rapid fall with a rate of -5. This distinct peak has a frequency much higher than the frequency of high-frequency internal waves, which are limited by buoyancy frequency N, and is more intense near the surface, suggesting that the peak of spectral energy at about 60 N observed in Figure 7.20b occurs due to surface waves. Note that applying a spectral analysis of isotherms, the analysis of the second part of the spectrum (Figure 7.20b) would not be possible due to resolution limitations.

./chapter7/.png

Figure 7.20 .

Although this is not clearly observed in Figure 7.20 due to the logarithmic scaling of the x-axis, the energy content, which can be obtained from the integration described in Equation 5.9, shows that most of the energy is concentrated in the high-frequency band, between 10^1 N and 10^2 N. This observation is consistent with studies that estimated the mechanical energy content distributed during periods of internal seiche dominance from the wind to the surface and the internal wave field, which corresponds to 10% and 1% of the wind energy input, respectively (Carvalho Bueno de et al., 2023; Guseva et al., 2021; Imboden, 2003).

7.6 Laboratory Experiments

7.7 Model

7.8 Application

Exercises

Exercises for 7.1 Internal Seiche

P7.1 Assuming a 60 km long lake that is susceptible to excite internal seiche with the first three vertical modes according to power spectral density, find the Rossby deformation radius for each mode. Explain why we should expect different values depending on the wave mode.

P7.2 Considering the regular Sturm-Liouville problem with infinite number of solutions F_j for distinct eigenvalues b_j:

$$\frac{\partial^2 F}{\partial x^2} + (A(x) + b)\, F(x) = 0,$$

with boundary condition $F(x=0) = F(x=1) = 0$, derive the orthogonality relation.

P7.3 Considering the regular Sturm-Liouville problem with infinite number of solutions F_j for distinct eigenvalues c_j:

$$\frac{\partial^2 F}{\partial x^2} + c\, A(x)\, F(x) = 0,$$

with boundary condition $F(x=0) = F(x=1) = 0$, derive the orthogonality relation.

Chapter 8

Introduction to Gravity currents

Gravity current is a primary horizontal flow driven by horizontal differences in temperature or salinity (Britter, Simpson, 1978), being observed in a wide range of natural situations and industrial processes, from atmospheric cold fronts to geostrophic ocean currents (Legg et al., 2009; Garratt, 1986). In lakes and reservoirs, river water flows can often promote the formation and propagation of gravity currents (Roget, Colomer, 1996), playing a crucial role in aquatic ecosystems and biogeochemical cycles by redistributing phytoplankton and zooplankton organisms (Scotti, Pineda, 2007), and causing the resuspension of sediments and chemical contaminants (Eames et al., 2001; Kyrousi et al., 2018). The increase in turbulence due to the evolution of the gravity current may also influence the mean flow and increase the mixing in the benthic boundary layer due to the change in the structure of the turbulence (Buckee et al., 2001). In the ocean, gravity currents are often generated by salinity differences, influencing large-scale ocean circulation and, consequently, playing an important role in the physical climate system (Legg et al., 2009; Jkedrasik, Kowalewski, 2019). Large turbidity currents have been observed in ocean basins due to sediment slumps on the upper continental slope, strongly affecting sediment transport (Pickering et al., 1992; Wynn et al., 2000; Azpiroz-Zabala et al., 2017). Gravity currents are also observed in the atmosphere, such as squalls (Auer Jr, Sand, 1966), sea-breeze fronts (Wiel van der et al., 2017), and avalanches (Hutter, 1996).

The gravity current is characterized by a thinner body and a head of the lobes formed by a series of lobes and clefts that generate frontal vortexes and shear instabilities (Hallworth et al., 1993). The head is followed by a shallower layer with low mixing with the ambient fluid, where intense mixing occurs at the back of the gravity current head (Simpson, Britter, 1979; Best et al., 2001) (Figure 8.1). Mixing is also followed by an entrainment mechanism that favors an increase in the current head volume and a dilution of the gravity current, losing part of its excess buoyancy.

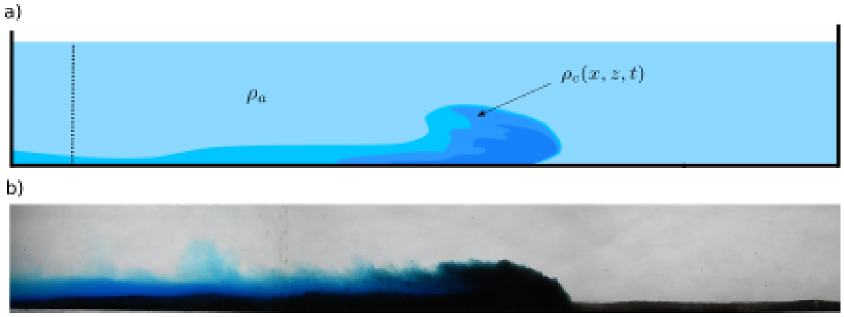

Figure 8.1 Gravity current propagating in laboratory tank. a) Illustration of the gravity current and b) image acquired by the camera of a released gravity current over an erodible bed.

8.1 The constant volume lock release

One of the simplest experiments for the gravity current and one of the most studied is the constant volume lock release, which is characterized by a fixed volume of fluid ρ_c released into a stationary ambient fluid ρ_a (Figure 8.4). Initially the system is divided by a vertical barrier in which a denser fluid is placed on one side, whilst the other is filled with a lighter fluid. When the barrier is removed, the denser fluid flows along the bottom of the channel, whereas the lighter fluid flows along the surface in the opposite direction. The gravity current propagates with speed

$$u_f = Fr\sqrt{g_o'\,h_o}, \tag{8.1}$$

where Fr is the Froude number, a dimensionless function of the density ratio ρ_a/ρ_c, h_o is the initial height occupied by the denser fluid, $g_o' = g\,\Delta\rho/\rho_c$ is the reduced gravity current, in which $\Delta\rho = \rho_c - \rho_a$.

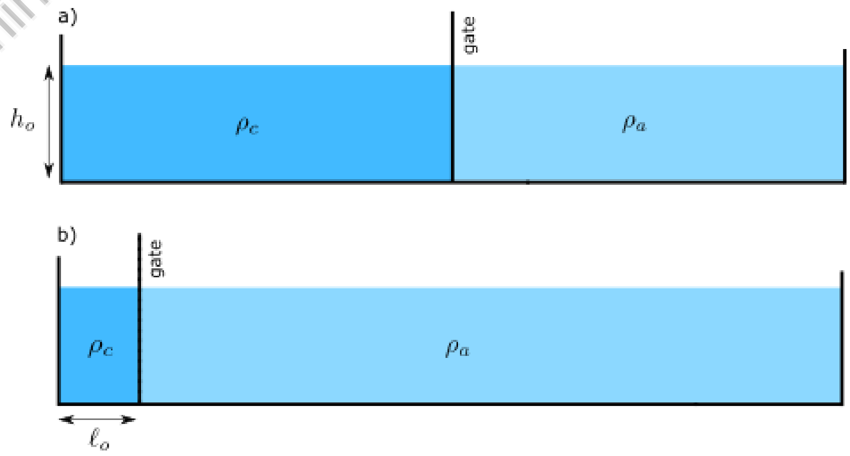

Figure 8.2 The setup of the lock-exchange experiment for a) a symmetric release and b) a non-symmetric release, in which the barrier is placed near the end of the tank.

Instantaneously after vertical barrier release, the potential energy of the denser water column is transferred to kinetic energy, accelerating the current horizontally. This initial phase is called *acceleration phase*, and occurs in a rapid time-scale. If the current has a sufficiently high Reynolds number, the gravity current reaches *slumping phase*, in which the current flows with constant speed due to the balance between inertial and buoyancy forces. Due to the finite extension of the fluid volumes, the gravity current decelerates in the subsequent stage, called *self-similar phase*. As the current decelerates, the viscous forces become important at some moment, and deceleration increases even more due to viscous forces. This phase is called *viscous phase*, and is accompanied by a strong change in head structure. All phases are detailed in sections 8.1.1 to 8.1.4, and are illustrated in Figure 8.3.

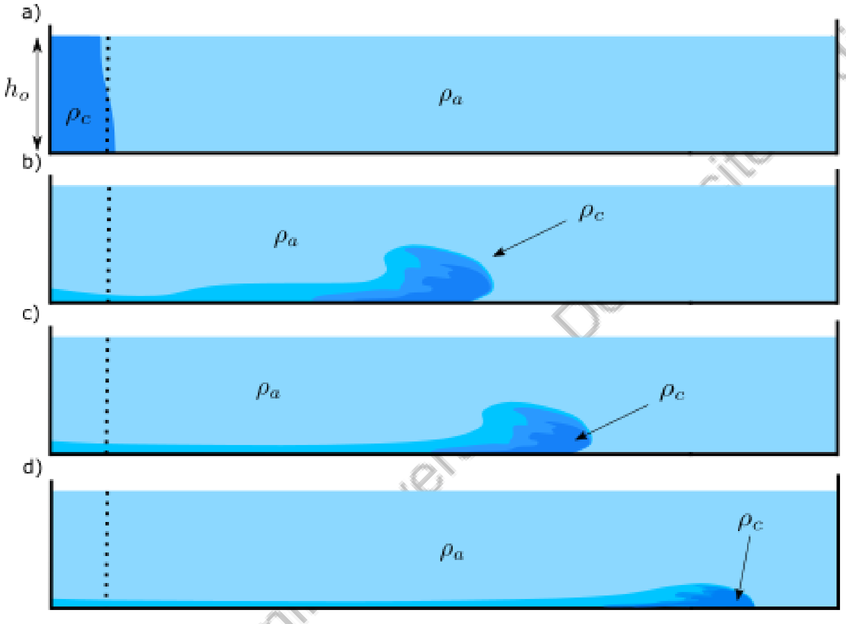

Figure 8.3 Illustration of the gravity current in each phase of the flow.

8.1.1 Acceleration phase

As the potential energy of the denser water column is transferred to kinetic energy, the gravity current starts to propagate horizontally, increasing its front speed until it is completely controlled by the balance between inertial and buoyancy forces.

The time-scale associated to the acceleration phase can be easily derived by assuming $Fr = 1$ (equation 8.1) and an uniformly accelerated motion ($a = \Delta u/\Delta t$):

$$T_a = \frac{u_f}{g'_o} = \frac{\sqrt{g'_o h_o}}{g'_o} = \sqrt{\frac{h_o}{g'_o}}, \tag{8.2}$$

where u_f is the speed of the gravity current, h_o is the height of the lock, and g'_o is the initial reduced gravity. Assuming a gravity current of $\Delta\rho = 30$ kg/m^3

and $h = 10$ cm, the time-scale associated to the acceleration phase is around 0.6 seconds, which means that the potential energy is transferred to kinetic energy in 0.6 seconds. After the acceleration phase, the gravity current reaches the constant velocity phase, where the current travels at a constant speed, characterized by a constant Froude number (equation 8.1).

8.1.2 Slumping phase

The speed of the current front is observed to be constant (within the experimental error) during the slumping phase. The current speed is controlled by the density difference between the two fluids and is described by equation 8.1, in which Fr is constant for the Boussinesq current ($\rho_a/\rho_c \approx 1$). For the classical symmetric lock-exchange release, in which the vertical barrier is placed in the center of the tank, as illustrated in Figure 8.4a, studies have shown that $Fr = 0.5$ (**?**).

Yih's analysis (1947)

Based on a finite box-shaped reservoir and assuming a non-slip condition at the upper and lower boundaries, Yih (1947) derived an expression for the current speed from the balance between potential and kinetic energy to find $Fr = 0.5$.

Assuming that the ambient and current flows have the same velocity ($u_f = u_f^c = u_f^a$), the change in potential energy per width E_P over an infinitesimal time step (Δt) can be written as:

$$\frac{\Delta E_P}{\Delta t} = \frac{\rho_i g h_i \, \Delta A s_i}{2\Delta t} = \frac{\rho_i g h_i^2}{2\Delta t} \cancelto{u_i \, \Delta t}{\Delta x_i}$$

$$\Delta E_P = \frac{\rho_c g \, u_f}{2} \left(-\frac{h_o}{2}\right)^2 + \frac{\rho_a g \, (-u_f)}{2} \left(\frac{h_o}{2}\right)^2$$

$$\Delta E_P = \frac{u_f \, h_o^2 \Delta \rho g}{4}, \tag{8.3}$$

in which g is the acceleration of gravity, u_f is the speed of the gravity current, h_o is the total water depth, and $\Delta\rho = \rho_c - \rho_a$.

The total gain of the kinetic energy E_K is

$$\frac{\Delta E_K}{\Delta t} = \frac{\rho_i u_f^2 \, \Delta A s_i}{2\Delta t} = \frac{\rho_i u_f^2 \, h \, \Delta x}{2\Delta t}$$

$$\Delta E_K = \frac{\rho_c u_f^3 \, h_o}{2} \frac{\rho_a u_f^3 \, h_o}{2}$$

$$\Delta E_K = \frac{u_f^3 \, h_o}{2} \Big(\rho_c + \rho_a\Big). \tag{8.4}$$

Taking into account $\Delta\rho \ll \rho$, we may simplify equation 8.4 to find

$$\Delta E_K = \frac{u_f^3 \, h_o}{2} \Big(\rho_c + \rho_c - \cancelto{=0}{\Delta\rho}\Big) = u_f^3 \, h_o \, \rho_c. \tag{8.5}$$

Balancing the potential and the kinetic energy, $E_P + E_K = 0$, we find that

$$u_f = \sqrt{\frac{g h_o}{4} \frac{\rho_c - \rho_a}{\rho_c}} = \sqrt{\frac{g' h_o}{4}}, \tag{8.6}$$

in which $g' = g \Delta\rho / \rho$ is the reduced gravity.

Rearranging the equation 8.6, give us

$$u_f / \sqrt{g' h_o} = 0.5, \tag{8.7}$$

where the $u_f / \sqrt{g' h_o}$ is know as the densimetric Froude number (Fr) and h_o is the initial height of the gravity current fluid.

However, since fresh water flows along the surface and the denser current flows along the bottom of the channel underneath fresh water, both currents suffer different shear stresses. Studies have formulated a more appropriate expression taking into account the conditions of the bottom and free surface. **?** found $Fr = 0.465$ and $Fr = 0.590$ for the bottom and surface gravity currents, respectively.

Local Froude number

Other studies have proposed different values of the Froude number, which extend the theoretical results for different conditions. Based on the shallow-water framework, the Froude number can be parameterized by the local values of the front, called *front Froude number* or *local Froude number* (Fr_f):

$$Fr_f = \frac{u_f}{\sqrt{g'_f \, \overline{h_h}}}, \tag{8.8}$$

in which u_f is the speed of the current front, g'_f is the local reduced gravity, and $\overline{h_h}$ is the height of the local gravity current.

The value of the Froude number based on the local current characteristics of the head has been studied by many authors (Benjamin, 1968; Rottman, Simpson, 1983; Huppert, Simpson, 1980).

Benjamin (1968)

During this constant velocity phase, Benjamin (1968) has proposed, considering energy conservation theory, that the local Froude number is only dependent on the relationship between the local current height and the depth of the ambient fluid ($\overline{h_h}/h_a$). When balancing the total pressure force (per unit of span) across a section up and downstream (Figure **??**), we may find that

$$P_1 = P_2,$$

$$\frac{\rho\, c_1^2\, h_a}{2} + \frac{\rho\, g\, h_a^2}{2} = \rho\, c_2^2\, h + \frac{\rho\, g\, h^2}{2}. \tag{8.9}$$

The conservation of mass, defined as

$$c_1 \, h_a = c_2 \, h, \tag{8.10}$$

can be applied to 8.9 to find the dimensionless velocity upstream:

$$\frac{c_1^2}{g \, h} = \frac{h^2 - h_a^2}{h_a \, h - 2 \, h_a^2}. \tag{8.11}$$

Another interesting result is the dimensionless coefficient of propagation velocity based on $\overline{h_h} = h_a - h$. From Equation 8.11 and considering $\overline{h_h} = h_a - h$, we can find that

$$\frac{c_1^2}{g \, h} = \frac{(h_a - \overline{h_h})^2 - h_a^2}{h_a \, (h_a - \overline{h_h}) - 2h_a^2},$$

$$\frac{c_1^2}{g \, h} = \frac{(h_a - \overline{h_h})^2 - h_a^2}{h_a(h_a - \overline{h_h}) - 2h_a^2},$$

$$\frac{c_1^2}{g \, \overline{h_h}} = \frac{(h_a - \overline{h_h})(-2 \, h_a \, \overline{h_h} + \overline{h_h}^2)}{-h_a \, \overline{h_h} - h_a^2}$$

$$\frac{c_1^2}{g \, \overline{h_h}} = \frac{(h_a - \overline{h_h})(2 \, h_a - \overline{h_h})}{h_a \, (h_a + \overline{h_h})} \tag{8.12}$$

Assuming $\phi = \overline{h_h}/h_a$, equation 8.12 becomes:

$$Fr_{\mathrm{B}} = \frac{c_1^2}{\sqrt{g' \, \overline{h_h}}} = \sqrt{\frac{(2-\phi)(1-\phi)}{1+\phi}}, \tag{8.13}$$

in which $c_1 = u_f$ is the front velocity. For the limit of $\phi = 0.5$, the solution leads to $Fr_{\mathrm{B}} = 1/\sqrt{2} = 0.71$. The local height is unlikely to generate $\phi > 0.5$ without any external input energy. Studies have shown that even $\phi = 0.5$ is not common since interfacial mixing reduces the height of the current, limiting ϕ to 0.347, when maximum dissipation is achieved within Benjamin's framework (Benjamin, 1968).

Shin et al. (2004)

To account for the influence of the backward-propagating wave that reflects on the end wall of the tank and propagates toward the current head, studies have suggested that, for a low Reynolds number (low mixing), the Froude number is given as (Shin et al., 2004; Marino et al., 2005):

$$Fr_f = 0.5\sqrt{\phi'\left(2 - \phi'\right)}, \tag{8.14}$$

in which $\phi' = h_o/h_a$, where h_o is the current height in the original lock position, as illustrated in Figure 8.6. Note that for $\phi' = 1.0$ (shallow release), equation 8.14 yields the same value obtained by Benjamin (1968) (Eq. 8.13). For infinitely deep ambient fluids ($\phi' \approx 0$), the local Froude number estimated by Benjamin (1968) is approximately 40% higher than the value found by Shin et al. (2004).

The constant-velocity phase persists until the upper and lower motion becomes asymmetric due to the finite extension of the volume release. The asymmetric behavior is observed in the experiment that places the vertical barrier near the end wall of the channel, as illustrated in Figure 8.4b. Initially, the current propagates exactly as in a classical symmetric lock-exchange experiment (Figure **??**a). However, due to the finite length of the tank, the secondary flow is reflected by the endwall (Figure **??**b), generating an internal bore that propagates away from the wall (Figure **??**c). The reflected wave (internal bore) propagates faster than the current front Rottman, Simpson (1983), and eventually catches up the gravity current front (Figure **??**d). Observations have suggested that it usually takes 3 to 10 lock-lengths ℓ_o (Marino et al., 2005). When it occurs, the gravity current decelerates, reaching the self-similar phase, in which the gravity current starts to slow down.

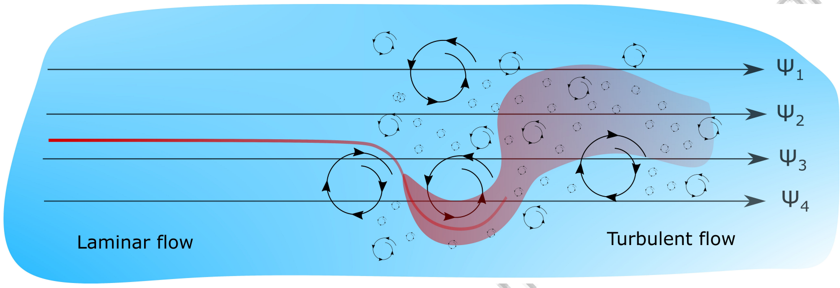

Figure 8.4 Illustrations of the collapse of a denser gravity current at successive times. The figure shows a) the symmetrical slumping phase, b) the flow reflection, c) the propagating internal bore in the current body, and d) the internal bore reaching the gravity current head, initiating the self-similar phase.

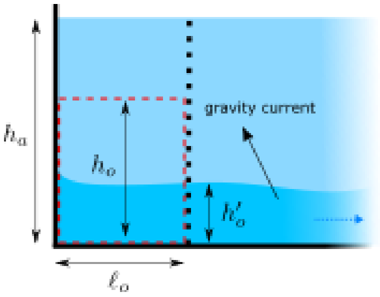

Figure 8.5 Current height definition for different theoretical framework.

Assuming that the release occurs ℓ_o from the left end wall of the tank (Figure 8.4), we can derive a timescale to determine when the flow is reflected due to the finite extension of the tank. Assuming that the upper motion travels with the same speed as the denser gravity current, we have the following.

$$T_v = \frac{\ell_o}{u_f} = \frac{\ell_o}{\sqrt{g'_o\, h_o}}, \tag{8.15}$$

in which ℓ_o is the lock length. Taking into account the same example previously and assuming that $\ell_o = 30$ cm, we obtain a $T_v = 1.8$ sec, indicating that the upper motion will reflect back in the end of the channel 1.8 seconds after the vertical release.

This time scale describes the time the flow is reflected at the end of the tank. The time-scale of the entire phase must take into account the time that takes to the internal bore catches up to the gravity current front.

8.1.3 Self-similar phase

When the finite initial volume becomes important, the speed of the gravity current starts to decrease. Although the denser fluids mix with their surroundings, mass conservation implies that the initial buoyancy ($B_o = g'_o \, \ell_o \, h$) is kept constant due to the increase in volume of the gravity current when it flows away from the release. The current length ℓ_x can be estimated by self-similar theory for a plane ($n = 0$) and axisymmetric ($n = 1$) flow (Huppert, Simpson, 1980; Rottman, Simpson, 1983). Neglecting mixing and treating the current front as an abrupt interface, the front position of the current may be determined as a function of the initial buoyancy only:

$$\ell_x(t) = \xi \underbrace{\left(g'_o \, h_o \, \ell_o\right)^{(2-n)/6}}_{\text{initial buoyancy}} t^{2/(3+n)}, \tag{8.16}$$

in which ξ is a dimensionless constant that has been estimated by many authors. Benjamin (1968) found $\xi \approx 1.89$, while Shin et al. (2004) estimated $\xi \approx 1.39$. Both theoretical coefficients have been found for slumping phase, and there is no guarantee that they are valid for the self-similar regime (Marino et al., 2005).

Studies have also suggested that ξ is related to the local Froude number Fr_f. Grundy, Rottman (1985) found ξ from the height profile for a self-similar plane gravity current:

$$\xi = \left(\frac{27Fr_f^2}{12 - 2Fr_f^2}\right)^{1/3}. \tag{8.17}$$

Deriving in time the ℓ_x we can find an expression for the gravity current speed for the self-similar phase:

$$u_f = \frac{2}{3+n} \, \xi \left(g'_o \, h_o \, \ell_o\right)^{(2-n)/6} t^{-(1+n)/(3+n)}, \tag{8.18}$$

which indicates that the gravity current decelerates as $t^{-1/3}$ and $t^{-1/2}$ for the planar and axisymmetric currents, respectively. In this phase, the gravity current head decreases until the flow becomes laminar, leading to small mixing and no formation of billowing structures. Studies have shown that equation 8.18 works in infinity deep ambient only, which is represented by partial depth release or large-time limits (**?**Grundy, Rottman, 1985).

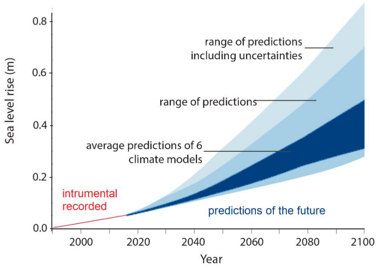

Figure 8.6 Shape of the gravity current head affected by viscous force.

8.1.4 Viscous phase

As the gravity current decelerates, the Reynolds number decreases and viscous forces starts to play an important role on the gravity current evolution, decelerating even more the current front. This effects leads to a higher decrease of the current head height, which may also lead to a changed in shape (Figure **??**)

To quantify the importance of viscous forces, the Reynolds number Re_f should be calculated,

$$Re_f = \frac{u_f \, h_f}{\nu}, \tag{8.19}$$

in which ν is the kinematic viscosity of the fluid (m^2/s), h_f is the relative height of the gravity current head, and u_f is the front speed of the gravity current. When $Re_f \gg 1,000$, the gravity current is essentially driven by the balance between buoyancy and inertial forces, resulting in a pronounced current head (Fig. **??**). When $Re_f \ll 1,000$, gravity current is susceptible to high dissipation rate due to viscous forces, leading to further dependence of velocity on time. In this phase, the balance between inertial and viscous forces leads to $U \sim t^{-4/5}$.

This phase does not come just after the self-similar phase. In case of a initial low Reynolds flow, the viscous forces may play an important role right after the acceleration phase. The time-scale associate to this phase is associated to the viscous phase quantities, and may not be described by the initial condition of the flow:

$$T_\nu = \frac{\nu\, \ell_\nu^2}{g'_\nu\, h_\nu^3}, \tag{8.20}$$

where each variable here is associated to the viscous phase.

Bibliography

Ahmed Sultan, Troy Cary D., Hawley Nathan. Spatial structure of internal Poincaré waves in Lake Michigan // Environmental Fluid Mechanics. 10 2014. 14, 5. 1229–1249.

Alford Matthew H, Peacock Thomas, MacKinnon Jennifer A, Nash Jonathan D, Buijsman Maarten C, Centurioni Luca R, Chao Shenn-Yu, Chang Ming-Huei, Farmer David M, Fringer Oliver B, others . The formation and fate of internal waves in the South China Sea // Nature. 2015. 521, 7550. 65.

Antenucci Jason P, Imberger Jörg. On internal waves near the high-frequency limit in an enclosed basin // Journal of Geophysical Research: Oceans. 2001. 106, C10. 22465–22474.

Antenucci Jason P, Imberger Jörg. The seasonal evolution of wind/internal wave resonance in Lake Kinneret // Limnology and oceanography. 2003. 48, 5. 2055–2061.

Antenucci Jason P, Imberger Jörg, Saggio Angelo. Seasonal evolution of the basin-scale internal wave field in a large stratified lake // Limnology and oceanography. 2000. 45, 7. 1621–1638.

Arakawa Akio, Lamb Vivian R. Computational design of the basic dynamical processes of the UCLA general circulation model // General circulation models of the atmosphere. 1977. 17, Supplement C. 173–265.

Auer Jr August H, Sand Wayne. Updraft measurements beneath the base of cumulus and cumulonimbus clouds // Journal of Applied Meteorology. 1966. 5, 4. 461–466.

Azpiroz-Zabala Maria, Cartigny Matthieu J B, Talling Peter J, Parsons Daniel R, Sumner Esther J, Clare Michael A, Simmons Stephen M, Cooper Cortis, Pope Ed L. Newly recognized turbidity current structure can explain prolonged flushing of submarine canyons // Science advances. 2017. 3, 10. e1700200.

Baracchini Theo, Hummel Stef, Verlaan Martin, Cimatoribus Andrea, Wüest Alfred, Bouffard Damien. An automated calibration framework and open source tools for 3D lake hydrodynamic models // Environmental Modelling \& Software. 2020. 134. 104787.

Bauerle E. Internal free oscillations in the Lake of Geneva // Annales Geophysicae. 3, 2. 1985. 199–206.

Bäuerle Erich. Transverse baroclinic oscillations in Lake Überlingen // Aquatic sciences. 1994. 56, 2. 145–160.

Benjamin T Brooke. Gravity currents and related phenomena // Journal of Fluid Mechanics. 1968. 31, 2. 209–248.

Bernhardt Juliane, Kirillin Georgiy. Seasonal pattern of rotation-affected internal seiches in a small temperate lake // Limnology and oceanography. 2013. 58, 4. 1344–1360.

Best J L, Kirkbride A D, Peakall J. Mean flow and turbulence structure of sediment-laden gravity currents: new insights using ultrasonic Doppler velocity profiling // Particulate gravity currents. 2001. 157–172.

Boegman Leon, Imberger Jorg, Ivey Greg N, Antenucci Jason P. High-frequency internal waves in large stratified lakes // Limnology and oceanography. 2003. 48, 2. 895–919.

Boegman Leon, Ivey G N, Imberger J. The degeneration of internal waves in lakes with sloping topography // Limnology and oceanography. 2005a. 50, 5. 1620–1637.

Boegman Leon, Ivey G N, Imberger J. The energetics of large-scale internal wave degeneration in lakes // J Fluid Mech. 2005b. 531. 159–180.

Boegman Leon, Ivey Gregory N. The dynamics of internal wave resonance in periodically forced narrow basins // Journal of Geophysical Research: Oceans. 2012. 117, C11.

Boehrer Bertram, Dietz Severine, Rohden Christoph von, Kiwel Uwe, Jöhnk Klaus D., Naujoks Sandra, Ilmberger Johann, Lessmann Dieter. Double-diffusive deep water circulation in an iron-meromictic lake // Geochemistry, Geophysics, Geosystems. 6 2009. 10, 6. n/a–n/a.

Boehrer Bertram, Herzsprung Peter, Schultze Martin, Millero Frank. J. Calculating density of water in geochemical lake stratification models // Limnology and Oceanography: Methods. 11 2010. 8, 11. 567–574.

Boehrer Bertram, Ilmberger Johann, Münnich Karl Otto. Vertical structure of currents in western Lake Constance // Journal of Geophysical Research: Oceans. 2000. 105, C12. 28823–28835.

Bouffard Damien, Zdorovennov Roman E, Zdorovennova Galina E, Pasche Natacha, Wüest Alfred, Terzhevik Arkady Y. Ice-covered Lake Onega: effects of radiation on convection and internal waves // Hydrobiologia. 2016. 780, 1. 21–36.

Britter R E, Simpson J E. Experiments on the dynamics of a gravity current head // Journal of Fluid Mechanics. 1978. 88, 2. 223–240.

Bruce Louise C, Jellison Robert, Imberger Jörg, Melack John M. Effect of benthic boundary layer transport on the productivity of Mono Lake, California // Saline Syst. 2008. 4, 1. 11.

Buckee C, Kneller B, Peakall J. Turbulence structure in steady, solute-driven gravity currents // Particulate gravity currents. 2001. 173–187.

Carvalho Bueno R. de, Bleninger T.B. Wind-induced internal seiches in vossoroca reservoir, PR, Brazil // Revista Brasileira de Recursos Hidricos. 2018. 23.

Carvalho Bueno Rafael de, Bleninger Tobias. Lake dynamic during thermal stratified periods: internal seiche formation // XXIII Simpósio Brasileiro de Recursos Hídricos. Foz do Iguaçu-PR, Brazil, 2019.

Carvalho Bueno Rafael de, Bleninger Tobias, Boehrer Bertram, Lorke Andreas. Physical mechanisms of internal seiche attenuation for non-ideal stratification and basin topography // Environmental Fluid Mechanics. 5 2023.

Carvalho Bueno Rafael de, Bleninger Tobias, Lorke Andreas. Internal wave analyzer for thermally stratified lakes // Environmental Modelling \& Software. 2020.

Chu Eleanor. Discrete and continuous fourier transforms: analysis, applications and fast algorithms. 2008.

Coman Melissa Anne, Wells Mathew Graeme. Temperature variability in the nearshore benthic boundary layer of Lake Opeongo is due to wind-driven upwelling events // Canadian Journal of Fisheries and Aquatic Sciences. 2 2012. 69, 2. 282–296.

Cooley James W, Tukey John W. An algorithm for the machine calculation of complex Fourier series // Mathematics of computation. 1965. 19, 90. 297–301.

Cossu Remo, Wells Mathew G. The interaction of large amplitude internal seiches with a shallow sloping lakebed: observations of benthic turbulence in Lake Simcoe, Ontario, Canada // PloS one. 2013. 8, 3. e57444.

Cushman-Roisin Benoit, Beckers Jean-Marie. Introduction to geophysical fluid dynamics: physical and numerical aspects. 101. 2011.

Delft Hydraulics W L. User Manual of Delft3D-FLOW—Simulation of Multi-dimensional Hydrodynamic Flows and Transport Phenomena, Including Sediments. 2003.

Dissanayake Pushpa, Hofmann Hilmar, Peeters Frank. Comparison of results from two 3D hydrodynamic models with field data: Internal seiches and horizontal currents // Inland waters. 2019. 9, 2. 239–260.

Dorostkar Abbas, Boegman Leon. Internal hydraulic jumps in a long narrow lake // Limnology and oceanography. 2013. 58, 1. 153–172.

Eames I, Hogg A J, Gething S, Dalziel S B. Resuspension by saline and particle-driven gravity currents // Journal of Geophysical Research: Oceans. 2001. 106, C7. 14095–14111.

Ekman Vagn Walfrid. On dead water // Sci. Results Norw. Polar Expedi. 1893-96. 1904. 5, 15. 152.

Etemad-Shahidi Amir, Imberger Jorg. Diapycnal mixing in the thermocline of lakes: estimations by different methods // Environmental Fluid Mechanics. 2006. 6, 3. 227–240.

Farge Marie. Wavelet transforms and their applications to turbulence // Annual review of fluid mechanics. 1992. 24, 1. 395–458.

Farmer David M. Observations of long nonlinear internal waves in a lake // Journal of Physical Oceanography. 1978. 8, 1. 63–73.

Fernando Harindra Joseph. Handbook of Environmental Fluid Dynamics, Volume Two: Systems, Pollution, Modeling, and Measurements. 2. 2012.

Flood Bryan, Wells Mathew, Midwood Jonathan D, Brooks Jill, Kuai Yulong, Li Jingzhi. Intense variability of dissolved oxygen and temperature in the internal swash zone of Hamilton Harbour, Lake Ontario // Inland Waters. 2021. 1–18.

Algorithms for the computation of fundamental properties of seawater. // . 1983.

Forcat Francesc, Roget Elena, Figueroa Manuel, Sánchez Xavier. Earth rotation effects on the internal wave field in a stratified small lake // limnetica. 2011. 30, 1. 27–42.

Forch Carl Knudsen Martin e. Hydrographical tables. 1901.

Fricker Paul D, Nepf Heidi M. Bathymetry, stratification, and internal seiche structure // Journal of Geophysical Research: Oceans. 2000. 105, C6. 14237–14251.

Frindte Katharina, Eckert Werner, Attermeyer Katrin, Grossart Hans-Peter. Internal wave-induced redox shifts affect biogeochemistry and microbial activity in sediments: a simulation experiment // Biogeochemistry. 2013. 113, 1-3. 423–434.

Gao Robert X, Yan Ruqiang. Wavelets: Theory and applications for manufacturing. 2010.

Garratt J R. Boundary-layer effects on cold fronts at a coastline // Boundary-layer meteorology. 1986. 36, 1-2. 101–105.

Garrett Christopher, Munk Walter. Space-time scales of internal waves // Geophysical \& Astrophysical Fluid Dynamics. 1972. 3, 1. 225–264.

Gill Adrian E. Atmosphere—ocean dynamics. 2016.

Gloor M, Wüest A, Imboden D M. Dynamics of mixed bottom boundary layers and its implications for diapycnal transport in a stratified, natural water basin // Journal of Geophysical Research: Oceans. 2000. 105, C4. 8629–8646.

Gloor M., Wüest A., Münnich M. Benthic boundary mixing and resuspension induced by internal seiches // Hydrobiologia. 5 1994. 284, 1. 59–68.

Govorushko Sergey M. Natural processes and human impacts: interactions between humanity and the environment. 2011.

Gray James R. Conductivity analyzers and their application // Environmental instrumentation and analysis handbook. 2005. 491–510.

Greenberg Michael D. Foundations of applied mathematics. 2013.

Grimshaw Roger. Environmental stratified flows. 2002.

Grundy R E, Rottman James W. The approach to self-similarity of the solutions of the shallow-water equations representing gravity-current releases // Journal of fluid mechanics. 1985. 156. 39–53.

Gubbins David. Time series analysis and inverse theory for geophysicists. 2004.

Guseva Sofya, Casper Peter, Sachs Torsten, Spank Uwe, Lorke Andreas. Energy Flux Paths in Lakes and Reservoirs // Water. 2021. 13, 22. 3270.

Hallworth Mark A, Phillips Jeremy C, Huppert Herbert E, Sparks R Stephen J. Entrainment in turbulent gravity currents // Nature. 1993. 362, 6423. 829–831.

Hazewinkel J. Attractors in stratified fluids. Netherlands, 3 2010.

Heaps Norman S, Ramsbottom A E. Wind effects on the water in a narrow two-layered lake. Part I. Theoretical analysis. Part II. Analysis of observations from Windermere. Part III. Application of the theory to Windermere // Phil. Trans. R. Soc. Lond. A. 1966. 259, 1102. 391–430.

Heinzel Gerhard, Rüdiger Albrecht, Schilling Roland. Spectrum and spectral density estimation by the Discrete Fourier transform (DFT), including a comprehensive list of window functions and some new at-top windows // Max Plank Inst. 2002.

Herman Stephen L. Electronics for electricians. 2011.

Hingsamer Peter, Peeters Frank, Hofmann Hilmar. The consequences of internal waves for phytoplankton focusing on the distribution and production of Planktothrix rubescens // PloS one. 2014. 9, 8. e104359.

Hodges Ben R, Imberger Jörg, Saggio Angelo, Winters Kraig B. Modeling basin-scale internal waves in a stratified lake // Limnology and oceanography. 2000. 45, 7. 1603–1620.

Hodges Ben R., Laval Bernard, Wadzuk Bridget M. Numerical error assessment and a temporal horizon for internal waves in a hydrostatic model // Ocean Modelling. 1 2006. 13, 1. 44–64.

Hongve Dag. Seasonal Mixing and Genesis of Endogenic Meromixis in Small Lakes in Southeast Norway // Hydrology Research. 4 2002. 33, 2-3. 189–206.

Horn D A, Imberger J, Ivey G N. The degeneration of basin-scale internal waves in lakes // Thirteenth Australasian Fluid Mechanics Conference. Monash University, 1998. 863–866.

Horn D A, Imberger Jorg, Ivey G N. The degeneration of large-scale interfacial gravity waves in lakes // Journal of Fluid Mechanics. 2001. 434. 181–207.

Horn Wilfried, Mortimer Clifford Hiley, Schwab David J. Wind-induced internal seiches in Lake Zurich observed and modeled // Limnol. Oceanogr. 1986. 31, 6. 1232–1254.

Huber Andrea M R, Peeters Frank, Lorke Andreas. Active and passive vertical motion of zooplankton in a lake // Limnology and Oceanography. 2011. 56, 2. 695–706.

Hunkins Kenneth, Fliegel Myron. Internal undular surges in Seneca Lake: A natural occurrence of solitons // Journal of geophysical research. 1973. 78, 3. 539–548.

Huppert Herbert E, Simpson John E. The slumping of gravity currents // Journal of Fluid Mechanics. 1980. 99, 4. 785–799.

Hutter Kolumban. Avalanche dynamics // Hydrology of disasters. 1996. 317–394.

Hutter Kolumban. Nonlinear internal waves in lakes. 2011.

Hutter Kolumban, Wang Yongqi, Chubarenko Irina P. Physics of Lakes, volume 2: lakes as oscillators. Advances in geophysical and environmental mechanics and mathematics. 2011.

Idso Sherwood B. On the concept of lake stability // Limnology and Oceanography. 7 1973. 18, 4. 681–683.

Imam Yehya E, Laval Bernard, Pieters Roger, Lawrence Gregory. The baroclinic response to wind in a multiarm multibasin reservoir // Limnology and Oceanography. 2020. 65, 3. 582–600.

Transport processes in lakes: A review. // . 1994.

Imberger Jorg. Physical processes in lakes and oceans. 54. 1998.

Imberger Jorg. Flux Paths in a Stratified Lake. 2013. 1–17.

Imberger Jorg, Loh Ian, Hebbert Bob, Patterson John. Dynamics of Reservoir of Medium Size // Journal of the Hydraulics Division. 5 1978. 104, 5. 725–743.

Imberger Jörg, Patterson John C. Physical limnology // Advances in applied mechanics. 27. 1989. 303–475.

Imboden Dieter. The Lakes Handbook, Volume 1. Malden, MA, USA: Blackwell Science Ltd, 12 2003.

Imboden Dieter M, Wüest Alfred. Mixing mechanisms in lakes // Physics and chemistry of lakes. 1995. 83–138.

Intergovernmental Oceanographic Commission , others . The International thermodynamic equation of seawater–2010: calculation and use of thermodynamic properties. Corrections – 2015. 2015.

Jkedrasik Jan, Kowalewski Marek. Mean annual and seasonal circulation patterns and long-term variability of currents in the Baltic Sea // Journal of Marine Systems. 2019. 193. 1–26.

Kell George S. Density, thermal expansivity, and compressibility of liquid water from 0. deg. to 150. deg.. correlations and tables for atmospheric pressure and saturation reviewed and expressed on 1968 temperature scale // Journal of Chemical and Engineering Data. 1975. 20, 1. 97–105.

Kranenburg Wouter, Tiessen Meinard, Veenstra Jelmer, Graaff Reimer de, Uittenbogaard Rob, Bouffard Damien, Sakindi Gaetan, Umutoni Augusta, Walle Jonas de, Thiery Wim, others . 3D-modelling of Lake Kivu: Horizontal and vertical flow and temperature structure under spatially variable atmospheric forcing // Journal of Great Lakes Research. 2020. 46, 4. 947–960.

Kyrousi Foteini, Leonardi Alessandro, Roman Federico, Armenio Vincenzo, Zanello Francesca, Zordan Jessica, Juez Carmelo, Falcomer Luca. Large Eddy Simulations of sediment entrainment induced by a lock-exchange gravity current // Advances in Water Resources. 2018. 114. 102–118.

The heat balance of the North Sea. // . 1989.

Legg Sonya, Briegleb Bruce, Chang Yeon, Chassignet Eric P, Danabasoglu Gokhan, Ezer Tal, Gordon Arnold L, Griffies Stephen, Hallberg Robert, Jackson Laura, others . Improving oceanic overflow representation in climate models: the gravity current entrainment climate process team // Bulletin of the American Meteorological Society. 2009. 90, 5. 657–670.

Lemckert C, Imberger Jorg. Turbulent benthic boundary layer mixing events in fresh water lakes // Physical processes in lakes and oceans. 1998. 54. 503–516.

Lemmin U, D'Adamo N. Summertime winds and direct cyclonic circulation: observations from Lake Geneva // Annales Geophysicae. 14, 11. 1997. 1207–1220.

Lemmin U, Mortimer C H, Bäuerle E. Internal seiche dynamics in Lake Geneva // Limnology and Oceanography. 2005. 50, 1. 207–216.

Lemmin Ulrich. The structure and dynamics of internal waves in Baldeggersee // Limnol. Oceanogr. 1987. 32, 1. 43–61.

Lemmin Ulrich, Mortimer Clifford Hiley. Tests of an extension to internal seiches of Defant's procedure for determination of surface seiche characteristics in real lakes // Limnology and oceanography. 1986. 31, 6. 1207–1231.

Likens Gene E. Lake ecosystem ecology: A global perspective. 2010.

Lin Henry. Hydropedology: Synergistic integration of soil science and hydrology. 2012.

Lin S, Boegman L, Rao Y R. Characterizing spatial and temporal distributions of turbulent mixing and dissipation in Lake Erie // Journal of Great Lakes Research. 2021. 47, 1. 168–179.

List John E., Fischer Hugo B., Koh C. Robert. Mixing in Inland and Coastal Waters. 1979.

Lorke Andreas. Boundary mixing in the thermocline of a large lake // Journal of Geophysical Research: Oceans. 2007. 112, C9.

Lorke Andreas, Peeters Frank, Bäuerle Erich. High-frequency internal waves in the littoral zone of a large lake // Limnology and oceanography. 2006. 51, 4. 1935–1939.

Lorke Andreas, Peeters Frank, Wüest Alfred. Shear-induced convective mixing in bottom boundary layers on slopes // Limnology and Oceanography. 2005. 50, 5. 1612–1619.

Lorke Andreas, Umlauf L., Mohrholz V. Stratification and mixing on sloping boundaries // Geophysical Research Letters. 7 2008. 35, 14.

Maas Leo R. M. Wave attractors: Linear yet nonlinear // International Journal of Bifurcation and Chaos. 9 2005. 15, 09. 2757–2782.

MacIntyre S. The Surface Mixed Layer in Lakes and Reservoirs // Biogeochemistry of Inland Waters. 2010. 207.

MacIntyre Sally, Clark Jordan F, Jellison Robert, Fram Jonathan P. Turbulent mixing induced by nonlinear internal waves in Mono Lake, California // Limnology and Oceanography. 2009. 54, 6. 2255–2272.

Mahrt L., Lenschow D. H. Growth Dynamics of the Convectively Mixed Layer // Journal of the Atmospheric Sciences. 1 1976. 33, 1. 41–51.

Marino B M, Thomas L P, Linden P F. The front condition for gravity currents // Journal of Fluid Mechanics. 2005. 536. 49–78.

Michallet H, Ivey G N. Experiments on mixing due to internal solitary waves breaking on uniform slopes // Journal of Geophysical Research: Oceans. 1999. 104, C6. 13467–13477.

Miles John W. On the stability of heterogeneous shear flows // Journal of Fluid Mechanics. 1961. 10, 4. 496–508.

Millette Pierre A. The heisenberg uncertainty principle and the nyquist-shannon sampling theorem // arXiv preprint arXiv:1108.3135. 2011.

Moreira Santiago, Schultze Martin, Rahn Karsten, Boehrer Bertram. A practical approach to lake water density from electrical conductivity and temperature // Hydrology and Earth System Sciences. 7 2016. 20, 7. 2975–2986.

Mortimer C H. The resonant response of stratified lakes to wind // Schweizerische Zeitschrift für Hydrologie. 1953. 15, 1. 94–151.

Mortimer C H. Some effects of the earth's rotation on water movements in stratified lakes. 1955.

Mortimer C. H. A treatise on limnology. Volume 1. Geography, physics and chemistry // Limnology and Oceanography. 1 1959. 4, 1. 108–114.

Mortimer C H. Strategies for coupling data collection and analysis with dynamic modelling of lake motions // Developments in Water Science. 1979. 11. 183–222.

Mortimer Clifford H, Horn Wilfried. Internal wave dynamics and their implications for plankton biology in the Lake of Zurich // Vier. Natur. Gesell. Zurich. 1982. 127. 299–318.

Mortimer Clifford Hiley. The use of models in the study of water movement in stratified lakes: With 6 figures in the text and on 2 folders // Internationale Vereinigung für theoretische und angewandte Limnologie: Verhandlungen. 1950. 11, 1. 254–260.

Mortimer Clifford Hiley. Water movements in lakes during summer stratification; evidence from the distribution of temperature in Windermere // Philosophical Transactions of the Royal Society of London B: Biological Sciences. 1952. 236, 635. 355–398.

Large-scale oscillatory motions and seasonal temperature changes in Lake Michigan and Lake Ontario. // . 1971.

Mortimer Clifford Hiley. Lake Michigan in motion: Responses of an inland sea to weather, earth-spin, and human activities. 2004.

Mowbray D. E., Rarity B. S. H. A theoretical and experimental investigation of the phase configuration of internal waves of small amplitude in a density stratified liquid // Journal of Fluid Mechanics. 4 1967. 28, 1. 1–16.

Münnich Matthias, Wüest Alfred, Imboden Dieter M. Observations of the second vertical mode of the internal seiche in an alpine lake // Limnology and oceanography. 1992. 37, 8. 1705–1719.

Murakami Mayumi, Oonishi Yukio, Kunishi Hideaki. A numerical simulation of the distribution of water temperature and salinity in the Seto Inland Sea // Journal of the oceanographical society of Japan. 1985. 41, 4. 213–224.

Mysak Lawrence A. Nonlinear internal waves // Hydrodynamics of Lakes. 1984. 129–152.

Nansen Fridtjof. Farthest North: The epic adventure of a visionary explorer. 1. 1897.

Niiler Pearn P. Deepening of the wind-mixed layer // Journal of Marine Research. 1975.

Ostrovsky L A, Kazakov V I, Matusov P A, Zaborskikh D V. Experimental study of the internal wave damping on small-scale turbulence // Journal of physical oceanography. 1996. 26, 3. 398–405.

Pannard Alexandrine, Beisner Beatrix E, Bird David F, Braun Jean, Planas Dolors, Bormans Myriam. Recurrent internal waves in a small lake: Potential ecological consequences for metalimnetic phytoplankton populations // Limnology and Oceanography: Fluids and Environments. 2011. 1, 1. 91–109.

Pickering Kevin T, Underwood Michael B, Taira Asahiko. Open-ocean to trench turbidity-current flow in the Nankai Trough: Flow collapse and reflection // Geology. 1992. 20, 12. 1099–1102.

Pollard Raymond T., Rhines Peter B., Thompson Rory O. R. Y. The deepening of the wind-Mixed layer // Geophysical Fluid Dynamics. 3 1973. 4, 4. 381–404.

Polli Bruna Arcie, Bleninger Tobias. Comparison of 1D and 3D reservoir heat transport models and temperature effects on mass transport // RBRH. 2019. 24.

Posada-Bedoya Andrés, Gómez-Giraldo Andrés, Román Botero Ricardo. Preliminary characterization of the dominant baroclinic modes of a tropical Andean reservoir during a dry period // Revista de la Academia Colombiana de Ciencias Exactas, Físicas y Naturales. 7 2019. 43, 167. 297.

Preusse Martina, Peeters Frank, Lorke Andreas. Internal waves and the generation of turbulence in the thermocline of a large lake // Limnology and oceanography. 2010. 55, 6. 2353–2365.

Ravens Thomas M, Kocsis Otti, Wüest Alfred, Granin N. Small-scale turbulence and vertical mixing in Lake Baikal // Limnology and oceanography. 2000. 45, 1. 159–173.

Read Jordan S, Hamilton David P, Jones Ian D, Muraoka Kohji, Winslow Luke A, Kroiss Ryan, Wu Chin H, Gaiser Evelyn. Derivation of lake mixing and stratification indices from high-resolution lake buoy data // Environmental Modelling \& Software. 2011. 26, 11. 1325–1336.

Rinke Karsten, Hübner Ina, Petzoldt Thomas, Rolinski Susanne, KÖNIG-RINKE MARIE, Post Johannes, Lorke Andreas, Benndorf Jürgen. How internal waves influence the vertical distribution of zooplankton // Freshwater Biology. 2007. 52, 1. 137–144.

Rodrigo María A., Miracle María R., Vicente Eduardo. The meromictic Lake La Cruz (Central Spain). Patterns of stratification // Aquatic Sciences. 12 2001. 63, 4. 406–416.

Roget E, Salvadé G, Zamboni F. Internal seiche climatology in a small lake where transversal and second vertical modes are usually observed // Limnol. Oceanogr. 1997. 42, 4. 663–673.

Roget Elena, Colomer Jordi. Flow characteristics of a gravity current induced by differential cooling in a small lake // Aquatic sciences. 1996. 58, 4. 367–377.

Rottman James W, Simpson John E. Gravity currents produced by instantaneous releases of a heavy fluid in a rectangular channel // Journal of Fluid Mechanics. 1983. 135. 95–110.

Rozas Carlos, Fuente Alberto de la, Ulloa Hugo, Davies Peter, Niño Yarko. Quantifying the effect of wind on internal wave resonance in Lake Villarrica, Chile // Environmental Fluid Mechanics. 12 2013.

Rudnick Daniel L, Boyd Timothy J, Brainard Russell E, Carter Glenn S, Egbert Gary D, Gregg Michael C, Holloway Peter E, Klymak Jody M, Kunze Eric, Lee Craig M, others . From tides to mixing along the Hawaiian Ridge // science. 2003. 301, 5631. 355–357.

Saggio Angelo, Imberger Jörg. Internal wave weather in a stratified lake // Limnology and oceanography. 1998a. 43, 8. 1780–1795.

Saggio Angelo, Imberger Jörg. Internal wave weather in a stratified lake // Limnology and oceanography. 1998b. 43, 8. 1780–1795.

Salvadè G, Zamboni F, Barbieru A. Three-layer model of the north basin of the Lake of Lugano // Annales geophysicae. Atmospheres, hydrospheres and space sciences. 6, 4. 1988. 463–474.

Schmidt Wilhelm. Über Die Temperatur- Und Stabili-Tätsverhältnisse Von Seen // Geografiska Annaler. 8 1928. 10, 1-2. 145–177.

Scotti Alberto, Pineda Jesus. Plankton accumulation and transport in propagating nonlinear internal fronts // Journal of Marine Research. 2007. 65, 1. 117–145.

Sherman F S, Imberger J, Corcos G M. Turbulence and Mixing in Stably Stratified Waters // Annual Review of Fluid Mechanics. 1 1978. 10, 1. 267–288.

Shimizu Kenji. A Theory of Vertical Modes in Multilayer Stratified Fluids // Journal of Physical Oceanography. 9 2011. 41, 9. 1694–1707.

Shimizu Kenji. Fully nonlinear simple internal waves over subcritical slopes in continuously stratified fluids: Theoretical development // Physics of Fluids. 1 2019. 31, 1. 016601.

Shimizu Kenji, Imberger Jörg. Energetics and damping of basin-scale internal waves in a strongly stratified lake // Limnol. Oceanogr. 2008. 53, 4. 1574–1588.

Shin J O, Dalziel S B, Linden P F. Gravity currents produced by lock exchange // J Fluid Mech. 2004. 521. 1–34.

Simpson J E, Britter R E. The dynamics of the head of a gravity current advancing over a horizontal surface // Journal of Fluid Mechanics. 1979. 94, 3. 477–495.

Simpson J. H., Wiles P. J., Lincoln B. J. Internal seiche modes and bottom boundary-layer dissipation in a temperate lake from acoustic measurements // Limnology and Oceanography. 9 2011a. 56, 5. 1893–1906.

Simpson J H, Wiles P J, Lincoln B J. Internal seiche modes and bottom boundary-layer dissipation in a temperate lake from acoustic measurements // Limnology and oceanography. 2011b. 56, 5. 1893–1906.

Smith Gordon D, Smith Gordon D, Smith Gordon Dennis Smith. Numerical solution of partial differential equations: finite difference methods. 1985.

Smith Steven. Digital signal processing: a practical guide for engineers and scientists. 2013.

Socolofsky Scott A., Jirka Gerhard H. Special Topics in Mixing and Transport Processes in the Environment. 1. Texas: Texas A&M University, 2005. 5.

Spigel Robert Hays, Imberger Jörg. The classification of mixed-layer dynamics of lakes of small to medium size // Journal of physical oceanography. 1980. 10, 7. 1104–1121.

Stelling Guss S, Duinmeijer S P Alex. A staggered conservative scheme for every Froude number in rapidly varied shallow water flows // International journal for numerical methods in fluids. 2003. 43, 12. 1329–1354.

Stevens Craig, Lawrence Gregory, Hamblin Paul, Carmack Eddy. Wind forcing of internal waves in a long narrow stratified lake // Dynamics of atmospheres and oceans. 1996. 24, 1-4. 41–50.

Stevens Craig L. Internal waves in a small reservoir // J Geophys Res Oceans. 1999. 104, C7. 15777–15788.

Stocker K, Hutter K, Salvadè G, Trosch J, Zamboni F. Observations and analysis of internal seiches in the southern basin of Lake of Lugano // Annales geophysicae. Series B. Terrestrial and planetary physics. 5, 6. 1987. 553–568.

Sutherland B. R., Linden P. F. Internal wave excitation by a vertically oscillating elliptical cylinder // Physics of Fluids. 2 2002. 14, 2. 721–731.

Internal Waves in Laboratory Experiments. // . 11 2014. 193–212.

Sutherland Bruce R. Internal gravity waves. 2010.

Tait P G. Voy. Challenger Rep. 2 (Phys. and Chem.). IV. Report on some of the physical properties of fresh and sea water. 1888.

Tanaka M, Girard G, Davis R, Peuto A, Bignell N. Recommended table for the density of water between 0 C and 40 C based on recent experimental reports // Metrologia. 8 2001. 38, 4. 301–309.

Taylor H Rosemary. Data acquisition for sensor systems. 5. 1997.

Thomson Richard E, Emery William J. Data analysis methods in physical oceanography. 2014.

Thorpe S A. On the interactions of internal waves reflecting from slopes // Journal of physical oceanography. 1997. 27, 9. 2072–2078.

Thorpe Steve A. The turbulent ocean. 2005.

Thoulet Julien. Contribution a l'Etude des lacs des Vosges. 1894.

Torrence Christopher, Compo Gilbert P. A practical guide to wavelet analysis // Bulletin of the American Meteorological society. 1998. 79, 1. 61–78.

Uittenbogaard R E, Van Kester JATM, Stelling G S. Implementation of three turbulence models in 3D-TRISULA for rectangular grids // Report Z81, Delft Hydraulics. 1992.

Umlauf Lars, Lemmin Ulrich. Interbasin exchange and mixing in the hypolimnion of a large lake: The role of long internal waves // Limnol. Oceanogr. 2005. 50, 5. 1601–1611.

Valerio Giulia, Pilotti Marco, Marti Clelia Luisa, Imberger Jö rg. The structure of basin-scale internal waves in a stratified lake in response to lake bathymetry and wind spatial and temporal distribution: Lake Iseo, Italy // Limnology and Oceanography. 2012. 57, 3. 772–786.

Vidal Javier, Casamitjana Xavier, Colomer Jordi, Serra Teresa. The internal wave field in Sau reservoir: Observation and modeling of a third vertical mode // Limnol. Oceanogr. 2005. 50, 4. 1326–1333.

Vidal Javier, MacIntyre Sally, McPhee-Shaw Erika E., Shaw William J., Monismith Stephen G. Temporal and spatial variability of the internal wave field in a lake with complex morphometry // Limnology and Oceanography. 9 2013. 58, 5. 1557–1580.

Vidal Javier, Rueda Francisco J, Casamitjana Xavier. The seasonal evolution of high vertical-mode internal waves in a deep reservoir // Limnology and oceanography. 2007. 52, 6. 2656–2667.

Wadzuk Bridget Marie, Hodges Ben R. Hydrostatic and non-hydrostatic internal wave models. 2004.

Watson E R. Movements of the waters of Loch Ness, as indicated by temperature observations // The Geographical Journal. 1904. 24, 4. 430–437.

Watson Edwin Roy. Internal oscillation in the waters of Loch Ness // Nature. 1903. 69. 174.

Wedderburn E M. Temperature Observations in Loch Earn; with a further Contribution to the Hydrodynamical Theory of the Temperature Seiche // Earth and Environmental Science Transactions of The Royal Society of Edinburgh. 1912. 48, 3. 629–695.

Wedderburn Ernest Maclagan, Williams A M. The Temperature Seiche. Part II. Hydrodynamical Theory of Temperature Oscillations in Lakes. // Earth and Environmental Science Transactions of The Royal Society of Edinburgh. 1911. 47, 4. 628–634.

Wedderburn Ernest Maclagan, Young Andrew White. Temperature Observations in Loch Earn, Part II. // Earth and Environmental Science Transactions of The Royal Society of Edinburgh. 1915. 50, 4. 741–767.

Welch Peter. The use of fast Fourier transform for the estimation of power spectra: a method based on time averaging over short, modified periodograms // IEEE Transactions on audio and electroacoustics. 1967. 15, 2. 70–73.

Wells Mathew Graeme, Sherman Bradford. Stratification produced by surface cooling in lakes with significant shallow regions // Limnology and Oceanography. 11 2001. 46, 7. 1747–1759.

Wetzel Robert G. Limnology: lake and river ecosystems. 2001.

Wiegand Ronald C, Chamberlain Vivian. Internal waves of the second vertical mode in a stratified lake // Limnol. Oceanogr. 1987. 32, 1. 29–42.

Wiel Karin van der, Gille Sarah T, Llewellyn Smith Stefan G, Linden P F, Cenedese Claudia. Characteristics of colliding sea breeze gravity current fronts: a laboratory study // Quarterly Journal of the Royal Meteorological Society. 2017. 143, 704. 1434–1441.

Wu Shu, Liu Qinyu. Some problems on the global wavelet spectrum // Journal of Ocean University of China. JOUC. 2005. 4, 4. 398.

Wüest A, Lorke A. Small-scale turbulence and mixing: Energy fluxes in stratified lakes // Encyclopedia of inland waters. 2009. 1, BOOK_CHAP. 628–635.

Wüest Alfred, Lorke Andreas. Small-scale hydrodynamics in lakes // Annual Review of fluid mechanics. 2003. 35, 1. 373–412.

Wüest Alfred, Piepke Gabriel, Van Senden David C. Turbulent kinetic energy balance as a tool for estimating vertical diffusivity in wind-forced stratified waters // Limnology and Oceanography. 2000. 45, 6. 1388–1400.

Wynn Russell B, Masson Douglas G, Stow Dorrik A V, Weaver Philip P E. Turbidity current sediment waves on the submarine slopes of the western Canary Islands // Marine Geology. 2000. 163, 1-4. 185–198.

Yih C. S. A study of the characteristics of gravity waves at a liquid interface. 1947.